NATIONAL AERONAUTICS AND SPACE ADMINISTRATION

Technical Memorandum 33-432

Surveyor Batteries

Final Engineering Report

A. J. Moses, W. M. Hetherington, D. Weinberger
Hughes Aircraft Co.,
Culver City, Calif.

A. A. Uchiyama, R. S. Bogner, W. L. Long
Jet Propulsion Laboratory
Pasadena, Calif.

JET PROPULSION LABORATORY
CALIFORNIA INSTITUTE OF TECHNOLOGY
PASADENA, CALIFORNIA

February 15, 1970

NATIONAL AERONAUTICS AND SPACE ADMINISTRATION

Technical Memorandum 33-432

Surveyor Batteries

Final Engineering Report

A. J. Moses, W. M. Hetherington, D. Weinberger
Hughes Aircraft Co.,
Culver City, Calif.

A. A. Uchiyama, R. S. Bogner, W. L. Long
Jet Propulsion Laboratory
Pasadena, Calif.

JET PROPULSION LABORATORY
CALIFORNIA INSTITUTE OF TECHNOLOGY
PASADENA, CALIFORNIA

February 15, 1970

Prepared Under Contract No. NAS 7-100
National Aeronautics and Space Administration

Preface

The work described in this report was performed by the Hughes Aircraft Company and the Guidance and Control Division of the Jet Propulsion Laboratory, under the cognizance of the *Surveyor* Project.

This summary provides a historical documentation of the development of the *Surveyor* main battery starting late in 1961 and continuing through February 1968 when all seven *Surveyor* spacecraft launchings were completed. The evolution of the battery design from sealed single cells to a manifold design is described in a chronological sequence. The vast amount of written material and test data available from the Jet Propulsion Laboratory, Pasadena, Calif., Hughes Aircraft Co., Culver City, Calif., and ESB Inc., Raleigh, N. C., (formerly Electric Storage Battery Co.), provided the basis of this report. Careful attention has been given to presentation of the most significant data so the reader will be able to follow the design decisions. In addition, these data may be useful in considering future battery designs.

Contents

I. Introduction 1

A. General 1

B. *Surveyor* Main Battery Models 4

C. Program Milestones and Schedule 5

II. Performance Requirements 5

A. System Electrical Energy Requirements 5

B. Battery Thermal Environment 6

C. Battery Electrical Performance Requirements 6

1. Discharge capability 6

2. Charge capability 7

3. Storage capability 7

4. Operating life 7

5. Changes in electrical requirements 8

D. Environmental Requirements 8

1. Electrical performance during tests 8

2. Shock test requirements 8

3. Acceleration test requirements 8

4. Vibration test requirements 9

III. Experimental Model *Surveyor* Main Battery 11

A. Description 11

1. Negative plates 11

2. Positive plates 11

3. Separators 11

4. Electrolyte 13

B. Tests on Cells and Monoblocks 13

1. Charge tests 13

2. Stand loss for charged storage 17

3. Stand loss for discharged storage 17

4. Direct current impedance test 18

C. Mission Simulation Tests 20

1. Simulation of lunar day 1 20

2. Lunar night simulation 20

D. Test Program on Experimental Model *Surveyor* Main Battery . . . 21

Contents (contd)

1. Types of tests 21
2. General inspection test and receiving procedure 22
3. Initial capacity test 22
4. Dynamic charge surge and internal impedance test 23
5. Charge matrix test 24
6. Discharge matrix test 25
7. Cycle life test 27
8. Magnetometer survey 27

E. Failure Analysis 28
1. Failure of cells by shorting 28
2. Failure of cells by cracking of cell cases 28
3. Premature charge termination 28

F. Battery Development 29
1. Density variations in negative active material (negative electrode) 29
2. Density variations in positive active material (positive electrode) 29
3. Effect of positive plate density on electrode performance . . . 29
4. Dynamic charge surge tests 29
5. Causes and potential remedies for charge surge 30
6. Separator material 32
7. Electrolyte 32
8. Intercell connectors 33
9. Cell case 33
10. Battery sterilization 36

G. Conclusions 36

IV. Development Model *Surveyor* Main Battery 37

A. General Features 37
B. Cell Details 38
C. Parametric Tests 38
1. Initial charge 38
2. Initial capacity 40
3. Float charge 40
4. Cycle life 41

Contents (contd)

D. Mission Simulation Tests 41

1. Lunar night discharge 41

2. Lunar day high rate discharge 41

3. Environmental tests 41

E. Conclusions 41

V. Prototype Model Surveyor Main Battery 42

A. Description of the Prototype Model Battery 42

1. General 42

2. Monoblock and canister development 42

3. Manifold 45

4. Pressure and temperature transducers 46

5. Cell details 46

6. Weight and balance 47

B. Test Program 47

1. Data processing 47

2. Battery charging 48

3. Discharge tests 57

4. Cycle life tests 63

C. Type Approval Tests 64

1. Vibration problems 64

2. Shock tests on cells 66

3. Thermal-vacuum tests 67

D. Conclusions Concerning the Prototype Model Battery Program 67

VI. Flight Model Surveyor Main Battery 68

A. Performance Tests 68

1. Battery operating limits 68

2. Discharge efficiency 68

3. Charge cutoff 69

B. Problem Areas and Solutions 69

1. Low pulse potential problem 69

2. Battery terminal potential problems from deletion of the auxiliary battery 71

Contents (contd)

C. Materials and Process Investigations 73

1. Measurement of bond strength of cements 73

2. Calculation of bonding area, joining cover to four-cell monoblock 73

3. Measurement of bond strength 73

D. Conclusions 74

VII. Special Tests and Flight Performance of Flight Model Battery 75

A. Lunar Night Survival Test 75

1. Test Program 75

2. Results 75

3. Discussion 75

4. Conclusions and recommendations 75

B. Low Temperature Operation 79

1. Test procedure 79

2. Results 83

3. Conclusions 83

C. The A-21E Program 85

1. Thermal behavior of the battery 86

2. Lunar surface operation simulation 101

D. Solar–Thermal–Vacuum Tests 103

E. Flight and Postflight Data 106

1. Data presentation 106

2. Discussion 107

F. Conclusions 115

VIII. Battery Reliability 116

A. Introduction 116

B. Reliability Test Program 116

1. Battery reliability tests (ESB) 116

2. Mission simulation tests (HAC) 116

C. Failure Analysis 117

1. Failure mode analysis 117

2. Analysis of typical flight battery failures 117

Contents (contd)

D. Reliability Growth of *Surveyor* Main Battery 131

1. Methods of calculation 136

2. Results and discussion 137

E. Conclusions 137

IX. *Surveyor* Auxiliary Battery 137

A. Purpose 137

B. Program Summary 137

C. Performance Requirements 138

D. Battery Design Description 138

1. General 138

2. Electrical 139

3. Activation 140

E. Auxiliary Battery Performance 140

1. Parametric tests 140

2. Flight acceptance tests 142

3. Reliability tests and reliability 142

4. Solar–thermal–vacuum tests 142

5. Flight experience 142

F. Conclusions 143

Appendix. Definition of terms 144

References 146

Tables

1. Program milestones for *Surveyor* main battery 5

2. System electrical energy consumption, generation, and capacity values 6

3. Mission power profile 7

4. Changes in power profile 8

5. Physical characteristics of *Surveyor* experimental model cell . . . 12

6. Voltage at start of gassing 14

7. Discharge voltage at 7 A for charged stand 18

8. Discharged stand test 19

Contents (contd)

Tables (contd)

9. Program for simulation test of lunar day 1 by a five-cell experimental model monoblock 20
10. Lunar night simulation test plan 21
11. Results of general inspection test and receiving procedure of experimental model batteries 23
12. Results of initial capacity test on experimental model batteries 24
13. Magnetometer survey data 28
14. Gassing rate at 160°F for positive plates 31
15. Voltage transient analysis 31
16. Intercell connector test 34
17. Cell case burst data 34
18. Material properties 35
19. Thermal stresses in cell cases 35
20. Sterilization samples 37
21. Weight estimate for experimental and development model *Surveyor* batteries 38
22. Characteristics of *Surveyor* development model battery cells . . . 39
23. Cell variation test I 39
24. Cell variation test II 40
25. Separator systems 40
26. Capacity data for development batteries 40
27. Characteristics of prototype and flight model cells 43
28. Burst pressure test data for prototype model battery 44
29. Volume available for electrolyte 47
30. Prototype battery weight and balance 48
31. Performance of prototype model test cells SNs Q-1 through Q-5 52
32. Effect of negative weight distribution on cell performance . . . 53
33. Effect of pack tightness on prototype model cell performance . . . 53
34. Prototype model test cells with positive plate from previous production run 53
35. Effect of positive plate separator on cell performance 54
36. Performance of cells using all cellophane separators 54

Contents (contd)

Tables (contd)

37. Performance of cells containing wicks 55
38. Test cell data 56
39. Positive plate characteristics 57
40. Charged stand test data for prototype model cells 58
41. Main battery discharge efficiency summary 63
42. Configuration characteristics of vibration test cells 64
43. Configuration changes to vibration test cells 65
44. Effect of vibration on test cells 66
45. Monoblock mechanical configurations 66
46. Second cycle charge acceptance 66
47. Type approval test vibration results inside cell 67
48. Shock test of prototype cell 67
49. Results of flight battery discharge efficiency tests 69
50. Summary of critical cell components 70
51. Surface area determination of silver powder 70
52. Silver lot characteristics 71
53. Porosity tests on positive plates 71
54. Cellophane tests 72
55. Matrix for special test cells 72
56. Results of discharge tests on special test cells 72
57. Main battery test data for terminal descent phase 73
58. Calculated strength for blue RMD-4511/PS-211 joint 73
59. Effect of operating temperature on bond strength of catalyzed polystyrene cement: test I 74
60. Effect of operating temperature on bond strength of catalyzed polystyrene cement: test II 74
61. Temperature profiles for lunar night survival test 75
62. Battery history, lunar night survival test 78
63. Summary of battery parameters, lunar night survival test 79
64. Sequence I, RADVS simulation 82
65. Sequence II, RADVS simulation 82
66. Cell potentials during −40°F, 1.0-A discharge 83
67. Approximate dc impedance values 86

Contents (contd)

Tables (contd)

68. Test sequence, SN 97 87
69. Test sequence, SN 98 87
70. *Surveyor* main battery capacity compilation (for each charge and discharge cycle) 94
71. Temperature profile 101
72. Load profile 101
73. Test schedule, A21-E lunar surface operation simulation 102
74. Dispersion of test data, A21-E lunar surface operation simulation 106
75. Electrical power performance data, *Surveyor VII* 106
76. Test sequence 116
77. Battery test assignments for reliability tests 117
78. Postmission battery capacity data for reliability test 117
79. Failure mode analysis 126
80. Calculated failure constants 136
81. Auxiliary battery program milestones 138
82. Auxiliary battery watt-hour requirements 138
83. Characteristics of the *Surveyor* auxiliary battery 139
84. Charge tests on discharged battery 141
85. Maximum charge voltage test summary 141

A-1. Trade names 145

Figures

1. Spacecraft system block diagram 2
2. Electrical power subsystem block diagram 3
3. *Surveyor* spacecraft 4
4. Silver–zinc cell voltage characteristics 5
5. Program schedule 5
6. Battery ambient temperature profile 8
7. Type approval, vibration test program 9
8. Type approval, vibration test program, main retroengine 10
9. Type approval, vibration test program, total spacecraft 11
10. *Surveyor* experimental model battery 12

Contents (contd)

Figures (contd)

11. Pressure gage-equipped *Surveyor* experimental model battery 12
12. View of positive and negative assembly—experimental cell 13
13. Negative assembly—experimental cell 13
14. Positive plate assembly—experimental cell 13
15. Details concerning positive plate wrap 14
16. Side view of five-cell container for experimental model battery 14
17. Assembly of monoblocks in experimental model battery 14
18. Charge characteristics of experimental three-cell monoblock for 1-A charge at 60°F 15
19. Charge input vs cutoff voltage for several charging rates at 0°F for experimental three-cell monoblock 15
20. Charge input vs cutoff voltage for several charging rates at 30°F for experimental three-cell monoblock 15
21. Charge input vs cutoff voltage for several charging rates at 60°F for experimental three-cell monoblock 15
22. Charge input vs cutoff voltage for several charging rates at 90°F for experimental three-cell monoblock 16
23. Charge input vs cutoff voltage for several charging rates at 125°F for experimental three-cell monoblock 16
24. Discharge capacity vs charge rate after charge to 40 psig at several temperatures for experimental three-cell monoblock . . . 16
25. Discharge capacity vs temperature after charge to 40 psig at several charging rates for experimental three-cell monoblock . . . 16
26. Capacity retention vs storage temperature for charged storage of experimental cells 17
27. Cell pressure during charged storage vs temperature for experimental cells 17
28. Effect of charged stand temperature on capacity loss rate for experimental cells 18
29. Plot of cell potential as a function of the discharge rate and environmental temperature for experimental model cell 18
30. Direct current impedance vs temperature for several discharge rates for experimental cells 19
31. Discharge curves, five-cell experimental monoblock—simulation test of lunar day 1 20

Contents (contd)

Figures (contd)

32. Experimental model charge curves, experimental model five-cell monoblock—runs 2 and 4—simulation of lunar day 1 . . . 21

33. Charge curves, experimental model five-cell monoblock—runs 6 and 8—simulation of lunar day 1 21

34. Charge curves, experimental model five-cell monoblock—runs 10 and 12—simulation of lunar day 1 22

35. Charge curves, experimental model five-cell monoblock—run 14—simulation of lunar day 1 22

36. Average cell potential of fully charged experimental model five-cell monoblock after 50-ms, 40-A pulse at 30°F 22

37. Simulated lunar night discharge of five-cell experimental model monoblock 23

38. Discharge characteristics of experimental battery X-4 at ambient temperature and constant current 24

39. Charge characteristics of experimental model battery X-4 at ambient temperature and constant current 24

40. Duration of voltage transient vs charging current at 82.8°F for experimental battery X-4 24

41. Maximum charge (transient) voltage vs charging current at 82.8°F for experimental battery X-4 25

42. Results of charge matrix test on experimental model battery 25

43. Typical cell pressure data, obtained during charging of experimental model battery 26

44. Results of discharge matrix test on experimental model battery 26

45. Maximum increase in battery temperature above environmental temperature during discharge matrix test of experimental model battery 27

46. Effect of battery temperature and discharge rate on watt-hour capacity of experimental model *Surveyor* main battery 28

47. Density distribution in active material for positive plates of experimental model cells 29

48. Positive plate density test with special experimental cells . . . 30

49. Peak voltage of initial transient during 1-A charge of five-cell monoblock experimental battery 30

50. Effect of positive plate additive on voltage transient at 1-A charge and 75°F with experimental cells 32

Contents (contd)

Figures (contd)

51. Discharge efficiency of experimental-type cells at 0°F vs KOH concentration 32
52. Discharge efficiency of experimental-type cells at 0°F vs rate 32
53. Capacity loss rate vs KOH concentration for experimental cells at 125°F 33
54. High-current cell discharge voltage as a function of KOH concentration for experimental cells at 35°F 33
55. *Surveyor* development battery (model ESB 204) 38
56. Cycle-life study on developmental model battery 41
57. Potential vs current for high-rate discharge of fully charged developmental model battery 41
58. Monoblock case prototype battery 42
59. Prototype battery 42
60. Side view of monoblock assembly of prototype battery 44
61. Top view of monoblock assembly of flight battery 44
62. End view of monoblock assembly of prototype battery 44
63. Results of burst pressure tests on prototype and flight battery cases and batteries 45
64. Cell construction of prototype battery 45
65. Transducer calibration for prototype battery 46
66. Prototype battery weight and balance 48
67. Typical prototype main battery data plot 49
68. Battery charge characteristics 50
69. Ampere-hour vs charge rate for prototype battery 50
70. Approximate ampere-hour input to 27.30 V vs battery temperature and charge rate for prototype battery 50
71. Charge time to 27.3-V cutoff as a function of charge rate for a prototype battery 50
72. Charge acceptance vs battery temperature for prototype batteries 51
73. Watt-hour charge input vs temperature for a prototype battery 51
74. Average of maximum charge pressures for all engineering test and prototype batteries 51
75. Weight distribution of negative material 52

Contents (contd)

Figures (contd)

76. Positive plate pore size distribution 57
77. Battery potential vs ampere-hour capacity at several temperatures for prototype battery 58
78. Range of discharge capacity (A-h) data vs temperature for prototype batteries 59
79. Voltage regulation of fully charged engineering test battery after 85-A, 5-s pulse 59
80. High current sweep on prototype battery in chamber at 0°F temperature 60
81. High current sweep on prototype battery in chamber at 40°F temperature 60
82. High current sweep on prototype battery at ambient temperature 60
83. High current sweep on prototype battery in chamber at 125°F temperature 60
84. Prototype battery discharge characteristics for upper plateau 61
85. Prototype battery discharge characteristics for lower plateau 61
86. Effect of charged stand temperature on capacity loss rate for prototype model cells 62
87. Voltage vs current for 10-s high current sweep with prototype battery 62
88. Calculated heat generation in prototype battery during discharge 63
89. Cycle life date for prototype battery—ampere-hour data 63
90. Cycle life data for prototype battery—watt-hour data 64
91. *Surveyor* battery in HAC vibration test facility 64
92. Vibration levels in type approval test of prototype batteries . . . 67
93. *Surveyor* main battery—alarm, action, abort 68
94. Charge input vs cutoff potential for flight model *Surveyor* main battery 69
95. Main battery pulse test data 73
96. Bond strengths of catalyzed polystyrene cements 74
97. Lunar night survival test, sequence I 76
98. Lunar night survival test, sequence II 77

Contents (contd)

Figures (contd)

99. Lunar night survival test, sequence I, on *Surveyor* main batteries 115, 119, and 124 80

100. Voltage rise during programmed charge at −40°F lunar night survival test sequence I, *Surveyor* main batteries 115, 119, and 124 80

101. Lunar night survival test sequence II, *Surveyor V* main batteries 105, 116, and 119 81

102. Voltage rise during programmed charge at 40°F, lunar night survival test sequence II, *Surveyor* main batteries 105, 116, and 128 81

103. Comparison of battery discharged at room temperature and voltage discharge characteristics of battery 99 at temperature reduced to −40°F at 5°F per hour 83

104. Low temperature, fully discharged, initial charge voltage . . . 84

105. Battery 99 low temperature charge, fully discharged, charge voltage after 60 s 84

106. Low temperature charge, fully discharged, initial charge voltage 84

107. Low temperature charge, fully discharged, charge voltage after 60 s 85

108. Battery 99 low temperature discharge, low state of charge, initial discharge voltage 85

109. Battery 99 low temperature discharge, low state of charge, discharge voltage after 60 s 85

110. Main battery voltage vs discharge current at various battery temperatures 86

111. Battery capacity vs temperature at discharge rates of 0.5–10.0 A 86

112. Negative plate assembly 87

113. Location of thermocouples 87

114. Thermal test, *Surveyor* main battery 97, summary of temperature–time data 88

115. Thermal test, *Surveyor* main battery 98, summary of temperature–time data 89

116. Thermal test, *Surveyor* main battery 97, 1-A run 90

117. Thermal test, *Surveyor* main battery 97, 3-A run 91

118. Thermal test, *Surveyor* main battery 97, 5-A run 92

119. Thermal test, *Surveyor* main battery 98, 2-A run 93

Contents (contd)

Figures (contd)

120. Thermal test, *Surveyor* main battery 98, open circuit room temperature cooldown 94
121. Thermal test, *Surveyor* main battery 98, 4-A run 95
122. Thermal test, *Surveyor* main battery 98, 5-A run 96
123. Hughes isothermal calorimeter for heat generation measurement by *Surveyor* main batteries 97
124. Isothermal calorimeter 98
125. *Surveyor* battery in isothermal calorimeter 99
126. Heat generation characteristics of *Surveyor* main battery at 24°C 99
127. Heat generation rates of battery 70—3-A charge 100
128. Heat generation rates of battery 70—7-A charge 100
129. Heat generation rates of battery 84, *Surveyor V* Mission profile 101
130. A-21E main power battery subsystem test 1—lunar operation phase—time after touchdown vs temperature, pressure, and voltage 103
131. A-21E main power battery subsystem test 1—lunar operation phase—time after touchdown vs charge current and cell voltages 104
132. A-21E main battery subsystem test 1—lunar operation phase—temperature vs main battery voltage 104
133. A-21E main battery power subsystems tests 1–7 (test 2 omitted), lunar operation phase—battery average voltage vs temperature 104
134. *Surveyor* main battery average voltage vs temperature and various operating rates 105
135. Recharge of main battery during lunar operation (no float charge) 105
136. Main battery potential, *Surveyor I* 106
137. Main battery discharge current, *Surveyor I* 107
138. Main battery temperature, *Surveyor I* 107
139. Main battery manifold pressure, *Surveyor I* 107
140. Battery capacity and total power consumption profile from *Surveyor I* flight 107
141. Main battery temperature during first lunar day, *Surveyor I* . . . 107
142. Main battery temperature, *Surveyor II* 107

Contents (contd)

Figures (contd)

143. Actual vs predicted battery capacity consumption, *Surveyor II* 108
144. Main battery discharge current, *Surveyor II* 108
145. Main battery voltage, *Surveyor II* 108
146. Main battery manifold pressure, *Surveyor II* 109
147. Main battery capacity remaining during transit, *Surveyor III* . . . 109
148. *Surveyor III* flight data for main battery SN 108 109
149. Main battery 123 operation during *Surveyor IV* flight 109
150. Battery capacity remaining, *Surveyor IV* 109
151. *Surveyor V* main battery SN 142 flight performance 110
152. *Surveyor V* battery SN 110 during STV phase A 110
153. Battery capacity profile during transit 110
154. Key spacecraft thermal and power parameters controlled during first lunar night operations 111
155. Battery performance during lunar day, *Surveyor V* 113
156. *Surveyor V* lunar night survival plan and predicted battery temperature profile 113
157. Main battery SN 150, *Surveyor VI* flight 114
158. Main battery SN 117 during *Surveyor VI* STV testing 114
159. Battery energy profile during transit, *Surveyor VII* 115
160. First lunar day battery temperature and energy level, *Surveyor VII* 115
161. *Surveyor VI* reliability test, SN 152 118
162. *Surveyor VI* reliability test, SN 152—7-A discharge 119
163. *Surveyor VI* reliability test, SN 152—2-A discharge 120
164. *Surveyor VI* reliability test, SN 152—2-A charge 121
165. *Surveyor VI* reliability test, SN 154 122
166. *Surveyor VI* reliability test, SN 154—7-A discharge 123
167. *Surveyor VI* reliability test, SN 154—2-A charge 124
168. *Surveyor VI* reliability test, SN 154—2-A charge 125
169. Configuration of positive plate in area of shorts 131
170. Silver content of separator in failed reliability battery, flight model 131
171. Oxalate crystals on positive plate 132

Contents (contd)

Figures (contd)

172. Typical deterioration of separator—*Surveyor* main battery . . . 133
173. Battery life and output characteristics 136
174. Life reliability growth presentation 137
175. Auxiliary battery load and temperature profiles 138
176. Auxiliary battery 138
177. Top view of auxiliary battery, cover removed 139
178. Simplified auxiliary battery schematic showing temperature sensor and Microdot connector 140
179. Simplified schematic of auxiliary battery control unit 140
180. Activation processor 140
181. Cell potential vs discharge rate plateau potential 80°F 141
182. Cell plateau potential vs discharge temperature (60-A discharge rate) 141
183. Auxiliary battery charge retention capacity at 80°F 141
184. Stand time to capacity of 1000 W-h vs temperature 142
185. Transit temperature of auxiliary battery 142
186. Auxiliary battery voltage during transit 142
187. Battery capacity remaining during transit 143

Abstract

Electrical power for the seven *Surveyor* spacecraft was provided by a planar solar panel and a secondary sealed, silver–zinc main battery. The main battery provided energy during transit, touchdown, and the lunar night. An auxiliary battery was used on the first four spacecraft to provide redundant energy storage capacity for the transit and landing phases.

The main battery design evolved over four distinct development phases that were designated: experimental, development, prototype and flight. Evolution of the final design, the test data relating to each model and the logic leading to the adoption of design improvements are described in this report. Problem areas and solutions are discussed as they relate to each of the phases.

Unique features of this limited-cycle-life silver–zinc battery include high energy density (80 W-h/lb), hermetically-sealed design, a common gas manifold and a pressure transducer that permitted automatic charge termination.

The battery electrical and physical characteristics are presented in detail for each model. Data are included from qualification, acceptance, solar–thermal–vacuum, and mission simulation testing and actual flight. Thermal and calorimetric measurements are presented with the lunar night survival data.

The auxiliary battery was a primary silver–zinc battery. A brief design description is presented along with limited laboratory and flight test data. Mission simulation and flight data, for both main and auxiliary battery models, indicate that design goals were either met or exceeded. This success was achieved by a thorough development and test program, followed by considerable emphasis on tight control of manufacturing processes during the fabrication and assembly of flight batteries.

Surveyor Batteries

FINAL ENGINEERING REPORT

I. Introduction

A. General

The *Surveyor* spacecraft was designed to effect a transit from earth to the moon, perform a soft lunar landing, gather basic scientific and engineering data relative to moon environment and characteristics, and transmit these data to earth. The spacecraft system is depicted in Fig. 1. Electrical power was provided to the spacecraft by the electric power subsystem during the 63–71 h transit, terminal descent, soft lunar landing, and during operation on the lunar surface. A block diagram of the *Surveyor* power subsystem is shown in Fig. 2. Basic components of the electric power subsystem and their functions were as follows:

(1) The solar panel served to charge the main battery and power the spacecraft during transit and the lunar day.

(2) The main battery provided electrical energy storage for the spacecraft.

(3) The auxiliary battery provided a backup source for emergency power, and power during peak loads on the main battery and solar panel, and additional power for the engineering payload.

(4) The battery charge regulator served to control and regulate the charging of the main battery from the solar panel.

(5) The auxiliary battery control provided the controlled application of auxiliary battery power to the unregulated 22-V bus in the event that main battery potential dropped below a pre-set level.

(6) The boost regulator converted unregulated battery power to regulated power for the spacecraft.

(7) The main power switch removed main battery potential (unregulated bus) from the spacecraft system.

(8) The engineering mechanisms auxiliary provided squib-firing power, and the control and power switching for various spacecraft circuits.

The major electrical components were located on the spacecraft as shown in Fig. 3. The main battery was located in compartment A and the auxiliary battery in a special compartment. The main battery was charged by conversion of solar panel energy through the optimum charge regulator circuits; the latter were located within the battery charge regulator in compartment A.

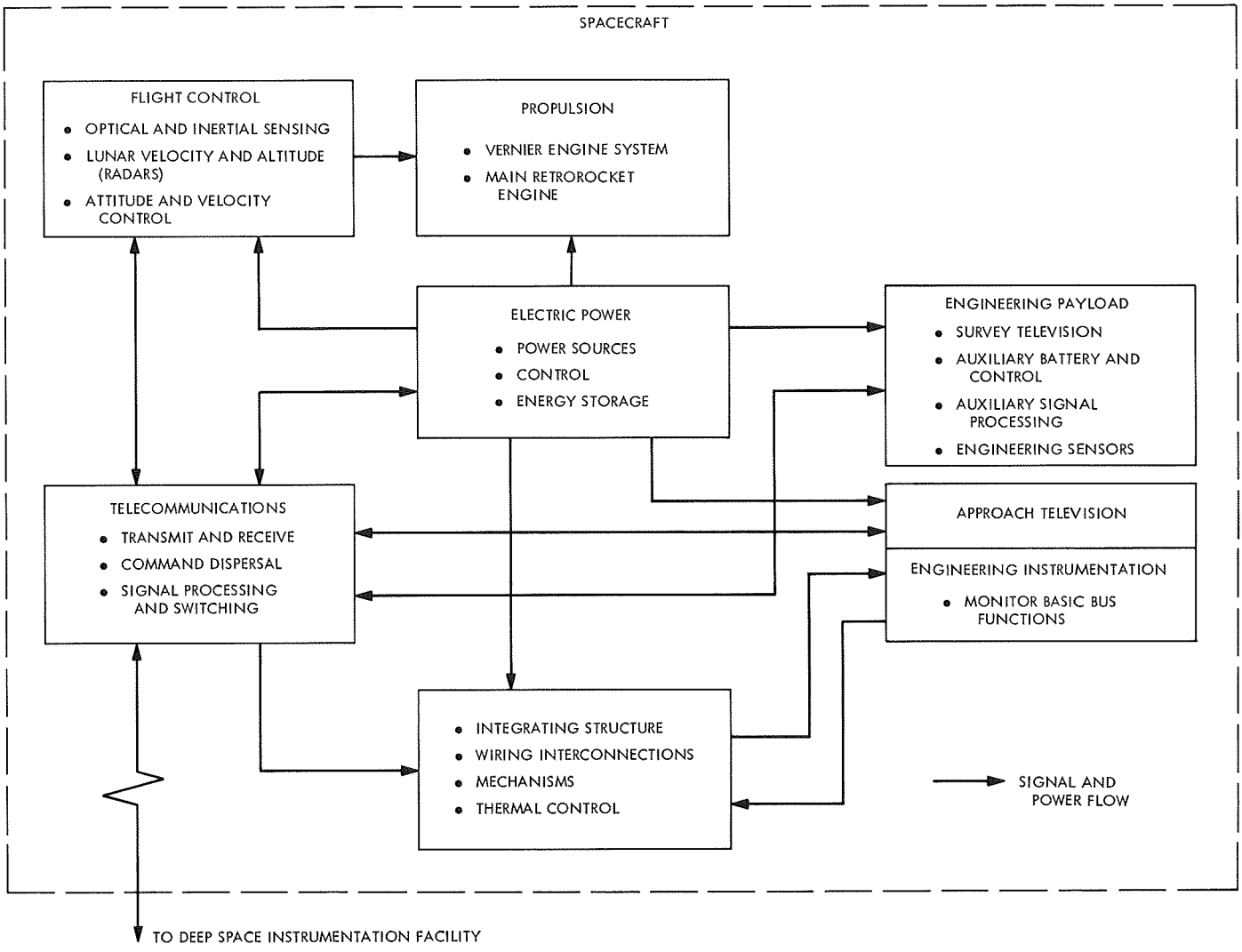

Fig. 1. Spacecraft system block diagram

Distribution of electric power took place over three, 29-V dc regulated buses and a 22-V unregulated bus, (see Fig. 2). Electric power subsystems in *Surveyors V, VI,* and *VII* did not contain auxiliary batteries and controls, and energy storage was limited to the main battery.

The silver–zinc[1] couple, or, more appropriately, the silver oxide–zinc couple, was selected for the spacecraft batteries on the basis of highest energy density (watt-hours per pound) and the ability to meet the mission requirements. Use of the silver–zinc couple on the *Ranger* and *Mariner* spacecraft also supported the selection.

Although there is some difference of opinion concerning exact cell reactions of the silver–zinc system, the following equations provide a reasonably valid indication of the major reactants and products:

$$2\,AgO + Zn + H_2O \underset{\text{charge}}{\overset{\text{discharge}}{\rightleftharpoons}} Ag_2O + Zn(OH)_2 \qquad (1.86\,V)$$

$$ZnO + H_2O$$

$$Ag_2O + Zn + H_2O \underset{\text{charge}}{\overset{\text{discharge}}{\rightleftharpoons}} 2\,Ag + Zn(OH)_2 \qquad (1.55\,V)$$

$$ZnO + H_2O$$

[1]In this report, the cell is referred to as silver–zinc.

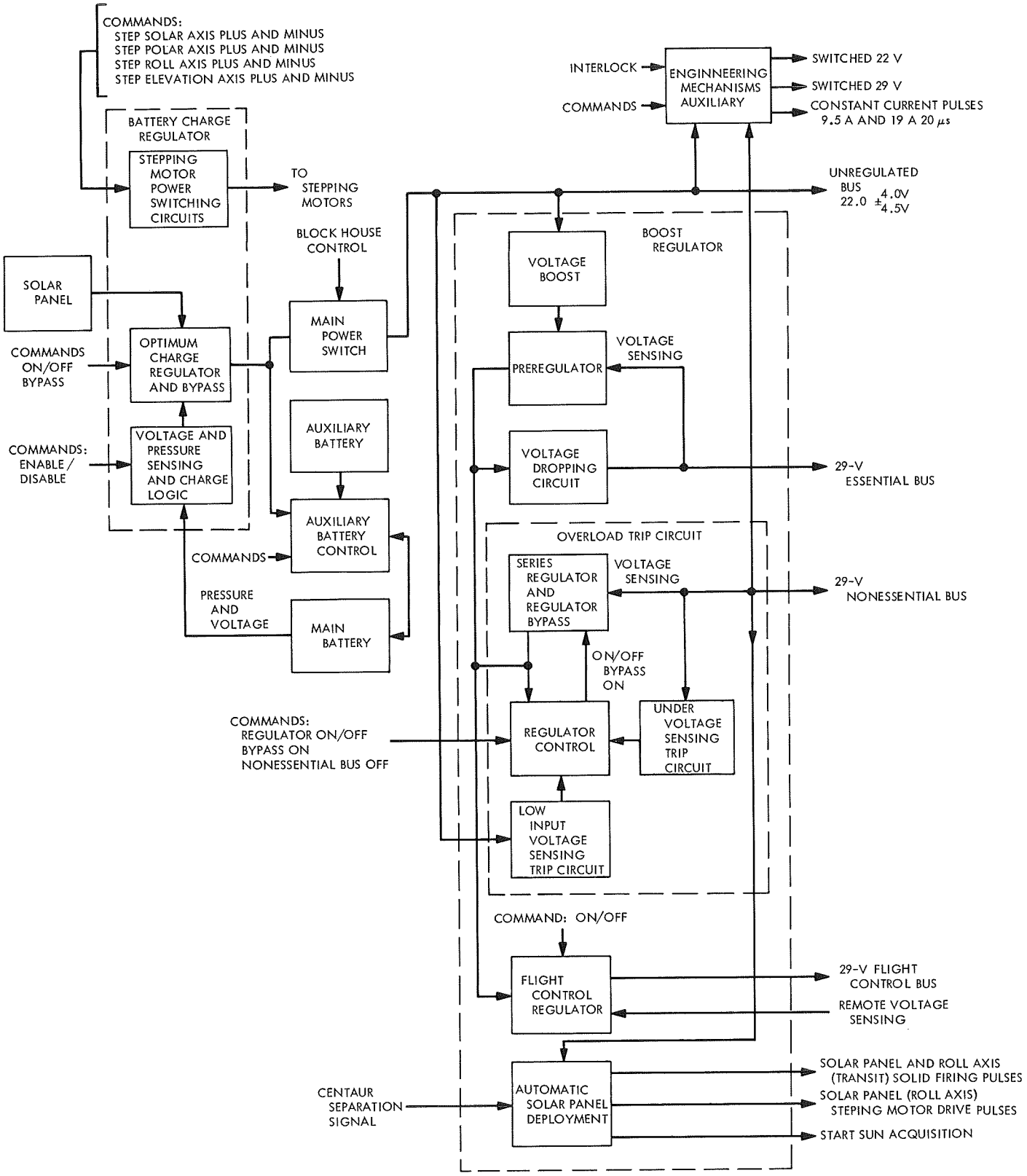

Fig. 2. Electrical power subsystem block diagram

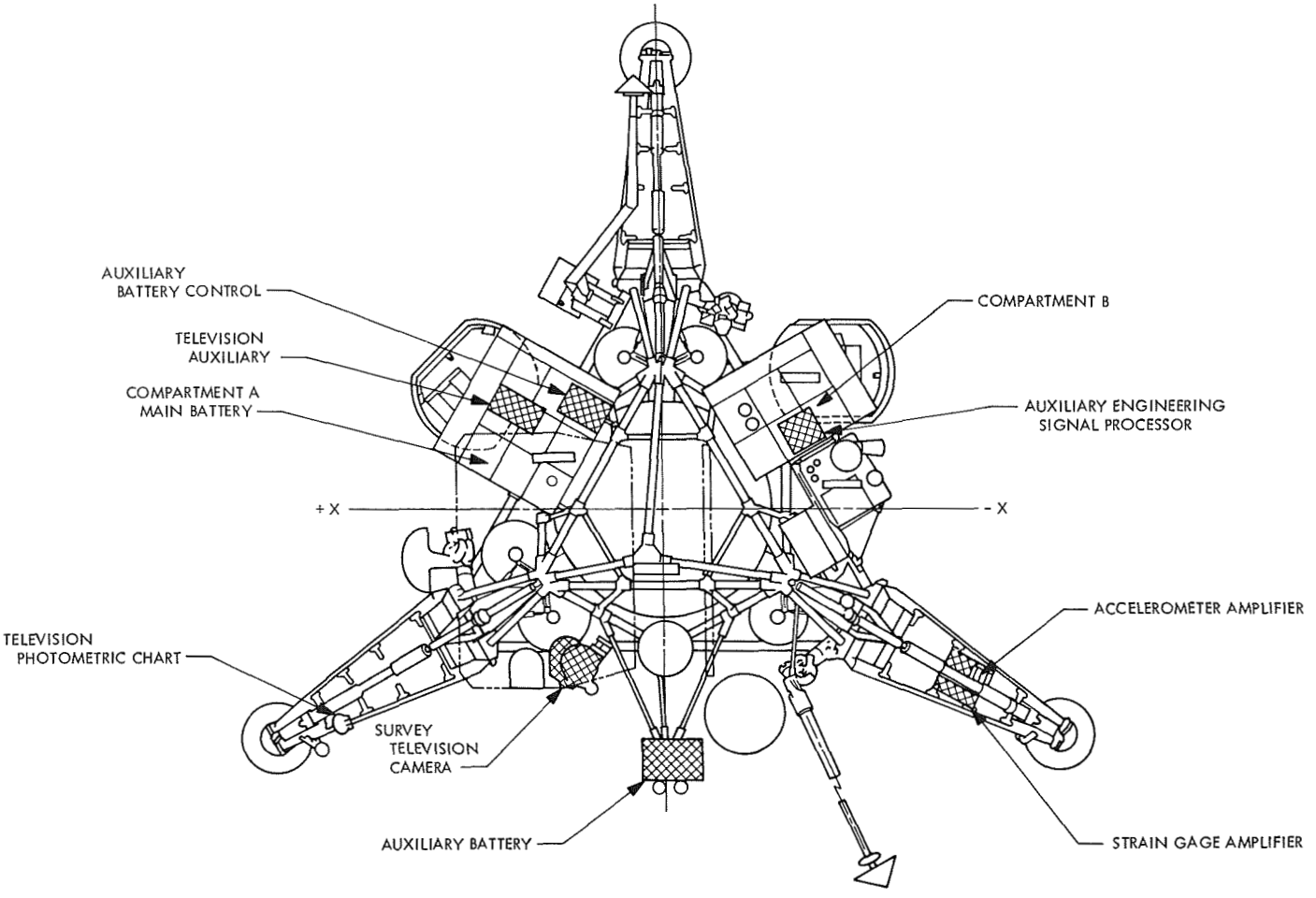

Fig. 3. *Surveyor* spacecraft

The potentials cited in the equations represent open circuit values for the upper and lower plateaus, respectively. Under load, potentials of 1.7 and 1.5 V are typical levels. Figure 4 shows the voltage characteristics of the silver–zinc couple. The reaction takes place in an electrolyte of aqueous potassium hydroxide. The electrodes are separated from each other by semipermeable membranes. The main battery was a secondary battery having limited recharge capability, while the auxiliary battery was a primary, manually activated battery.

It is apparent from Fig. 4 that the silver (I) oxide (Ag_2O) lower plateau constitutes approximately 70% of the discharge capacity with the silver (II) oxide (AgO) furnishing the remaining 30%. On charge, the contributions are reversed. These percentages may be appreciably altered by conditions of temperature and current rate. Further information concerning silver–zinc cell characteristics may be found in subsequent sections of this report.

B. *Surveyor* Main Battery Models

Development of the *Surveyor* main battery proceeded in the following four distinct stages:

(1) Experimental model (203)[2].

(2) Development model (204)[2].

(3) Prototype model (205)[2].

(4) Flight model (205)[2].

The function of each of the models was as follows:

(1) The experimental model consisted of the complete equipment and was constructed to demonstrate the technical soundness of the basic ideas.

[2]Model number assigned by the manufacturer, ESB, Inc., (formerly, Electric Storage Battery Co.) Raleigh, N.C.

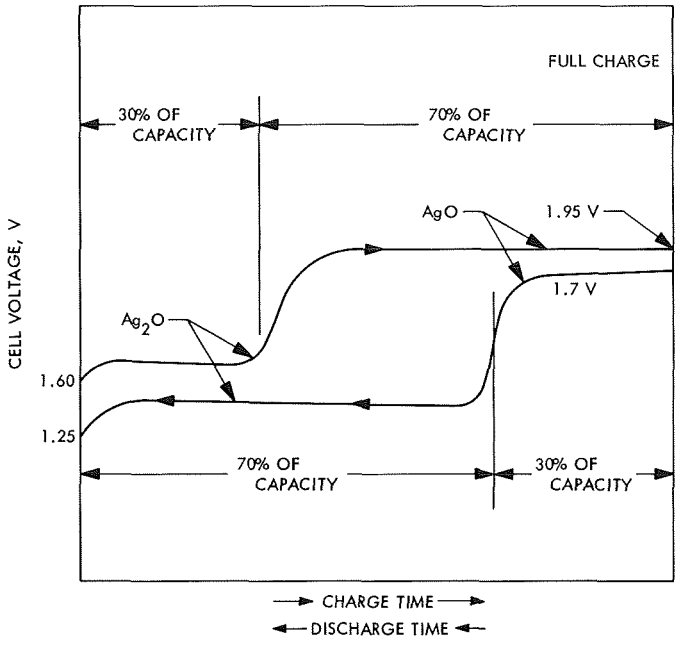

Fig. 4. Silver–zinc cell voltage characteristics

(2) The development model was designed to meet specification performance requirements and establish technical requirements for the final article. This model conformed to the required space envelope and mounting dimensions.

(3) The prototype (preproduction) model was representative of the final mechanical, electrical power, and performance design. This model employed the parts, materials, and processes used in the model that was submitted for quality assurance tests.

(4) The flight (production) model incorporated the final mechanical and electrical power performance design, that was fully certified by a quality assurance test program to meet all requirements of the governing specifications and drawings.

C. Program Milestones and Schedule

Table 1 is a tabulation of milestones including contract awards, battery deliveries, and launches. The program schedule, from design to delivery and acceptance, is shown in Fig. 5.

II. Performance Requirements

A. System Electrical Energy Requirements

The system electrical energy requirements for the *Surveyor* spacecraft are summarized in Table 2. The

Table 1. Program milestones for *Surveyor* main battery

Action	Date
Contract award to HAC by JPL	Mar 12, 1961
Subcontract to ESB, Inc.	Dec 4, 1961
Delivery of first experimental battery	Mar 14, 1962
Delivery of first developmental battery	Jun 28, 1962
Delivery of first prototype battery	May 8, 1963
Delivery of first flight battery	Jun 26, 1964
First flight battery qualified	Sep 17, 1964
First spacecraft launch (*Surveyor I*)	May 30, 1966
Launch of *Surveyor II*	Sep 20, 1966
Launch of *Surveyor III*	Apr 17, 1967
Launch of *Surveyor IV*	Jul 14, 1967
Launch of *Surveyor V*	Sep 8, 1967
Launch of *Surveyor VI*	Nov 7, 1967
Launch of *Surveyor VII*	Jan 7, 1968

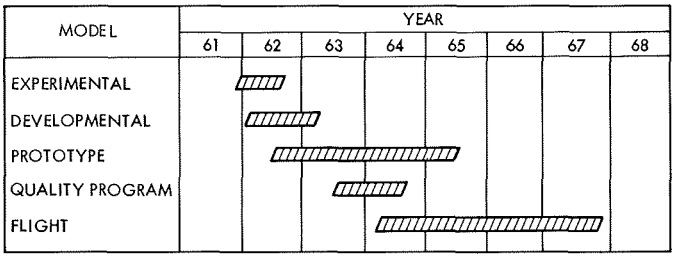

Fig. 5. Program schedule

electrical energy was provided primarily by a sun-oriented solar panel, but power during prelaunch, launch, transit, lunar nights and electrical peak loads was supplied by a secondary silver–zinc (rechargeable) battery. On *Surveyors I–IV*, additional peak load capability during transit and the lunar landing was furnished by an auxiliary primary silver–zinc battery.

The following information is supplementary to Table 2:

(1) The main battery energy capacity is based on a 2-A discharge rate, over a temperature range of 70–125°F.

(2) The base of the auxiliary battery energy capacity is explained in Section IX-C.

(3) Unusable energy remaining at touchdown in the auxiliary battery is based on the desire to keep voltage on the flat portion of the discharge curve and on the uncertainty about actual battery capacity.

Table 2. System electrical energy consumption, generation, and capacity values

Parameter	Surveyor							
	I	II	III – IV			V[c]	VI[c]	VII[c]
	Transit time, h							
	63	63	63	66	71	63	66	71
Required system energy, W-h								
Nominal	7400	7400	6290	6550	7020	6180	6460	6900
Dispersion	±370	±370	±315	±328	±351	±309	±323	±345
Net solar panel energy								
Nominal (71[a] and 78 W[b])	4400	4400	4400	4615	4970	4836	5070	5460
Dispersion	±220	±220	±220	±231	±249	±242	±254	±273
Solar intensity variation	±154	±154	±154	±162	±174	±169	±177	±191
Net battery energy used through touchdown								
Nominal	3000	3000	1890	1935	2050	1344	1390	1440
Dispersion	±430	±430	±383	±401	±430	±392	±411	±440
Main battery energy								
Nominal	3450	3450	3450	3450	3450	3450	3450	3450
Dispersion	±200	±200	±200	±200	±200	±200	±200	±200
Auxiliary battery energy								
Nominal energy at activation	1060	1060	1060	1060	1060			
Dispersion	±60	±60	±60	±60	±60			
Loss of capacity after 10 days of activation (minimum launch window)	60	60	60	60	60			
Loss of capacity after additional 8 days of activation (maximum launch window)	85	85	85	85	85			
Unusable energy remaining at touchdown	125	125	125	125	125			
Usable battery energy remaining at touchdown								
Nominal (launch at first day of window)	1325	1325	2435	2390	2275	2106	2060	2010
Total dispersion	+479	+479	+437	+453	+479	±440	±457	±483
Minimum	607	607	1759	1690	1537	1497	1426	1336

[a]*Surveyor I, II, III, and IV.*
[b]*Surveyor V, VI, and VII.*
[c]Without auxiliary battery.

(4) Conversion between ampere-hours and watt-hours is based on an average unregulated bus of 21.6 Vdc.

(5) In the event of an earth shadow eclipse of 1 h, the usable battery energy remaining at touchdown will be reduced by a maximum of 100 W-h.

(6) In the event that the *Surveyor* TV vidicon heater is required to operate continuously throughout transit, the usable battery energy, remaining at touchdown will be reduced by a maximum of 259 W-h for a 71-h transit.

B. Battery Thermal Environment

Type approval requirements for flight model batteries are summarized in Table 3. The environmental temperature conditions are plotted in Fig. 6. The temperature graph shown was based on an electrical power subsystem containing two 150 A-h batteries, and with sufficient current drain to maintain a minimum battery temperature of 0°F. In actual practice, however, it was not possible to maintain a current drain at this level with the single main battery and consequently the battery was permitted to freeze. The minimum battery temperature during the lunar night was estimated to be less than −150°F. Realistic lunar night survival tests were conducted to determine the performance of the main battery in a severe thermal environment.

C. Battery Electrical Performance Requirements

1. Discharge capability. The specified output potential of the 14-cell battery, as measured on the load side

Table 3. Mission power profile

Sequence number	Mission operation	Battery state,[a] at 10^{-4} torr	Duration, h	Equivalent load, Ω ±1%	A[b]	W	W-h	Average charge, A[c]
A-1.0	Transit	D	1.00	13.75	1.60	35.2	35.20	—
A-1.1		D	15.00	11.00	2.00	44.0	660.0	—
A-1.2		D	1.00	4.4	5.00	110.0	110.00	—
A-1.3		D	41.0	11.00	2.0	44.0	18.00	—
A-1.4		D	3.0	4.4	5.00	110	330.	—
A-1.5		D	0.05	0.26	85.00	1870.0	0.026	—
A-2.0	Lunar day 1	D	1.50	36.70	0.60	13.2	19.80	—
A-2.1		C	15.00	—	—	22.0	330.00	1.00
A-2.2	Perform	D	0.05	0.55	40.00	880.0	0.012	—
A-2.3	five times	D	0.25	1.38	16.00	352.0	88.00	—
A-2.4		D	10.00	27.50	0.80	17.6	176.00	—
A-2.5		C	1.00	—	—	110.0	110.00	5.00
A-2.6		C	3.00	—	—	66.0	198.00	3.00
A-2.7		C	11.00	—	—	22.0	242.00	1.00
A-2.8		D	0.05	0.79	28.00	620.0	0.0086	—
A-2.9		D	0.25	1.38	16.00	352.0	88.00	—
A-2.10		C	20.00	—	—	22.0	440.00	1.00
A-3.0	Lunar night 1	D	58.00	73.40	0.30	6.6	392.00	—
A-3.1		D	1.50	7.34	3.00	66.0	99.00	—
A-3.2	Perform	D	0.20	12.20	1.80	39.6	7.92	—
A-3.3	twelve times	D	16.00	91.50	0.24	5.3	84.70	—
A-3.4		D	8.00	44.00	0.50	11.0	88.00	—
A-4.0	Lunar day 2	C	10.00	—	—	110.0	1100.00	5.00
A-4.1		C	10.00	—	—	66.0	660.00	3.00
A-4.2		C	30.00	—	—	22.0	660.00	1.00
A-4.3		D	0.05	0.55	40.00	880.0	0.012	—
A-4.4	Perform	D	0.25	1.38	16.00	352.0	88.00	—
A-4.5	five times	D	5.00	55.00	0.40	8.8	44.00	—
A-4.6		C	25.00	—	—	15.7	392.00	0.70
A-4.7		C	1.00	—	—	110.0	110.00	5.00
A-4.8		C	3.00	—	—	66.0	198.00	3.00
A-4.9		C	145.00	—	—	22.0	3190.00	1.00
A-5.0	Lunar night 2—repeat A-3.0 through A-3.4.							
A-6.0	Lunar day 3—repeat A-4.0 through A-4.9.							
A-7.0	Lunar night 3—repeat A-3.0 through A-3.4.							
A-8.0	Lunar day 4—repeat A-4.0 through A-4.9.							

[a]The battery ambient temperature shall comply with Fig. 2.

[b]Values shown are constant current except for sequence numbers A-1.5, 2.2, 2.8, and 4.3 where the resistive load is constant. Tolerance on discharge currents shall be ±5.0%.

[c]The battery shall be charged at the average rate indicated with a tolerance of ±5.0%. If the battery is fully charged prior to the end of the period of time allowed for charging, the battery shall remain within 5% of the fully charged condition for the remainder of the period allowed for charging.

of the mating electrical connector, was 22 (+4.0, −4.5) V under all test conditions. The battery minimum discharge capacity was 2950 W-h when discharged in accordance with Table 3.

2. *Charge capability.* The battery had to be capable of accepting charge for extended periods at levels ranging from 0.1 to 5.0 A. Charging was to be accomplished at maximum available potential of 27.30 (+0.00, −0.14) V. Float charging at a constant potential of 27.0 (+0.1, −0.0) V for a period of 85 h was not to result in battery internal pressure above 25 psia.

3. *Storage capability.* The battery had to be capable of withstanding unactivated storage for a minimum of one year at temperatures between 40 and 100°F and a relative humidity not exceeding 50%.

4. *Operating life.* The operating life of the battery had to be at least 120 days when operated in accordance

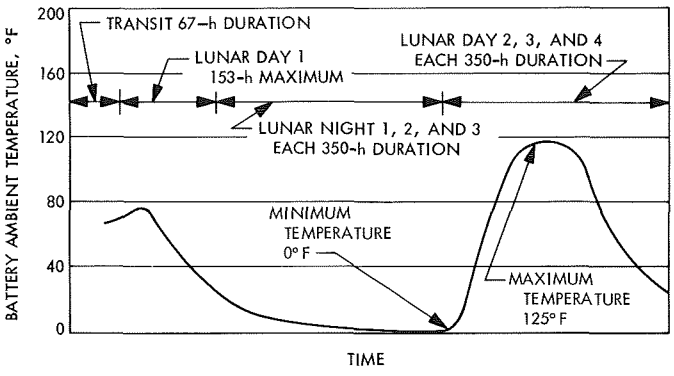

Fig. 6. Battery ambient temperature profile

with the specifications in Table 3. Operation beyond the 250 h of the second lunar day was desirable, but not required.

5. Changes in electrical requirements. Changing energy requirements caused revisions in the power profile. These changes are summarized in Table 4. Revisions B and D are not included in Table 4 since these were minor changes.

D. Environmental Requirements

1. Electrical performance during tests. The battery had to be discharged at a constant 7.0-A rate prior to, during, and after each test. During this discharge, the battery potential had to be between 17.5 and 26.0 V. At the conclusion of each test, the battery was discharged for at least 5.0 s using a 0.260 $\pm$0.020-Ω resistive load. The battery potential had to be within the specified limits.

2. Shock test requirement. The battery had to be capable of meeting the specified electrical requirements when subjected to shock simulating the environments to be encountered by the spacecraft during the descent phase.

a. Thrust axis. The battery was subjected to four 5-ms, 25-*g*, half-sine-wave shocks along the positive thrust axis. An acceptable substitute was a 4- to 6-ms terminal sawtooth shock of 40 *g*, repeated four times.

b. Lateral axes. The battery was subjected to four (two in each direction), 5-ms, 15-*g*, half-sine-wave shocks along each of two orthogonal axes perpendicular to the thrust axis. An acceptable substitute was a 4- to 6-ms terminal sawtooth shock of 24 *g*, repeated four times.

3. Acceleration test requirement. The battery had to be capable of meeting the specified electrical requirements when subjected to acceleration simulating the quasi-steady state acceleration encountered by the spacecraft during the *Atlas*, *Centaur*, and retroengine burning phases.

Significant accelerations were to be produced in the thrust axis only. Accelerations in the lateral axes were considered negligible. The battery was subjected to

Table 4. Changes in power profile

Profile affected	Original requirements Jul, 1961	Revision A Nov, 1961	Revision C May, 1962	Revision E Aug, 1963	Revision F Aug, 1964	Revision G Jul, 1966
Output voltage	22 $\pm$ 4 V	—	22 $^{+4.0}_{-4.5}$	—	—	—
Capacity	2650 W-h, 121 A-h	—	—	—	—	2950 W-h, 134 A-h
Charge	Constant current 0.1-2 A at 28 V maximum	0.1-5 A	—	27.3 V maximum 72 h float	85 h float	—
Operating temperature	0–125°F 80°F maximum during transit	—	—	—	—	130°F maximum during transit
Life	56 days minimum, 120 days desired	—	—	120 days minimum	—	—
Weight	47.5 lb maximum	46 lb maximum	—	46.5 lb maximum	—	—
Maximum current	23.4 A	—	85 A	—	—	—

steady-state accelerations of 10 g for 4 min and 5 g for 7 min along the thrust axis.

4. Vibration test requirement. The battery had to be capable of meeting the specified electrical requirements when subjected to the specified vibration level with the battery firmly attached to a vibration exciter without attempt to simulate the spacecraft installation. The battery was loaded in such a manner as to make it dynamically similar to the flight configuration. The vibration level was to be observed on the exciter positioned as near the supporting bracket as possible.

The battery was subjected to vibration tests in a direction essentially parallel to the thrust axis and in two critical orthogonal directions perpendicular to the thrust axis.

a. Provisions. The vibration test levels in Figs. 7–9 represent the mechanical inputs at the attachment of the battery to the supporting substructure of the spaceframe.

b. Test levels. The test levels of Figs. 7–9 represent vibration level, frequency range, sequence, and durations that were applied to the battery under test. Measurements were taken in the spacecraft thrust and lateral axes directions, either at the supports to the spacecraft structure, or at the specified interface.

c. Test description. Each battery was subjected to vibration test levels based upon the overall test levels, frequency ranges, sequences, and the durations specified in the preceding paragraph. The frequency ranges that followed were modified to reflect the actual fundamental resonant frequencies existing within the battery. These frequencies did not have to be lower than one-half of the first fundamental resonance frequency observed. The test consisted of a variable frequency sine-wave (VFSW), logarithmically swept over the specified frequency range, a band-limited random vibration of uniform spectral density, and gaussian instantaneous amplitude distribution with the specified frequency band —white gaussian acceleration (WGA). A logarithmic sweep is defined as a change in frequency, either in an increasing, or decreasing, direction over the specified frequency range in a uniform time span, where the rate of change of frequency is directly proportional to the instantaneous frequency. That is, the sweep rate had to

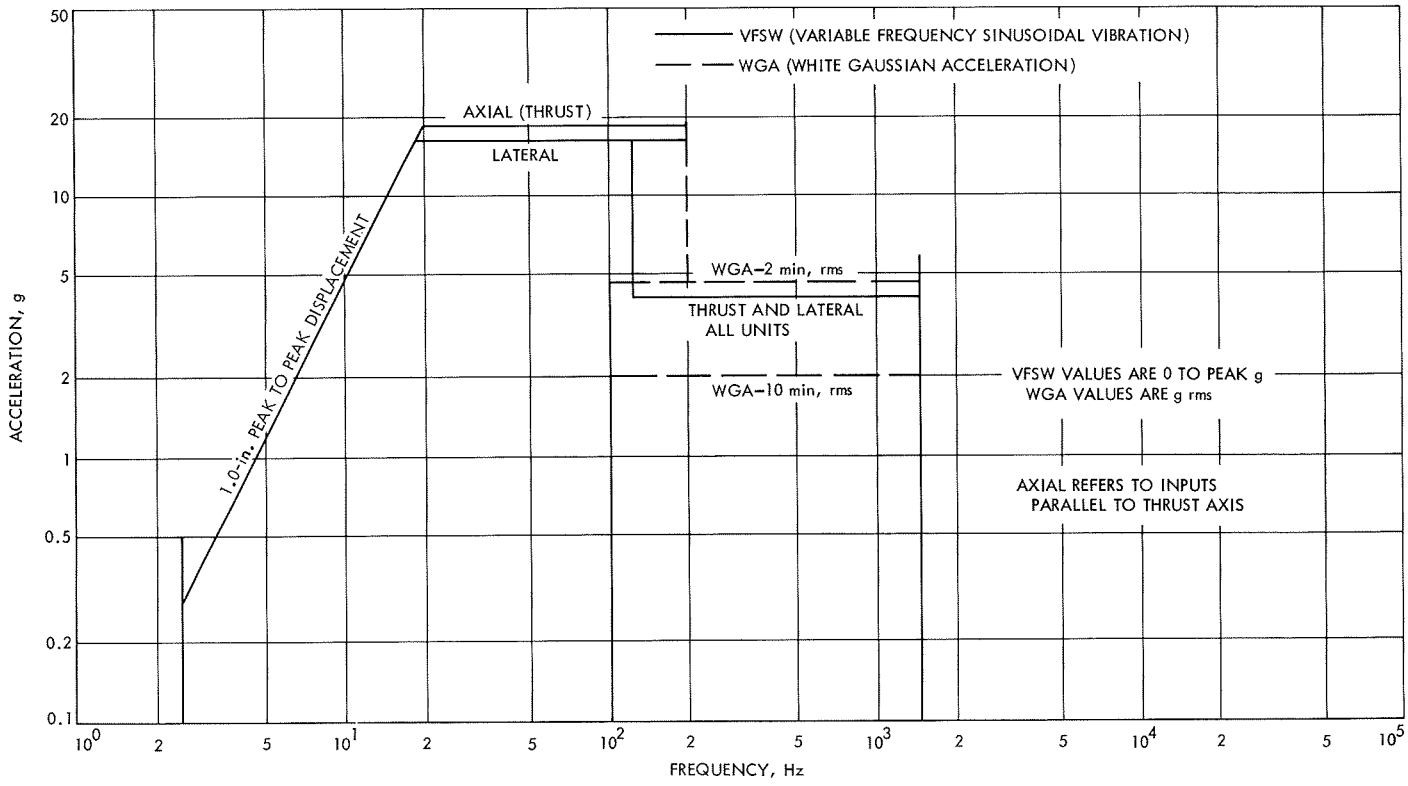

Fig. 7. Type approval, vibration test program

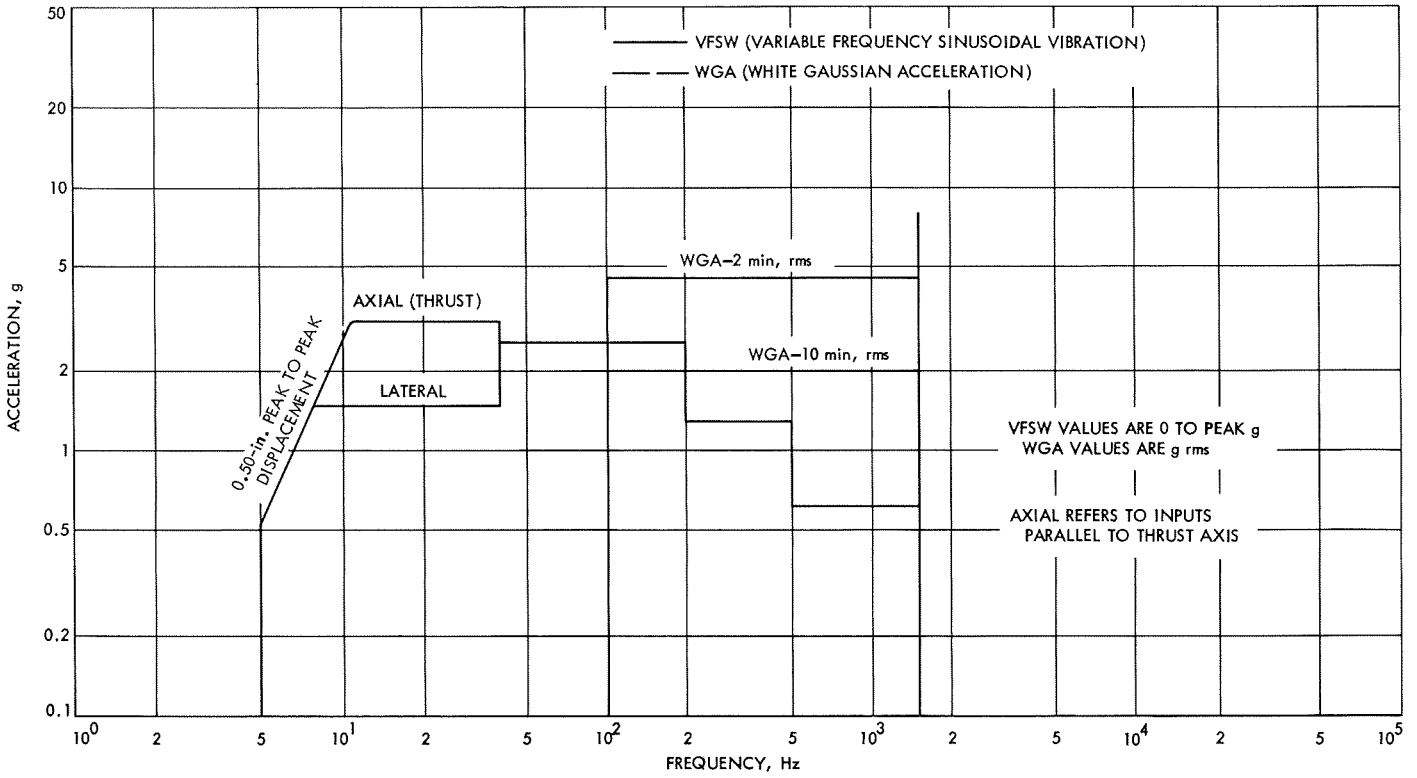

Fig. 8. Type approval, vibration test program, main retroengine

be a constant number, or fraction of an octave, per uniform time period.

The vibration tests of the battery were based upon the sequence of environmental levels given in the subsequent paragraphs for each of the specified orthogonal directions. One orthogonal axis is defined as the axis essentially parallel with the spacecraft thrust axis. The lateral orthogonal axes included at least one other critical axis. The total time in each orthogonal direction was 12 min for a total vibration test time on the battery of 36 min.

d. Test sequence. The battery was subjected to one increasing frequency sweep of 2 min at the VFSW level and frequency range as specified in Figs. 7 or 9, or the detail specification combined with random vibration WGA of 4.5-*g* rms acceleration band limited between 100 and 1500 Hz.

The battery was then subjected to either, one increasing and one decreasing frequency sweep of 5 min each, or five increasing and decreasing frequency sweeps of 2 min each at the VFSW levels and the frequency range specified in Figs. 7 or 9. The detail specification requirements could also be used, combined with random vibration WGA of 2.0-*g* rms acceleration band limited between 100 and 1500 Hz.

e. Standard complex wave test tape. The complex wave, specified in the description, could be executed by means of magnetic recording tape. The signal recorded on the tape had to have the characteristics noted in Figs. 7, 8, or 9. The VFSW had to be combined with the WGA as follows:

$$\text{rms } g\,(\text{WGA}^2 + \text{VFSW}^2)^{1/2}$$

where all *g* values are rms.

f. Random noise. For creating the random noise WGA, the output of a random noise generator, General Radio Model 1390-A or its equivalent could be used if proper care was taken to ensure the correct amplitude distribution of the signal. For ensuring correct noise bandwidth, a filter with an asymptotic slope, of at least 24 dB per octave and 3-dB points at 100 and 1500 Hz, was considered acceptable.

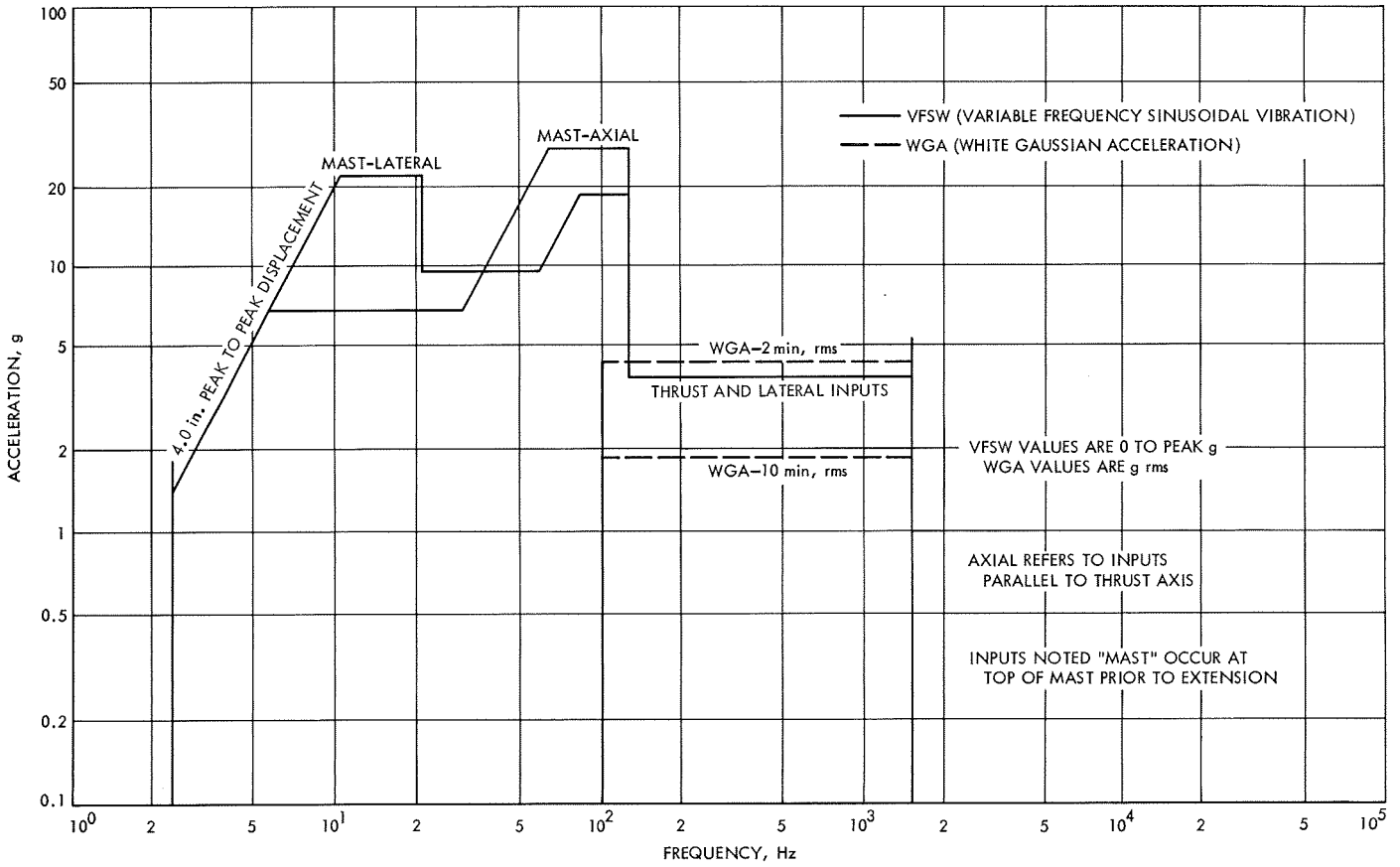

Fig. 9. Type approval, vibration test program, total spacecraft

III. Experimental Model *Surveyor* Main Battery

A. Description

The experimental model *Surveyor* main battery consisted of 14, sealed, silver–zinc cells connected in series. The capacity was approximately 150 A-h. The output potential was 22 ±4 V at an ambient temperature of 70°F. The battery weight was 46.0 lb, except for the four batteries that were equipped with pressure gages on each cell for monitoring the cell pressures during tests. Batteries X1–X4 are shown in Fig. 10. The pressure gage-equipped batteries, X5–X8, are shown in Fig. 11.

Structural details of the cells are given in Figs. 12–15. The cell characteristics are summarized in Table 5. Cells were located in two- and five-cell containers (Fig. 16). One two-cell and one five-cell monoblock were joined to form a seven-cell unit. A pair of seven-cell units was combined to form the battery (Fig. 17). The battery was placed in a magnesium canister for strength and mountability. Figure 10 shows a battery installed in a canister.

The temperature of the batteries and monoblocks was measured with thermistors, positioned as shown in Fig. 17.

1. Negative plates. The negative plates consisted of active material pressed onto a silver grid, as illustrated in Fig. 13. The active material mix also contained a binder[3] and mercuric oxide.

2. Positive plates. The positive plates, illustrated in Fig. 14, contained active material that was pressed onto a silver grid and a binder[3] that was destroyed by subsequent sintering.

3. Separators. The separator system (Fig. 15) consisted of six layers. Synpor, with its relatively high resistance to attack by silver oxide, and its ability to permit permeation of electrolyte by virtue of a fairly open structure, was the material used in contact with the silver

[3]ESB, Inc. proprietary materials. See appendix for listing of material manufacturers.

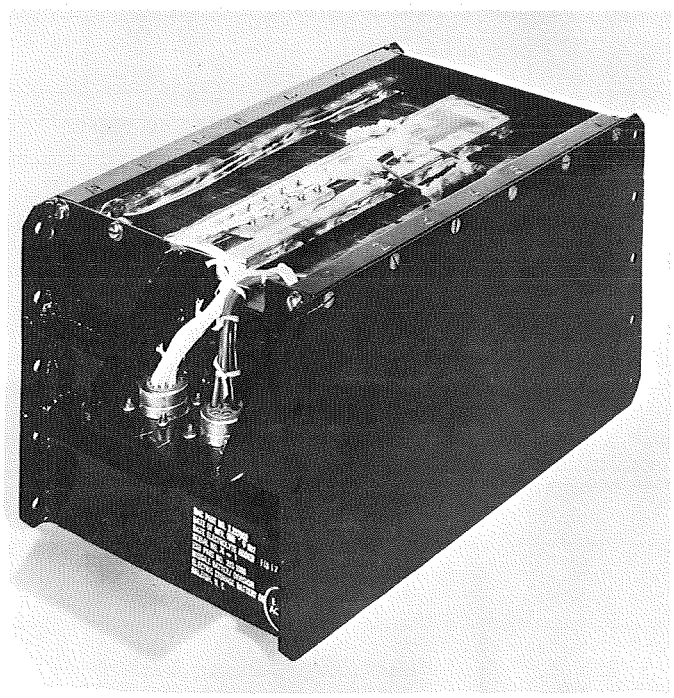

Fig. 10. *Surveyor* experimental model battery

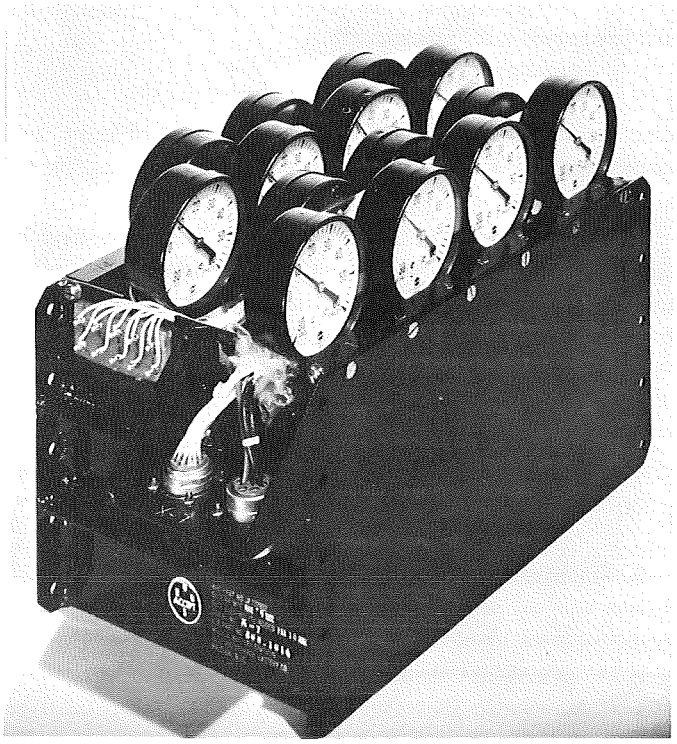

Fig. 11. Pressure gage-equipped *Surveyor* experimental model battery

electrode. The next layer was Polypor, which had demonstrated its ability to resist penetration by silver oxide. The final four layers were cellophane, which has limited resistance to silver oxide, but resists zinc treeing and permits a relatively free flow of electrolyte ions.

Table 5. Physical characteristics of *Surveyor* experimental model cell

Characteristic	Result
Positive	
Height, in.	4.750
Width, in.	3.125
Thickness, in.	0.072
Type of grid	1/0
Total plate area, $in.^2$	178
Silver per cell, lb	1.07
Active material density, $lb/in.^3$	0.172
Number of plates	6
Negative	
Height, in.	4.750
Width, in.	3.125
Center plate thickness, in.	0.091
End plate thickness, in.	0.051
Type of grid	2/0 expanded
Number of center negatives/cell	5
Number of end negatives/cell	2
Zinc-oxide per cell, lb	0.682
Active material density, $lb/in.^3$	0.108
Active plate area, $in.^2$	178
Remarks	
Electrolyte	
Type	M-40[a]
Amount per cell, $in.^3$	11.0
Separator[b]	
No. 1 Type	White Synpor
Number of layers	1
No. 2 Type	Polypor WA
Number of layers	1
No. 3 Type	193 PUDO Cellophane
Number of layers	4
Free space ratio for cellophane	4.58
Ratio of positive	
Capacity to negative	
Capacity theoretical	1.175
Battery	
Terminal	Screw

[a]40 wt% KOH, containing dissolved zinc oxide.
[b]Listed from positive to negative.

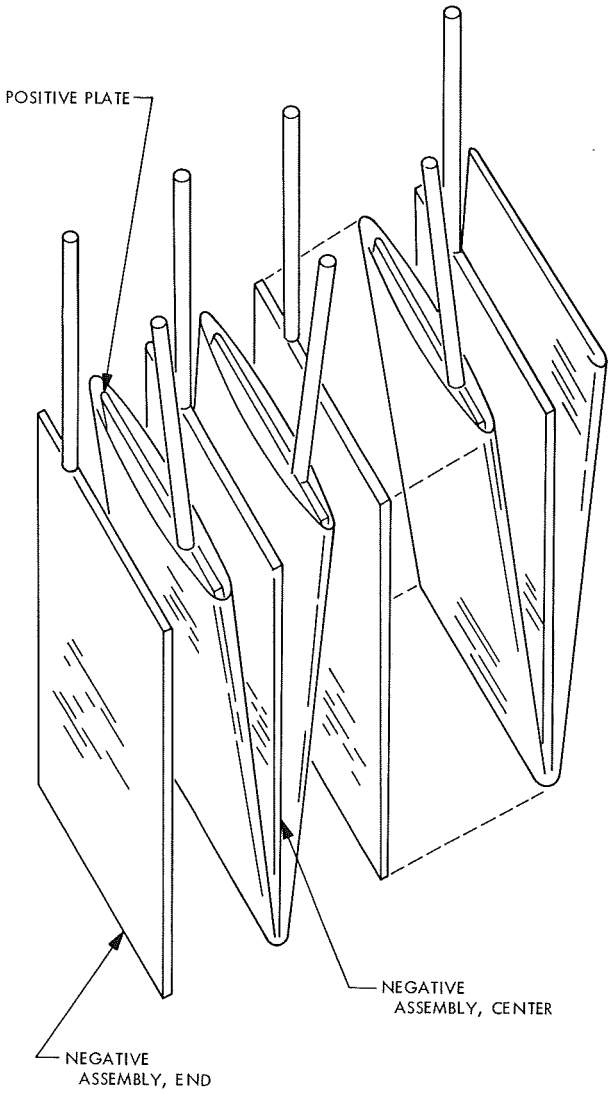

Fig. 12. View of positive and negative assembly—experimental cell

4. Electrolyte. The electrolyte in the battery was an aqueous solution of 40% potassium hydroxide, saturated with zinc oxide.

The ratio of active negative material to active positive material was optimized to minimize gas pressure buildup during charge.

B. Tests on Cells and Monoblocks

This subsection describes performance tests using experimental model cells and monoblocks.

1. Charge tests. The charge tests were performed to determine the charge characteristics of experimental

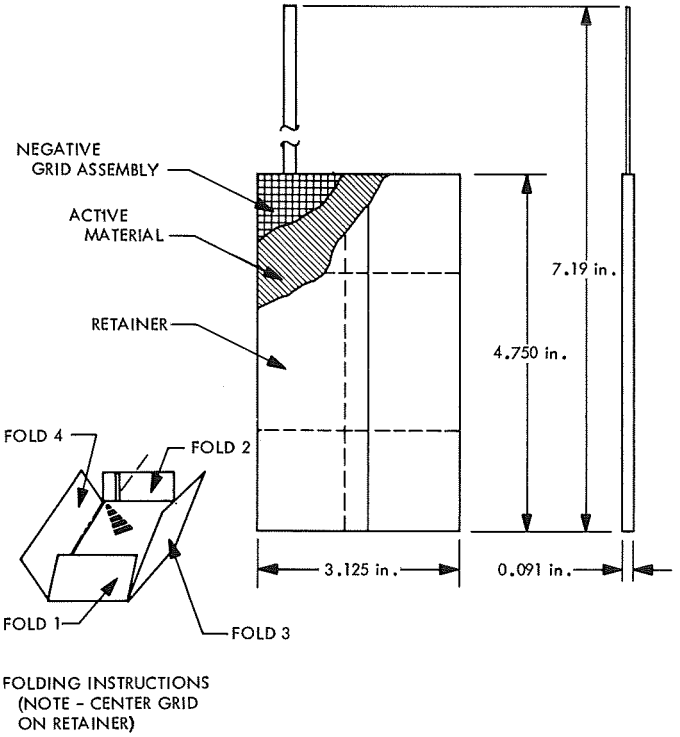

Fig. 13. Negative assembly—experimental cell

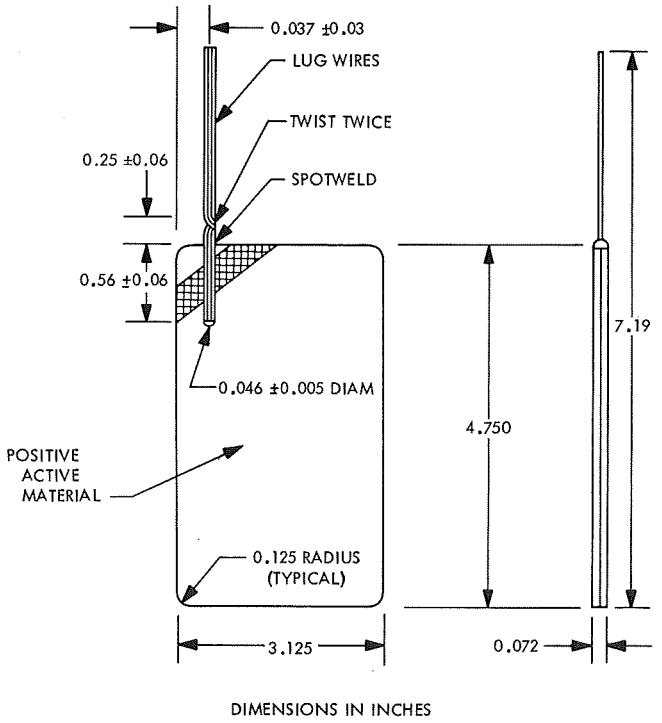

Fig. 14. Positive plate assembly—experimental cell

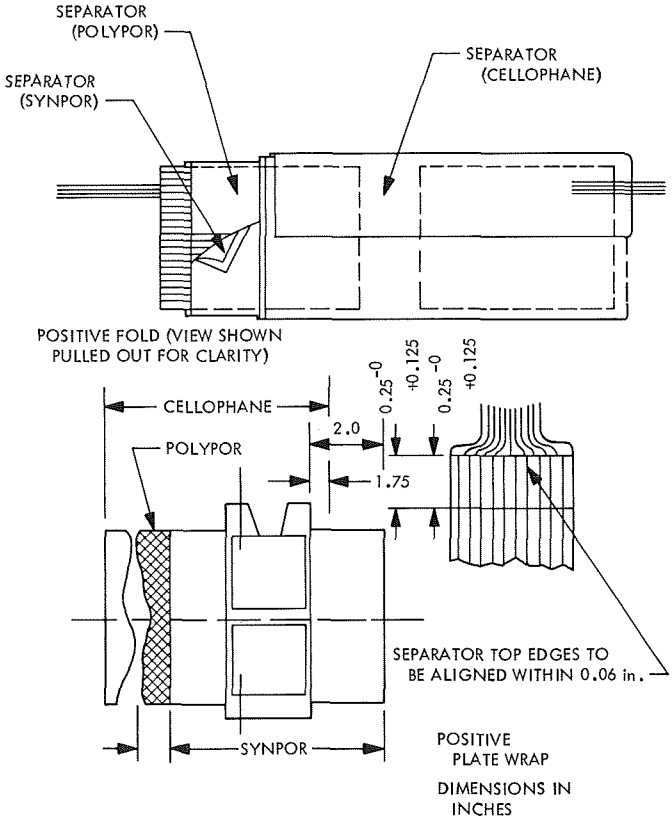

Fig. 15. Details concerning positive plate wrap

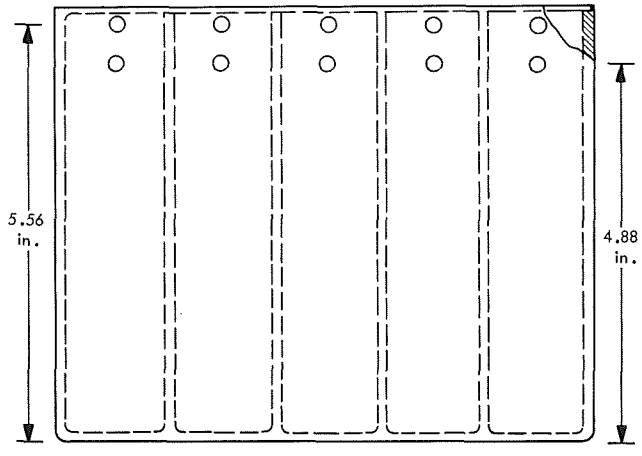

Fig. 16. Side view of five-cell container for experimental model battery

cells over a wide range of charge rates and battery temperatures.

a. Procedure. The charge test procedure involved discharging three-cell monoblocks at the 7 A rate to 3.75 V (1.25 V-cell), and charging at 0.1, 1.0, 3.0, and

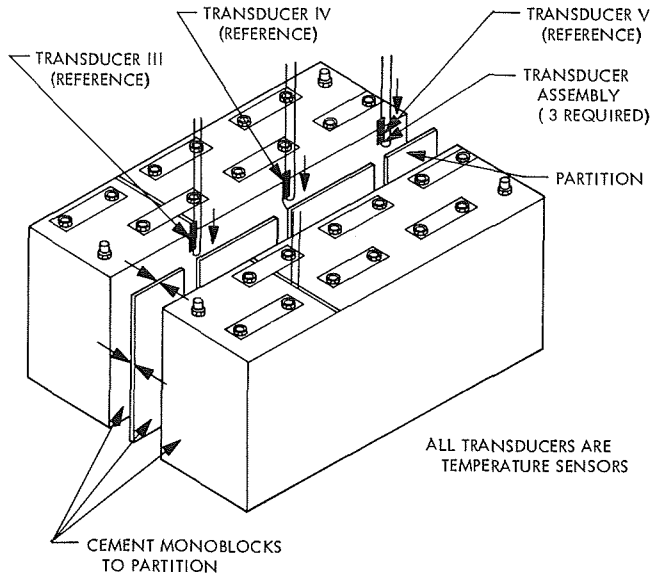

Fig. 17. Assembly of monoblocks in experimental model battery

5.0 A and 0, 30, 60, 90, and 125°F to a maximum cell pressure of 40 psig and a range of cutoff voltages.

b. Results. The results of the charge tests are presented in a series of graphs and a table. Figure 18 shows a typical charge curve, in which the end of charge is indicated by a sharp rise in potential and internal cell pressure. Owing to the possibility of cell rupture and in keeping with the requirement to minimize weight, a maximum cell pressure of 40 psig has been adopted. The onset of gas pressure buildup is a function of temperature and charge rate, as indicated in Table 6. The attainable charge input as a function of charge rate and cutoff potential is summarized for the test temperatures in Figs. 18–23. The discharge capacity (70°F) after charging at selected temperatures is indicated in Figs. 24 and 25. A thorough discussion of the voltage surge (at 70 h of charge) in Fig. 18 appears in subsections III-E-3, III-F-4, and III-F-5.

Table 6. Voltage at start of gassing

Temperature, °F	Charge rate, A			
	5	3	1	0.1
	Voltage, V			
0	2.01 – 2.10	1.97 – 2.02	1.99 – 2.05	1.97 – 1.98
30	1.975– 2.00	1.97 – 2.06	2.00 – 2.05	1.96 – 1.98
60	1.975– 1.99	1.97 – 2.00	2.00 – 2.01	—
90	1.93 – 1.96	1.93 – 1.98	1.97 – 1.98	1.98 – 2.00
125	1.95 – 1.97	1.93 – 1.97	1.96 – 1.98	1.95 – 1.97

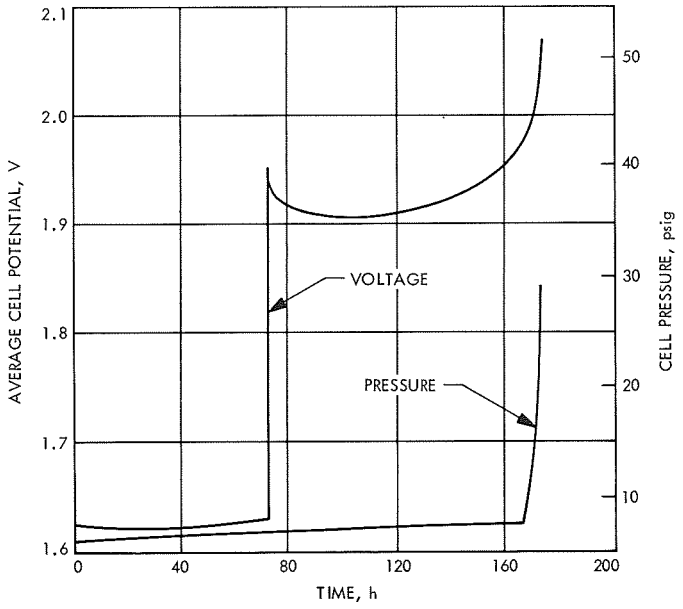

Fig. 18. Charge characteristics of experimental three-cell monoblock for 1-A charge at 60°F

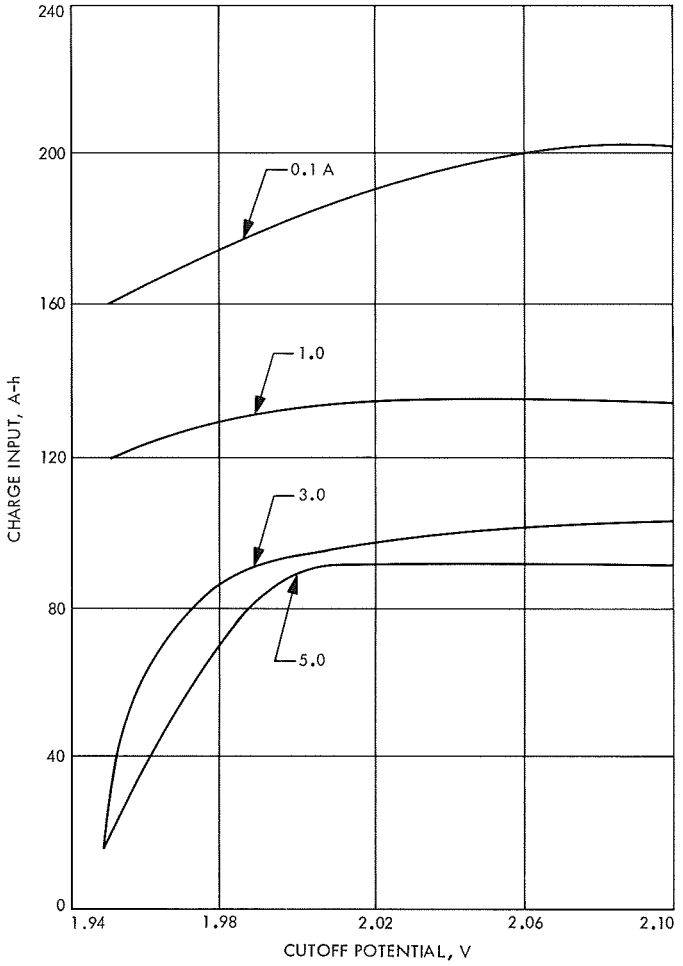

Fig. 19. Charge input vs cutoff voltage for several charging rates at 0°F for experimental three-cell monoblock

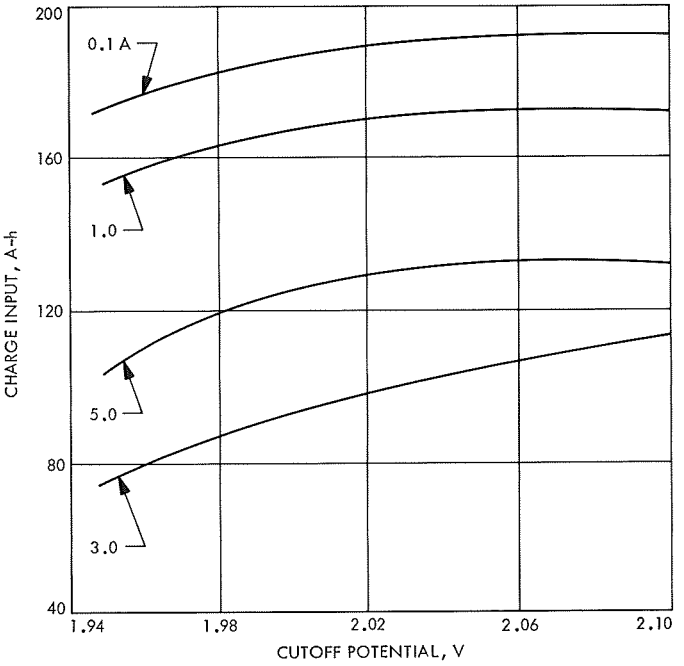

Fig. 20. Charge input vs cutoff voltage for several charging rates at 30°F for experimental three-cell monoblock

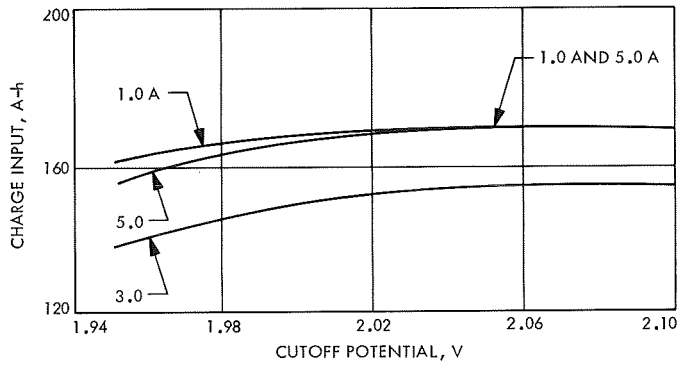

Fig. 21. Charge input vs cutoff voltage for several charging rates at 60°F for experimental three-cell monoblock

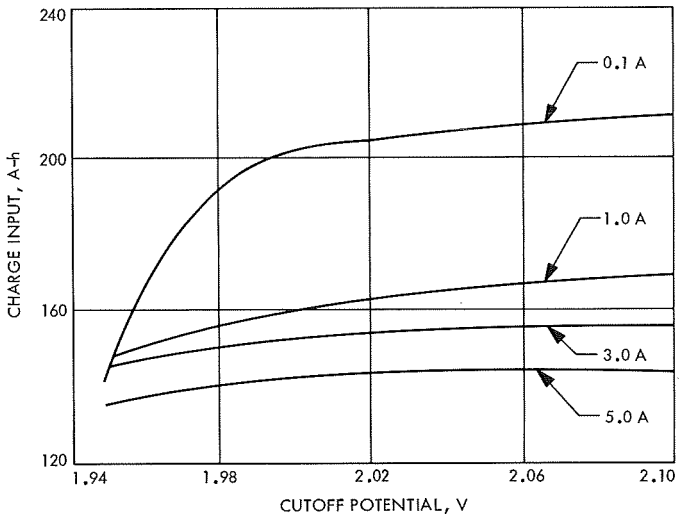

Fig. 22. Charge input vs cutoff voltage for several charging rates at 90°F for experimental three-cell monoblock

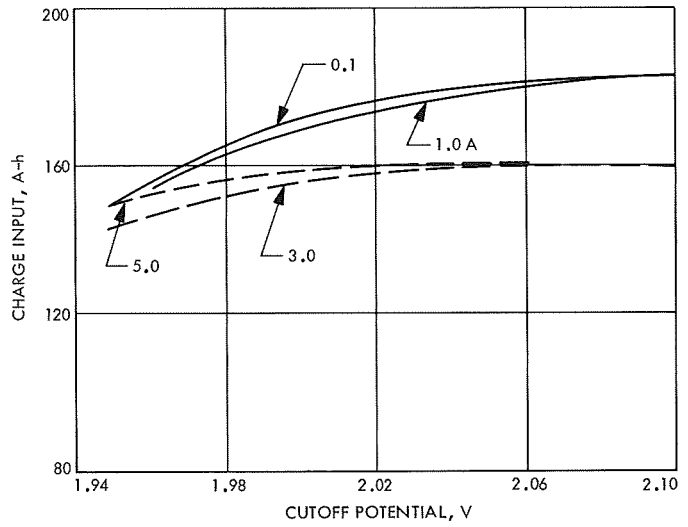

Fig. 23. Charge input vs cutoff voltage for several charging rates at 125°F for experimental three-cell monoblock

c. Conclusions. Charge tests on experimental model cells and monoblocks yielded the following conclusions:

(1) Charge input can be increased by charging at a lower rate or charging to a higher cutoff potential.

(2) Cutoff potential and charge rate have a much greater effect on charge input at low temperatures than above 70°F.

(3) The gas pressure buildup starting at approximately 1.96 V and above, resulted in recommendations to limit charging to this potential at a temperature above 30°F. Charging at a lower temperature requires a higher potential that would lead to unsafe conditions at higher temperatures because of excessive pressure buildup.

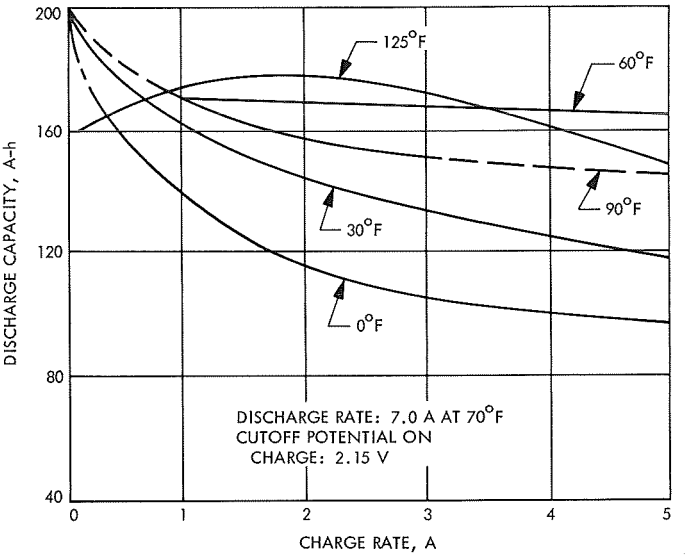

Fig. 24. Discharge capacity vs charge rate after charge to 40 psig at several temperatures for experimental three-cell monoblock

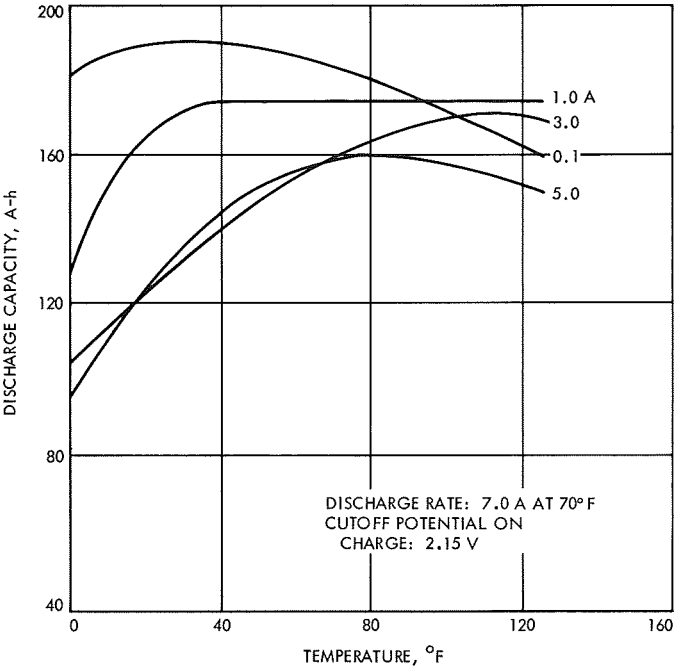

Fig. 25. Discharge capacity vs temperature after charge to 40 psig at several charging rates for experimental three-cell monoblock

2. *Stand loss for charged storage.* Discharge tests were conducted on experimental cells to determine the stand loss in charged cells.

a. Procedure. The discharge test procedure involved placing cells equipped with pressure gages in a controlled temperature environment, measuring the open circuit potential, and discharging the cells at the 7.0-A rate to a cutoff potential of 1.25 V.

b. Results and conclusions. Results of the stand loss test on initially charged cells are expressed in terms of capacity retention in Fig. 26 with equilibrium cell pressures shown in Fig. 27. The stand loss data nearly fits the equation

$$K = \frac{2.303\,(\log C_1 - \log C_2)}{t}$$

where

K = a rate constant

C_1 = capacity at time = 0, %

C_2 = capacity at time = t, %

t = storage time, mo

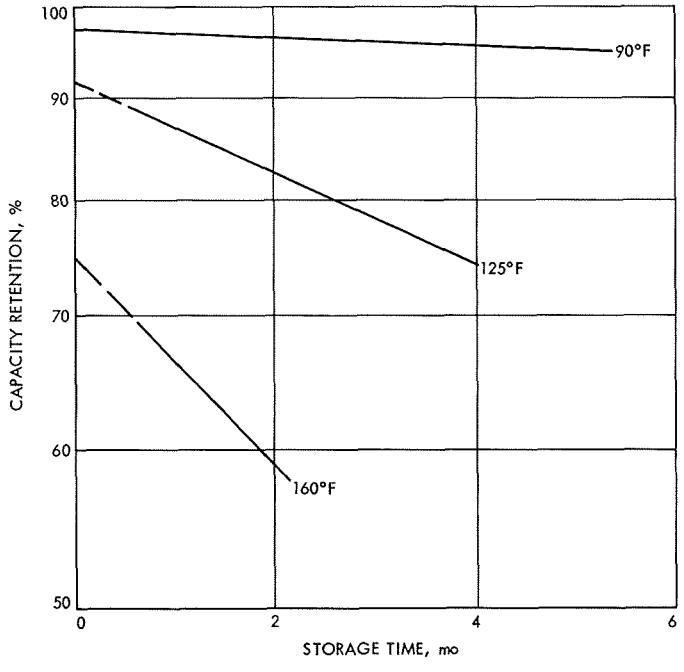

Fig. 26. Capacity retention vs storage temperature for charged storage of experimental cells

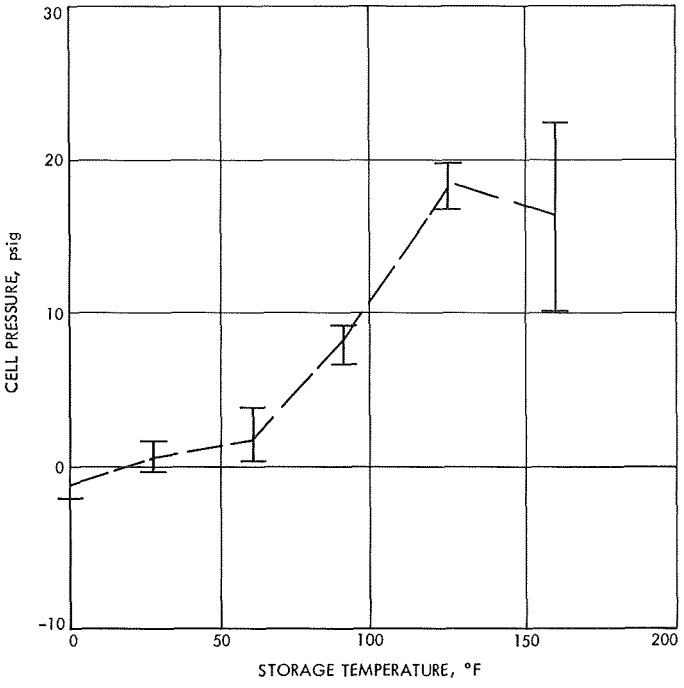

Fig. 27. Cell pressure during charged storage vs temperature for experimental cells

Calculated capacity loss rates for experimental cells and a commercially available high rate cell are plotted in Fig. 28. The nonlinearity of the plot for the experimental cell may be due to the surface-controlled nature of the discharge reaction, contrasted to the linear plot for the high-rate (thin-plate) cell[4].

Voltage degradation during charged storage was rather low and independent of temperature, as shown by the data in Table 7. Inasmuch as losses in capacity and potential are very low at low temperatures, storage below 60°F was recommended.

3. *Stand loss for discharged storage.* This discharge test was accomplished to determine the stand loss in experimental model cells during discharged storage.

a. Test procedure. The test procedure involved: (1) storing the charged cells for 26 days; (2) discharging the cells at 7.0 A to a 1.25-V cutoff to determine cell capacity; (3) storing the cells for 60, 180, and 365 days at 30 and 90°F; (4) charging the cells after storage at 2.0 A to a 1.96-V cutoff; and (5) discharging the cells at 7.0 A to a cutoff of 1.25 V to redetermine the cell capacity.

[4]Personal communication from J. J. Rowlette, Hughes Aircraft Company, Culver City, Calif.

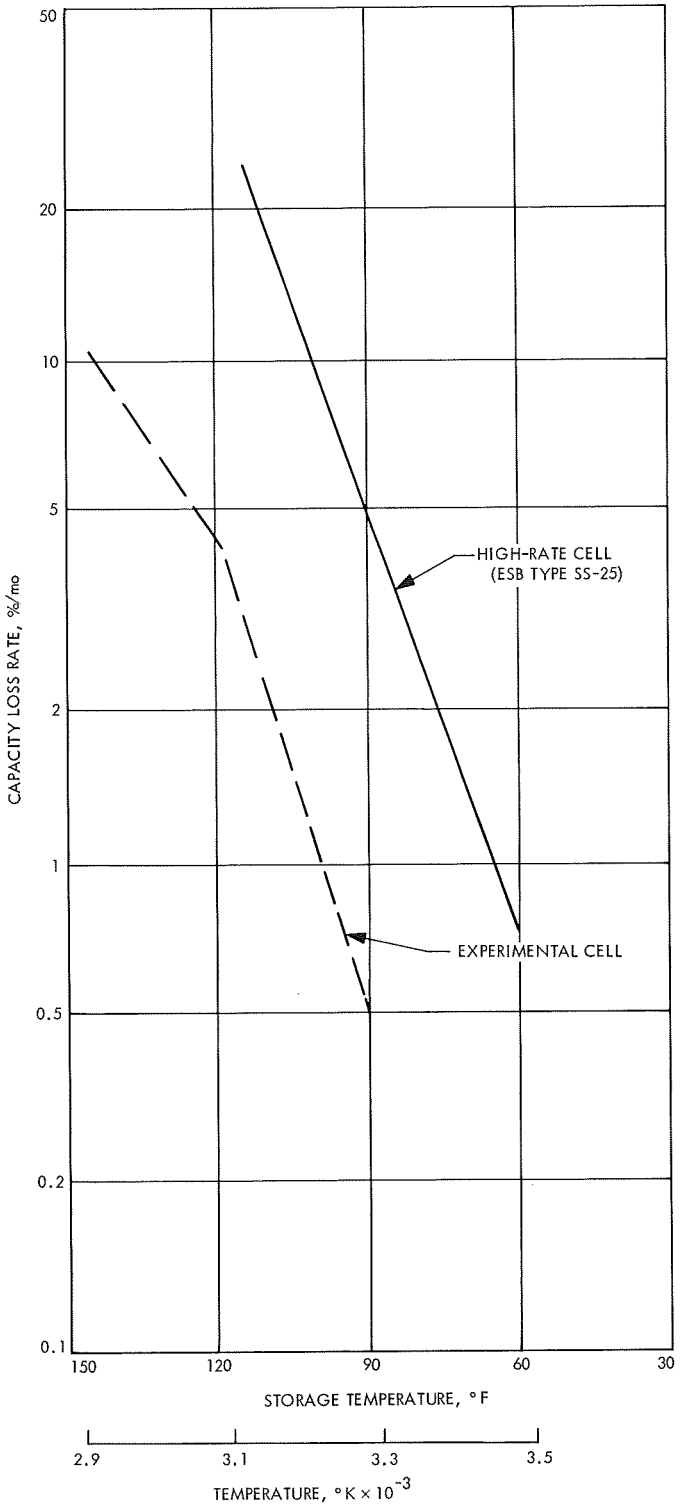

Fig. 28. Effect of charged stand temperature on capacity loss rate for experimental cells

b. Results and conclusions. Results of the discharge storage test are summarized in Table 8. The data indicate

Table 7. Discharge voltage at 7 A for charged stand

History, °F	Stand time before discharge, mo	Plateau voltage on 7A discharge
New		1.52 – 1.535
160	½	1.49 – 1.50
160	1	1.50 – 1.51
160	2	1.49 – 1.50
125	1	1.49 – 1.50
125	4	1.48 – 1.49
90	1	1.51 – 1.52
90	4	1.51 – 1.52
90	12	1.50 – 1.52
60	1	1.51 – 1.52
60	4	1.51 – 1.52
60	12	1.51 – 1.52
30	1	1.51 – 1.52
30	4	1.51 – 1.52
30	12	1.51 – 1.52
0	1	1.51 – 1.52
0	4	1.51 – 1.52
0	12	1.51 – 1.525

a considerable variability in discharged stand loss, but a significantly larger stand loss for long term storage at 90°F is apparent. The variability in these results caused ESB to recommend that all long term storage be conducted in the charged state.

4. Direct current impedance test. The dc impedance test was performed to determine the dc impedance of the experimental cell, when being discharged on the lower voltage plateau.

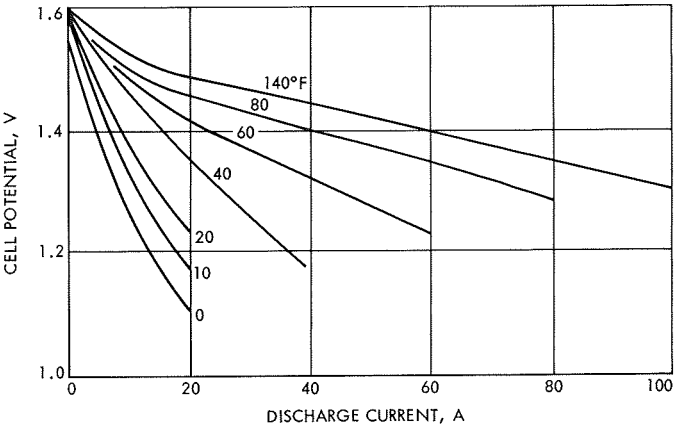

Fig. 29. Plot of cell potential as a function of the discharge rate and environmental temperature for experimental model cell

Table 8. Discharged stand test

Cell, SN	Charge input, A-h	Stand time, days	Output at 7A	Storage		Charge input, A-h	Output at 7A, A-h	Charge input at 2 A, A-h	Output at 7A, A-h
				Time, days	Temperature, °F				
59	171	26	163	60	30	134	142	—	—
89	171	26	150	60	30	113	112	—	—
39	171	26	163	60	90	148	150	—	—
61	171	26	163	60	90	160	164	—	—
77	171	26	157.6	180	30	164	166.6	—	—
141	171	26	150	180	30	162	166	—	—
99	171	26	160	180	90	120	119	—	—
91	171	26	150	180	90	92.5	78.5	—	—
66	171	26	157.3	365	30	170	—[a]	—	—
101	171	26	154	365	30	150	148.4	136.8	138
100	171	26	163	365	90	91.8	91	119.8	122
67	171	26	163	365	90	107.6	105	121.8	124

[a]Automatic charger cutoff failed to operate and resulted in cell failure due to overcharge.

a. Test procedure. The test procedure consisted of: (1) charging the cells at room temperature at the 2.0-A rate to a 1.96-V cutoff; (2) permitting the cells to stabilize at the test temperature for 1 day; and (3) discharging the cells at the following rates:

Rate, A	Time, h
1	0.5
3	0.5
5	0.5
8	0.5
10	0.5
15	0.5
20	0.5
30	0.5
40	0.25
60	0.1
80	0.1
100	0.05
1	0.5
5	0.5
10	0.5
20	0.5

At some combinations of temperature and current, the cells did not support the desired load long enough to determine a stable potential. From the data, the dc impedance was to be calculated by the slope of the voltage–current curve (slope = $\Delta V/\Delta I$).

b. Results and conclusions. The results of the discharge runs are shown in Fig. 29. Slopes of curves in Fig. 29 yielded the dc impedance data, plotted in Fig. 30.

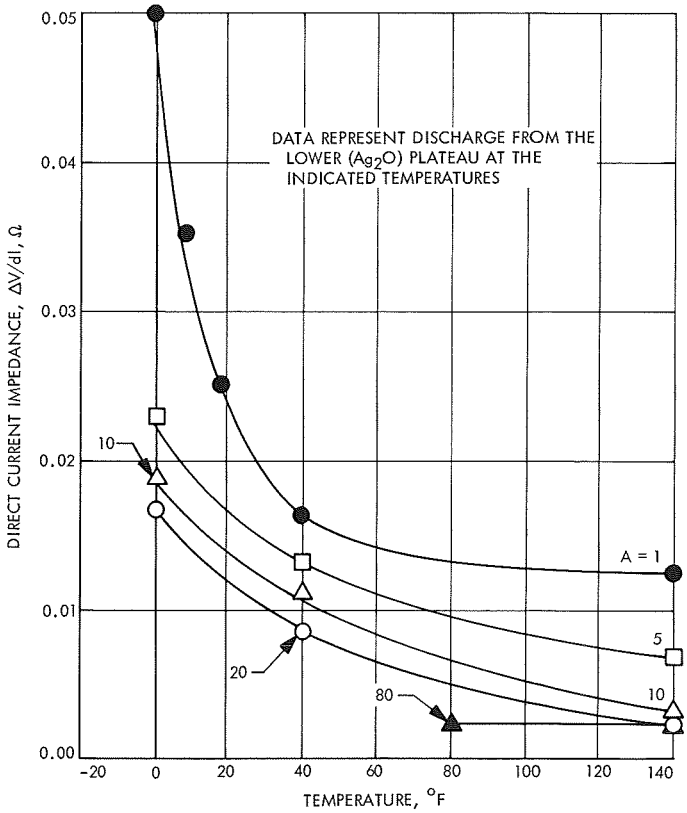

Fig. 30. Direct current impedance vs temperature for several discharge rates for experimental cells

There is considerable doubt concerning the validity of the low temperature data because electrode temperatures will change rapidly when high currents are drawn as indicated in tests with thermocouple-equipped batteries (Section VI). The dc impedance data in general should be used with caution when attempting to calculate cell potentials, as the latter are also a function of cell history, state of charge, and duration of the applied discharge current.

C. Mission Simulation Tests

This subsection describes mission simulation tests that were performed with experimental model cells and monoblocks. The tests were limited to simulation of parts of lunar day 1, the full lunar night power profile, and parts of lunar day 2.

1. Simulation of lunar day 1. The simulation of lunar day 1 test was an examination of the performance of a five-cell experimental model monoblock.

a. Procedure. The test procedure involved a series of charge–discharge cycles at temperatures from 30–75°F, charging for 1.0–5.0 h at 1.0, 3.0, and 5.0 A, and discharging for 0.25–0.75 h at the 16.0-A rate. The test schedule is shown in Table 9. In addition, a series of 50-ms, 40-A discharge pulses were applied to simulate the pulse loads (see Fig. 36).

Table 9. Program for simulation test of lunar day 1 by a five-cell experimental model monoblock

Run number	Battery state	Duration, h	Current, A	Temperature, °F	Remarks, see Fig.
1	Discharge	0.25	16	30	31
2	Charge	5.0	1	30	32
3	Discharge	0.25	16	40	31
4	Charge	5.75	1	40	32
5	Discharge	0.25	16	50	31
6	Charge	5.5	1	50	33
7	Discharge	0.25	16	60	31
8	Charge	5.65	1	60	33
9	Discharge	0.25	16	75	31
10	Charge	5.75	1	75	34
11	Discharge	0.75	16	50	—
12	Charge	13	1	50	34
13	Discharge	0.75	16	35	—
14	Charge	1.0	5	35	35
15	Charge	1.75	3	35	—

b. Results and conclusions. Results of the simulation of lunar day 1 are presented in Figs. 31–36. Except for the pulse discharge, the monoblock met requirements. The average minimum cell potential, resulting from a 50-ms, 40-A discharge at an environmental temperature of 30°F was 1.185 V. This potential is equivalent to a battery potential of 16.6 V, which is below the minimum acceptable value of 17.5[5] V. Therefore, an increase in cell capacity by 10% was indicated.

2. Lunar night simulation. The lunar night simulation test was run on a five-cell experimental monoblock to determine if the experimental model battery was capable of fulfilling the requirements for lunar night performance.

[5]18.0 V in early specifications.

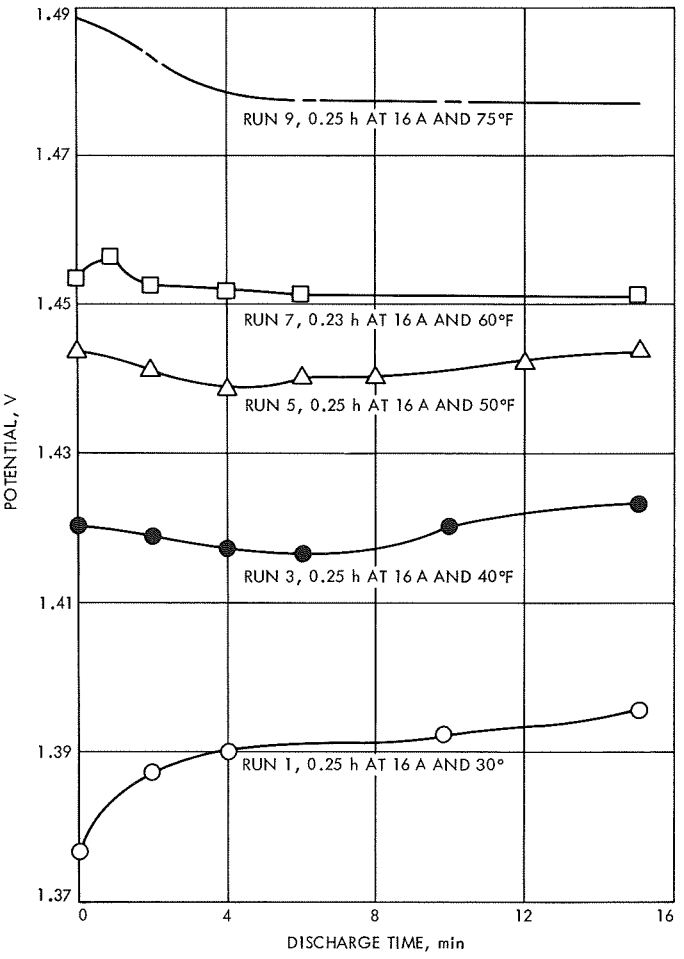

Fig. 31. Discharge curves, five-cell experimental monoblock—simulation test of lunar day 1

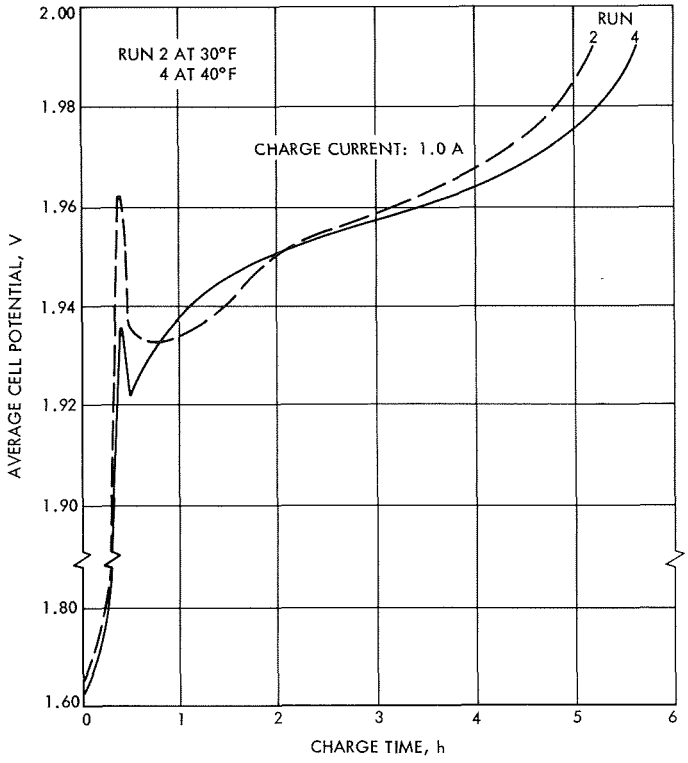

Fig. 32. Experimental model charge curves, experimental model five-cell monoblock—runs 2 and 4—simulation of lunar day 1

a. Procedure. The test procedure is summarized in Table 10. The observed voltages during the third cycle have been entered for comparison.

b. Results and conclusions. The results, plotted in Fig. 37, indicate that discharge of 118.9 A-h would result in a battery potential of approximately 16.8 V; this potential is below the minimum permissible level of 17.5 V. Retention of the loads, therefore made it necessary to increase the battery capacity by approximately 10% in the development model. A similar increase was recommended as a result of tests simulating the first lunar day.

Table 10. Lunar night simulation test plan

Sequence number	Load, Ω	Average current, A	Average battery potential, V		Accumulated A-h
			Estimated	Observed	
A-3.0	73.4	0.33	21.9	21.9	18.92
A-3.1	7.34	2.8	20.5	20.5	23.10
A-3.2	12.2	1.7	21.1	21.0[a]	—
A-3.3	91.5	0.24	21.5	21.6[a]	—
A-3.4	44.0	0.46	21.4	Approximately 16.8	118.9 after 12 repetitions of sequence A-3.2 to A-3.4.

[a]Observed during third performance of A-3.2 to A-3.4. After the third performance, high current discharges were omitted, but the total ampere-hour discharge simulated the lunar night discharge.

D. Test Program on Experimental Model *Surveyor* Main Battery

1. Types of tests. The objective of the test program for the experimental model *Surveyor* battery was to verify the basic soundness of the battery selected for use in the *Surveyor* spacecraft.

The tests comprising this phase of the program were:

(1) General inspection test and receiving procedure.

(2) Initial capacity test.

(3) Dynamic charge surge and internal impedance test.

(4) Charge matrix test.

(5) Cycle life test.

(6) Magnetometer survey.

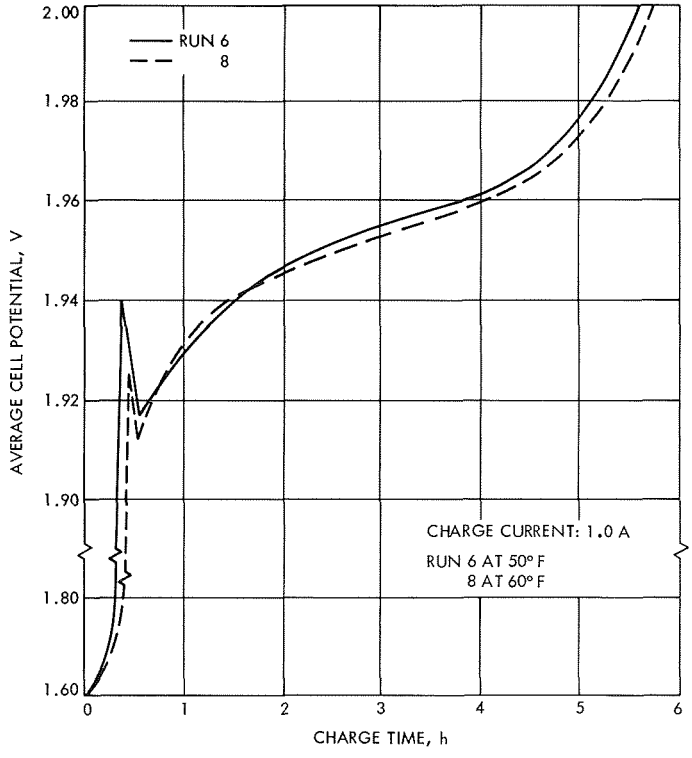

Fig. 33. Charge curves, experimental model five-cell monoblock—runs 6 and 8—simulation of lunar day 1

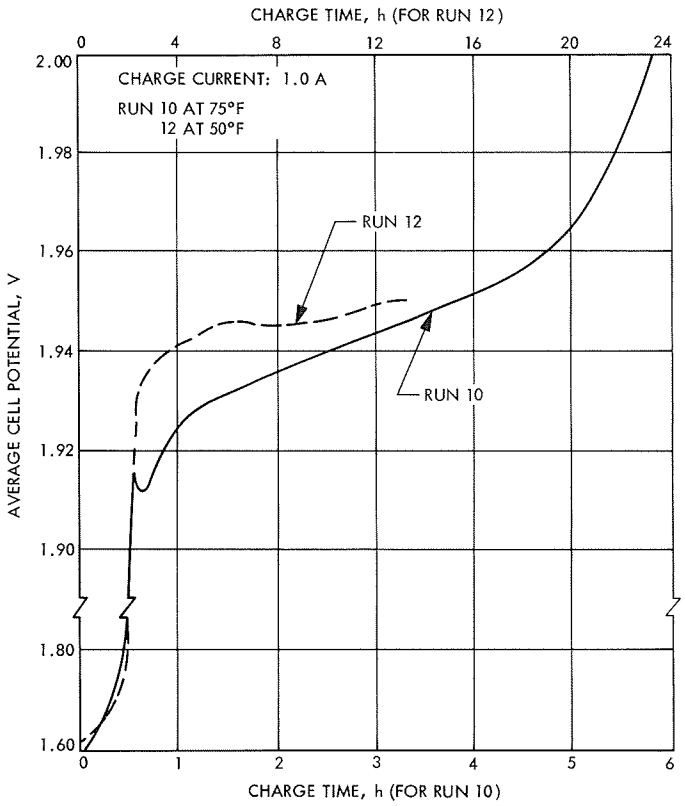

Fig. 34. Charge curves, experimental model five-cell monoblock—runs 10 and 12—simulation of lunar day 1

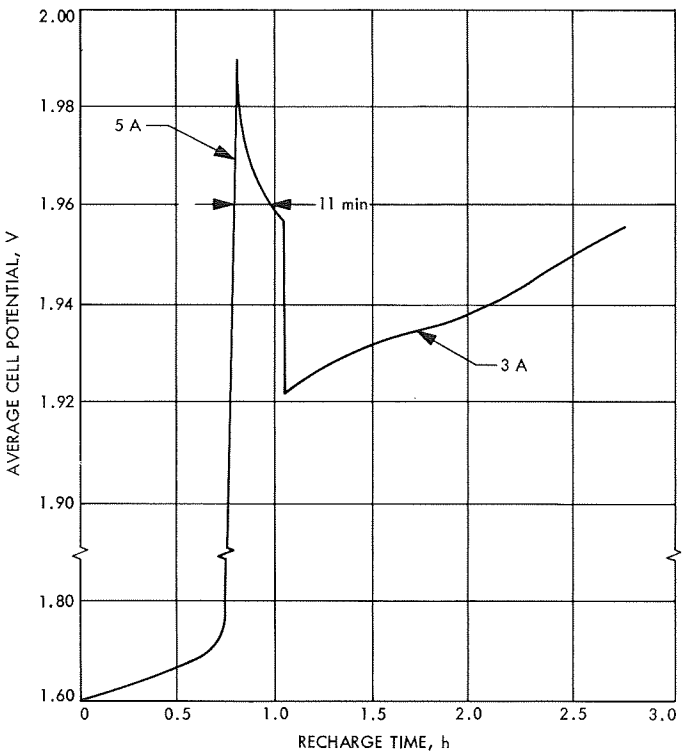

Fig. 35. Charge curves, experimental model five-cell monoblock—run 14—simulation of lunar day 1

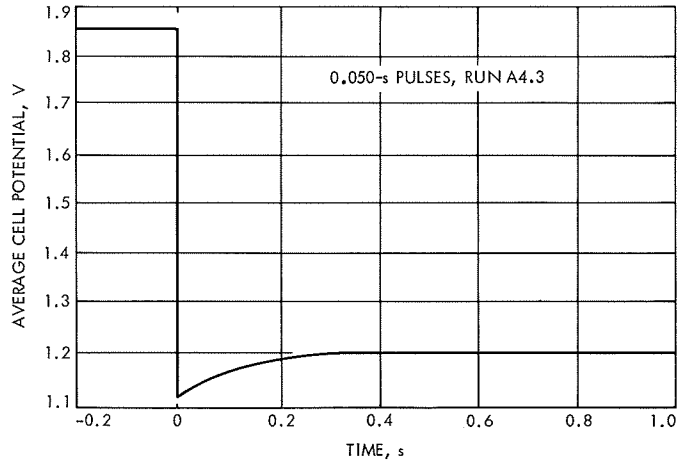

Fig. 36. Average cell potential of fully charged experimental model five-cell monoblock after a 50-ms, 40-A pulse at 30°F

2. *General inspection test and receiving procedure.* The general inspection test and receiving procedure was performed to detect defects in performance, workmanship, and general quality of the experimental model *Surveyor* battery.

a. Procedure. The test procedure included: (1) inspection for visible defects and general quality of workmanship; (2) measurement of battery open circuit potential and cell open circuit potential; (3) measurement of insulation resistance between each external terminal of the battery connector and the battery case with a 500-Vdc potential; and (4) determination of battery weight and battery dimensions.

b. Results. The results of the tests performed on all eight experimental model *Surveyor* batteries are presented in Table 11.

3. *Initial capacity test.* The purpose of this test was the determination of battery capacity by performing a discharge–charge cycle.

a. Procedure. The test procedure consisted of: (1) discharging the factory-charged battery at the 7.0-A rate to a cutoff potential of 17.5 V; (2) charging the battery at the 2.0-A rate to a potential of 27.3 V at an ambient temperature of 70°F; and (3) applying a topping charge

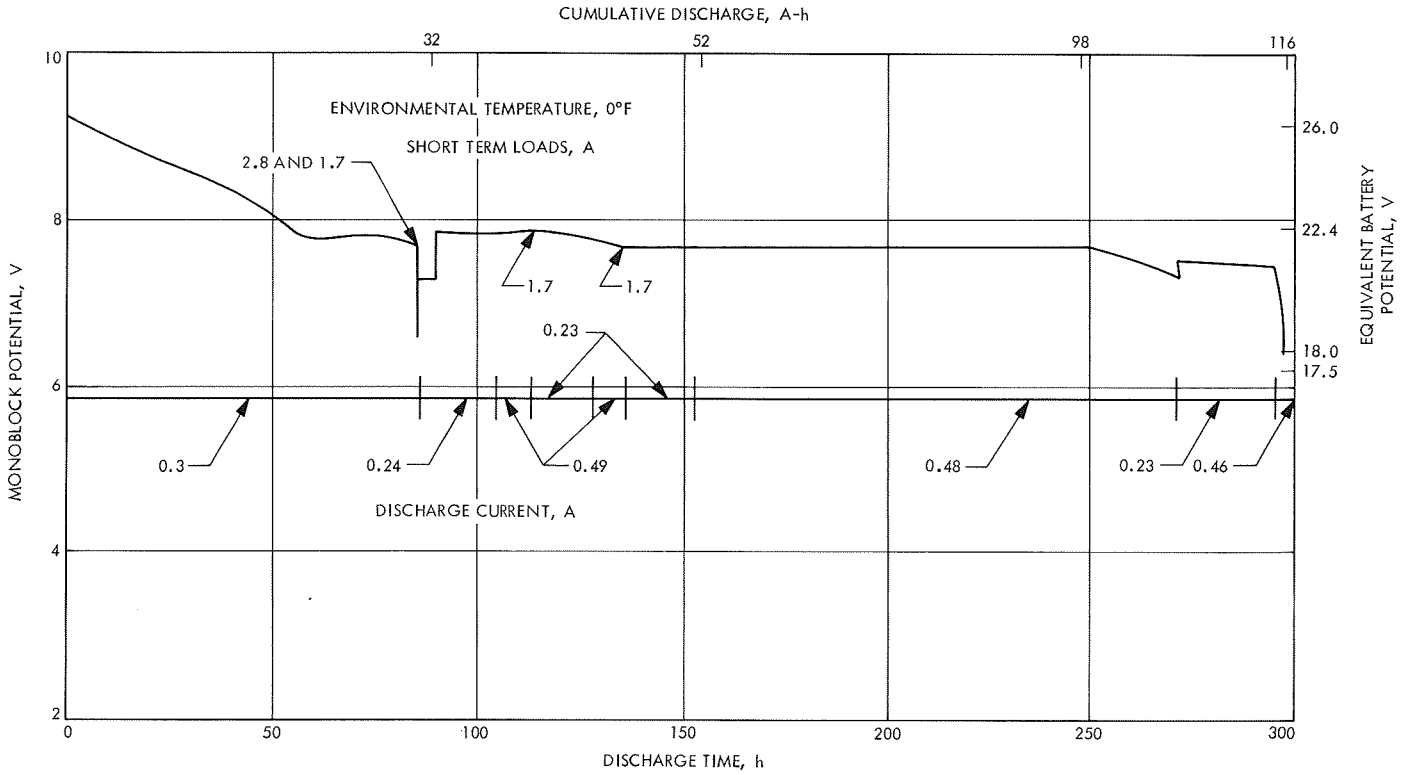

Fig. 37. Simulated lunar night discharge of five-cell experimental model monoblock

of 1.0 A to a potential of 27.3 V at the same ambient temperature. In several cases, the 1.0-A charge was omitted. Testing of batteries X5–X8 further included observation of cell pressures by means of attached Bourdon gages.

Table 11. Results of general inspection test and receiving procedure of experimental model batteries

Characteristic	Test results	Nominal specification values
Battery open circuit potential	25.998 – 26.037 V	25.6 V
Cell open circuit potential	1.856 – 1.885 V	1.83 V
Length	13.900 – 13.925 in.	13.90 in.
Width	7.240 – 7.265 in.	7.26 in.
Height	6.700 – 6.720 in.	6.69 in.
Cell pressure (as received)	0.0 – 14.1 psig	—
Weights		
SN X1–X4	45.760 – 45.940 lb	46.0 lb
SN X5–X8[a]	51.600 – 51.990 lb	—
Insulation resistance	≥10 MΩ	≥10 MΩ

[a]Includes Bourdon pressure gage on each cell.

b. Results and conclusions. The results of the initial capacity test are summarized in Table 12. The initial discharge efficiency of the batteries ranged from 88.0% to 98.0% with an overall average for the eight batteries of 93.5%. On recharge at HAC, a relatively large charge input at 1.0 A was required for two of the batteries to restore the charge input to an acceptable level. Owing to the far lower polarization of the electrodes at low charge rates, charging at low charge rates will generally permit the attainment of a higher state of charge. Typical discharge and recharge curves are shown in Figs. 38 and 39. The discharge capacity of the batteries (147.0–158.5 A-h) is marginal at ambient temperature and insufficient to meet low temperature power demands. The maximum observed pressure during the test was 36 psig. Pressure variations between cells and batteries were appreciable.

4. Dynamic charge surge and internal impedance test. The dynamic charge surge and internal impedance test served to establish the transient response of the battery as a function of the charge rate at various states of charge and temperatures.

Table 12. Results of initial capacity test on experimental model batteries

Battery SN	Initial charge at ESB, A-h			Initial discharge at HAC, A-h at 7 A	Efficiency, %	Subsequent charge at HAC, A-h			Maximum observed pressure, psig
	at 2 A	at 1 A	Total			at 2 A	at 1 A	Total	
X1	157.0	4.5	161.5	154.2	95.6	153.0	9.6	162.6	—
X2	157.0	4.5	161.5	158.4	98.3	170.0	—	170.0	—
X3	157.0	4.5	161.5	155.0	96.1	165.2	—	165.2	—
X4	157.0	4.5	161.5	158.0	98.0	173.5	—	173.5	—
X5	159.5	8.0	167.5	147.0	87.7	147.2	21.6	168.8	18
X6R[a]	159.5	8.0	167.5	147.5	88.0	139.5	31.2	170.7	36
X7	159.5	8.0	167.5	155.0	92.6	154.0	8.3	162.3	30
X8	159.5	8.0	167.5	155.0	92.6	166.9	—	166.9	20

[a]Replacement for X6.

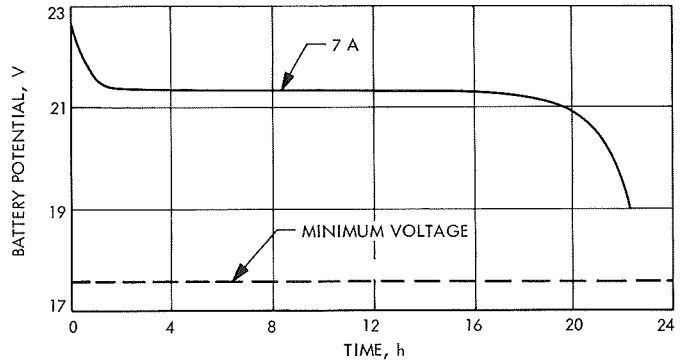

Fig. 38. Discharge characteristics of experimental battery X-4 at ambient temperature and constant current

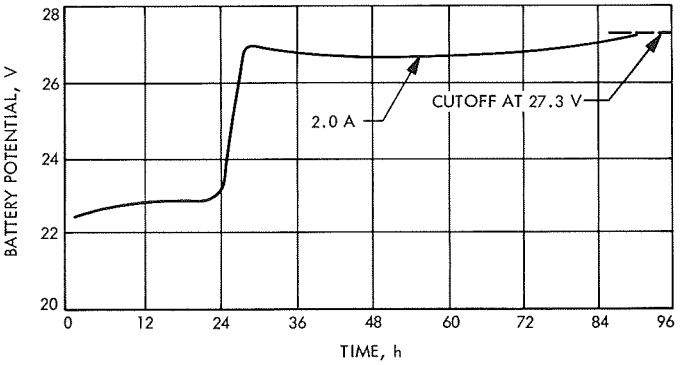

Fig. 39. Charge characteristics of experimental model battery X-4 at ambient temperature and constant current

a. Test procedure. The test procedure consisted of charging the battery in sequence at 5.0, 4.0, 3.0, 2.0, and 1.0 A with charge termination each time when the potential stabilized. Following each charge, the battery was discharged to withdraw the number of ampere-hours, charged in the preceding charge. The test was conducted at ambient temperature in the laboratory.

b. Results and conclusions. Results of the test are shown in Figs. 40 and 41. Briefly, the data indicate: (1) a correlation exists between duration of the charge surge and the charge rate, and (2) a correlation exists between maximum transient potential and the charge rate. A detailed discussion of this subject is included in Subsections III-E-3 through III-F-5.

5. Charge matrix test. The charge matrix test was performed to determine the charge characteristics of the experimental model *Surveyor* battery at various charge rates and environmental temperatures.

a. Test procedure. The test procedure consisted of charging the battery to a 27.3-V cutoff at environmental temperatures of 0 and 70°F, and at rates of 2.0, 5.0, and 0.5 A, and discharging the battery at the 7.0-A rate to a 17.5-V cutoff between charges at the environmental charge temperature.

b. Results and conclusions. Charging potential–time curves are plotted in Fig. 42 and cell pressure data in Fig. 43. The data permit the following conclusions:

(1) Charge input is a function of temperature (larger at 70°F than at 0°F).

(2) Charge input is an inverse function of the charge rate (larger at low rates).

(3) Charging occurs on two plateaus.

(4) Cell pressures during high rate charging can be high and out of balance (5-A data).

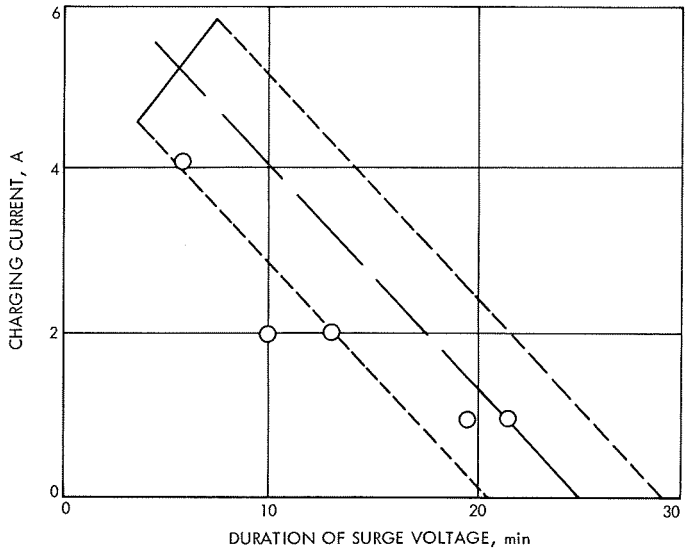

Fig. 40. Duration of voltage transient vs charging current at 82.8°F for experimental battery X-4

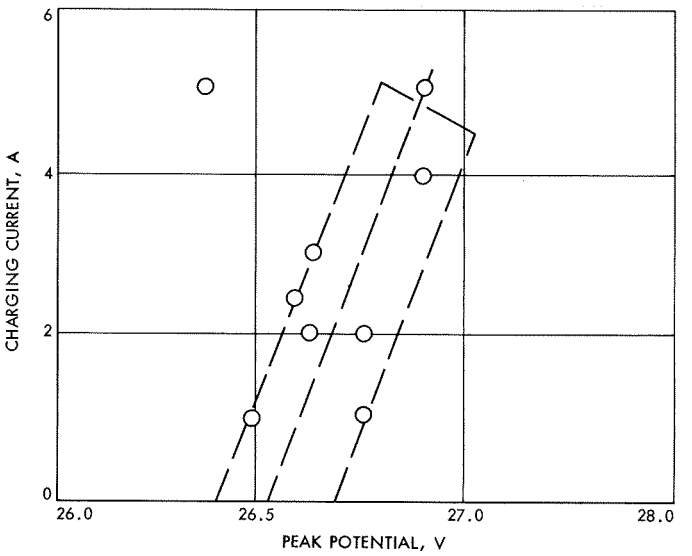

Fig. 41. Maximum charge (transient) voltage vs charging current at 82.8°F for experimental battery X-4

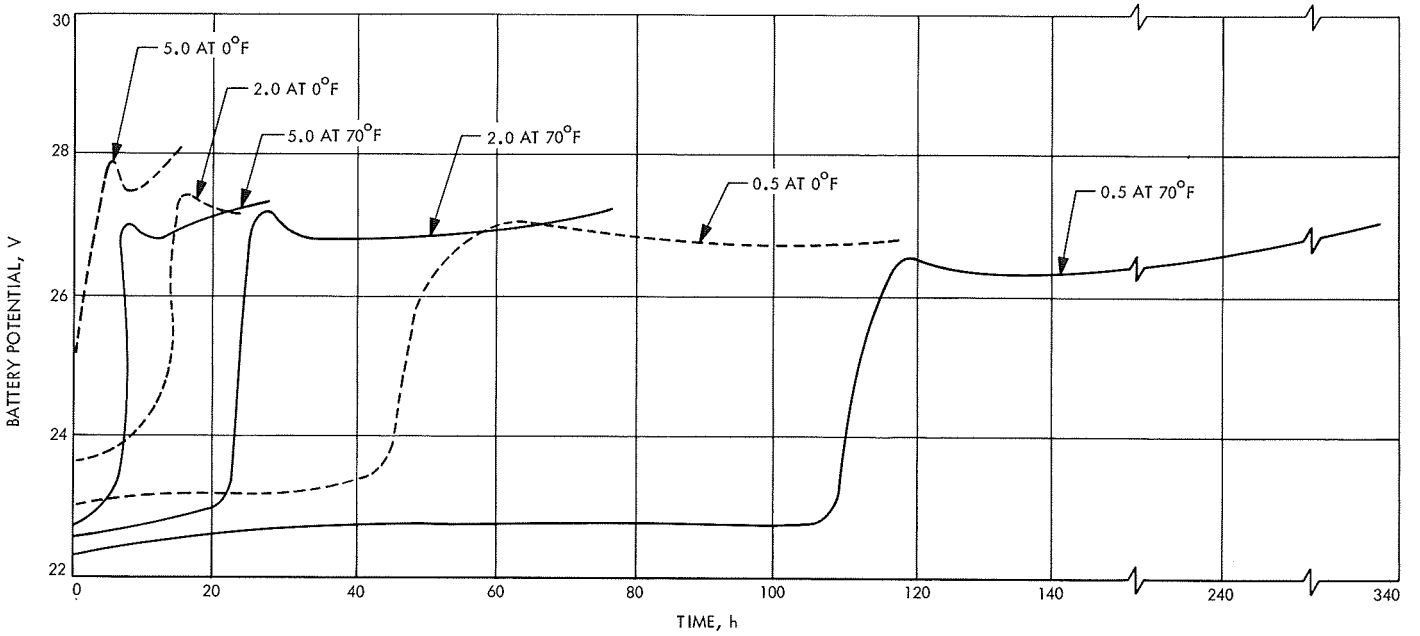

Fig. 42. Results of charge matrix test on experimental model battery

6. Discharge matrix test. The discharge matrix test was designed to determine the constant current discharge characteristics of the experimental model *Surveyor* battery at various discharge rates and environmental temperatures.

a. Test procedure. The test procedure consisted of discharging the fully-charged battery at each of the following rates (at temperatures of 0, 70, and 125°F): 0.5, 2.0, 10.0, and 20.0 A to a 17.5-V cutoff. The battery was charged at the 2.0-A rate to a 27.3-V cutoff at 70°F between each of the discharges. When required by battery characteristics, certain discharges were omitted.

b. Results and conclusions. Discharge potential–time curves are plotted in Fig. 44, battery temperature data

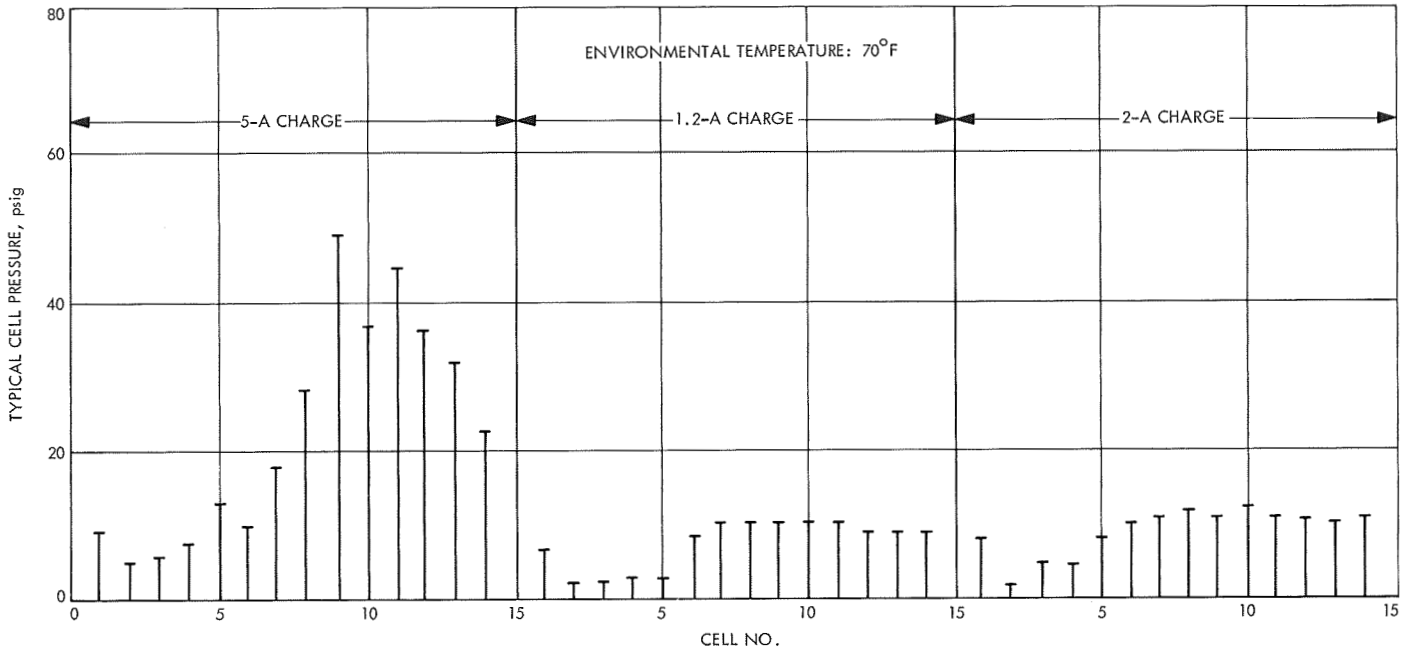

Fig. 43. Typical cell pressure data, obtained during charging of experimental model battery

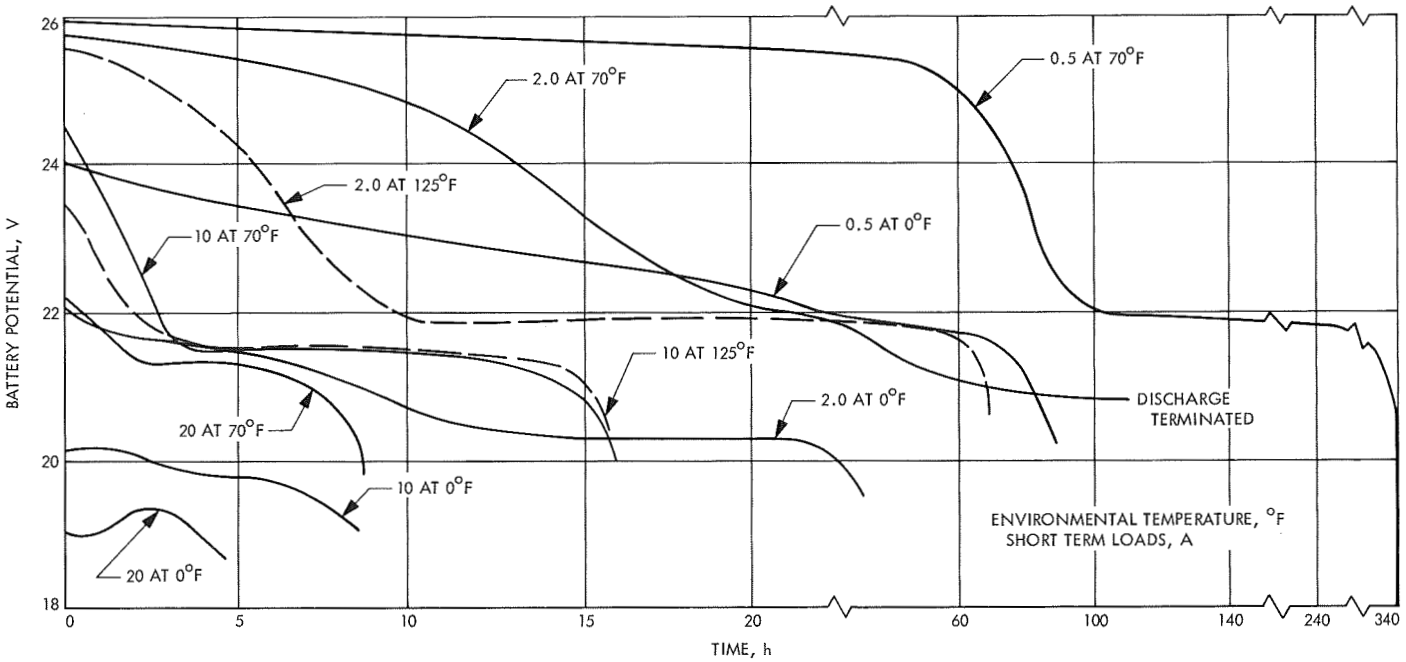

Fig. 44. Results of discharge matrix test on experimental model battery

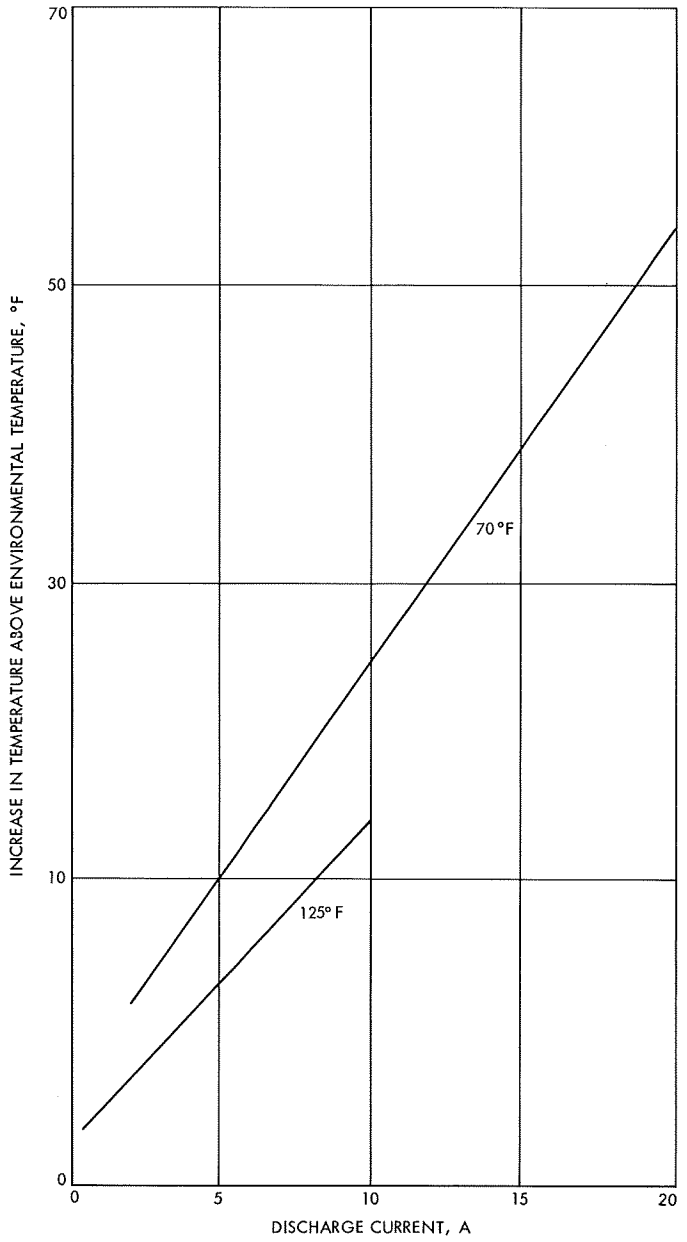

Fig. 45. Maximum increase in battery temperature above environmental temperature during discharge matrix test of experimental model battery

in Fig. 45, and watt-hour capacity data in Fig. 46. The results yield the following conclusions:

(1) Discharge of the silver–zinc couple takes place on two plateaus and this two-step discharge is most prominent at low discharge rates, becoming almost unobservable at high rates (0.5 vs 20 A).

(2) High discharge rates cause a large increase in battery temperature that may ultimately damage the separator with resultant cell failure (e.g., 20-A discharge rate in a 70°F environment caused the battery temperature to reach 130°F).

(3) The battery potential is an inverse function of the discharge rate (potential is lower at high discharge rates).

(4) The battery potential is a function of the battery temperature (potential is lower at lower temperatures).

(5) The battery watt-hour capacity is proportional to the battery temperature (capacity is lower at low temperatures).

(6) The battery watt-hour capacity is an inverse function of the discharge rate (capacity is lower at high discharge rates).

7. Cycle life test. The cycle life test was to be accomplished to determine the number of discharge–charge cycles that the experimental model *Surveyor* battery can survive under a set of simulated conditions.

a. Test procedure. The test procedure consisted of repetitive discharge–charge cycles involving discharge at 7.0 A to 17.5 V and charge at 2.0 A to a 27.3-V cutoff. The test was performed at laboratory ambient temperature.

b. Results. No results were obtained. Because of prior battery failures, batteries were not available for this test.

8. Magnetometer survey. The purpose of the magnetometer survey was the determination of the dc magnetic field at a distance from the experimental model *Surveyor* battery, when operating under typical conditions.

a. Test procedure. This test was performed by JPL. The test procedure consisted of: (1) fixing the magnetometer sensor, with the axis along which the field is sensed, in the horizontal plane; (2) adjusting the magnetometer to read zero field; and (3) bringing the battery to a distance of 3.0 ft from the magnetometer sensor, rotating it about a vertical axis through the approximate geometric center of the battery, and recording maximum values of the indicated magnetic field.

b. Results and conclusions. The results of this JPL-conducted test, summarized in Table 13, indicated compliance with the battery requirements.

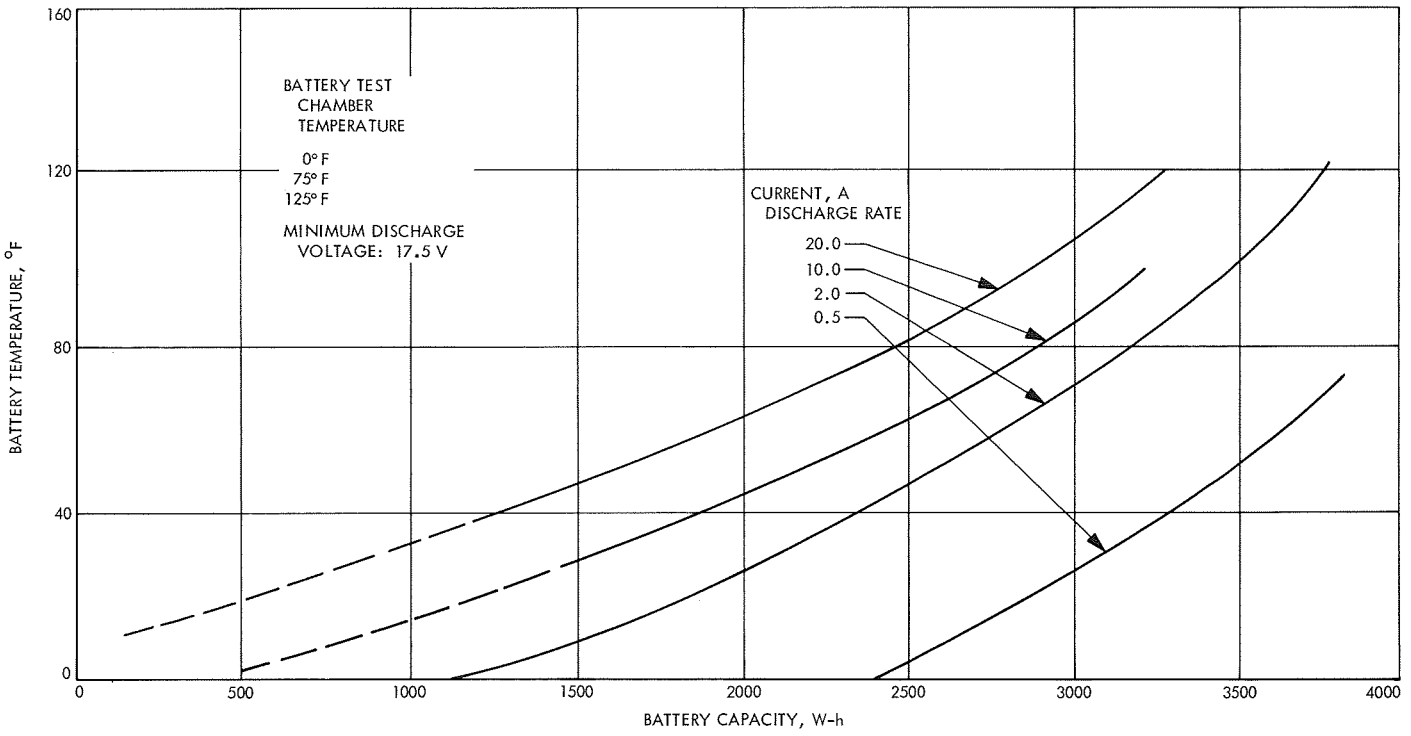

Fig. 46. Effect of battery temperature and discharge rate on watt-hour capacity of experimental model *Surveyor* main battery

Table 13. Magnetometer survey data

Discharge current, A	Distance from battery, ft	dc field strength, γ	
		Measured	Allowed
0	2	2	—
16	4	54	100

E. Failure Analysis

The test program for the experimental model *Surveyor* battery, its component cells, and monoblocks revealed a number of deficiencies that resulted in: (1) shorted cells, (2) cracked cell cases, and (3) premature charge termination because of a voltage surge.

1. Failure of cells by shorting. The cause of shorted cells in most cases was cell plate contact resulting from the tearing of tightly wrapped separator material.

Correction for this deficiency consisted of using additional separator material, allowing more generous folds to be made, during assembly.

2. Failure of cells by cracking of cell cases. The cracking of the cell cases, and consequent shorting of cells, during tests at temperature extremes of 0–125°F, was caused by the difference in the thermal expansion rates of the magnesium battery canister and the polystyrene cell cases.

This deficiency was corrected by inhibiting the polystyrene cell case surfaces during potting by application of silicone grease, so that the mechanical bond of the epoxy to the cell cases was eliminated.

3. Premature charge termination. Premature charge termination that was caused by voltage surge is treated in detail in Subsection III-F-4.

Correction of this deficiency was deferred to the prototype battery phase. In the interim, a temporary increase in charge cutoff voltage to 29.0 V was recommended during the surge period, while monitoring the battery potential until it drops below 27.3 V. At that time the automatic voltage cutoff was reset to 27.3 V. Approaches under consideration included: (1) internal modification of the battery to eliminate the tendency to produce voltage surges; (2) modification of the battery charging

system to include some means of discriminating between the transient voltage surges and the final increase in battery potential that is indicative of the need to terminate the charge; (3) charging the battery at a constant potential in contrast to the constant current mode that was employed with the experimental model *Surveyor* battery (in constant potential charging, the current would reduce to the trickle level as the battery attains a fully charged state); and (4) redesigning the battery so that it can be overcharged without damage (e.g., use of a common manifold). The ultimate solution, adopted in the prototype model *Surveyor* battery, consisted of a manifold battery and constant power charging with limiting potential.

F. Battery Development

This subsection deals with work performed to optimize certain design parameters, and with some peripheral matters, such as, battery sterilization.

1. Density variations in negative active material (negative electrode). X-ray studies were performed by ESB on negative plates without grids in an attempt to determine variations in the density of active material. No variations were detectable. The sensitivity of the technique was then established by fabrication and testing of negative plates that were 20% too dense and 20% below standard density. These ±20% variations were detectable by radiography. It was therefore concluded that the negative plates had density variations of less than 20% from the standard density.

2. Density variations in positive active material (positive electrode). Density variations in active positive material were determined by weight-volume measurements on punchings, using specially made gridless plates. The average plate density was calculated to be 0.170 ±0.0023 lb/in.^{3} (where the deviation represents $\pm\sigma$).

$$\overline{X} = \frac{\sum_{1}^{R} F_i X_i}{N}$$

where

R = number of intervals

$\overline{X}$ = average plate density

X_i = midpoint of interval i

F_i = frequency of observations in interval i

N = number of observations

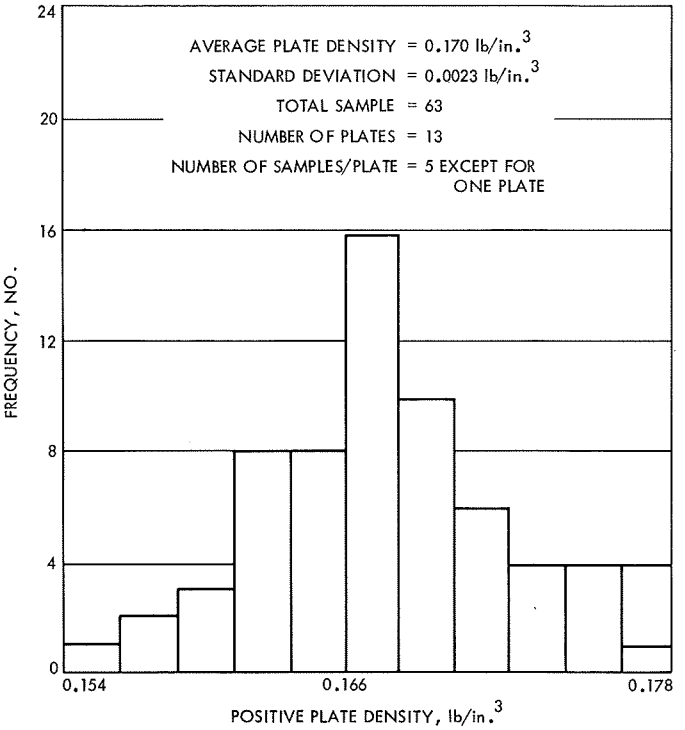

Fig. 47. Density distribution in active material for positive plates of experimental model cells

The density distribution, as determined by these measurements, is illustrated in Fig. 47. The small samplings and the fact that the material was not typical production line output make it difficult to pass a judgment concerning the uniformity of positive plate material in batteries.

3. Effect of positive plate density on electrode performance. In order to determine if the positive plate efficiency is higher at densities exceeding 0.172 lb/in.^{3}, positive plates of a number of densities were prepared and subjected to charge–discharge steps. Figure 48 shows the results obtained when charging electrodes at a 2.0-A rate, at the 2.0-A rate with subsequent 1.0-A charge, and when discharged at the 10.0-A rate. The data indicate a decrease in efficiency at higher positive plate densities; thus, the density was maintained at the standard (0.172 lb/in.^{3} level).

4. Dynamic charge surge tests. During the charging of silver–zinc cells, a transient voltage pulse was frequently observed (see Fig. 18) when the cell potential changed from the Ag_2O level (1.60–1.65 V) to the Ag_2O level (1.86–1.93 V) and when an interrupted charge on the Ag_2O level was resumed. This transient could be of sufficient magnitude to cause premature charge termination when a battery or cell was charged in the constant

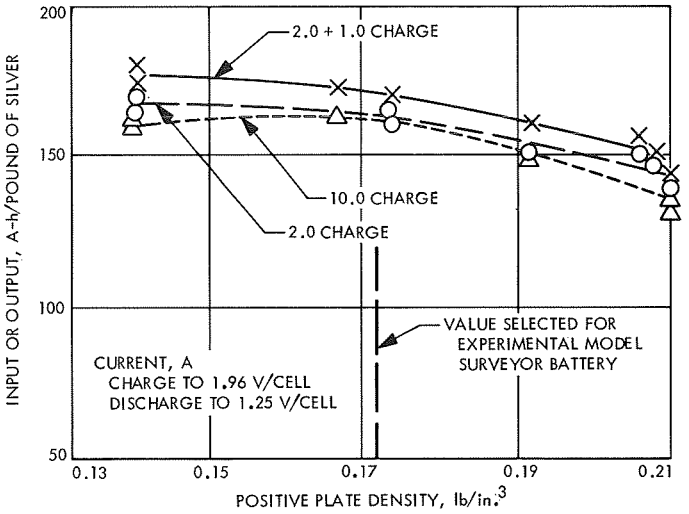

Fig. 48. Positive plate density test with special experimental cells

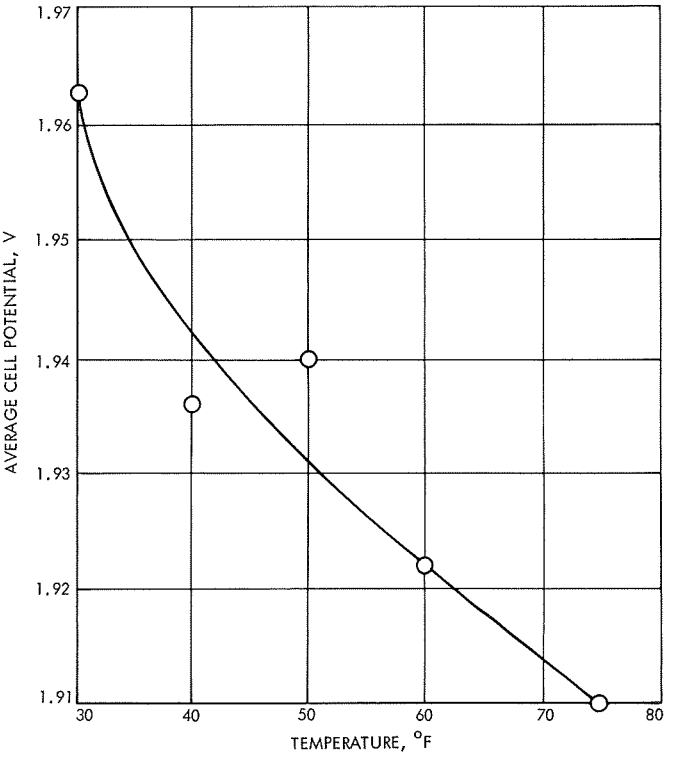

Fig. 49. Peak voltage of initial transient during 1-A charge of five-cell monoblock experimental battery

current mode to a fixed end-of-charge potential. The characteristics of this dynamic charge surge and potential remedies for it were investigated by ESB with results as indicated in the subsequent paragraphs.

a. Duration of surge vs charge rate. A plot showing the effect of the charge rate on the duration of the surge was prepared on the basis of tests with an experimental model battery (see Fig. 40).

b. Magnitude of surge potential vs charge rate. The relation between the maximum surge potential and the charging rate for an experimental model battery has been previously presented (see Fig. 41).

c. Temperature dependence of charge surge. The temperature dependence of the charge surge, as determined by a test with a five-cell experimental model monoblock, is illustrated by Fig. 49.

d. Conclusions based on the tests. The conclusions were as follows:

(1) The surge is greater at low temperatures, reaching a negligible level at temperatures in the vicinity of 70°F and above.

(2) The surge is proportional to the charge rate.

(3) The duration of the surge shows a trend toward shorter times at higher charge rates.

5. Causes and potential remedies for charge surge. In preceding paragraphs, a number of phenomenological aspects of the charge surge have been presented. This subsection provides information concerning the theory of the surge and possible schemes for its elimination.

a. Theory of the charge surge. One theory has indicated that the charge surge is caused by an increase in positive plate resistance due to a coating of nonconducting Ag_2O on the silver powder. It was then concluded that a low resistance shunt through the Ag_2O coating should eliminate the surge. This appears to be incorrect in view of the following statement from Ref. 1:

> The mechanism responsible for the peak in the anodization curve of Ag in KOH solution at the beginning of the AgO step is due to passivation, forcing the currents to small areas and producing a high overvoltage. It is not due directly to an ohmic resistance.

Reference 1 makes mention of the incorporation of a special inert conductive matrix in the positive material with the function of making electrical contact with individual AgO particles, thus minimizing the passivation due to the Ag_2O. In any case, the ESB Missile Battery Division's work proceeded on the basis of seeking a low

resistance shunt through the Ag_2O coating as a means for eliminating the charge surge.

b. Elimination of charge surge by positive plate modification. A number of low resistance materials were incorporated in positive plates as additives. On the basis of their low gassing rate during stand and their ability to withstand sintering temperatures, the following additives were tested: graphite, nickel, cadmium oxide, and lead oxide. The evolution of gas during charged stand from doped positive plates provided the data shown in Table 14. It is significant that nickel-doped plates evolved three to five times as much gas as standard (undoped) plates; gas release from the 3% graphite-doped plate was also higher. The other additives showed no significant change in gassing.

Table 14. Gassing rate at 160°F for positive plates

Additive in positive plate	Gassing rate in.^{3}/day/in.^{2}
1% graphite	0.31
2% graphite	0.26
3% graphite	0.64
1% nickel	1.02
2% nickel	1.02
3% nickel	1.56
1% CdO	0.26
2% CdO	0.37
1% PbO	0.26
2% PbO	0.34
3% PbO	0.34
No additive	0.38

Thus excessive gassing eliminated nickel and 3% graphite as additives. Two charge–discharge cycles were then performed on cells that contained doped positive plates. The results of these cycle tests are summarized in Table 15. On the basis of a relatively low surge potential, low outgassing rate, and unimpaired capacity, lead oxide-doped positive plates were selected for further study. Cells containing lead oxide doped positive plates were subjected to repeated charge steps in order to determine the effect of additive concentration on the magnitude of the surge. The results, shown in Fig. 50, indicated for all runs a reduction in surge potential when two or three percent of lead oxide has been added to the positive plate. Complete elimination of the surge by this means would require optimization of the method of addition and the concentration level of the additive. Further investigation of transient elimination was terminated in favor of a change in charge mode and use of a sealed-manifold type battery.

c. Other proposed remedies for elimination of charge surge. Other possible remedies for the charge surge problem included: (1) modification of the battery charging system to permit discrimination between charge surge potential rise and the final increase in battery potential which indicates that the charge is to be terminated; (2) charging the battery at a constant potential, where

Table 15. Voltage transient analysis

Construction variation	Input capacity at 1 A, A-h	Peak voltage first charge, V	Output at 5 A, A-h	Peak voltage second charge, V	Second cycle input at 1 A, A-h
1% graphite in positive	52.95	1.973	49	1.97	35
2% graphite in positive	55.05	1.975	53	2.05	33
3% graphite in positive	55.05	1.98	52.8	1.97	22
1% nickel in positive	55.05	1.967	52.5	1.98	26
2% nickel in positive	46.6	1.981	44	1.97	29
3% nickel in positive	46.6	1.973	43.5	1.98	32
1% CdO in positive	53.7	1.974	51	1.98	27
2% CdO in positive	46.6	1.976	43.5	—	21
3% plates[a]	—	—	—	—	—
1% PbO in positive	57.1	1.943	53.4	1.965	30
2% PbO in positive	53.95	1.935	51.5	1.94	19
3% PbO in positive	61.95	1.945	59	1.935	29
Cellophane next to positive Ag tested cellophane	54.3	1.973	52	1.99	28
Next to positive	46.6	1.965	44.8	1.98	28
Standard	39.6	1.966	35.8	1.969	27
Positive made from Ag_2O	53.7	1.965	51	1.985	29

[a]The 3% plates could not be constructed because of flaking.

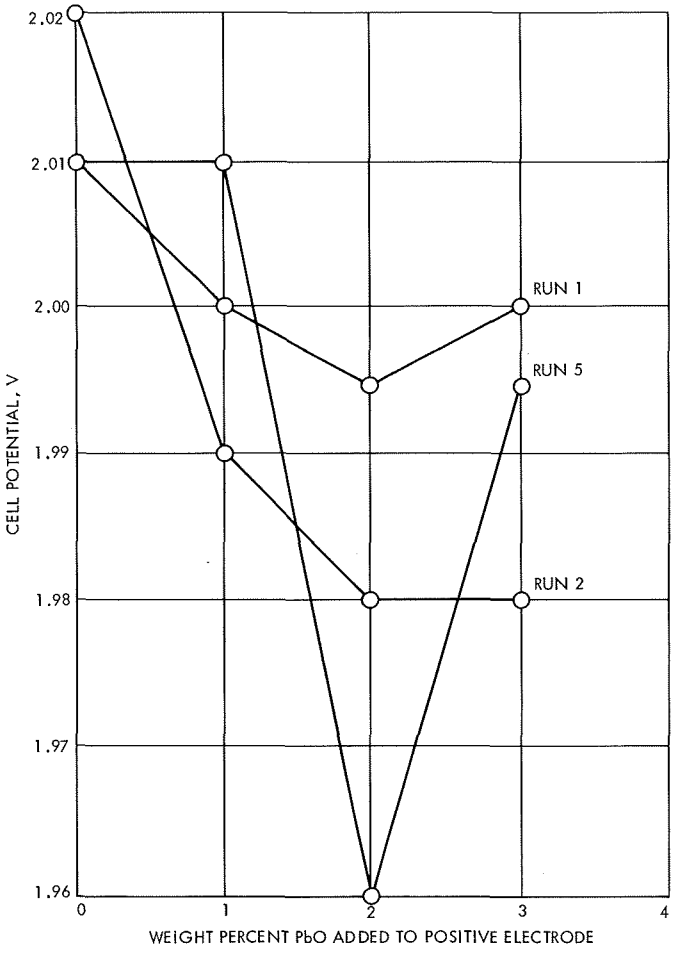

Fig. 50. Effect of positive plate additive on voltage transient at 1-A charge and 75°F with experimental cells

the charging current would reduce to a trickle as the battery reached the fully-charged condition; and (3) redesigning the battery so that it may be overcharged without damage.

The remedy adopted for the flight and prototype models used approach (3). The principal features being the adoption of constant power charging, subsequent float at a 27.3-V limit, and the use of a common manifold between cells.

6. Separator material. No change in separator materials was made from earlier composition (see Subsection III-A-1).

7. Electrolyte. Battery discharge capacity is relatively low at low temperatures (see Figs. 44 and 46). This reduced performance is particularly marked at higher discharge rates, and it is under such conditions that the battery must discharge during the lunar night. Therefore, work was undertaken to optimize the electrolyte concentration for low temperature performance.

a. Discharge efficiency vs electrolyte concentration. The results of tests for the determination of the maximum discharge efficiency as a function of electrolyte concentration at 0°F are shown in Fig. 51. It is significant that at all discharge rates (0.2–1.5 A), maximum discharge efficiency was obtained at a potassium hydroxide concentration of 40%, and that the efficiency was inversely proportional to the discharge rate. Similar data, including information on 40% potassium hydroxide saturated with zinc oxide, are presented in Fig. 52. Again, 40% potassium hydroxide appeared to be the best electrolyte.

b. Stand loss vs electrolyte concentration. It has been shown (see Fig. 28), that the loss in capacity during charged stand is negligible at low temperature (e.g., 35°F), but may be relatively high at elevated temperatures (e.g., 125°F). Therefore, it was imperative to determine the stand loss as a function of electrolyte concentration. The pertinent data are plotted in Fig. 53. Although at 40% potassium hydroxide, the capacity loss rate was not minimal, but it was considered to be tolerable.

c. Cell discharge potential vs electrolyte concentration. Cells containing four and five layers of cellophane separator were discharged repeatedly at the 35-A rate for 50-ms periods in an ambient 35°F environment and

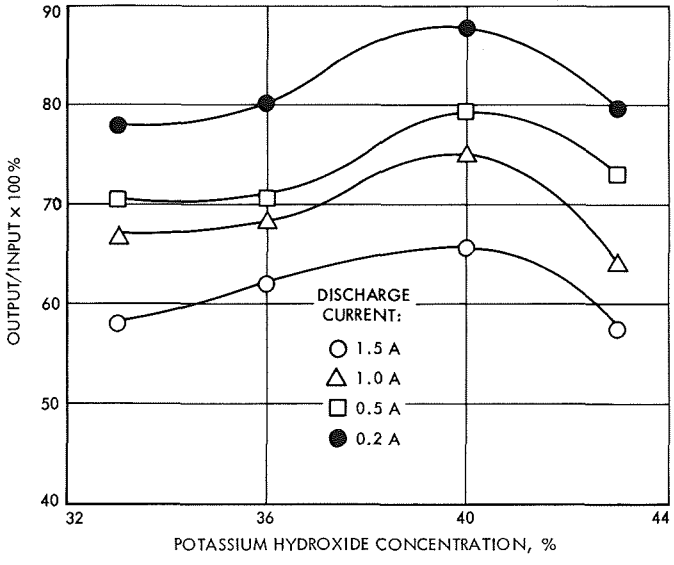

Fig. 51. Discharge efficiency of experimental-type cells at 0°F vs KOH concentration

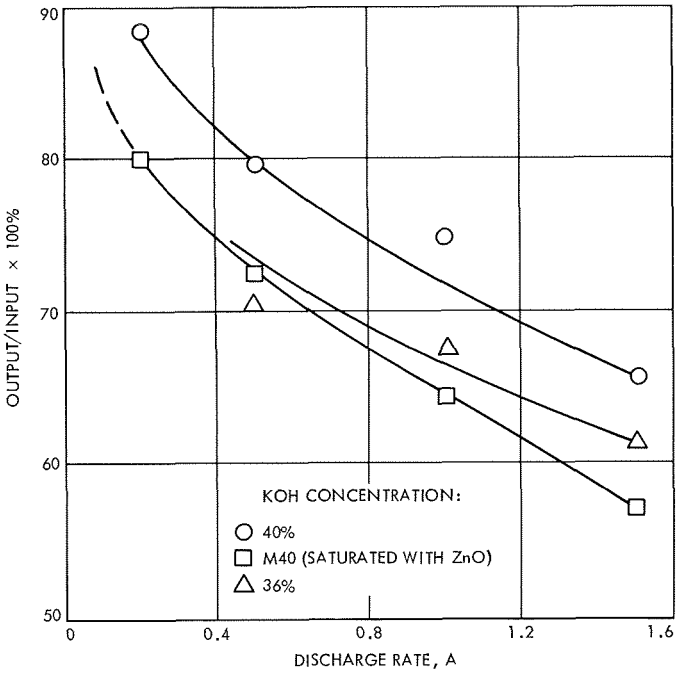

Fig. 52. Discharge efficiency of experimental-type cells at 0°F vs rate

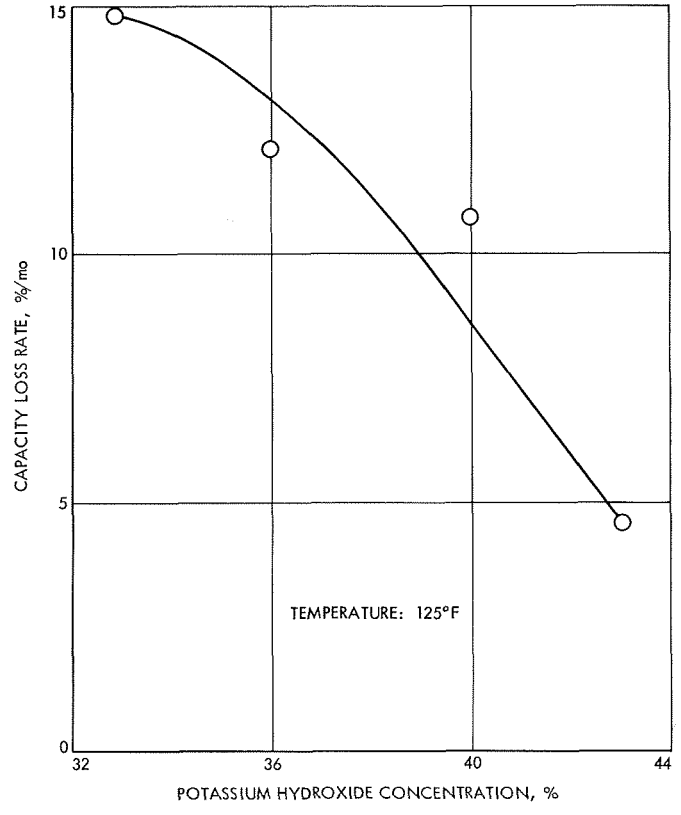

Fig. 53. Capacity loss rate vs KOH concentration for experimental cells at 125°F

the resulting discharge potential was observed. At an electrolyte concentration of 40% potassium hydroxide, the potential was a maximum, as illustrated in Fig. 54.

d. Conclusions regarding the electrolyte concentration. Based on discharge efficiency, tolerable stand loss, and discharge voltage, it was decided to retain the electrolyte concentration at 40% and to omit the addition of zinc oxide to the electrolyte.

*8. **Intercell connectors.*** The battery requirements called for temperature rise limits of 40°F when a current of 32 A flowed for 0.5 h through current-carrying components such as intercell connectors. The experimental model battery used copper strips of 0.060-in. thickness and a width of approximately 1.5 in. as intercell connectors. No experimental data for the temperature rise under these conditions are available. However, preparatory to the design of the development model battery, a 4-ft length of No. 8 AWG (American wire gage), lead was tested by passing 32 A through it for 30 min and measuring the temperature of the lead with a thermocouple. The results of this test (Table 16), indicated a temperature rise of 15°F, where a maximum permissible rise of 40°F was specified.

*9. **Cell case.*** The *Surveyor* battery used the cell case as the primary structure of the battery case. The battery

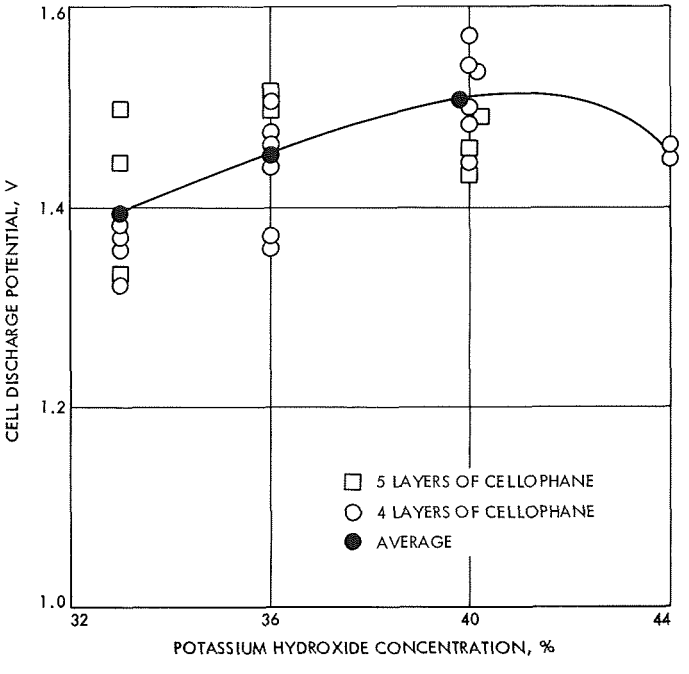

Fig. 54. High-current cell discharge voltage as a function of KOH concentration for experimental cells at 35°F

Table 16. Intercell connector test

Time, min	Temperature, °F	Current, A
0	80	32
5	93	32
10	95	32
15	95	32
20	95	32
25	95	32
30	95	32

case was potted into a magnesium canister that provided mechanical support as well as mounting provisions. This subsection is concerned with cell case material studies, performed to evaluate the experimental model cell case, and potential improvements.

a. Cell case burst strength. Experimental model batteries, made with Cycolac T-1000, Cycolac T-2502, and polystyrene cell cases, were subjected to burst strength tests at 0, 75, and 125°F. The results are presented in Table 17. At 0°F, both Cycolac plastics were inferior

Table 17. Cell case burst data

Tested	Test temperature, °F	Burst pressure, psig	Remarks
Model 203 monoblock polystyrene with a cover cemented in place, end walls supported	75	75	
	75	78	
	75	71	
	75	100	
Model 203 monoblock polystyrene with top seal (pot), end walls supported	75	100	
	75	105	
Fourteen cell Model 203 polystyrene case in a magnesium chassis	0	115	
	75	120	
	75	150	
	25	115	
Model 203 monoblock, natural Cycolac T-1000 cover cemented in place, end walls supported	75	145	
	75	120	
	0	195	
Model 203 monoblock, Cycolac T-2502 appliance white, cover cemented in place, end walls supported	75	165	Polystyrene cover burst
	0	155	
Model 203 14-cell battery 7 cells Cycolac T-2502 7 cells Cycolac T-1000 Potted with 815 + TETA	125	220	End cell broke in corner
	125	210	End cell broke in corner
Model 203 14-cell battery 7 cells Cycolac T-2502 7 cells Cycolac T-1000 Potted with 815 + TETA	75	110	End cell broke between Cycolac and epoxy .
	75	160	Side walls failed
Model 203 14-cell battery 7 cells Cycolac T-2502	0	50	Cement failure
7 cells Cycolac T-1000	0	50	Cement failure
Model 203 14-cell battery 7 cells Cycolac T-2502	0	70	
7 cells Cycolac T-1000	0	70	
Model 203 14-cell battery flexible potting compound 7 cells Cycolac T-2502	0	5	Random cracks
7 cells Cycolac T-1000	0	5	

to polystyrene in burst strength, while at the higher temperatures Cycolac T-1000 was superior to polystyrene. The low burst strength of the Cycolac plastics at low temperatures and the requirement in the procurement specification that the battery be capable of withstanding a differential pressure of 65 psi for 5 min, led to the decision to retain polystyrene as cell case material and to use 815 + TETA + Eccospheres as potting materials for potting cell cases into the magnesium canister. Burst strength data for this combination of polystyrene and potting material are presented in Subsection V-A-2.

b. Leak test. Cell cases, encased in epoxy and magnesium, were subjected to helium leak tests where the cases were pressurized with helium and the pressure decay measured. A leak rate of 4.3×10^{-5} cm³/atm-s was obtained at 125°F for a 14.7 psi differential pressure, compared to a maximum allowable leak rate of 1×10^{-3} cm³/atm-s. The leak rate of these encased cell cases was therefore well within requirements.

c. Differential expansion between cell cases and canister. Failure of the experimental batteries at temperature extremes in four out of a total of eight batteries has been attributed to differences in the thermal expansion and contraction between the outer magnesium canister and the individual polystyrene cell cases. The ratio of thermal expansion of polystyrene to magnesium is approximately 3:1 (Table 18). Using the following equation, calculations were made to establish the magnitude of the stress, resulting in the cell cases from exposure to temperature extremes:

$$\frac{S}{\Delta T} = E(\alpha_1 - \alpha_2)$$

Table 18. Material properties

Material	Coefficient of thermal expansion, in./in.°F	Modulus of elasticity, psi
Polystyrene	38×10^{-6}	0.52×10^{6}
Synpor	39×10^{-6}	—
Polypor	55×10^{-6}	—
Silver	10.4×10^{-6}	—
Zinc	14.6×10^{-6}	—
Magnesium	14.4×10^{-6}	6.5×10^{6}
Epoxy	29×10^{-6}	0.35×10^{6}
Cycolac	55×10^{-6}	0.28×10^{6}
Viskon	70×10^{-6}	—

where

S = stress in cell case, psi

ΔT = temperature change, °F

α_1 = coefficient of thermal expansion of the cell case material, in./in.°F

α_2 = coefficient of thermal expansion of the battery case material, in./in.°F

E = modulus of elasticity of the cell case material, psi

Assuming that the cell case was strained to acquire the same size as the battery canister in the absence of strain (a valid assumption in view of the greater elasticity of the battery case), the stress generated in the cell case was calculated at 12.3 psi/°F for polystyrene and 11.3 psi/°F for Cycolac cell cases. If manufacture takes place at 70°F, then at temperature extremes, the thermal stresses listed in Table 19, could result.

Table 19. Thermal stresses in cell cases

Material	Thermal stress, psi	
	Tension at 0°F	Compression at 125°F
Polystyrene	860	675
Cycolac	790	620

The use of a flexible epoxy to bond the cell cases to the magnesium canister has been suggested as a means for reducing the thermal stress.

d. Separator expansion. As a part of the thermal expansion analysis, the effect of temperature on space available for the cellophane separator has been calculated, based on the assumption that the size of the cell case is determined by the dimensions of the magnesium canister. The change in space available to the cellophane separator as a result of a 70°F temperature change has been calculated by the following formula and data from Table 19:

$$\frac{\Delta X}{\Delta T} = L_M \alpha_M - l_a \alpha_a - l_z \alpha_z - l_s \alpha_s - l_p \alpha_p - l_v \alpha_v$$

where

ΔX = change in space available for cellophane, in.

ΔT = temperature change, °F

L_M = thickness of magnesium canister, in.

αM = coefficient of thermal expansion of magnesium, in./in.°F

1_a = thickness of silver, in.

α_a = coefficient of thermal expansion of silver, in./in.°F

1_z = thickness of zinc, in.

α_z = coefficient of thermal expansion, in./in.°F

1_s = thickness of Synpor, in.

α_s = coefficient of thermal expansion of Synpor, in./in.°F

1_p = thickness of Polypor, in.

α_p = coefficient of thermal expansion, in./in.°F

1_v = thickness of Viskon, in.

α_v = coefficient of thermal expansion of Viskon, in./in.°F

The calculated value was 3.4×10^{-6} in./°F, or 0.24 mil for the 70°F change. This small change was considered to be negligible.

10. Battery sterilization. Preliminary requirements specified sterilization of the interior and exterior of the battery. Sterilization of the exterior surfaces of the battery was to be accomplished by exposure of the battery to a sterilizing gas mixture, composed of 12% ethylene oxide and 88% Freon-12, for a period of 24 h at 100°F in the absence of air. Sufficient water vapor was to be added to raise the relative humidity of the change to 35 (+15, −5)%.

Sterilization of internal components of the battery was to be accomplished as follows:

(1) Internal cell components (plates, separators, etc.) were sterilized by the KOH electrolyte.

(2) Metal parts, wires, connectors, and lacing tape were heat sterilized by heat soaking at 257°F for 24 h.

(3) Injection-molded polystyrene parts were inherently sterile due to molding process.

(4) Polystyrene cement was made self-sterilizing by the addition of 3 wt% of a mixture consisting of 37% formaldehyde and 63% methyl alcohol.

(5) Mating parts were sterilized by wiping with a mixture consisting of 37% formaldehyde and 63% methyl alcohol.

(6) Use of sporicidal cements and compounds.

Sterilization qualification consisted of successful completion of sporicidal tests on specimens, contaminated with *B. Subtilis Variety Niger* at 10^4 viable organisms per gram. All spore concentrations were determined at JPL. The first five of the above sterilization techniques were accepted by JPL. Evaluation of the last technique was in progress when the sterilization requirement was waived by JPL and all work in this area terminated.

Preliminary results of studies on cements and potting compounds are given in Table 20 and they indicate that Emerson and Cuming X1216 + Catalyst 9 and Epon 815 + TETA were the only nonsporicidal agents on the list. Cycolac plastics were negative after sterilization by molding at 300°F.

G. Conclusions

The test program revealed that the basic design of the *Surveyor* main battery was adequate for the intended mission. Several minor deficiencies were uncovered and corrected in subsequent phases of the *Surveyor* main battery program. These deficiencies included the following:

(1) The discharge capacity of the experimental model battery was approximately 10% too low to provide acceptable performance during the lunar night.

(2) Cell failures occurred as a result of excessively tight wrapping of the separator material during the manufacturing process and this situation was rectified by using additional separator material to allow a more generous fold.

(3) Cell failures, because of shorted cells, occurred during tests at temperature extremes (0 and 125°F) as a result of differences in the thermal expansion rate of the magnesium canister and the polystyrene cell cases. The solutions to this failure mode were proposed for the next phase of the program.

(4) During charging of the battery, a surge (voltage transient) occurred when the potential changed

Table 20. Sterilization samples

Sample No.	Components	Ratio	Contaminated	Preparation method	Results
1 and 17	ESB 815 / ESB TETA	100/12	Yes	JPL	+
2 and 13	ESB 815 / ESB TETA	100/10	Yes	JPL	+
3 and 16	JPL 815 / JPL TETA	100/10	Yes	JPL	+
4 and 14	JPL 815 / JPL TETA	100/12	Yes	JPL	+
5 and 20	JPL 815 / ESB TETA	100/10	Yes	JPL	+
6 and 15	ESB 815 / JPL TETA	100/10	Yes	JPL	+
7	JPL 815 / JPL TETA	100/10	Yes	ESB	+
8	X1216 / Cat. 9	100/12	Yes	ESB	+
9 and 21	X1216 / Cat. 9	100/12	Yes	JPL	+
10	X1216 / Cat. 9	100/12	No	ESB	−
19	X1216 / Cat. 9	100/12	No	JPL	−
11	X1216 / Cat. 9	100/12	No	JPL	+
12 and 18	ESB 815 / ESB TETA	100/12	No	JPL	−
22	ESB 815 / ESB TETA	100/12	Yes / In TETA only	ESB	+
23	JPL 815 / JPL TETA	100/12	Yes / In TETA only	ESB	+
24	ESB 815 / ESB TETA	100/12	Yes	ESB cure at 50°F	+
25	ESB 815 / ESB TETA	100/12	Yes	ESB cure at 30°F	+

from the univalent silver (Ag_2O) level to the divalent silver (AgO) level and when an interrupted charge on the divalent level was resumed.

The surges were of sufficient magnitude to cause termination of constant current, voltage limited charging long before the battery was fully charged. The characteristics of this charge surge were investigated and attributed to a coating of nonconducting Ag_2O on the positive electrode. An effort was undertaken to incorporate inert conductive material in the positive electrode to minimize the effect. Addition of 2–3% lead oxide produced some reduction in surge, but the investigation was terminated before the additive program was completed. A different charge mode, and replacement of sealed cells by a common manifold between cells, were adopted.

IV. Development Model *Surveyor* Main Battery

A. General Features

In common with the experimental model battery, the development model had individually sealed cells, polystyrene monoblock material, and the magnesium canister. A picture of the development model battery is presented in Fig. 55. A 10% increase in capacity was achieved by increasing the amount of positive active material proportionately, but the weight was held at approximately the same level by weight reduction in the positive grid

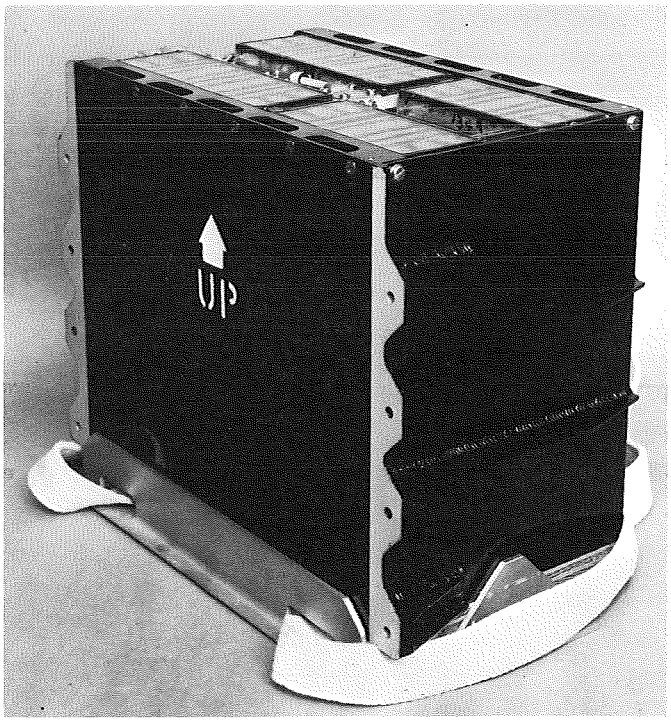

Fig. 55. *Surveyor* development battery (model ESB 204)

and in cell potting. A weight breakdown for both model batteries is shown in Table 21. The battery incorporated a temperature transducer to monitor battery temperature. The transducer is described in Subsection V-A-4.

B. Cell Details

Except for a change in electrode dimensions to accommodate the increased amount of positive material, the cells of the two models differed little. The same electrolyte and separator system was maintained, as indicated in Table 22.

C. Parametric Tests

Owing to a number of reasons including poor performance of the initial lot of development model batteries, a tight schedule, and use of the batteries in system integration studies, the test program for this battery was rather limited.

1. Initial charge. During the manufacturing cycle, certain batteries did not accept the expected 180 A-h charge input, reaching the 27.3-V cutoff with an input of only 110 A-h. The initial charge consisted of charging to a 27.3-V cutoff at the 3.0-A rate, followed by a similar charge at the 1.5-A rate. During this cycle, excessive electrolyte (3.7–4.0 $in.^3$) was expelled, compared to an expected volume of 3.4 $in.^3$. Addition of more electrolyte permitted the cells to accept a normal charge.

Tests, conducted with positive plates from experimental and developmental model batteries, indicated that the development model positive plates evolved

Table 21. Weight estimate for experimental and development model *Surveyor* batteries

Component	Experimental model, weight		Development model, weight	
	Pounds	% of total weight	Pounds	% of total weight
Chassis	2.33	5.13	2.30	5.03
Electrolyte	8.50	18.71	8.90	19.45
Positive material	15.00	33.02	16.50	36.06
Negative material	10.40	22.89	10.50	22.95
Positive grid	1.08	2.38	0.68	1.48
Negative grid	1.58	3.48	1.74	3.80
Separators and retainers	0.05	0.11	0.06	0.13
Polystyrene cell case	2.44	5.37	2.67	5.84
Plate wires	0.09	0.20	0.12	0.26
Cell potting	1.50	3.30	1.00	2.18
Wiring channel potting	0.24	0.53	0.22	0.47
Cell terminals and nuts	1.10	2.42	—	—
Intercell connectors	0.22	0.48	0.20	0.47
Wiring connectors	0.20	0.44	0.20	0.47
Final potting	0.70	1.54	0.65	1.41
Total	45.43	100.00	45.74	100.00

approximately 2.5 times as much gas as the experimental model positive plates and this discrepancy occurred only during the first charge. Probably the evolved gas forced the electrolyte away from the positive plates and prevented them from accepting a normal charge.

Initially, silver was suspected and special test cells were constructed to test this supposition. The types of test cells and the test results are presented in Table 23. The data indicated that the poor performance was due to Synpor or Polypor separator and not the silver powder. The variable performance evident in the first cycle of the development model battery and in the second cycle of the special test cells was never fully understood, but was attributed to differences in soak time prior to charge.

Concurrently conducted microscopic analysis of positive plates and silver powder as well as surface area

Table 22. Characteristics of *Surveyor* development model battery cells

Characteristics	Results	Characteristics	Results
Positive		Active material density, lb/in.^{3}	0.108
Height, in.	5.938	Active plate area, in.^{2}	196
Width, in.	2.750	Remarks	—
Thickness, in.	0.071	Electrolyte	
Type of grid	1/0 Ag	Type	M-40
Total plate area, in.^{2}	196	Amount per cell, in.^{3}	11.2
Silver per cell, lb	1.18	Separator[a]	
Active material density, lb/in.^{3}	0.172	No. 1 Type	White Synpor
Remarks	—	No. of layers	1
Negative		No. 2 Type	Polypor WA
Height, in.	5.938	No. of layers	1
Width, in.	2.750	No. 3 Type	193 PUDO cellophane
Center plate thickness, in.	0.084	No. of layers	4
End plate thickness, in.	0.047	Free space ratio for cellophane	4.80
Type of grid	2/0 expanded Ag	Ratio of positive capacity to negative capacity theoretical	1.295
No. of center negatives per cell	5	Battery	
No. of end negatives per cell	2	Terminal	Crimped
Zinc oxide per cell, lb	0.682		

[a]Listed from positive to negative.

Table 23. Cell variation test I

Construction variable	Silver lot	First input, A-h[b]	First output, A-h[b]	Second input, A-h[b]
Standard 203	898–905	56–62	52–58	42.9–50.6
No Synpor or Polypor	898–905	56	52.5–53	63.1–64.2
Pressed powder positives	898–905	56–61	53–57.5	44.6–51
No. 1 grid in positives	898–905	63–64	58–58.5	44.4–47.4
No grid in positives	898–905	62–65	58–58	42.4–48.6
Sintex positive at 1150°F	898–905	55–56	51.5–53	47.4–53.4
Standard 203	133	55–57	51.3–53	33.4
No Synpor or Polypor	113	55–56	50.5–52.2	53.6–60.2
Pressed powder positives	113	56–57	52.5–53	36.9–38.6
No. 1 grid in positives	133	58–62	53.5–57	39.4–44.2
No grid in positives	133	58–62	56.5–57.3	36.9–37.3
Sinter positive at 1150°F	133	55	51	33–41
Standard 203	800–804[a]	56.3	52	46.1–51.7

[a]Silver powder used on Model 204.

[b]Cells contained one-third the number of positive plates of a normal cell.

measurements of the positive plates by the Brunauer, Emmett and Teller (BET) technique indicated no significant variation between plates from several silver lots.

A second set of cells was constructed for use in tests to determine which of the suspect separator materials (Synpor or Polypor) was giving rise to gases. The results in Table 24 clearly indicate Synpor to be the cause of the poor performance of the development model battery. Subsequent chemical analysis of Synpor lots from both types of batteries indicated that the lot used in the development model contained 15 ±3% starch, while the Synpor in the experimental model contained 45 ±5% starch. The reason for better performance from high-starch Synpor has not been established. Repeated attempts to obtain Synpor with uniform characteristics were unsuccessful. Difficulties in obtaining lots of Polypor that met KOH wetting specifications further contributed to the dissatisfaction with the separator system, used in the development model battery and the decision was made to consider use of a new separator system for the prototype batteries. Table 25 provides a list of candidate separator systems.

Table 24. Cell variation test II

Positive plate model	Synpor model	Polypor model	Charge input,[a] A-h	
			Cell No. 1	Cell No. 2
203	204	203	33.7	26.0
203	204	204	37.2	34.4
204	None	204	53.3	61.1
204	204	204	48.7	61.1
204	204	None	47.6	25.3
204	None	None	54.0	61.1

[a]Cells contained one-third the number of positive plates of a normal cell.

2. ***Initial capacity.*** The initial discharge capacity of the ten development model batteries and subsequent charge–discharge data are presented in Table 26. The initial discharge capacity of five of the batteries was below the design value of 165 A-h, even though their initial charge acceptance was normal. Batteries X-15 and X-16 had a low charge acceptance during the second charge. Battery X-15 was short-lived as two shorted cells vented. Battery X-16 was much longer-lived and its initially low discharge capacity did not drop further after additional cycles.

3. ***Float charge.*** Tests for float charge capability have been conducted using pressure-gage equipped cells (Bourdon gages), arranged in monoblocks. Owing to cell

Table 25. Separator systems

Separator system	System impedance 60 Hz ac in 40% KOH (mΩ/in²)
1 layer nylon cloth 7 layers cellophane	39
1 layer nylon cloth 6 layers cellophane 1 layer nylon	33.6
2 layers fibrous sausage casing 2 layers cellophane 1 layer Dynel	35.6
2 layers fibrous sausage casing 3 layers cellophane	39.7

Table 26. Capacity data for development batteries[a]

Battery No.	Initial charge, A-h	Initial discharge, A-h at 7.0 A	Discharge, %	Second charge, A-h at 2.0 A	Additional charge, A-h at 1.0 A	Total second charge, A-h
X-9	183	163[b]	89.0	172	7	179
X-10	193	177	91.7	184	—	184
X-11	180	153[b]	85.0	—	—	—
X-12	194	173	89.2	175	—	175
X-13	184	167	90.7	163	9	172
X-14	187	160[b]	85.5	175	5	180
X-15	187	141[b]	75.4	139	18	158[b]
X-16	184	134[b]	72.9	131	18	149[b]
X-17	193	182	94.4	174	13	187
X-18	183	182	99.4	168	14	182

[a]Cutoff potentials: 27.3 V for charge, 17.5 V for discharge.
[b]Below expected value.

mismatch, wide pressure differences occurred between cells, resulting in shorted cells and high cell pressures with ultimate venting at pressures above 50 psig. It is significant that these cells were individually sealed.

4. Cycle life. A cycle life test was conducted on one development model battery; in spite of one low capacity cell, this battery was able to complete eleven cycles having a depth of discharge above 90%. Other conditions were: ambient temperatures, 2.0-A charging current to 27.3-V cutoff, and 5.0-A discharge current to a 18.0-V cutoff. The discharge limit was raised to this 18.0-V limit from the initial 17.5-V value after the third cycle to prevent cell reversal of the low cell. This battery may well have been able to operate for additional cycles, were it not for an equipment failure at the end of the eleventh cycle, resulting in complete discharge and cell reversals. The cycling data (Fig. 56) show a marked trend toward lower charge acceptance and discharge capacity with an increasing number of cycles. The discharge capacity was below the limit of 165 A-h in the seventh cycle.

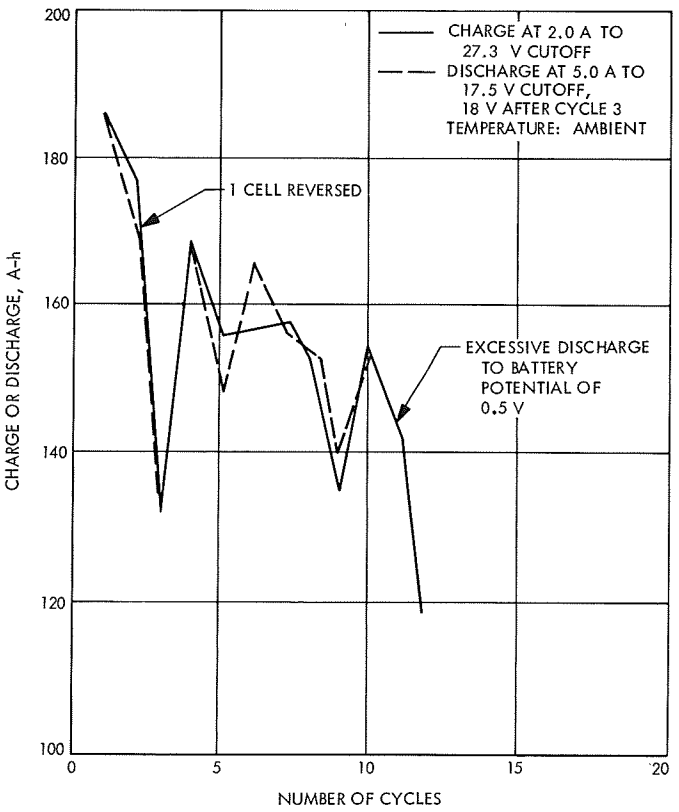

Fig. 56. Cycle-life study on developmental model battery

D. Mission Simulation Tests

A very limited mission simulation program was undertaken with the development model battery.

1. Lunar night discharge. Sequence No. A-3 (see Table 3) required discharge at a relatively low rate for approximately 84 h at low ambient temperatures. A lunar night discharge capacity test has been conducted with a development model battery at an ambient temperature of 40°F and a constant 0.5-A discharge rate. A total of 147 A-h was discharged to a potential of 19.0 V at an average potential of 22.2 V. At the battery potential of 19.0 V, one cell had a potential of only 0.063 V, causing premature termination of the test.

2. Lunar day high rate discharge. As indicated in Table 3, several short-term high current discharges are required from the battery during lunar days. A 10-s high-current sweep, obtained from a development model battery that was over two years old, indicated that at ambient temperature the battery can furnish the required 50-ms pulses at 85 A and less (Fig. 57).

3. Environmental tests. One development model battery was subjected to a series of type approval tests and it passed the required vibration, shock, and acceleration tests (see Subsection II-D), but one of the cells reversed its potential during the 7.0-A discharge at the end of the test. Subsequent charging revealed a shorted cell.

E. Conclusions

The studies with the development model battery were accompanied by a number of problems, caused by poor performance and nonuniformity of separator materials. As a result of separator problems, a change in the separator system was made in subsequent models of the battery. In most instances, the battery ampere-hour capacity was increased by the desired 10% to enable it to

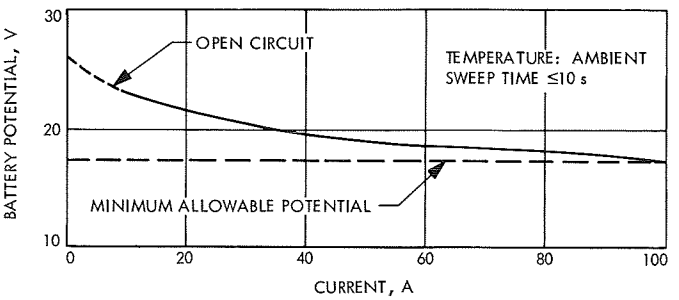

Fig. 57. Potential vs current for high-rate discharge of fully charged developmental model battery

meet the lunar night requirements. Use of individually sealed cells gave rise to large pressure differences between cells during float-charge and the hazards associated with high cell pressures were instrumental in the later adoption of a manifold system. In retrospect, it is evident that the design of the development model battery was frozen too early to take advantage of the findings from the experimental model battery phase, so that the development model contributed relatively little to the advancement of the program. Undoubtedly, scheduling pressures were responsible for the early freeze.

V. Prototype Model *Surveyor* Main Battery

The prototype battery program encompassed five versions that differed from each other in some details (Table 27), but had many features in common including: manifold[6], electrolyte, amount and density of negative active material, positive plate area, and major dimensions. Each prototype version identified problems and contributed to their solution. For example, batteries T-1 and T-2 uncovered fabrication problems that were associated with the manifold design, and problems encountered in type approval vibration tests. A description of the prototype battery principal features is included in the subsequent paragraphs.

A. Description of the Prototype Model Battery

1. General. In common with the development model, the battery is made up from three- and four-cell monoblocks that use polystyrene as case material. The basic change in monoblock design comes from incorporation of a manifold. A typical monoblock case with manifold is shown in Fig. 58, and a prototype battery (No. X-32), is shown in Fig. 59. Except for the absence of reinforcing braces around the periphery, the flight model resembled the prototype battery in outer appearance. Detailed drawings of a monoblock assembly are presented in Figs. 60–62.

2. Monoblock and canister development. The major features of monoblock and canister development are discussed in the following paragraphs.

a. Low temperature burst pressure. A copolymer of styrene and acrylonitrile (called "polystyrene" for brevity in this report) has been selected as monoblock material

[6]U.S. Patent 3,282,740, assigned to ESB, Incorporated.

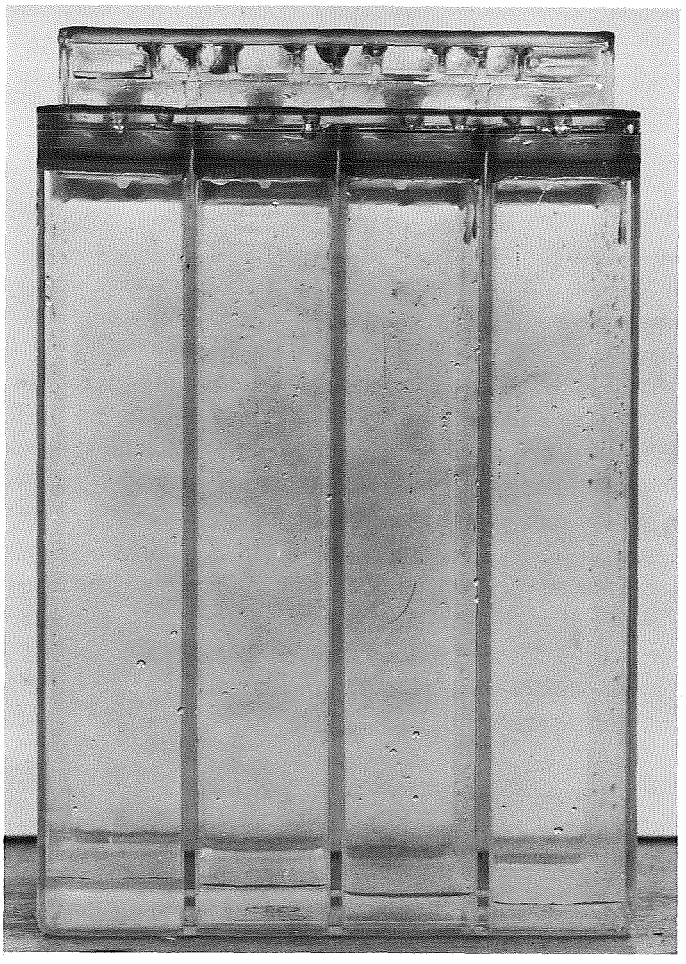

Fig. 58. Monoblock case prototype battery

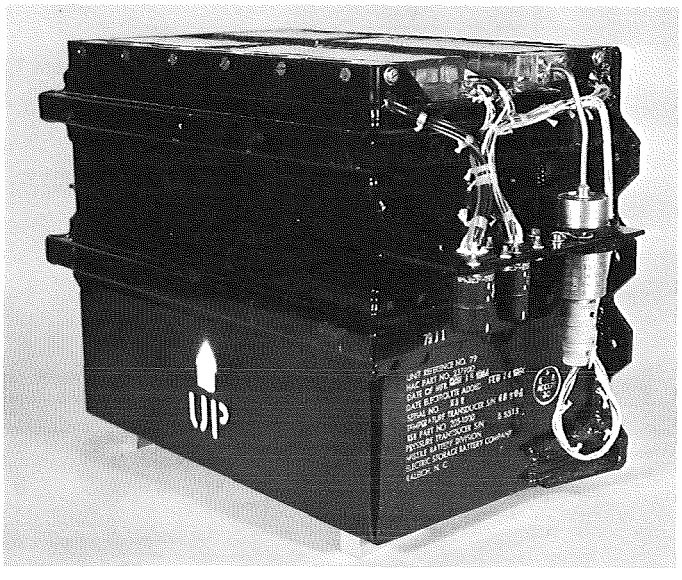

Fig. 59. Prototype battery

Table 27. Characteristics of prototype and flight model cells

Characteristics	Preproduction, sealed manifold	SN T1 and T2, sealed manifold	SN X-23 and X-24, sealed manifold	SN X-19 through X-22, X-25 through X-36, sealed manifold	SN X-37 through X-44, SN 1 and up, sealed manifold
Positive					
Height, in.	5.94	5.94	5.97	5.97	5.94
Width, in.	2.72	2.72	2.72	2.72	2.72
Thickness, in.	0.071	0.066	0.077	0.077	0.077
Type of grid	No. 1	No. 1	No. 1	No. 1	35-X 40 mesh screen
Total plate area, in.^{2}	194	194	195	195	194
Silver per cell, lb	1.17	1.10	1.00	1.00	0.961
Active material density, lb/in.^{3}	0.172	0.172	0.136	0.136	0.136
No. of plates	6	6	6	6	6
Remarks	—	—	—	2 struts/plate	2 struts/plate
Negative					
Height, in.	5.94	5.94	5.94	5.94	5.94
Width, in.	2.75	2.75	2.75	2.75	2.75
Center plate thickness, in.	0.082	0.088	0.094	0.094	0.100
End plate thickness, in.	0.042	0.045	0.048	0.048	0.046
Type of grid	2/0 expanded	2/0 expanded	2/0 expanded	2/0 expanded	2/0 expanded
No. of center negatives per cell	5	5	5	5	5
No. of end negatives per cell	2	2	2	2	2
Zinc-oxide per cell, lb	0.678	0.728	0.783	0.783	0.783
Active material density, lb/in.^{3}	0.108	0.108	0.108	0.108	0.108
Active plate area, in.^{2}	194	194	195	195	194
Remarks					X frame in plate
Electrolyte					
Type	40%	40%	40%	40%	40%
Amount per cell, in.^{3}	11.6	11.9	12.5	12.5	11.8
Separator[a]					
No. 1 type	Nylon cloth	193 PUDO cellophane	193 PUDO cellophane	193 PUDO cellophane	193 PUDO cellophane
No. of layers	1	6	6	6	6
No. 2 type	193 PUDO cellophane	—	—	—	—
No. of layers	7	—	—	—	—
No. 3 type	—	—	—	—	—
No. of layers	—	—	—	—	—
Free space ratio for cellophane	3.60	3.77	3.82	2.72	2.34
Ratio of positive capacity to negative capacity, theoretical	1.295	1.140	0.962	0.962	0.99
Battery					
Terminal	Crimped	Crimped	Crimped	Crimped	Crimped
Canister potting	Release agent	Release agent	Release agent	Release agent	Release agent

[a]Listed from positive to negative.

and a combination of EPON 815 + TETA + Eccospheres[7] as potting compound for the prototype battery. Molded prototype cell cases were fabricated into several 14-cell units and potted into magnesium canisters, where several plastic materials and potting compounds were used. Low temperature burst pressure tests were performed on these units in order to ascertain the performance of the selected combination and obtain data on possible substitutes, in the event the selected combination failed. The results of the burst pressure tests, summarized in Table 28, indicate a burst pressure range of 105–135 psig for six units of the selected composition, while other combinations failed at lower pressures. Burst pressures of this magnitude were far above operating pressures and the polystyrene-EPON 815/TETA/Eccospheres combination was retained.

[7]See Appendix for trade names.

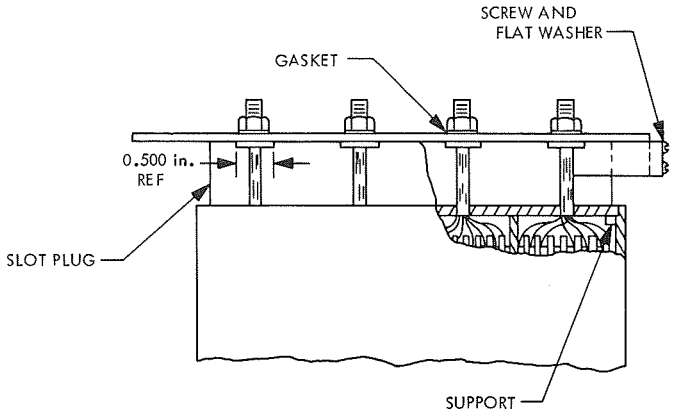

Fig. 60. Side view of monoblock assembly of prototype battery

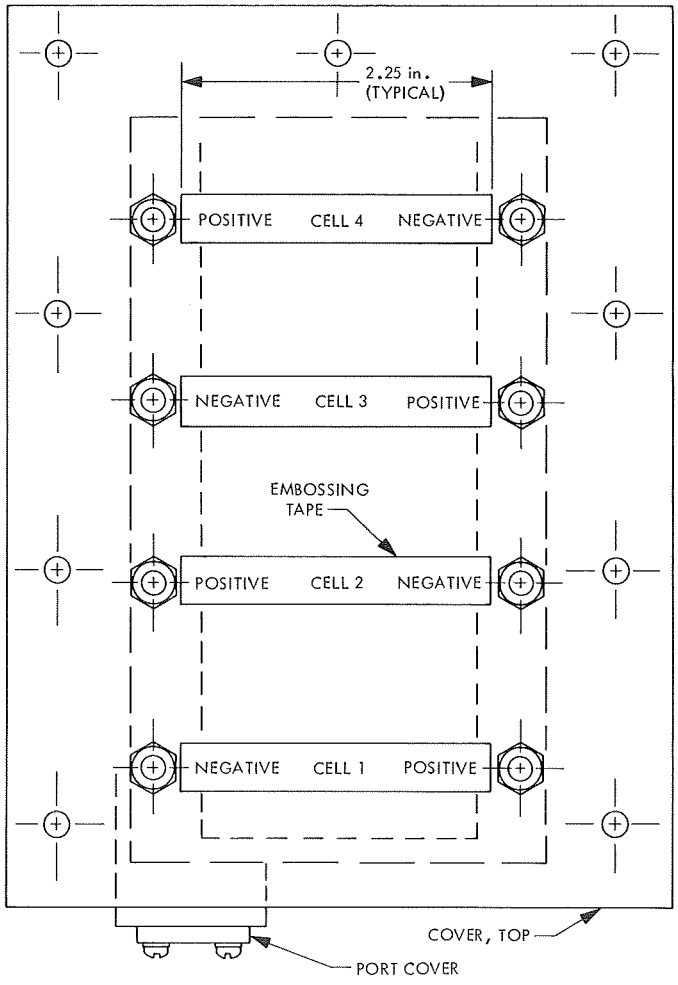

Fig. 61. Top view of monoblock assembly of flight battery

b. Bonding of monoblocks to canister. Problems associated with cell case cracking due to the differential thermal expansion of cases and canister were solved in the prototype model battery by application of a fluorocarbon spray (MS-222) to the monoblock exterior to prevent bonding of EPON 815 + TETA + Eccospheres to the magnesium canister.

c. Surveyor main battery burst pressure as a function of battery temperature. In order to establish solar thermal vacuum abort limits for the battery, the dependence

Table 28. Burst pressure test data for prototype model battery

Case material	Potting compound	Test temperature, °F	Burst pressure, psig
Cycolac Coated with PVA	Shell 815 + TETA	0	70 and 93
Cycolac Coated with PVA	X71/828/NAEP	0	45 and 60
Cycolac	X71/828/NAEP	0	50 and 65
Polystyrene	815 + TETA	0	80, 105, 120, 126
Polystyrene	815 + TETA + Eccospheres	0	105, 110, 118, 135

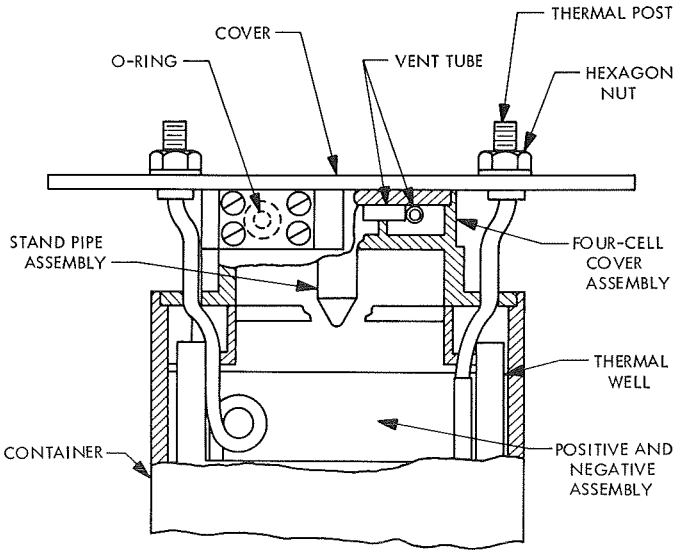

Fig. 62. End view of monoblock assembly of prototype battery

of burst pressure on battery temperature had to be determined. Tests on prototype battery cases were performed at ESB, followed by tests on prototype and flight batteries at HAC. Results of the tests are plotted in Fig. 63. The large difference between ESB and HAC results may have been caused by a different rate of pressure application; owing to the lack of such information, no definite explanation can be offered.

3. *Manifold.* The experimental and development model batteries contained individually sealed cells. Such seals offered the advantage of avoiding electrolyte leakage from cell to cell, that would result in self-discharge and lowered capacity retention. The use of individually sealed cells required a close match of individual cell capacities in a battery and available manufacturing techniques made attainment of a close match costly. Extended overcharge, or reversal of a sealed cell in a battery, can lead to buildup of significant gas pressure (see Fig. 18) in the cell with eventual cell rupture. Owing to the possible premature termination of charge by a transient voltage spike (see Subsection III-F-5), the *Surveyor* battery charger logic had to be redesigned to accommodate extended periods of overcharge. Overcharging in the float condition provided increased capacity. As indicated, individual sealed cells, unless very closely balanced, could not withstand the overcharge successfully. Therefore, production prototype and flight batteries were equipped with a common manifold into which all cells were vented. The manifold was designed to allow ample volume for expansion of gas generated during extended overcharge (float). A pressure transducer was installed as an added safety measure. This permitted automatic charge termination when a predetermined pressure had been reached. An initial setting of 65 psia was selected on the basis of battery case burst pressure tests. Pressures during discharge were generally well below overcharge pressures.

Transfer of electrolyte between cells was avoided by installation of an electrolyte trap on each cell, whereby the path between cells becomes long and tortuous. The trap contained a narrow tube that was filled with absorbent cellulose. Figure 64 illustrates the design of the redesigned cell. The efficiency of the trap to block the passage of electrolyte was tested by inversion of a monoblock case with attached manifold (see Fig. 58). The

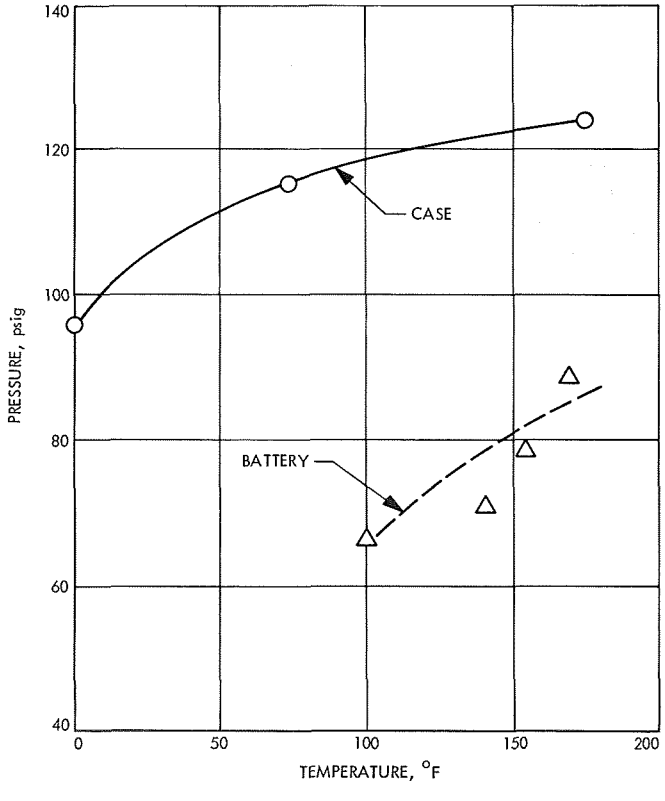

Fig. 63. Results of burst pressure tests on prototype and flight battery cases and batteries

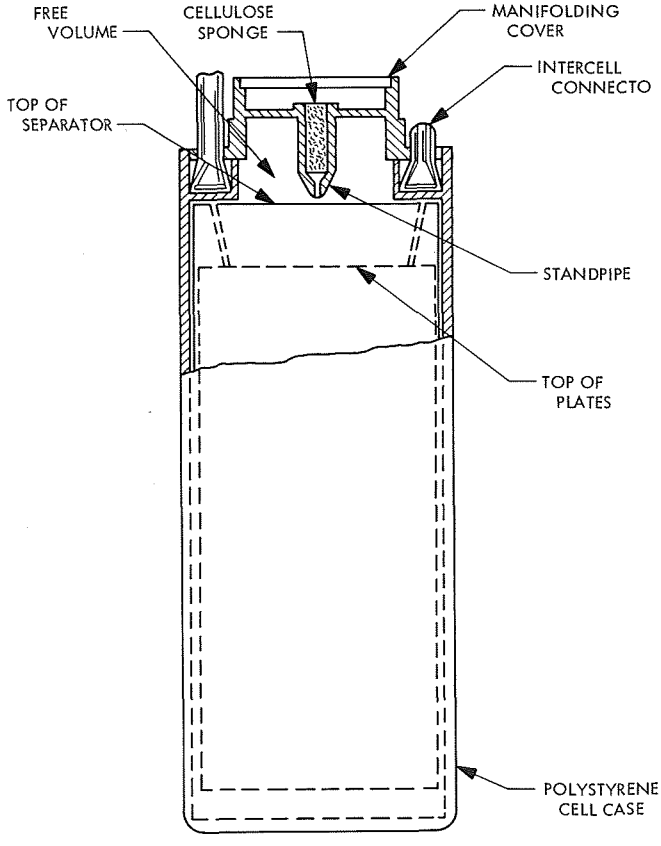

Fig. 64. Cell construction of prototype battery

manifold dimensions were governed by strength of materials, weight, and volume limitations.

4. Pressure and temperature transducers. The *Surveyor* main battery was equipped with one sensor for pressure measurement, and one sensor for measurement of the battery temperature. Following are some details for these sensors.

a. Pressure transducer. The battery pressure transducer monitored the absolute pressure in the manifold and caused charge termination in the event the pressure reached 65 psia. The transducer (Bourns, Inc. part) used a bellows that drove a counterbalanced wiper arm to multipy the motion of the bellows. The wiper contacted a variable resistance element of 2,000-Ω resistance. The total element resistance was 11,600 Ω. The allowable static error band was ±0.17%. A 29.0-V potential was applied across the total resistance element and the output was linear over the range of 0–150 psia with an output of 0–5.0 V (Fig. 65). The resolution of the transducer was within ±0.25% and the overall accuracy band within ±2.0% over the temperature range of 0–125°F with a similar accuracy found by the vendor to extend at least 100°F beyond each of these limits. The pressure transducer was connected to the manifold, using an O-ring. The pressure transducer and its connection to the manifold are shown in Fig. 59.

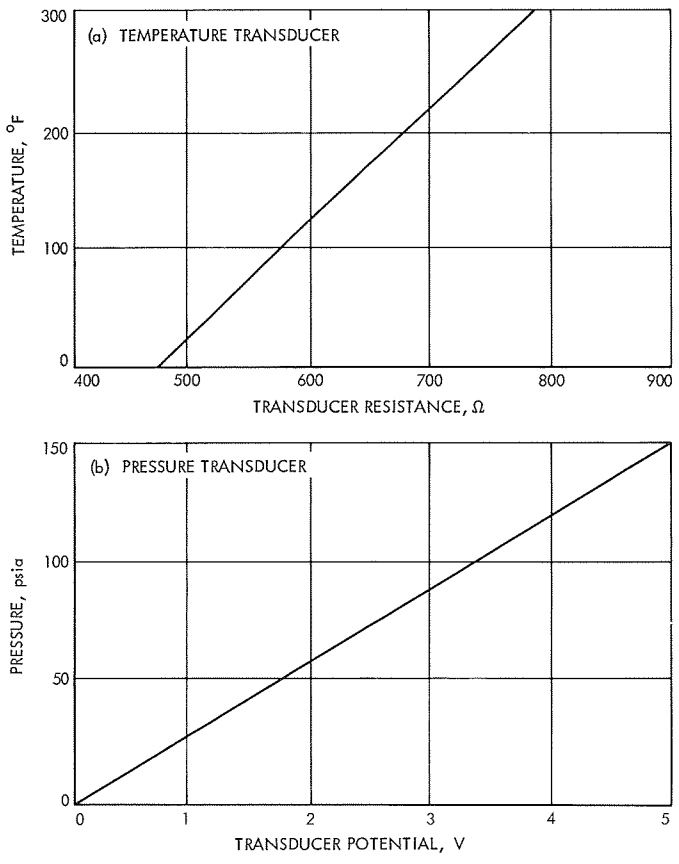

Fig. 65. Transducer calibration for prototype battery

b. Temperature transducer. The temperature transducer (Trans-Sonics, Inc. part) uses a platinum resistance element having a resistance of 500.0 Ω at a temperature of 32°F. Application of a constant current of 5.0 mA resulted in a potential that was directly proportional to the temperature. A typical temperature transducer calibration curve is shown in Fig. 65. The accuracy of the transducer was within ±2°F over the range of 0–125°F, and a similar accuracy extends to much higher temperatures. The transducer mounting was located on top of the battery, thermally connected to a vertical plate, near the junction of the three- and four-cell monoblocks, and the resistance element reached to the center of the battery to measure the case temperature of the centermost cell.

5. Cell details. It was indicated in the Section V introductory paragraph that the five versions of the prototype battery had a number of features in common. Differences in design stemmed from the conduct of tests and the resultant fixes to correct unsatisfactory cell behavior. The following paragraphs provide some specifics concerning cell design and evolution. An overall view of changes in cell design is given in Table 27.

a. Negative plate. Except for changes in plate thickness and plate loading, only one other significant change was made on the negative electrode. This change, effective only for the last version of the prototype and all flight batteries, involved strengthening the plate by providing a polystyrene X frame, and is discussed in Subsection V-C-1.

b. Positive plate. Changes were made in plate thickness, type of grid, plate loading, active material density, and increasing the vibration resistance of the plates by use of two polystyrene struts per plate that permitted securing the plate at the top to the cell jar. Polystyrene struts are discussed in Subsection V-C-1.

c. Separator. The first preproduction prototypes had one layer of nylon separator near the positive plate, followed by seven layers of cellophane. Later prototypes and flight batteries used just six layers of cellophane.

d. Electrolyte. The electrolyte development is discussed in the following paragraphs relative to concentration and volume.

Electrolyte concentration. The superior discharge efficiency of 40% potassium hydroxide at low temperatures (see Fig. 52) led to the selection of this electrolyte concentration for the prototype and flight batteries. The relatively high capacity loss rate of cells with 40% potassium hydroxide at high temperatures such as 125°F (see Fig. 53) was not considered to be sufficiently serious to cause operational problems.

Electrolyte volume. First prototype batteries used 11.6 in.^{3} of electrolyte per cell. Based on a suspicion that these cells might be deficient in electrolyte, a closer look was taken at the method used to determine the amount of electrolyte. The method used in the past by ESB was to allow a fixed volume, X in.^{3} of electrolyte per in.^{3} of cell pack volume, where X was made equal to that of similar successful cells. It was decided that a better approach would involve:

(1) Calculation of the apparent volume occupied by the fully wetted cell pack, including the volume occupied by the portion of separator material extending beyond the plates.

(2) Determination of the actual volume occupied by the cell pack by multiplying the apparent volume of each component by its percent solids.

(3) Determination of the volume available for electrolyte by subtracting the actual volume from the apparent volume.

Performance of these calculations on several models of the *Surveyor* main battery gave the information shown in Table 29.

It was concluded by ESB that, to contain the same relative amount of electrolyte as the experimental model cells, the prototype cells should contain 12.8 in.^{3} of electrolyte. This volume exceeds the available volume in the prototype cell, and, possibly for this reason, an electrolyte volume of 12.5 in.^{3} was selected for prototype batteries bearing serial numbers X-19 to X-36. Later prototype batteries as well as all flight batteries had an electrolyte volume of 11.8 in.^{3}, based on consideration of: (1) recombination of oxygen with zinc near the end of charge, (2) pack tightness, (3) amount of active materials, and (4) separator characteristics.

Table 29. Volume available for electrolyte

Battery model	Electrolyte volume, in.^{3}	
	Calculated	Measured
Experimental	10.9	11.0
Development	—	11.3
Prototype	12.4	11.8

e. Ratio of active materials. Silver–zinc cells are designed in such a manner as to minimize internal pressure buildup during charge. Gas evolution near the end of charge arises from generation of hydrogen at the negative electrode and oxygen at the positive electrode. By designing the cell with an excess charge capacity in the negative plate (positive limited), the only gas evolved will be at the positive electrode in the form of oxygen and this gas can migrate to the negative electrode where it may combine with zinc, thereby reducing the internal pressure.

Gas chromatographic analysis of samples of gas from an early prototype battery that had been float charged revealed a high percentage of hydrogen and a low percentage of oxygen, indicative of a negative-limited condition. This condition led to changes in the theoretical ratio of positive capacity to negative capacity, as shown in Table 27. This ratio became 0.99 for the last generation of prototype batteries and the flight batteries. The magnitude of the ratio is misleading as the negative active material is used more efficiently than is the positive material, so that a sufficient amount of actual excess negative capacity is available.

6. Weight and balance. Integration of the battery into the spacecraft necessitated knowledge of the center of gravity of the battery and a weight and balance control was instituted. Figure 66 shows the axes in which the center of gravity has been defined. Table 30 gives the $\overline{X}$, $\overline{Y}$ and $\overline{Z}$ dimension to the battery center of gravity at six attitudes for a fully charged and discharged battery. The maximum change in the battery center of gravity location, because of state of charge, or attitude of the battery, was 0.1 in. The battery weight was 46.5 lb.

B. Test Program

This subsection describes electrical performance tests of the several versions of the prototype model battery.

1. Data processing. In the earlier parts of the program, watt-hour and ampere-hour capacities for battery

Table 30. Prototype battery weight and balance

Battery attitude	Location, in.					
	Charged			Discharged		
	$\bar{X}$	$\bar{Y}$	$\bar{Z}$	$\bar{X}$	$\bar{Y}$	$\bar{Z}$
W1	5.91	3.26	5.02	5.91	3.26	5.02
W2	5.91[a]	3.26[a]	4.92	5.91	3.26	5.02
W3	5.90	3.26	4.97	5.91	3.26	5.02
W4	5.92	3.26	4.97	5.91	3.26	5.02
W5	5.91	3.29	4.97	5.91	3.26	5.02
W6	5.91	3.23	4.97[a]	5.91	3.26	5.02

[a]Based on measurements on X-23 and X-24. Other values are calculated.

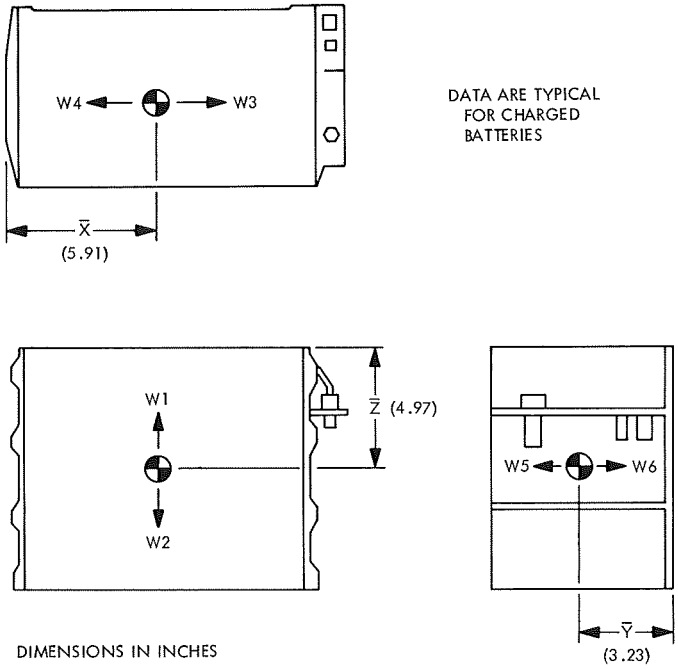

Fig. 66. Prototype battery weight and balance

charge–discharge tests were obtained at HAC by hand computation. Battery parameters such as cell and battery potentials, current, temperature, and manifold pressure were presented in tabular form and then plotted manually. The HAC computer program was modified to plot all parameters and to sum watt-hours and ampere-hours. Data points were plotted every 12 min, and the accuracy improved.

The watt- and ampere-hour summations included small variations in charge and discharge current and potential and were computed as follows:

$$\text{A-h} = \sum_{j=0}^{n-1} \frac{i_j + i_{j+1}}{2} \Delta t$$

where

n = the number of data points

t = time interval

$$\text{W-h} = \sum_{j=0}^{n-1} \tfrac{1}{4} (i_j + i_{j+1}) (V_j + V_{j+1}) \Delta t$$

The accumulation of tabular data was also continued as it proved useful in determining cell balance at the end of discharge and during the float charge. A typical set of computer plots for discharge and charge of a prototype battery is shown in Fig. 67.

2. Battery charging. The battery charging performance tests are discussed in the paragraphs that follow.

a. Charge design. The design approach to the *Surveyor* flight model main battery and its prototypes involved a radical departure from that of the earlier models, as will become evident from the ensuing discussion of battery charging. The new design incorporated: (1) constant power battery charge with potential limited to 27.3 V, (2) use of a manifolded cell with pressure transducer which provided battery charge operation up to a pressure, equivalent to cell case proof pressure (65 psia), and (3) implementation of a cell forming charge technique during manufacture to balance voltages at the full charge condition instead of the full discharged conditions by charging monoblocks to a cutoff potential then combining monoblocks with similar ampere-hour input into a battery. A typical battery charge cycle under the new regime is illustrated in Fig. 68. The new design had the following advantages:

(1) Free volume available for gas containment was increased from 4.6 in.^{3} per cell to approximately 128 in.^{3} overall.

(2) Excessive pressure conditions could be detected by the pressure transducer. The pressure transducer signal terminated charging if pressure level equalled battery case proof pressure.

(3) Balancing the cells at the end of charge during the manufacturing cycle diminished the probability of excessive gassing near the full charge state.

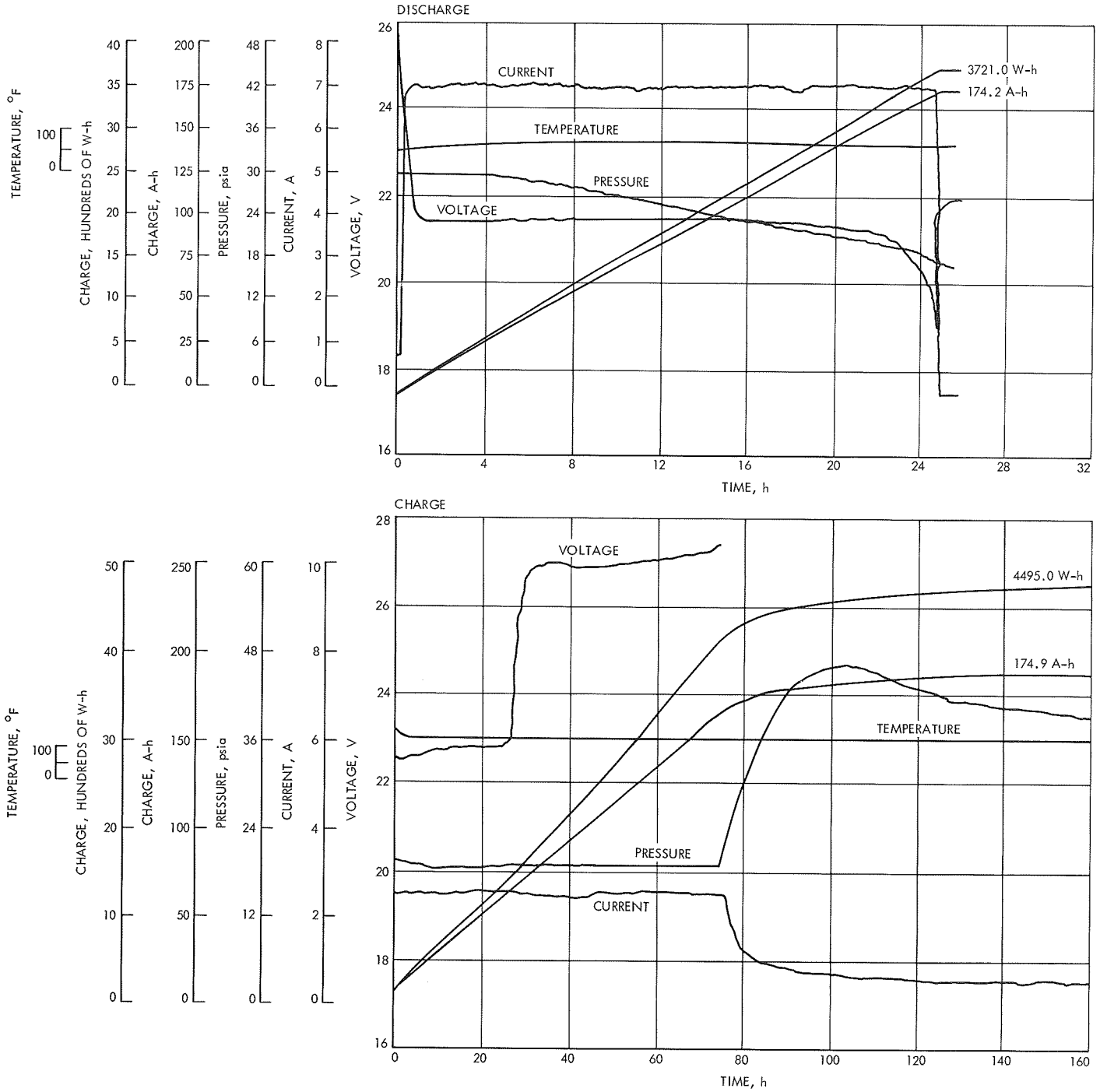

Fig. 67. Typical prototype main battery data plot

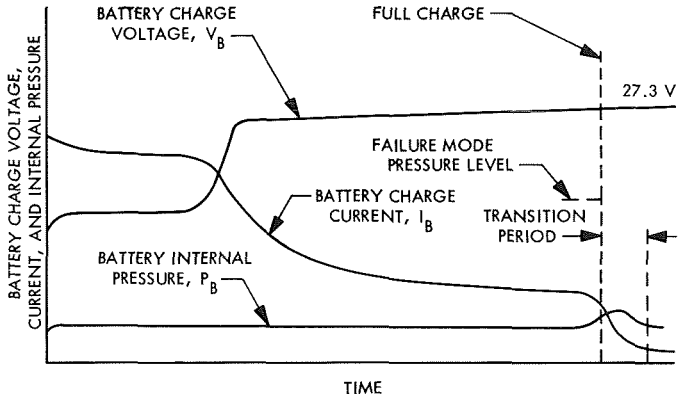

Fig. 68. Battery charge characteristics

(4) Battery charging became highly effective because float conditions at the end of charge increased battery capacity.

(5) The battery dynamic voltage surge characteristic no longer influenced power system operation.

b. Charge tests. A plot of ampere-hour input as a function of charge rate at ambient temperature (Fig. 69) indicated that charging to an acceptable level must take place at a low rate and to a cutoff potential above 27.1 V. Earlier tests (see Subsection III-B-2) have shown that pressure buildup limits the maximum charging potential to a level below 28.0 V. A value of 27.3 V was adopted for the *Surveyor* main battery. The prototype battery can accept a significant charge at low temperatures, when charged at a rate below 3A (Fig. 70).

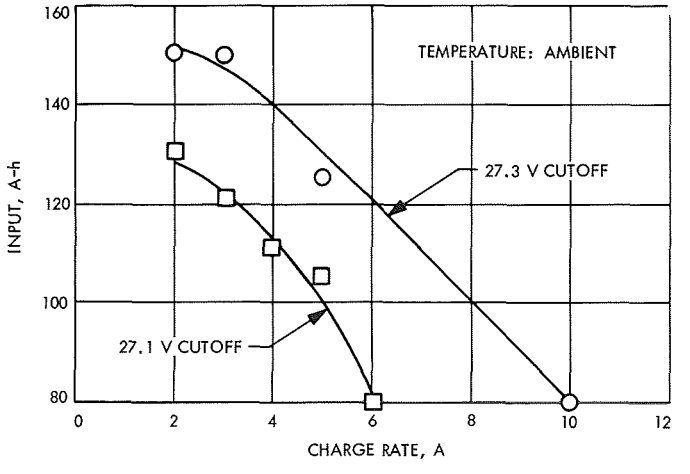

Fig. 69. Ampere-hour vs charge rate for prototype battery

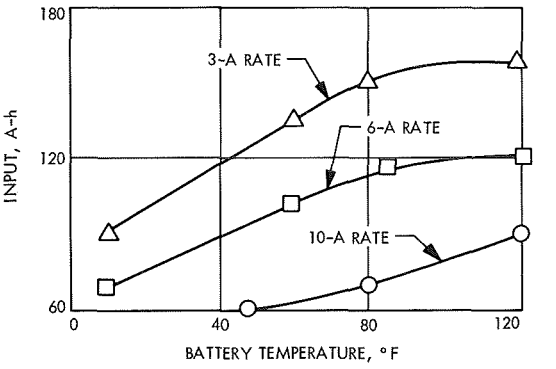

Fig. 70. Approximate ampere-hour input to 27.30 V vs battery temperature and charge rate for prototype battery

The time required to obtain an input of 125 to 150 A-h when charging at ambient temperature to a 27.3-V cutoff is shown for various charge rates in Fig. 71. This figure clearly shows that an input of 150 A-h was attainable only at the 2- and 3-A rates.

A comparison of attainable charge input when charging at 1 A to a 27.3-V cutoff is presented in Fig. 72, where all data are normalized to results from charging at 75°F. It is evident from Fig. 72 that charge acceptance at low temperatures may only be one-half of the high temperature value.

The watt-hour input for a 1-A charge rate to a 27.3-V cutoff is plotted as a function of temperature in Fig. 73. It is of interest that the low input of 2600 W-h at 0°F was raised to a respectable 3760 W-h by an 85-h float charge.

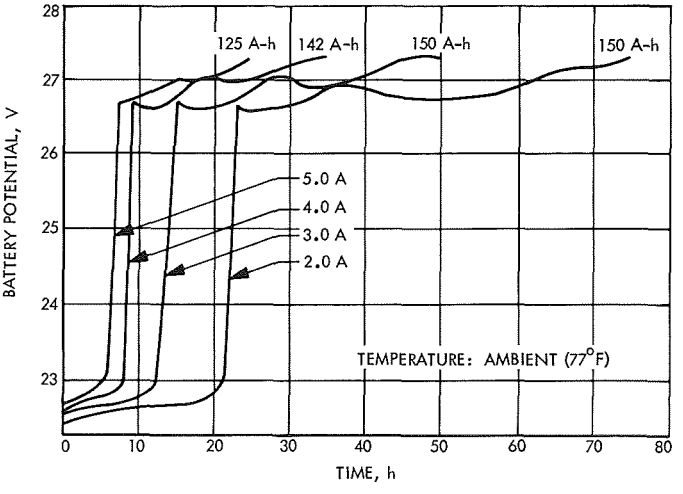

Fig. 71. Charge time to 27.3-V cutoff as a function of charge rate for a prototype battery

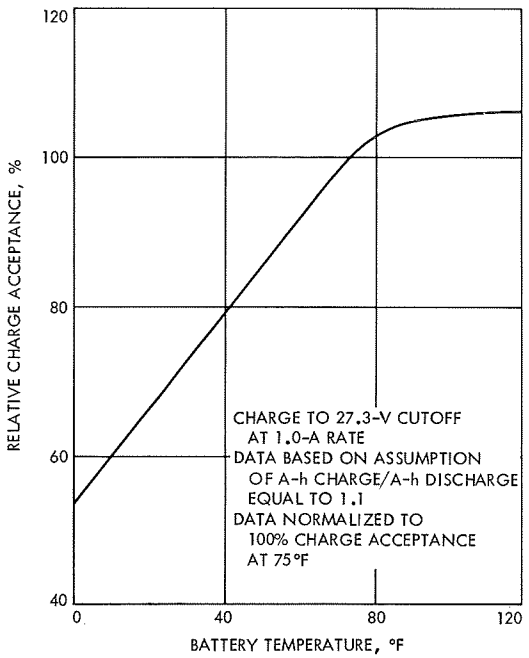

Fig. 72. Charge acceptance vs battery temperature for prototype batteries

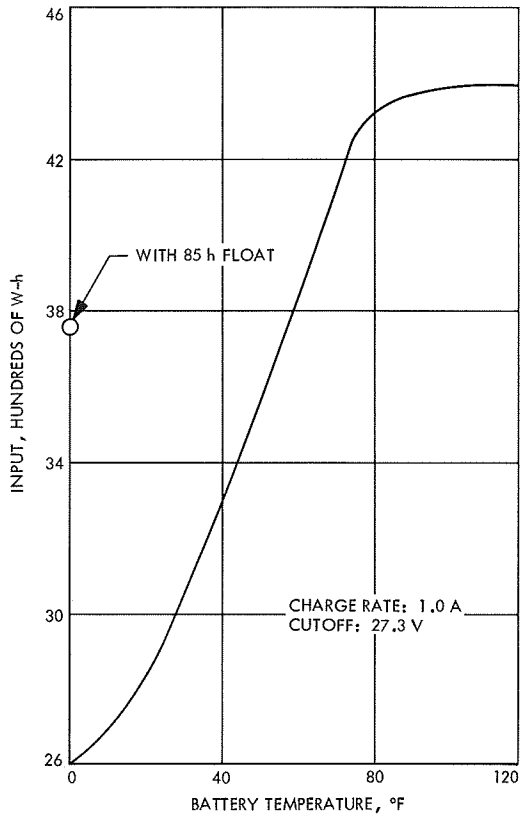

Fig. 73. Watt-hour charge input vs temperature for a prototype battery

Maximum on-charge pressures for all versions of the prototype battery were average and the results are summarized in Fig. 74. The highest average pressure occurred during float-charging at 75°F and this pressure of 32 psia was well within acceptable limits.

c. Charge acceptance problem and solutions. The data in Table 31 show a low charge acceptance in prototype cells during the second charge cycle, even though an acceptable charge acceptance was obtained during the initial charge. Even forced charging to a 2.00-V limit did not provide full restoration of cell capacity, though some increase in input was obtained relative to charging to a 1.95-V limit. In order to determine the source of this deficiency, the following studies were made:

(1) An autopsy of cells Q-1 to Q-5 to seek evidence of malperformance.

(2) Measurement of density variations in the negative plate.

(3) Analysis of the ratio of components in the negative plate.

(4) Build and test cells containing 5, 6, and 8 layers of cellophane to determine the effect of pack tightness.

(5) Build and test cells with positive plates from a different lot.

(6) Separator-electrolyte systems.

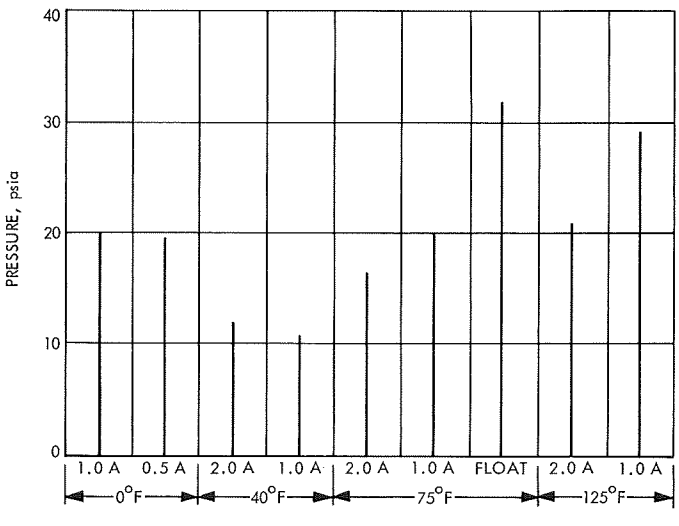

Fig. 74. Average of maximum charge pressures for all engineering test and prototype batteries

Table 31. Performance of prototype model test cells SN Q-1 through Q-5

Parameter	Cell SN				
	Q-1	Q-2	Q-3	Q-4	Q-5
Volume of electrolyte first charge, in.^{3}	13.6	13.4	13.6	13.6	13.3
Input at 2 A, A-h	164.4	183	174	164.4	162.0
Input at 2 A + 1 A, A-h	182.2	190.2	195.9	194.7	185.5
Output, A-h	174	182	189	188	172
Discharge efficiency, %	95.6	95.6	96.5	96.7	92.7
Volume of electrolyte at discharge, in.^{3}	11.9	11.9	11.9	11.9	11.9
Second input to 1.96 V, A-h	105	105	144	120	65
Volume of KOH at second charge, in.^{3}	11.9	11.9	11.9	11.9	11.9
Total input on second charge to 2.00 V, A-h	155+	155+	165+	155+	165+
Remarks	Negative limited at end of charge	Negative limited at end of charge	Positive limited at end of charge	Negative limited at end of charge	Negative limited at end of charge
Second output, A-h	162.9	177.8	169.1	172.6	Disassembled

d. Autopsy of cells. Autopsy of cells Q-1 to Q-5 showed both negative and positive plates to be nonuniformly charged and the negative plates to be relatively dry. The single layer of nylon separator adjacent to the positive plates was also quite dry. The dryness of the nylon separator indicated a need for its replacement by a material with better wetting characteristics.

e. Density variations of negative material. Samples were taken with a cork borer from nine different locations on each plate from five cells, the separator and grid material removed from each sample, and the negative powder weighed. The weight distribution is plotted in Fig. 75 as standard technique, and the data show a variation of ±35% in weight per unit area. Techniques examined for achieving a more uniform weight distribution were vibration, and use of improved spreading tools. Vibration brought no significant improvement in material distribution, but use of an improved spreading tool resulted in a better weight distribution, as shown in Fig. 75. Cells were built with negative plates having better weight distribution (Q-11 to Q-15) and compared in performance to cells using earlier negative plates; cellophane separator was used in both sets of cells to avoid the previously mentioned dry separator problem. The data in Table 32 show no significant improvement in performance when the improved negative plates were used, but the technique was adopted for all future cells as a forward step in production control. The similarity in performance between standard and improved negative plates was probably due to migration of zinc oxide from high points into deficient areas via a solution phase, resulting in the equalization of the material distribution.

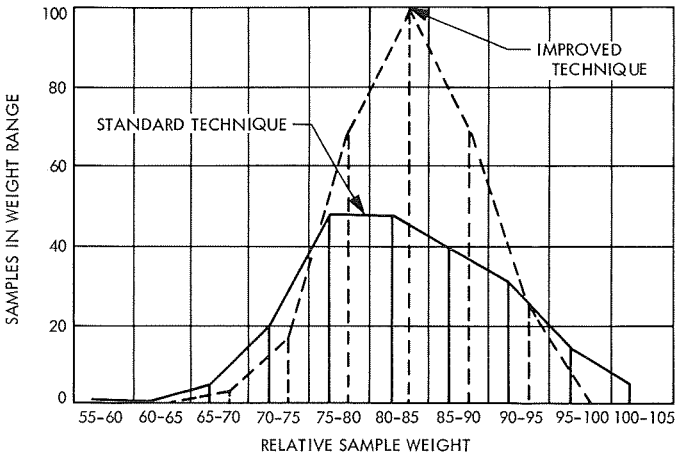

Fig. 75. Weight distribution of negative material

f. Ratio of components in negative plate. In addition to active material, the negative plate contained a proprietary binder and mercuric oxide. Samples of negative material were taken from lots used to manufacture the cells in question (Q-1 to Q-5) and analyzed for uniformity of composition. The plastic binder varied in content between 2.002% and 2.228%, and the mercuric oxide concentration was within 0.1% of the specified content. These variations in binder and mercuric oxide were not large enough to cause the large loss in charge acceptance.

g. Cell pack tightness. The effect of pack tightness on charge acceptance was investigated by tests with cells

Table 32. Effect of negative weight distribution on cell performance

Parameter	Cell SN						
	E-37	E-38	Q-11	Q-12	Q-13	Q-14	Q-15
Cell description	Eight layers of cellophane separator system most nonuniform negative plates		Eight layers of cellophane separator system—negative plates made with improved spreading techniques				
Volume of KOH first charge, in.^{3}	14.6	14.6	14.0	14.0	14.0	14.0	14.0
Input, A-h	203.3	204.2	205.6	205.6	208.3	210.1	208.3
Output, A-h	193.2	193.7	191	190	195.5	191.5	190
Discharge efficiency, %	95.2	95	92.8	92.5	93.8	91.3	91.2
Volume of KOH at discharge, in.^{3}	12.8	12.8	12.8	12.8	12.8	12.8	12.8

that contained five to eight layers of cellophane in addition to the nylon separator; the free space ratio of these test cells ranged from 5.42 to 3.38, respectively. The results of charge–discharge tests with these cells, summarized in Table 33, show that pack tightness was not the source of the poor charge acceptance in cells Q-1 to Q-5.

h. Positive plate investigation. Test cells were built with positive plates from a previous production run and charge–discharge sequences performed to determine if variation in silver powder or in plate processing may have caused poor charge acceptance. The results, summarized in Table 34, show a similar reduction in charge input during the second charge. Therefore, the positive plate material was ruled out as source of the problem.

Table 34. Prototype model test cells with positive plate from previous production run

Parameter	Cell SN			
	E-20	E-21	E-22	E-23
Volume of KOH first charge, in.^{3}	9.15	9.15	9.15	9.15
Input[a], A-h	133	131	128	128
Output, A-h	113	109	107	104
Discharge efficiency, %	85	83.2	83.5	81.2
Volume of KOH at discharge, in.^{3}	7.95	7.95	7.95	7.95
Second input[a], A-h	100.2	98.4	89.6	60

[a]Multiply data by 1.39 to compare with standard Model 205 cell data.

Table 33. Effect of pack tightness on prototype model cell performance

Cell SN	Number of layers of cellophane	Free space ratio	Input at 2 A, A-h	Volume of KOH at charge, in.^{3}	Output, A-h	Discharge efficiency, %	Volume of KOH at discharge, in.^{3}	Second input, A-h	Remarks	Output A-h	Third input at 2 A, A-h	Net input, A-h
E8	6	4.52	184	14.0	157	85.3	12.2	100.2	Added 3.05 in.^{3} KOH	104	183	206.2
E9	6	4.52	196	14.0	17	87.2	12.2	104.2	Added 3.05 in.^{3} KOH	106	183	206.2
E10	6	4.52	177	14.0	142	80.3	12.2	100.2	Added 3.05 in.^{3} KOH	92	62	105.2
E11	6	4.52	199	14.0	178	89.5	12.2	121.8	Disassembled			
E12	5	5.42	170	14.0	145	85.3	12.2	102.2	Added 3.05 in.^{3} KOH	104	188	211.2
E13	5	5.42	161	14.0	129	80.2	12.2	96.4	Added 3.05 in.^{3} KOH	107	179	200.4
E14	5	5.42	173	14.0	148	85.5	12.2	128		114	62	101
E15	5	5.42	204	14.0	187	91.6	12.5	138		124	62	93
E16	8	3.39	161	14.0	108	67.1	12.2	85.4	Added 3.05 in.^{3} KOH	107	135	176.4
E17	8	3.39	167	14.0	119	71.3	12.2	86.4	Added 3.05 in.^{3} KOH	112	179	201.4
E18	8	3.39	181	14.0	136	75.2	12.2	94.4		88	62	113.4
E19	8	3.39	177	14.0	135	76.3	12.2	89.8		88	62	105.8

Table 35. Effect of positive plate separator on cell performance

Parameter	Cell SN							
	E-29	E-30	E-31	E-32	E-33	E-34	E-35	E-36
Separator system	Seven layers cellophane		Seven layers cellophane + one layer Dynel		Seven layers cellophane + one layer Viskon		Seven layers cellophane + one layer Viskon + one layer Dynel	
Volume of KOH first charge, in.^{3}	13.4	13.4	13.4	13.4	13.4	13.4	13.4	13.4
Input A-h at 2 A	196.6	200.0	176.2	196.8	172.2	182.2	184.2	160
Output, A-h	176.2	186.9	162.7	179.7	167.7	166.6	168.7	125.7
Discharge efficiency, %	89.6	93.3	92.3	91.3	85.8	91.5	91.5	78.6
Volume of KOH at discharge, in.^{3}	11.9	11.9	11.9	11.9	11.9	11.9	11.9	11.9
Input second charge, A-h	174	185.2	169.5	165	155.3	172.4	159.8	—[a]
Volume of KOH second charge, in.^{3}	12.4	12.4	12.4	12.4	12.4	12.4	12.4	—[a]
Output, A-h	181	193	176	176	154.5	178	156	—[a]
Input, A-h	172	182	160	142	133	172	110	—[a]

[a]Disassembled.

i. Separator-electrolyte systems. With the elimination of the positive plate, negative plate and pack tightness from the list of suspects for low charge acceptance, attention was focused on the separator system. Previously mentioned cell autopsies showed the nylon separator to be excessively dry. The search for a more wettable separator led to the fabrication and testing of cells that used cellophane only or combinations of cellophane with additional layers of Dynel, Viskon, and a combination of both of these materials. Results of charge–discharge tests with these cells (E-29 to E-36) showed the all-cellophane system (cells E-29 and E-30) to be best (Table 35), but further improvement was desired. Additional cells containing eight layers of cellophane and negative plates made with improved spreading techniques were fabricated and tested (cells Q-11 to Q-15). Data, summarized in Table 36, show good performance on the first cycle, but reduced and variable charge acceptance during the second cycle. Disassembly of cell Q-15 yielded the following observations:

(1) Free electrolyte (1.16 in.^{3}).

(2) Negative plate appeared partially charged and well wetted.

(3) Positive plates dry in appearance and to touch. Weight increase of 0.0042 lb/plate (1.9 g/plate) after soak in electrolyte.

(4) No silver attack beyond second layer of cellophane. The first layer of cellophane next to the positive was dry to the touch, but was fully expanded in thickness. The second layer was moist, while the remaining six layers were wet on the surface.

Table 36. Performance of cells using all cellophane separators

Parameter	Cell SN				
	Q-11	Q-12	Q-13	Q-14	Q-15
Volume of KOH first charge, in.^{3}	14.0	14.0	14.0	14.0	14.0
Input, A-h	205.6	205.6	208.3	210.1	208.3
Output, A-h	191	190	195.5	191.5	190
Discharge efficiency, %	92.8	92.5	93.8	91.3	91.2
Volume of KOH at discharge, in.^{3}	12.8	12.8	12.8	12.8	12.8
Input, A-h	162.8	162.8	162.8	137	157.2
End of charge voltage, V	1.947	1.950	1.946	1.960	1.960
Output, A-h	153	159	160	132	Disassembled
Input, A-h	166.2	173	180	130.2	Disassembled

The dryness of the positive plate following charge may be explained by the following electrochemical reactions for charging silver-zinc cells:

At the positive electrode

$$2\,OH^- + Ag_2O \rightarrow 2\,AgO + H_2O + 2\,e$$

$$2\,OH^- + 2\,Ag \rightarrow Ag_2O + H_2O + 2\,e$$

At the negative electrode

$$ZnO + H_2O + 2\,e \rightarrow Zn + 2\,OH^-$$

$$Zn(OH)_2 + 2\,e \rightarrow Zn + 2\,OH^-$$

These equations indicate that hydroxyl (OH) ions are consumed during charge and water molecules formed, while hydroxyl ions are formed simultaneously at the negative electrode. As a result, an electrolyte concentration gradient is formed between the electrolyte at each electrode. The gradient causes hydroxyl ions to diffuse from the negative electrode to the positive electrode. Water molecules are transferred from the positive electrode to the negative electrode due to osmotic pressure, resulting in a rise of the electrolyte level around the negative electrode and a fall around the positive electrode. A lowering in electrolyte level around the positive electrode may produce a dry interface between the positive electrode and the separator with resulting poor charge acceptance.

An investigation was made of a possible increase in the electrolyte diffusion rate between the positive and negative plate surfaces. This was accomplished through the use of wicking materials for maintaining the desired electrolyte distribution in the vicinity of the plates.

A four cell monoblock was constructed to determine the effect of a wick on the operation of *Surveyor* prototype cells. The positive plates were wrapped with seven layers of cellophane. Webril (EM 312), consisting of 75% nylon and 25% Dynel, served as wick, connecting the positive plates to the negative plates. Each wick was separated from contact with the negative plate by an additional piece of cellophane. The four cells were connected to a common manifold. After a series of charge–discharge cycles, summarized in Table 37, the following conclusions were drawn:

(1) The use of a wick to transfer electrolyte between the positive and negative electrodes was effective in eliminating the loss in capacity by electrolyte depletion.

(2) The use of a positive to negative wick lowered the electrolyte level around the negative electrode at the end of charge and increased the rate at which oxygen can recombine with the negative active material.

(3) The use of cellophane between the wick and the negative plates and operation in a positive limited condition eliminated the tendency toward the growth of zinc trees in the wick.

Although cells containing wicks performed satisfactorily in these tests, they were not selected for flight cells because of some unknown qualities, such as; performance with increasing cycle life, and the possibility of intercell shorts in the event of "treeing" up the wick. Subsequent prototype and flight batteries used positive plates of lower density combined with an increased volume of electrolyte.

Table 37. Performance of cells containing wicks

Parameter	Cell SN											
	Q-16	Q-17	Q-18	Q-19	Q-20	Q-21	Q-22	Q-23	Q-24	Q-25	Q-26	Q-27
Volume of KOH first charge, in.^{3}	14.6	14.6	14.6	14.6	14.6	14.6	14.6	14.6	14.6	14.6	14.6	14.6
Input at 5 A, A-h									180	180	180	180
Input at 2 A, A-h	197.4	197.4	197.2	203.2	207.4	203.2	199	199				
Output, A-h	188.5	188.5	188	193	198.5	193.5	190.5	190.5	169.6	170	170	169.3
Discharge efficiency, %	95.5	95.5	95.3	95	95.7	95.2	95.7	19.7	94.3	94.4	94.4	94.2
Volume of KOH at discharge, in.^{3}	12.8	12.8	12.8	12.8	12.8	12.8	12.8	12.8	12.8	12.8	12.8	12.8
Input at 2 A, A-h	184	184	184.2	182.2	175.8	182	183.8	182	191	191	191	191
Input during float, A-h	203	203	203	203					210	210	210[a]	210[a]
Output, A-h	203	205	202	204	178	182	183	182	212	212	212	212
Volume KOH at discharge, in.^{3}	12.8	12.8	12.8	12.8	12.2	12.2	12.2	12.2	12.8	12.8	12.8	12.8
Input at 5 A, A-h	175.5	175.5	175.5	175.5					172	172	172	172
Input at 5 + 2 A, A-h	185.1	185.1	187.7	187.7	183.0	187.4	184.4	187.4	184.2	185.2	185.2	187
Output, A-h	189.5	189	190	191	188	190	186	189	187	189	188	175
Input at 5 A, A-h					165.4	168.4	168.4	165.4	175.9	171.9	164.4	Shorted
Input at 2 A, A-h	187.4	187.4	186.6	189.4								

[a]Container broke.

Table 38. Test cell data

Cell SN	Cell configuration	First charge input at 5 A, A-h[a]	Remarks	First discharge output, A-h	Discharge efficiency, %	3-min volume at 85 A, V	Volume of KOH at discharge, in.^{3}	Second input at 2 A, A-h	Second output, A-h	Third input at 5 A, A-h	Third output, A-h	Fourth input at 5 A, A-h
E46	1	192.5		183	95.1	1.382	13.2	177.6	177.5	160	164	160
E47	1	192.5		181	94.1	1.383	13.2	177.6	176.5	160	163.6	160
E48	1	192.5		184	95.5	1.376	13.2	180.9	181.5	160	163.6	160
E49	1	192.5		184	95.5	1.362	13.2	165	160.5	142	143.4	150
E50	2	179		169	94.3	1.474	13.5	180.8	181	165.5	168.4	171
E51	2	179		169	94.3	1.472	13.5	182	176.6	164.5	166.6	161.5
E52	2	179		169	94.3	1.491	13.5	180.8	182	170.5	174	172.5
E53	2	179		168	94.1	1.489	13.5	178.8	180	163.5	171	169.7
E54	3	182.5		174	95.4	1.454	11.0	195.7	187.5	183	187	169
E55	3	182.5		175	95.9	1.484	11.0	187.5	196	187.5	188	170
E56	3	182.5		174	95.4	1.492	11.0	186.6	187.5	183	189	168
E57	3	182.5		174	95.4	1.490	11.0	189.9	188.5	183	186	168
E58	4	177.5		169	95.3	1.429	12.3	183.5	181.5	166.3	167	160
E59	4	177.5		169	95.3	1.447	12.3	183.5	183.5	166.3	169	160
E60	4	177.5		169	95.3	1.464	12.3	181.5	182.5	170.5	173	160
E61	4	177.5		168	94.6	1.448	12.3	180.9	179.5	166.3	169	160
E62	5	158.8	Floated	167			11.0[b]	151 at 5 A	143.6	159.4	163	164.6 at 2 A
E63	5	158.8	Floated	179			11.0[b]	156 at 5 A	158	150.9	153	171 at 2 A
E64	5	158.8	Floated	178			11.0[b]	146 at 5 A	149	155.1	157	171 at 2 A
E65	5	158.8	Floated	165			11.0[a]	169 at 5 A	167.4	159.4	158	171 at 2 A

Cell SN	Cell configuration	Fourth output at 10 A, A-h	Volume of KOH, in.^{3}	Fifth input at 2 A, A-h	Fifth output at 10 A, A-h	Sixth input at 2 A, A-h	Sixth output at 10 A, A-h	Volume of KOH, in.^{3}	Seventh input at 2 A, A-h	Seventh output, A-h	Volume of KOH at discharge, in.^{3}	Eighth input at 2 A, A-h
E46	1											
E47	1											
E48	1											
E49	1											
E50	2	183	12.8	181.6	184.3	176	177	12.2	176	165	12.2	160
E51	2	179	12.8	181.6	183.5	178	178	12.2	178.2	171	12.2	153
E52	2	185	12.5	188	186.7	180	179	12.5	176	177	11.9	145
E53	2	181	12.5	186.4	180.7	173	170	12.5	168.8	149	11.9	138
E54	3											
E55	3											
E56	3											
E57	3											
E58	4			Shorted								
E59	4											
E60	4											
E61	4											
E62	5											
E63	5											
E64	5											
E65	5											

[a]Each type cell charged as a monoblock.

[b]KOH amount was incorrect and was corrected to 12.8 in.^{3} during vent charge.

j. Optimization of charge acceptance. Further improvement in charge acceptance was sought by constructing and testing cells with the following variations from standard:

(1) Positive plate density equal to 89% of standard.

(2) Positive plate density equal to 79% of standard.

(3) Four layers of cellophane separator.

(4) Three layers of fibrous sausage casing separator.

(5) Increased negative to positive ratio, EM-312 wicks, cellophane wick shields.

Results of charge–discharge tests with these cells are tabulated in Table 38. All configurations gave acceptable performance, but configurations three and four were ruled out because of inability to detect separator imperfections with available equipment. Characteristics were determined for standard as well as 89 and 79% of standard positive plates and the data are shown in Table 39 and Fig. 76. The good performance of the low density (79% of standard) plate with its high porosity and resultant high electrolyte retention was significant.

k. Conclusions and design changes. The conclusions and design changes resulting from the charge test program were as follows:

(1) The wetting characteristics of nylon was established as inadequate.

(2) The use of cellophane as exclusive separator material was adopted; owing to the need for an increased electrolyte diffusion rate, the number of cellophane layers had to be reduced from eight to a lesser number.

Table 39. Positive plate characteristics

Characteristic	Positive plate density		
	Standard	0.9 × standard	0.8 × standard
Density, lb/in.^{3}	0.173	0.155	0.138
Surface area, in.^{2}/lb[a]	70,500	77,500	84,500
Pore volume, in.^{3}/lb[b]	2.02	2.36	3.03
Percent void	54.2	59.3	63.8
Percent pores larger than 20 μm	20.6	11.6	9.2

[a]Multiply by 0.0142 to obtain cm^2/g.
[b]Multiply by 0.0361 to obtain cm^3/g.

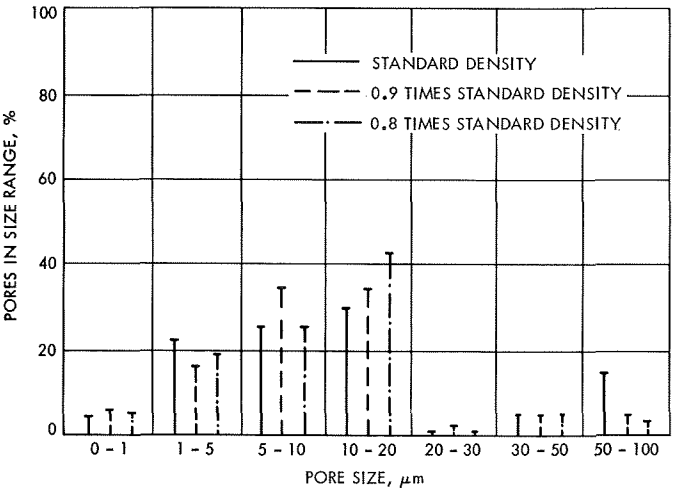

Fig. 76. Positive plate pore size distribution

(3) Six layers of cellophane separator permitted charging to full capacity and provided sufficient reliability. This number of layers was used in the *Surveyor* main battery.

(4) The manufacturing process for the negative plate was modified to yield plates with a more uniform density distribution.

(5) The lighter and more porous, 0.8 density, positive plate in conjunction with six layers of cellophane separator produced excellent results because the more porous positive plate with its ability to retain more electrolyte compensated for the reduced diffusion rate of electrolyte through six layers of separator. This combination (No. 2, Table 40) was adopted for the *Surveyor* main battery.

(6) Tests with wicks to increase the electrolyte diffusion rate were successful, but wicks were not recommended because of uncertainties concerning long-term performance. Instead, a more porous positive plate was used to assure the presence of sufficient electrolyte at this plate.

(7) The amount of electrolyte was increased from 11.8 to 12.5 in.^{3}

3. Discharge tests. A considerable number of discharge tests were performed on prototype batteries with emphasis on determining their pulse capability over the temperature range from 0 to 125°F.

a. Constant current discharge. A typical discharge curve for a prototype battery is shown in Fig. 77. In

Table 40. Charged stand test data for prototype model cells

Cell SN	Charge input, A-h	Output at 10 A, A-h	Charge input, A-h	Output at 10 A, A-h	Charge input, A-h	Storage		Output at 10 A, A-h	Capacity retention, %
						Time, days	Temperature, °F		
Q51	181.2	166.9	165.7	165.2	170.9	30	125	167	97.8
Q49	195.6	181.4	165.7	165.1	178.7	60	125	168.8	94.5
Q52	161.6	147.4	168.3	Not cycled		120	125	145	86.5
Q53	161.6	147.4	168.3	Not cycled		15	160	105	62.3
Q50	194	179.2	161.2	163.7	177.7	30	160	65	42.8
Q54	159.4	145.2	167.7	Not cycled		60	160	Shorted	

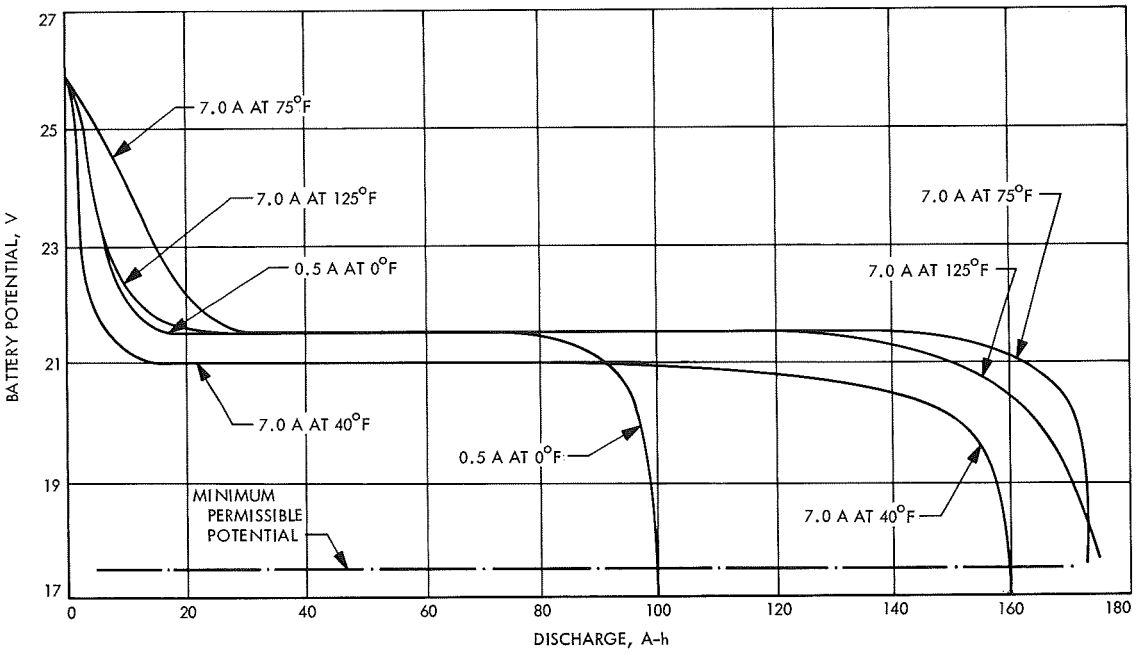

Fig. 77. Battery potential vs ampere-hour capacity at several temperatures for prototype battery

general, this test did not reveal any major departure from similar tests with experimental model batteries. A plot of discharge capacity as a function of temperature (Fig. 78) indicates a relatively wide spread among prototype batteries in discharge capacity, that may be partly due to design changes.

b. High rate discharge. The final revision of the battery requirements called for a battery discharge sweep in which a current sweep from 0 to 100 A was to be performed at a sweep rate not to exceed 10 s at ambient temperature. The potential at the load side of the mating electrical connector of the battery receptacle was to be between 17.5 and 26.0 V. An equivalent test was performed by ESB, by drawing 85 A from the fully charged battery for a time not to exceed 10 s. Figure 79 shows a graphic record of a high-rate discharge, in which the battery furnished two 5-s, 85-A pulses; the minimum potential of 19.0 V was well above the allowable minimum of 17.5 V.

Sweeps not exceeding 10 s duration were performed by HAC at ambient temperatures ranging from 0 to 125°F with the batteries at various states of charge. The results are presented in Figs. 80–83. The prototype battery whose output is shown in Fig. 80 was unable to deliver 85 A at the low temperature.

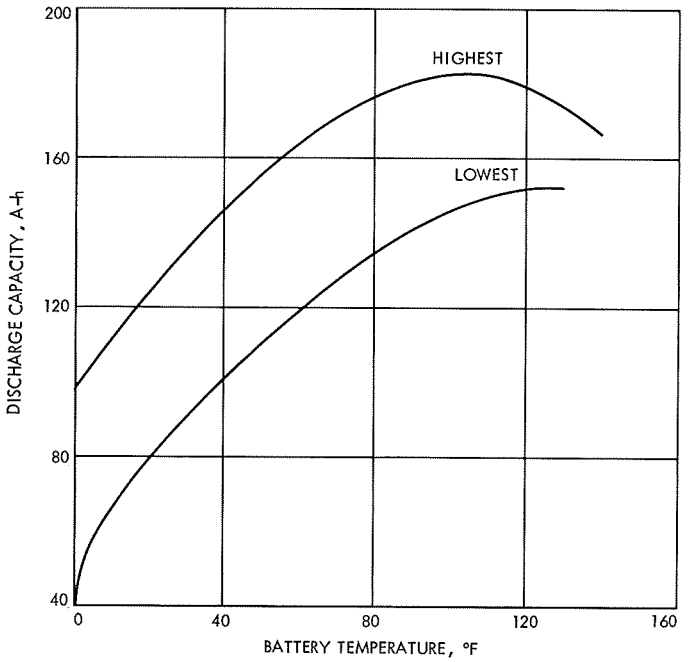

Fig. 78. Range of discharge capacity (A-h) data vs temperature for prototype batteries

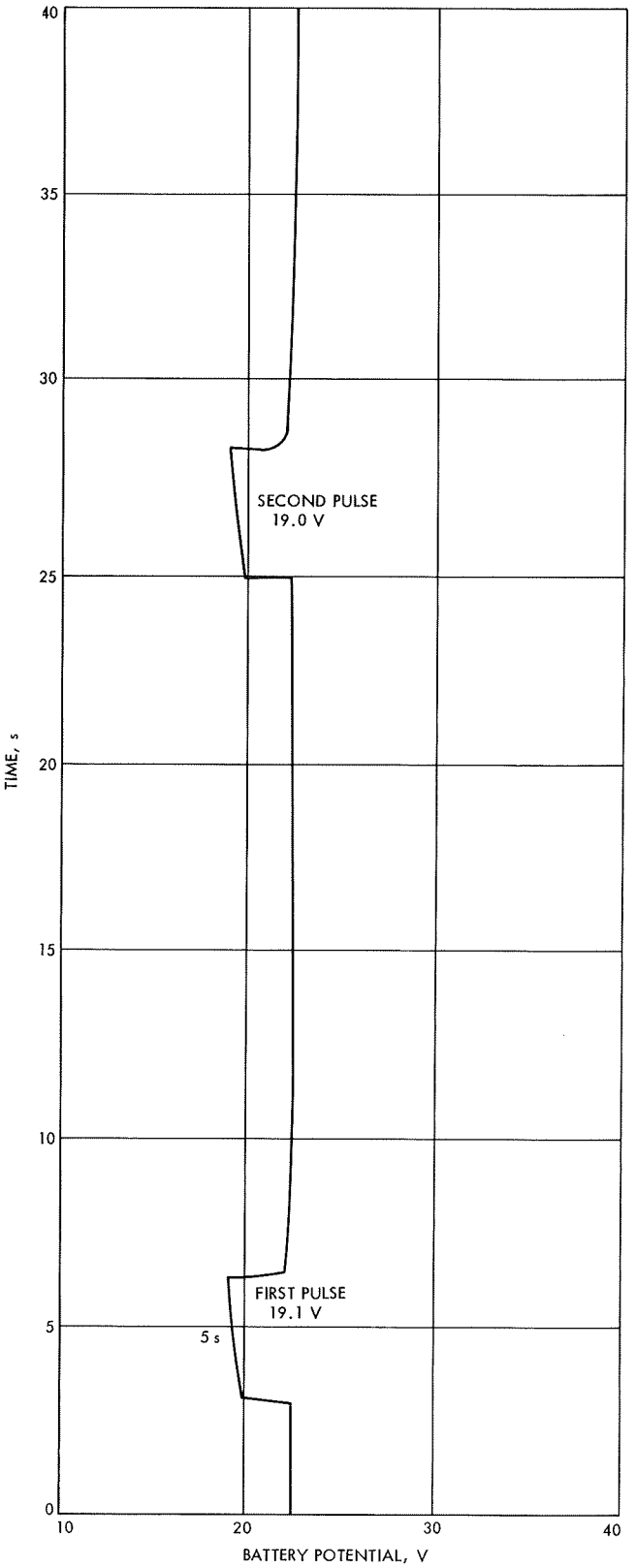

Fig. 79. Voltage regulation of fully charged engineering test battery after 85-A, 5-s pulse

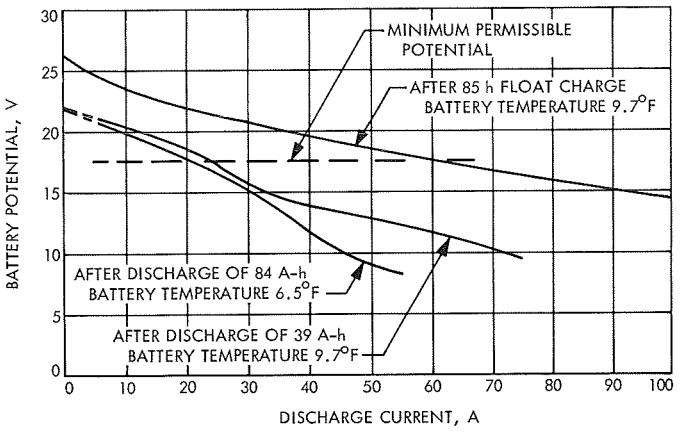

Fig. 80. High current sweep on prototype battery in chamber at 0°F temperature

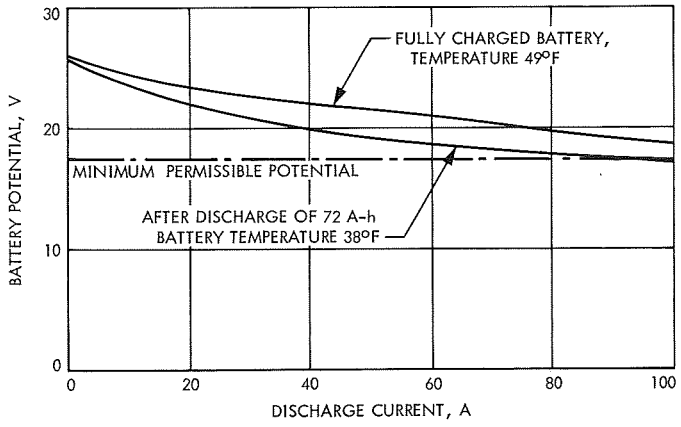

Fig. 81. High current sweep on prototype battery in chamber at 40°F temperature

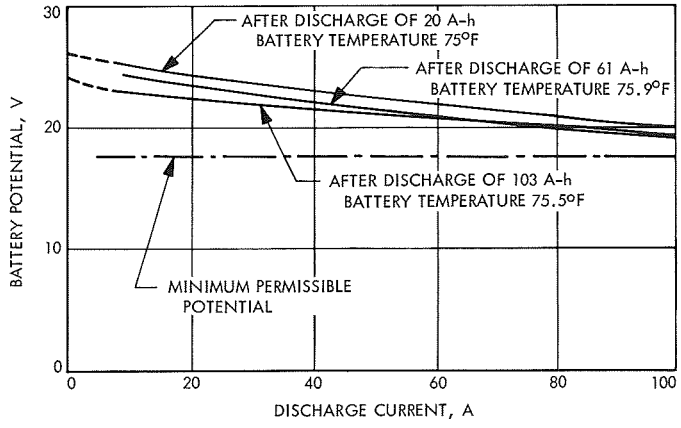

Fig. 82. High current sweep on prototype battery at ambient temperature

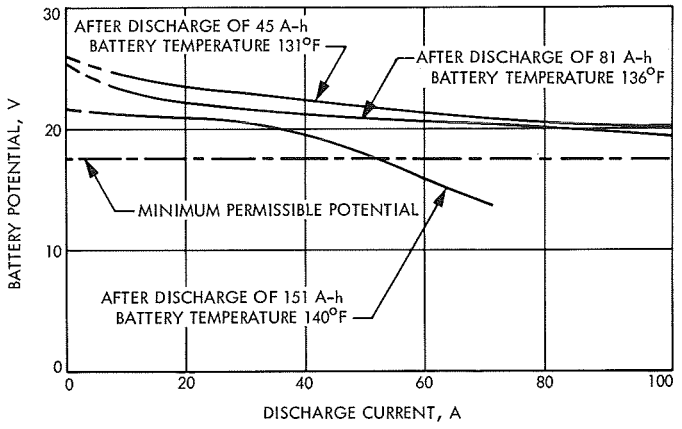

Fig. 83. High current sweep on prototype battery in chamber at 125°F temperature

Battery potentials for high rate discharge from the upper and lower plateau, respectively, for another battery is shown in Figs. 84 and 85. Comparison of the various graphs from low temperature sweeps shows a considerable range of potentials that may in part be due to design differences (see Table 27).

c. Charged stand loss. Charged stand loss of experimental model cells has been treated in Subsection III-B-2. Similar tests were also run on prototype cells and the results are indicated in Table 40 and Fig. 86. The charged stand capacity loss rate of the prototype model cell at 125°F was equal to or less than that of the experimental model cell, while at 160°F, the loss rate of the prototype model was much greater. The initial capacity loss, observed on the experimental model cell at 125 and 160°F, did not occur on the prototype model cell. Comparison of stand loss for a high rate cell, the experimental model cell, and the prototype model cell indicated a similarity between the high-rate cell and the prototype cell, whereas the experimental model cell acted like a lower-rate cell.

This difference in behavior is probably due to the use of higher porosity positive plates with greater electrolyte retension in the prototype cell, as contrasted to the experimental model cell, and an improved separator system.

d. Direct current impedance. From high rate sweeps, dc impedances were calculated for several states of charge. In contrast to experimental cell data, presented in Subsection III-B-4, these results are of greater validity as the rapid sweep prevented a major temperature rise. Results for an ambient temperature test are shown in Fig. 87.

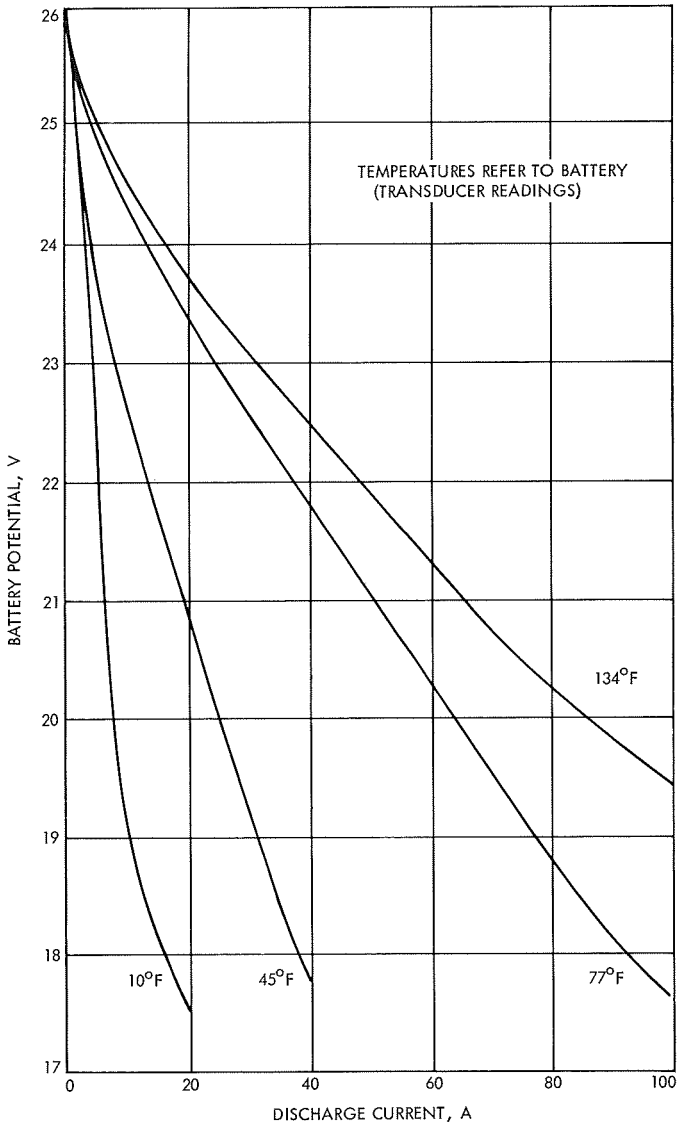

Fig. 84. Prototype battery discharge characteristics for upper plateau

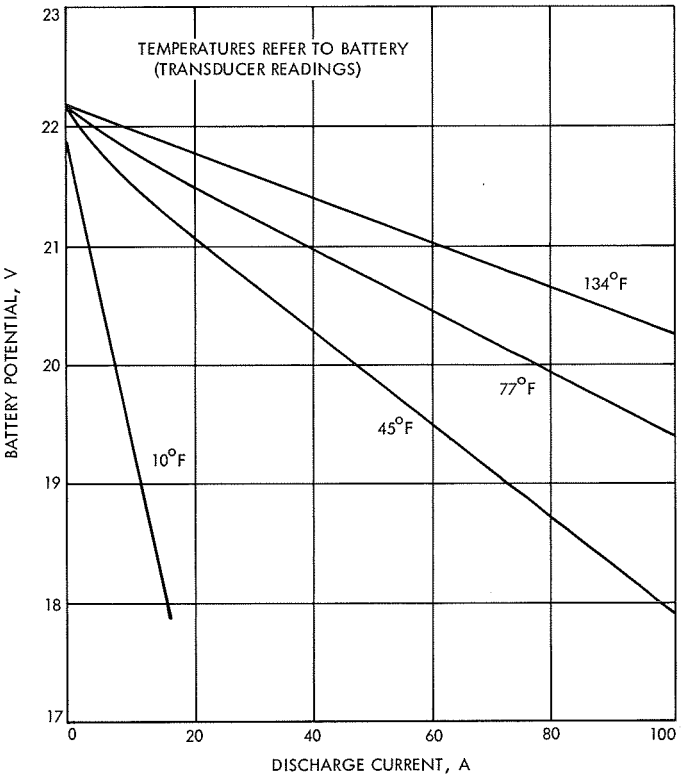

Fig. 85. Prototype battery discharge characteristics for lower plateau

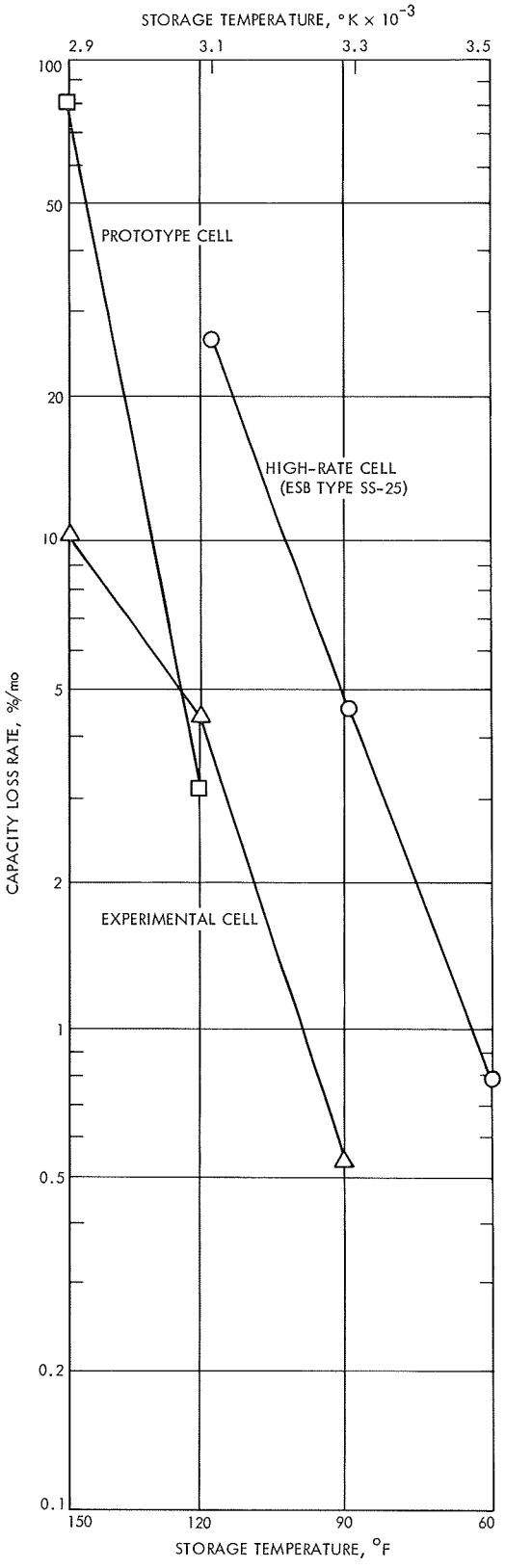

Fig. 86. Effect of charged stand temperature on capacity loss rate for prototype model cells

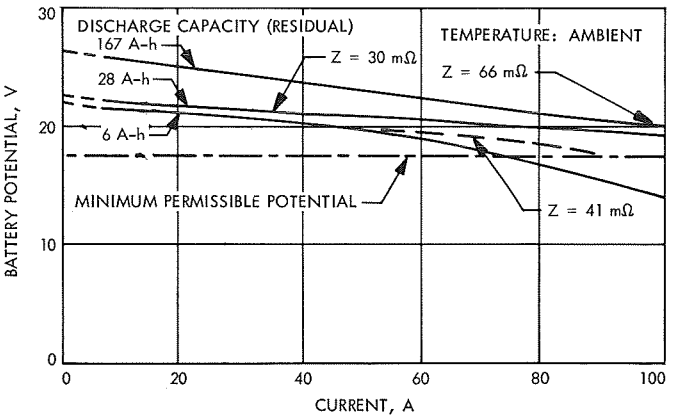

Fig. 87. Voltage vs current for 10-s high current sweep with prototype battery

e. Heat generation. Heat generation during discharge was calculated and the resultant estimates are plotted in Fig. 88. Such data are vital to a determination of the thermal behavior of the spacecraft. Later calorimetric measurements provided more accurate heat generation rates.

f. Battery discharge efficiency. Based on matrix tests and additional engineering test data, a battery capacity model was formulated. The model expresses the first discharge capacity following flight acceptance testing in terms of the first charge capacity and the discharge efficiency:

$$(\text{A-h})_o = \frac{\eta}{100}\,(\text{A-h})_i$$

where

$(\text{A-h})_o$ = first discharge capacity, A-h

η = discharge efficiency, %

$(\text{A-h})_i$ = first charge input, A-h

The discharge efficiency, η, was determined statistically from battery data and is summarized in Table 41. Batteries were charged at 2 A and discharged at 7 A, at a temperature of 70 $\pm$5°F.

$$\bar{x}\,\text{of}\,\eta = 97.2$$

$$\sigma = 0.433$$

The efficiency, η, is taken as $\eta = 97.2 \pm 1.29\%$ (3σ)

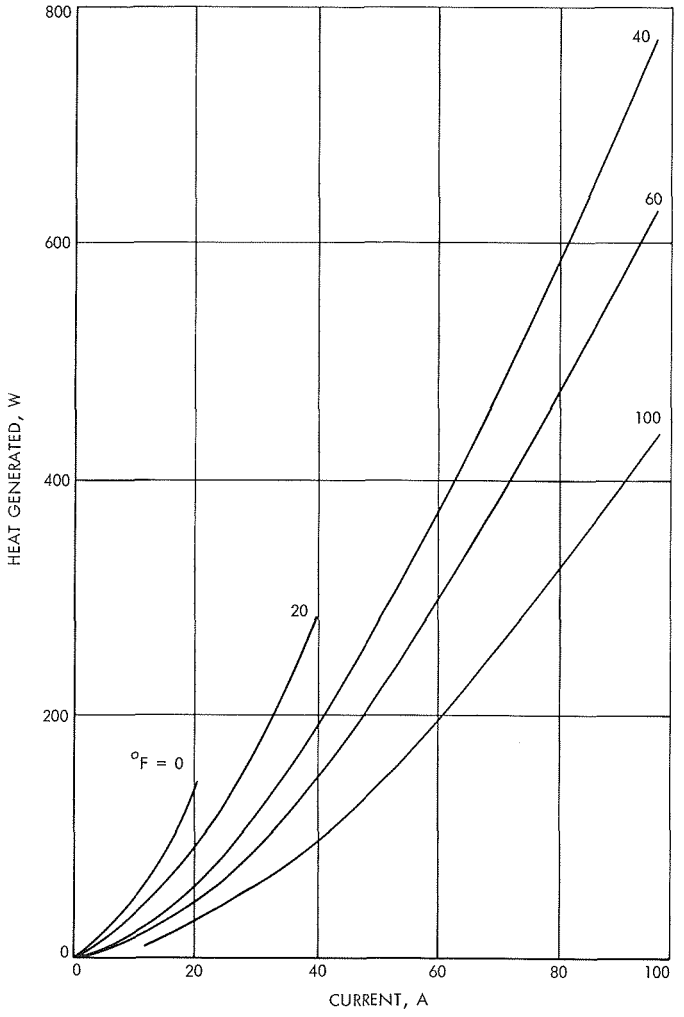

Fig. 88. Calculated heat generation in prototype battery during discharge

Table 41. Main battery discharge efficiency summary

Battery SN	First charge input, $(A\text{-}h)_i$	First discharge capacity, $(A\text{-}h)_o$	Discharge efficiency η, %
X-22	159	155	97.5
X-25	181	177	97.8
X-26	184	179	97.4
X-27	184.8	179.9	97.5
X-28	188.9	180	95.2
X-30	173	165	95.5
X-31	177.9	176.2	99.0
X-34	178.8	174.9	97.8
X-35	175.3	174.6	99.5
X-36	182.7	175.6	96.1
8	186.5	179.2	96.1

Allowing for instrumentation errors of ±3%, the first discharge capacity in ampere-hours becomes

$$(A\text{-}h)_o = \left[\frac{97.2 \pm 1.29\%}{100}\right] \times \left[(A\text{-}h)_i \pm \frac{3.0\%}{100}\right]$$

The value for $(A\text{-}h)_i$ is determined as part of the battery flight acceptance testing.

4. Cycle life tests. A cycle life test was performed on an engineering test battery where charging took place at 2.0 A, 1.0 A, and float with a cutoff potential of 27.3 V; discharge was at the 7.0-A rate to a 17.5-V cutoff and the test temperature was ambient. Both ampere-hour input and ampere-hour output are shown as a function of the number of cycles in Fig. 89, and it is to be noted that both degraded at the average rate of 2.5 A-h per cycle. The battery failed due to a shorted cell after 22 cycles. There appears to be a trend toward a higher 2-A charge contribution as the battery ages under cycling. Similar watt-hour data are shown in Fig. 90, and average watt-hour degradation rates are included. The difference in slopes (watt-hours/cycle) between charge and discharge data may not be real. The life of 22 cycles is well above minimum requirements, but the cycle regime did not simulate the intended use. The lower half of Fig. 89 presents the contribution that the charge at the 2-A rate makes to the total charge.

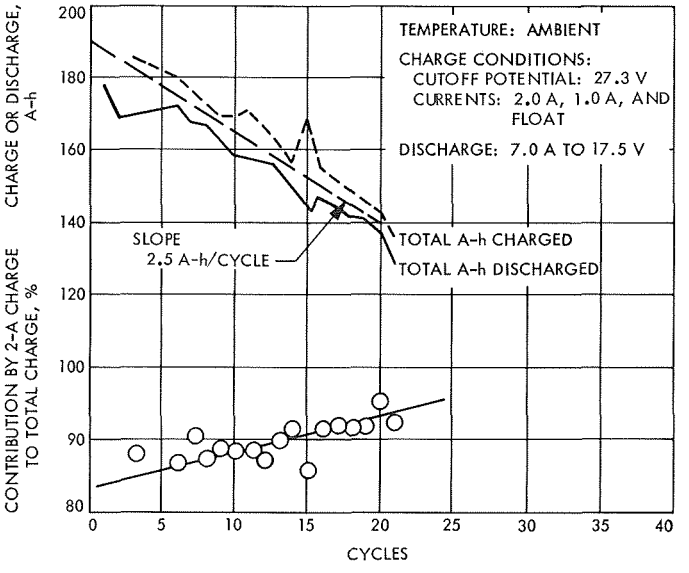

Fig. 89. Cycle life data for prototype battery—ampere-hour data

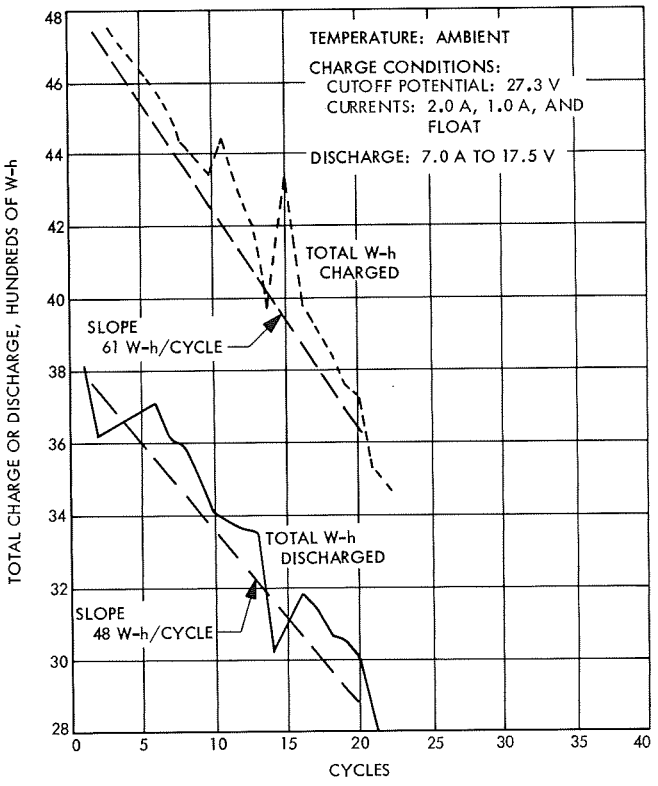

Fig. 90. Cycle life data for prototype battery–watt-hour data

C. Type Approval Tests

Failure of prototype batteries to pass type approval vibration tests led to an intensive development effort which is discussed in the subsequent paragraphs.

1. Vibration problems. Failure of a number of prototype batteries to pass type approval vibration tests was attributed to breakage of lug wires and positive plate fracture. Such vibration tests were performed in facilities that were adapted to testing the *Surveyor* main battery. The HAC battery vibration facility is depicted in Fig. 91. A prototype battery, with attached accelerometers, is shown installed in the vibration fixture that is attached to the vibration table.

Resolution of the vibration-induced failures was achieved by a two-phase test program, with one phase devoted to solving the wire breakage problem, the other toward solving the positive plate fracture problem.

a. Wire breakage. Fourteen types of test cells were designed and fabricated with the object of determining the most vibration-resistant cell configuration, commensurate with the need to minimize weight. Pertinent characteristics of the test cells are summarized in Table 42.

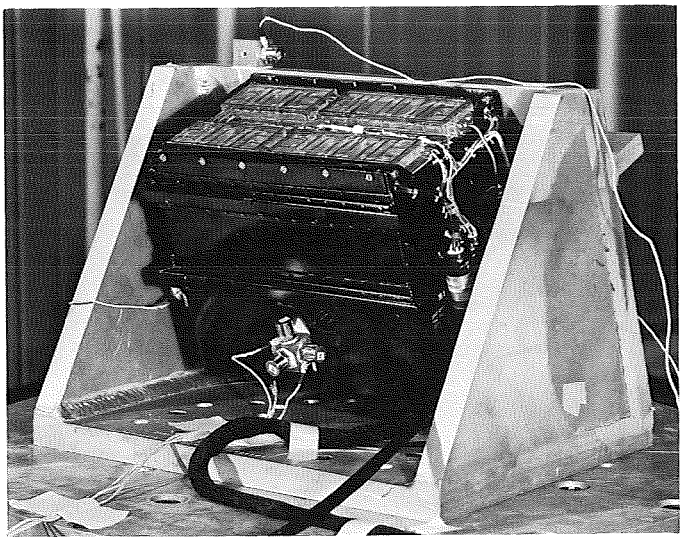

Fig. 91. *Surveyor* battery in HAC vibration test facility

Two cells of each configuration were subjected to the required vibration test (see Subsection II-D-4) and configurations 1, 3, 6, 11, and 14 successfully passed this test. On the basis of minimum weight, ease of manufacture, reproducibility, and minimum change to the cell pack design, configuration 14 was selected as a tentative solution to the problem. The weight increase associated

Table 42. Configuration characteristics of vibration test cells[a]

Test cell configuration	Characteristics
1	0.25 × 0.06 in. silver lug to an anchor positive plate to cell case Loop in negative lead Free space ratio equal to 2.92
2	Free space ratio equal to 2.92 PVA binder in negative Loop in both positive and negative lug wires
3	Free space ratio equal to 2.92 PVA binder in negative Loop in lug wires of both plates Three grids in negative Pot bottom of separators 0.010 silver strip between positive plate

[a]This table lists only characteristics which are not already included in the standard Model 205 battery design.

Table 42 (contd)

Test cell configuration	Characteristics
4	Both lug wires looped Free space ratio equal to 2.37
5	Both lug wires looped Free space ratio equal to 2.92 Three grids in negative
6	Free space ratio equal to 2.92 Pot bottom of separators 0.010 silver strips between positives
7	Free space ratio equal to 2.92 Both lug wires looped Three grids in negative Wrap negatives in cellophane
8	Free space ratio equal to 2.92 Absorbers at edge of cell pack
9	PVA binder in negative Both lug wires looped Three grids in negative Free space ratio equal to 2.92
10	Free space ratio equal to 2.92 Pot top of separators PVA binder in negative
11	Free space ratio equal to 2.92 0.25 × 0.06 in. silver lug to anchor positive plate to cell case 0.25 × 0.06 in. polystyrene strip to anchor other side of positive plate to cell case
12	Free space ratio equal to 2.92 PVA binder in negative Bottom of separator potted 0.010 silver strips between positives Plastic holddown in "I" fold Absorbers at edge of cell pack
13	Free space ratio equal to 2.92 0.25 × 0.60 in. silver lug to anchor positive plate to cell case
14	Free space ratio equal to 2.92 Both lug wires looped 0.25 × 0.062 in. polystyrene strut on both sides of positive plates

with this design was 0.5 lb, or an increase in battery weight from 46.0 to 46.5 lb.

Prototype batteries containing cells of configuration 14 were constructed and subjected to the same vibration test, but a number of cells failed. The cause of the failure was determined to be breakage of lug wires as a result of displacement of positive plates away from the plastic struts, and negative plate displacement. Finally, a third group of test cells was designed, fabricated, and tested to determine their ability to withstand the vibration environment. The types of cells are summarized in Table 43. The results of the vibration test were satisfactory for all cells. Vibration testing and teardown of cells (Table 44) showed cell SK 8497-14 to have suffered no damage at all and this configuration was selected for future *Surveyor* prototype batteries. The design necessitated a 4% reduction in the amount of positive (limiting electrode) active material, but produced no increase in weight.

Table 43. Configuration changes to vibration test cells

Part number	Characteristics[a]
SK8497-1	Two 0.015-in. thick polystyrene shims were added to the cell pack to increase pack tightness
SK8497-2	One polystyrene shim (0.015-in. thick in the center and 0.047-in. thick on the edges) was added to the cell pack to increase pack tightness
SK8497-5	The thickness of a portion of the positive plate strut was reduced to make the strut more flexible and reduce the stress on the positive plate during vibration motion
SK8497-7	A 35 × 40 mesh silver screen was substituted for the expanded silver grid in the positive plate
SK8497-8	The positive plate strut was extended so that it went from the top to the bottom of the plate
SK8497-9	An X frame of polystyrene was added to the negative grid to make the negative plate less compressible
SK8497-10	An X frame in a box of polystyrene was added to the negative grid to make the negative plate less compressible
SK8497-11	Same as SK8497-1A Same as SK8497-8A Same as SK8497-7A
SK8497-13	Same as SK8497-1A Same as SK8497-8A
SK8497-14	Same as SK8497-7A Same as SK8497-10A
SK8497-15	Add 5 vertical polystyrene ribs to the positive plate

[a]This table lists only characteristics which are not applicable to Battery SN X-19.

Table 44. Effect of vibration on test cells (II)

Type cell	Negatives displaced			Observed during teardown of one cell				
	After thrust	After longitudinal	After lateral	No. of positive plates broken at strut	No. of positive leads broken	No. of negatives displaced	No. of negative leads broken	Total defects
Control	No	Yes	Yes	10	4	3	0	17
SK8497-1	Yes	Yes	Yes	4	0	3	0	7
SK8497-2	No	Yes	Yes	3	0	2	½	5½
SK8497-5	No	Yes	Yes	0	0	4	0	4
SK8497-7	No	Yes	Yes	0	0	5	0	5
SK8497-8	No	Yes	Yes	9	0	4	0	13
SK8497-9	No	No	No	4	0	0	0	4
SK8497-10	No	No	No	4	0	0	0	4
SK8497-11	No	Yes	Yes	6	0	2	0	8
SK8497-13	No	Yes	Yes	10	0	3	0	13
SK8497-14	No	No	No	0	0	0	0	0
SK8497-15	No	Yes	Yes	0	0	3	0	3

b. Positive plate fracture. Monoblocks of twelve mechanical configurations were designed and fabricated. Pertinent design information is offered in Table 45.

Table 45. Monoblock mechanical configurations

Cell design number	Mechanical configuration
371	Preliminary *Surveyor* battery cell design
-1	371 design with 0.015 in. shim on internal cell case weld
-2	371 design with concave shim 0.015 in. at center, 0.055 in. at sides on internal cell case wall
-5	371 design with more flexible positive plate struts
-7	371 design with 36 × 45 mesh screen for positive plate grid
-8	371 design with full length strut on positive plate
-9[a]	371 design with X-frame on negative plate
-10[a]	371 design with full frame and X-frame on negative body
-11	Combination of -7, -8, and -1
-13	Combination of -1 and -8
-14[a]	Combination of -7 and -10
-15	371 designs with five 0.093 in. wide struts on the face of positive plate

[a]These cells were constructed without one of the end negative plates as a result of assembly difficulty.

Following the vibration at type approval test levels, capacity tests were performed on the monoblocks to determine the second cycle charge acceptance. Table 46 summarizes the charge acceptance data. The charge acceptance proved to be satisfactory in view of the cell construction.

The teardown of typical cells after the test provided the status report given in Table 47.

On the basis of these tests, configuration 14 was selected for future testing after incorporation of its features into prototype batteries. The resultant prototype batteries successfully passed type approval vibration tests, when subjected to such a test at HAC in accordance with test criteria specified earlier (Section II). Vibration levels for this test are shown in Fig. 92.

2. Shock test on cells. The cell structure, evolving from the solution to the vibration problem, provided for struts to restrain the positive plates from any movement.

Table 46. Second cycle charge acceptance

Cell design number	Second cycle charge input, A-h
-5	188.2
-7	186.5
-9[a]	175.3
-10[a]	173.5
-14[a]	163.2

[a]These cells were constructed without one of the end negative plates as a result of assembly difficulty.

Table 47. Type approval test vibration results inside cell

Condition	Cell design number											
	-1	-2	-5	-7	-8	-9	-10	-11	-13	-14	-15	371
Positive plate leadwires broken	0	0	0	0	0	0	0	0	0	0	0	0
Positive plates fractured	4	3	0	0	6	4	3	2	5	0	0	6
Negative plates slipped	3	5	5	5	5	0	0	3	5	0	5	5
Negative material washout	Yes	Yes	Yes	Yes	Yes	Slight	Slight	Yes	Yes	Slight	Yes	Yes
End voltage under 85-A load	1.287	1.255	1.259	1.329	1.247	1.260	1.265	1.300	1.269	1.339	1.281	1.156

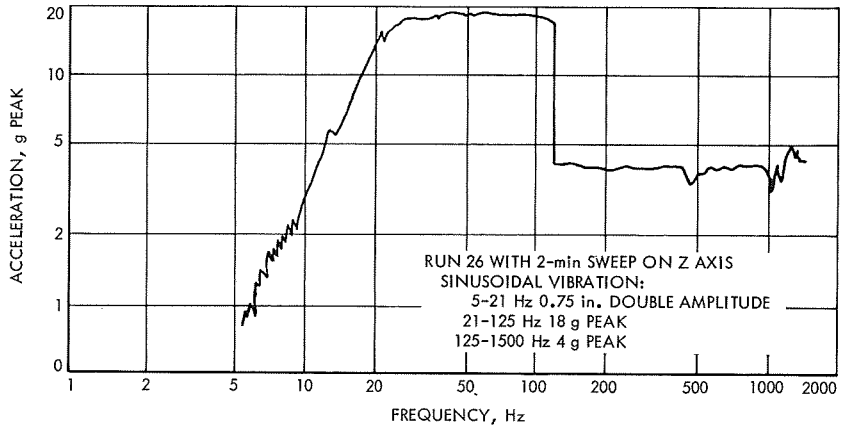

Fig. 92. Vibration levels in type approval test of prototype batteries

Before this new feature was incorporated in the prototype battery design, a shock test was run on a strut-containing cell. This cell was shocked to destruction after 11 (7- to 8-ms) shocks at a 68- to 98-*g* level. The results are summarized in Table 48. Autopsy of the cell revealed that the cell pack had moved down into the cell jar and that four of the positive plates had sheared away from the struts, which were undamaged. This shock test was far more severe than specified in Section II and the design was considered successful.

Table 48. Shock test of prototype cell

Shock number	Direction	Shock level, g	Shock duration, ms
1	Upright	68	7 – 8
2	Inverted	68	7 – 8
3	Inverted	68	7 – 8
4	Inverted	68	7 – 8
5	Inverted	68	7 – 8
6	Inverted	90	7 – 8
7	Inverted	90	7 – 8
8	Inverted	90	7 – 8
9	Upright	90	7 – 8
10	Upright	90	7 – 8
11	Upright	90	7 – 8
12	Upright	98	7 – 8

3. Thermal-vacuum tests. Of the first five batteries that passed the vibration and shock type approval tests, four subsequently passed the thermal-vacuum test, described in Subsection II-D.

D. Conclusions Concerning the Prototype Model Battery Program

The prototype model battery program culminated in a battery that was adequate for the intended mission. During this phase of the program, a number of facts and deficiencies were revealed, including:

(1) The concept of a manifold-battery was successfully adapted, charged in the constant power mode to a cutoff, followed by a float charge. Pressure limits for the battery were established and a

provision for automatic charge termination in case of excessive pressure was implemented.

(2) The low charge acceptance of early prototype batteries was pinpointed to the use of nylon separator that had poor wetting characteristics.

(3) The use of six layers of cellophane as separator system proved adequate and was accepted for the flight battery.

(4) A saving in weight was achieved by the development of a lighter, more porous positive plate.

(5) The uniformity of the negative plates was improved by modification of the manufacturing process.

(6) The use of wicks to reduce electrolyte depletion at the positive electrode during charge was shown to be feasible, but not adopted because of inadequate performance history. Instead, additional electrolyte was provided at the positive plate by increasing the plate porosity.

(7) Type approval vibration tests produced severe battery damage in the form of breakage of lug wires and fracture of positive plates. These faults were corrected by: substituting a mesh silver screen for the expanded silver grid in the positive plate, strengthening the negative plate by adding a polystyrene X-frame to the negative grid, looping lug wires, and strutting positive plates. The resultant batteries were generally capable of meeting all type approval tests including vibration, shock, and thermal-vacuum.

VI. Flight Model *Surveyor* Main Battery

The flight model *Surveyor* main battery was essentially identical to prototype batteries, SN X-37 and subsequent (see Table 27). For this reason, the description of the battery will not be repeated here. This section covers reporting, and evaluation, of tests that were run to provide needed performance input, and the solutions to technical problems.

A. Performance Tests

This subsection presents some of the electrical performance data for the flight model battery.

While the major test effort on the flight model battery dealt with flight approval and mission simulation tests, several smaller, but significant efforts consisting of charge and discharge tests involved: (1) establishment of a guide to safe operating limits, (2) discharge efficiency, and (3) effect of constant current charging to a lower cutoff potential on battery capacity.

1. Battery operating limits. Based on limited burst pressure tests, a graphic aid was prepared to define safe battery temperature and pressure limits for test personnel. In these tests monoblocks, with supported sides, were warmed to the desired temperature, and then pressurized slowly with helium until a leak developed. The pressure at that instant served as the basis for specifying abort conditions. The resultant visual aid, shown in Fig. 93, was applicable to flight batteries, SN 36 and subsequent.

2. Discharge efficiency. The battery discharge efficiency as discussed for the prototype model (Subsection V-B-3), has also been determined for a number of flight batteries. However, the term $(A\text{-}h)_i$ was redefined to provide a more accurate efficiency by accounting for stand loss and certain changes in capacity due to testing.

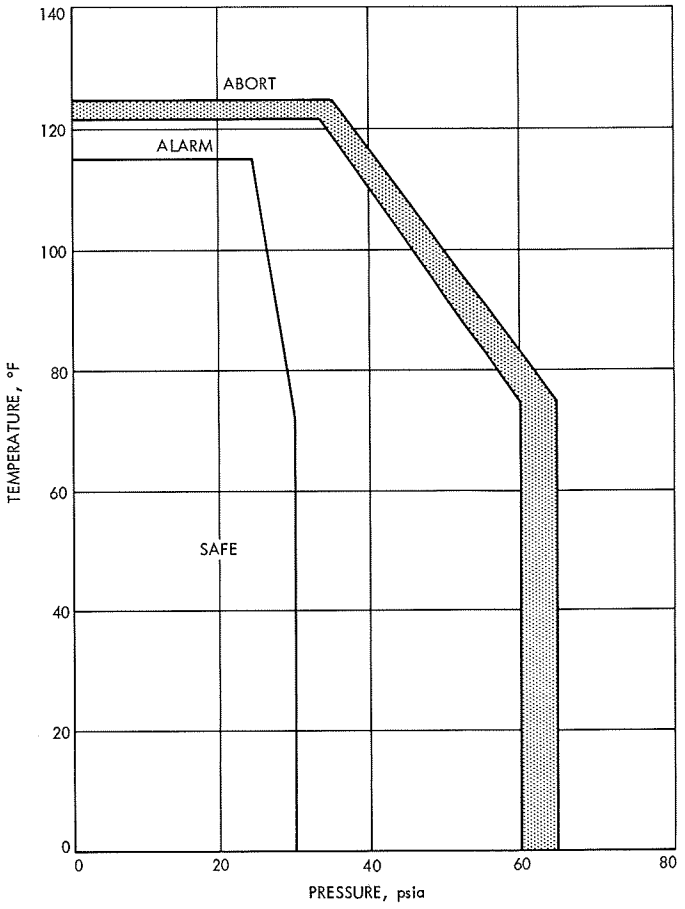

Fig. 93. Surveyor main battery—alarm, action, abort

Table 49. Results of flight battery discharge efficiency tests

Battery	Vendor charge	Stand loss	HAC charge	Stand loss	Vibration	Total	First discharge[a]	Efficiency, %
	A-h							
29	174.2	7.0	25.0	2.9	5	184.3	177.1	96.5
30	177.4	7.1	29.5	3.0	5	191.8	177.1	93.0
31	176.6	7.0	26.8	2.0	5	188.5	176.3	94.0
32	172.8	6.0	31.6	3.0	5	189.5	177.2	93.5
33	178.0	7.0	25.3	2.0	5	188.4	184.7	98.0
34	171.6	7.0	31.4	2.9	5	188.1	183.3	97.0

[a]Batteries discharged at 7.0 A, temperature 75 ±5°F.

The revised definition became:

$(A\text{-}h)_i$ = First charge input from vendor's data (lowest monoblock) in ampere-hours, minus stand loss (3% per month at 75°F, 1% at 30°F), plus HAC charge and float charge, minus 5 A-h for capacity used during vibration testing, minus stand loss to time of use (plus top charge, if any).

Results of the redetermination of battery discharge efficiency are summarized in Table 49. The battery discharge efficiency was derived statistically to be 95.3 ±3.82% (+ 2σ) for discharge at 75°F. For each 5°F above 75°F, the efficiency was considered to degrade by 1%.

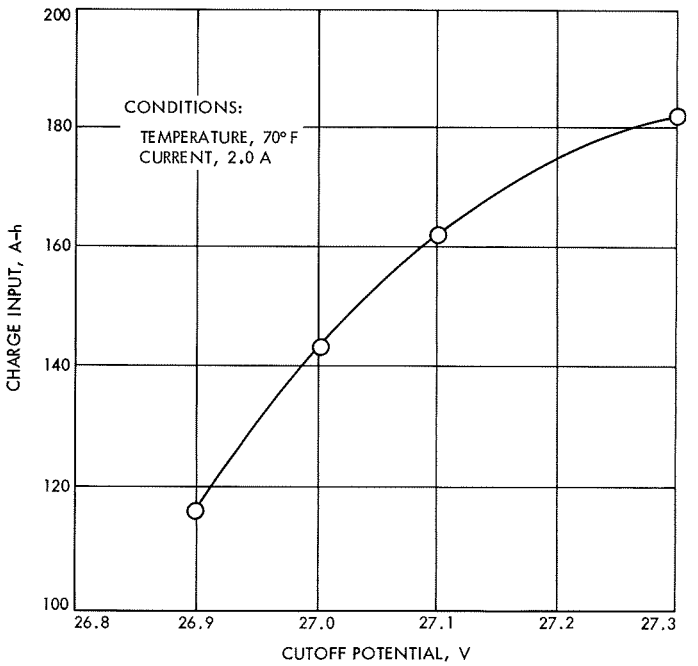

Fig. 94. Charge input vs cutoff potential for flight model Surveyor main battery

3. Charge cutoff. In order to determine the consequences of charging to a lower cutoff potential than the adopted value of 27.3 V, and then float-charging at the lower potential, the charge input resulting from constant current charging at 2.0 A to selected cutoff potentials was obtained for twelve batteries. The average value is plotted in Fig. 94. It is significant that below 27.2 V, a reduction in charge input was obtained. It was concluded that charging to a cutoff potential as low as 26.9 V with subsequent float-charge at that potential would consume excessive time and a constant current charge to 27.3 V cutoff with subsequent float-charge at 27.0 (+0.1, −0) V was used for all flight batteries, from SN 36 and subsequent. Float-charge at the lower potential resulted in maximum pressures below 25 psia, compared to a limit of 45 psia under the 27.3-V float-charge. This reduction in pressure increased the safety margin greatly. Available charging time was sufficient to float-charge the battery to full capacity when limited to 27.0 V.

B. Problem Areas and Solutions

1. Low pulse potential problem. As a part of acceptance testing of batteries at ESB, discharge pulses of 85 A for 10 s were applied. Batteries, SN 43–SN 47, fell below the minimum permissible potential of 17.5 V with an average five-battery value of 16.8 V, compared to much higher values from previous batteries (18.5–19.5 V). Owing to the great need for batteries by the *Surveyor* program at that time, the batteries were accepted on a waiver basis. A fast (< 10 s) 0–100 A sweep at HAC on the fully charged batteries gave minimum potentials ranging from 15.80 to 16.92 V with an average of 16.2 V. Critical cell components that were considered suspects for the deficiency of over 2 V were:

(1) Positive plates.

(2) Negative plates.

(3) Cellophane separator.

(4) Electrolyte.

(5) Plate leads.

(6) Cell jars.

Table 50 presents a summary of cell components for the last normal battery (SN 42) and the substandard batteries (SN 43–47).

Table 50. Summary of critical cell components

Cell component	Last normal battery, SN 42	Defective batteries, SN 43–47
Positive plate lots[a]	07065P1	01146P1
	04145P1	01216P1
	08064P1	
Silver lot[a]	190	217
	191	
	197	
	198	
	199	
Negative plate lots[a]	04145M3	01146M2 (47 only)
	04145M4	01146M1
	04145M2	04145M2
	(04145M5 in SN 34)	04145M5
Zinc oxide lot	132	132
		135
Mercuric oxide lot	277	277
		290
Binder lot	280	280
Cellophane lot[a]	C-0244	C-0356
	C-0318	
Electrolyte lot	106	111
		(106 in battery SN 44)

[a]The positive plates, silver powder, negative plate lots 01146M2 and 01156M1 and cellophane were prime suspects.

a. Investigation of positive plates. Determination of a number of properties of silver powder (Table 51) showed that the positive plates from suspect lot 217 did not differ significantly in these properties from lots used in good batteries. Although surface area was believed to have a significant bearing on pulse discharge capability, the results of a surface area determination by the Brunauer, Emmett and Teller (BET) nitrogen absorption technique (Table 52) again showed that lot 217 was similar to the other lots. Although the 10% difference in surface area may be significant, an evaluation was not reported by ESB. Possibly, silver powder was ruled out as a source of the low voltage trouble on the basis of concurrent cell tests.

Table 51. Surface area determination of silver powder

Lot number	Surface area, $in.^2/lb$
190	9.16×10^4
217	8.44×10^4

The porosity of the positive plates was determined by their ability to absorb 40% potassium hydroxide electrolyte. The results are summarized in Table 53. The data indicate that both lots have essentially the same porosity.

b. Investigation of negative plates. Only negative plates taken from lots 01146M1 and 01156M1 were common to all low performance batteries. Owing to the unavailability of additional plates from lot 01156M1, tests were performed using plates from lot 01146M1. The negative plate tests were a part of the cell tests described in subsequent paragraphs of this section.

c. Investigation of cellophane separator. As indicated in Table 50, batteries SN 43–47 were fabricated using a new lot of separator material—cellophane lot C-0356. A number of separator material properties were tested on dry material and also after immersion in 40% potassium hydroxide solution. Table 54 presents test results from five lots of cellophane separators. Results were not significantly different for lot C-0356. The test methods were basically those of Cooper and Fleischer (Ref. 2). A clear pattern did not emerge from these data to distinguish lot C-0356 from the other lots. Differences within lots were partly sampling, and partly operator error. The magnitude of differences in the same lot was later established by tests on sixteen sheets from lot C-0318, where pore diameters ranged from 4.92×10^{-8} in. to 6.41×10^{-8} in.

Tests on cellophane did not show lot C-0356 to be significantly different from other lots in the properties that were tested. However, the observed nonuniformity of material in a given lot was established and future specifications were tightened.

d. Matrix (cell) test. The tests previously discussed, failed to isolate the cause of the encountered low voltage. Cellophane was later isolated as the cause by an

Table 52. Silver lot characteristics

Lot	Batch	Moisture content, %	Apparent density, lb/in.^{3}	Mean particle diameter, mils	Screen analysis			
					+150	+150 −200	−200 +325	−325 mesh
190	2198	0.005	0.0617	—	0	0.2	7.2	92.5
191	2200	0.005	0.0584	—	0	0.2	7.0	92.8
196	2206	0.016	0.0588	—	0	0.2	7.4	92.3
197	2211	0.001	0.0607	—	0	0.2	6.9	92.9
198	2213	0.010	0.0650	0.193	0	0.2	6.4	93.4
199	2215	0.008	0.0591	0.165	0	0.1	4.9	95.0
204	2223	0.005	0.0628	0.267	0	0.1	9.6	90.3
216R[a]	2282	0.005	0.0620	—	0.1	0.1	7.0	92.8
217[b]	2285	0.006	0.0651	0.236	0	0.1	9.4	90.5
218	2286	0.007	0.0593	0.256	0	0.1	9.1	90.8
219	2292	0.011	0.0596	0.228	0	0	6.0	94.0
222	2297	0.016	0.0609	0.236	0	0.1	4.9	95.0

[a]Reject lot.
[b]Lot used in Model 205 batteries having low pulse voltages.

Table 53. Porosity tests on positive plates

Property	Positive plate lot	
	07056P1	01216P1[b]
Wet weight, lb	0.228	0.223
Dry weight, lb	0.191	0.191
KOH absorbed, lb	19.2	20.1
Porosity, %[a]	59.75	60.75
Plate density, lb/in.^{3}	0.156	0.153

[a]Based on nominal plate volume of 1.231 in.^{3}
[b]Suspect lot.

electrochemical performance test of the cell components. This test used suspected components in combination with good components. The matrix of the components used is shown in Table 55.

Results of discharge tests on the cells tested are summarized in Table 56. The difference in potential between cells A and B, and cells C and D, amounts to approximately 1 V for a 14-cell battery. Cells C and D used cellophane from lot C-0356, while the other cells were made with cellophane from a different lot. Therefore, it was concluded that cellophane lot C-0356 was the cause of the low pulse discharge potential.

e. Conclusions. The low pulse discharge potential was caused by some undefined fault in cellophane separator, lot C-0356. This cause was detected by a matrix cell test, whereas a number of physical measurements had failed to select the defective lot. Large differences in properties, such as pore size, existed in sheets from the same lot of cellophane. A more rigid inspection of cellophane was instituted as the result of this finding. The use of matrix cell tests is recommended as the most effective means for determining the cause of low pulse discharge potenials and other malperformances.

2. Battery terminal potential problems from deletion of the auxiliary battery. With the decision to delete the auxiliary battery from spacecraft SC-5, SC-6 and SC-7, a marginal level of battery potential during the high power operations of terminal descent had to be evaluated. A detailed analysis of load and critical potential indicated a need for a battery potential minimum of 18.0 V to maintain proper system operation.

During terminal descent with the radar altimeter and doppler velocity sensor (RADVS) on, the current demand was approximately 45 A with 20-ms pulses of approximately 14 A superimposed at the time of retro release squib firing. A test was run simulating this condition, with somewhat larger currents, as depicted in Fig. 95. A total of 64 A-h were removed from a fully charged battery to use in performing this test. Results of the test, listed in Table 57, indicate that the main battery can provide the required current, if maintained at temperatures of 78–93°F. A more complete evaluation of the

Table 54. Cellophane tests

Test	Unit	Technician	ESB 193-PUDO lot				
			234	244	318	356[a]	438
1	Thickness, mils						
	Dry	A	1.1	1.2	1.1	1.0	1.1
		B	1.2	1.5	1.2	1.2	1.4
		C	1.0	—	1.0	—	—
	Wet	A	3.6	3.3	3.4	3.7	3.9
		B	3.6	3.8	3.8	3.8	3.9
		C	3.5	—	—	—	—
2	Dimensional changes, %						
	Length	A	3.2	5.2	2.4	5.2	3.8
		B	5.6	4.8	1.5	4.2	2.6
		C	4.0	—	3.3	—	—
	Width	A	−3.8	−3.4	−3.6	−3.0	−4.0
		B	−4.2	−3.8	−4.0	−3.8	−4.2
	Thickness	A	240	174	222	255	255
		B	211	150	214	225	182
		C	250	—	240	—	—
3	Weight, $10^5 \times$ lb/in.^{2}						
	Dry	A	5.25	5.20	5.18	5.18	5.30
		B	5.25	5.18	5.20	5.15	5.40
		C	5.16	—	—	—	—
	Wet	A	20.6	19.7	19.7	19.2	20.0
		B	20.1	20.0	21.0	19.6	21.6
		C	19.8	—	19.3	—	—
4	Unit electrolyte	A	292	281	280	287	277
	Absorption, %	B	282	287	306	281	298
5	Specific resistivity, ohm-in.	—	—	—	27.9	—	30.5	—
		—	—	—	30.5	—	30.5	—
6	*Mean pore diameter, in.* $\times 10^8$	—	—	—	8.83	—	9.70	—

[a]Suspected lot.

Table 55. Matrix for special test cells

Cell component	Cell A	Cell B	Cell C	Cell D
Silver lot	190	217	190	217
Positive plate lot	5315	1216	5315	1216
Cellophane lot	C-0234	C-0234	C-0356	C-0356
Electrolyte lot	112	S[a]	S	S
Negative plate lot				
Centers	1146M1	S	S	S
Ends	4145M2	S	S	S

[a]S = same.

Table 56. Results of discharge tests on special test cells

Discharge rate, A	Potential, V		Capacity output, A-h
	Cells A and B	Cells C and D	
10	1.53	1.48 – 1.49	52
50	1.43 – 1.44	1.36	52
85	1.35 – 1.36	1.28 – 1.29	52
85 calculated[a]	18.97 (14 cell)	17.99 (14 cell)	52

[a]Without allowance for potential drop in the wiring.

Table 57. Main battery test data for terminal descent phase

SN	Age at test, days	Discharge rate, A	Minimum discharge voltage[a]	Test description	Battery test temperature, °F
				Flight acceptance	
82	76	50	18.9	1	78
86	67	50	19.2	1	78
88	53	50	19.2	1	78
89	53	50	19.2	1	78
94	45	50	19.2	1	78
95	46	50	19.2	1	78
83	81	50	18.8	2[b]	78
84	79	50	18.8	2	78
87	69	50	18.8	2	78
91	57	50	18.8	2	78
93	56	50	18.9	2	78
SC-3	Under 120	41.5	19.6	Solar-thermal vacuum	98
SC-4	Under 120	45.0	19.2	Solar-thermal vacuum	93
	Under 120	43.0	19.1	Simulated 71-h transit	93
	Under 120	47.0	18.4	Simulated 71-h transit	93

[a]Values during fifth pulse. [b]Rerun of RADVS simulation.

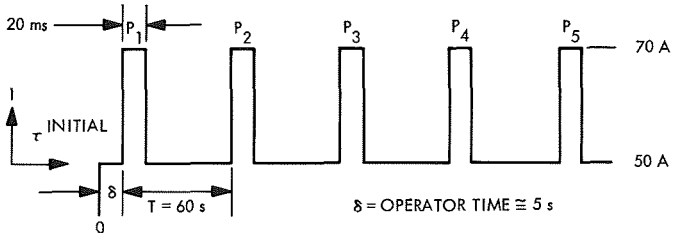

Fig. 95. Main battery pulse test data

main battery's capability to meet power requirements during *Surveyors V, VI,* and *VII* Missions is presented in Section VII.

C. Materials and Process Investigations

A limited test program was conducted to solve a plastics joining weakness. The results are summarized in the subsequent paragraphs.

1. Measurement of bond strength of cements. As a result of some failures of seals made with ESB's proprietary catalized polystyrene cement (PS-211), an investigation was undertaken to determine the effect of temperature on the bond strength.

2. Calculation of bonding area, joining cover to four-cell monoblock. The shear bonding area and tensile bonding area restraining the flat 205-1016 cover to the 205-2013 four-cell molded monoblock cover is:

Peripheral shear area

$$2(1.75 \times 0.135) + 2(5.130 \times 0.135) = 0.472 + 1.385 = 1.857 \text{ in.}^2$$

Peripheral tensile area

$$2(1.75 \times 0.062) + 2(5.130 \times 0.062) = 0.217 + 0.635 = 0.852 \text{ in.}^2$$

Cross member tensile area

$$9(1.626 \times 0.060) + 4(0.725 \times 0.060) - 13(0.135 \times 0.060) = 0.878 + 0.174 - 0.105 = 0.947 \text{ in.}^2$$

Using blue RMD-4511 polystyrene and PS-211 cement in conjunction with the above areas, the force necessary to lift the cover at 125, 150, and 170°F and the equivalent monoblock pressure over the 8.88 in.^{2} area were calculated as shown in Table 58.

Table 58. Calculated strength for blue RMD-4511/PS-211 joint

Temperature, °F	Bond area, in.^{2}		Restraining force, lbs			Equivalent pressure,[a] psi
	Shear	Tensile	Shear	Tensile	Total	
125	1.86	1.80	270	2060	2330	263
150	1.86	1.80	149	905	1054	119
170	1.86	1.80	99	581	680	77

[a]Gas pressure in monoblock required to break the bond between cover plate and molded monoblock cover.

3. Measurement of bond strength. The bond strength of blue and amber RMD-4511 specimens, joined by PS-211 and PS-282M proprietary cements, was determined by ESB, Atlas Division, Mertztown, Pennsylvania, using butt and lap test specimens pulled at 0.25 in./min after equilibration at test temperatures at 80, 125, 150, and 170°F. The results of these tests are shown in Tables 59 and 60, and graphically in Fig. 96.

Table 59. Effect of operating temperature on bond strength of catalyzed polystyrene cement: test I

Test material		Bond type	Tensile strength, psi			
Base	Cement		80°F	125°F	150°F	170°F
RMD-4511 Blue	PS-211	Butt[a]	2302[c]	1142	504	323
RMD-4511 Blue	PS-211	Lap[b]	937	354	155	107

[a]Specimen: 4.0 × 1.0 × 0.090 in.
Butt joint area: 0.0876 in.²–0.0950 in.² range in 16 specimens.

[b]Specimen: 4.0 × 1.0 × 0.090 in. end to end overlapped 0.25 in. giving bonding area 0.24–0.30 in.².

[c]Each value is the mean of 3 specimens tested, at the temperature shown, and at a pull rate of 0.25 in./min.

Table 60. Effect of operating temperature on bond strength of catalyzed polystyrene cement: test I

Test material		Bond type	Tensile strength, psi			
Base	Cement		80°F	125°F	150°F	170°F
RMD-4511 Amber	PS-211	Lap	3540[a]	1895[b]	459	322
RMD-4511 Blue	PS-211	Lap	4660[a]	145	80	53
RMD-4511 Amber	PS-282M	Lap	4240[a]	3103[a]	423	198
RMD-4511 Blue	PS-282M	Lap	4353[a]	342	115	71

[a]Failure in RMD-4511 base material with strength calculated as tensile strength. All others are failures in cement bond calculated as shear strength in psi.

[b]*Four specimens tested at each temperature: each specimen* 1.0" × 4.0" × *t* where *t* was 0.125–0.150 for amber RMD-4511, and 0.090–0.150 for blue RMD-4511, with 0.50 lap.

It is apparent that the amber polystyrene provides a superior high temperature bond with PS-211 cement. The materials specifications were changed accordingly from blue to amber polystyrene.

D. Conclusions

Extensive mission simulation tests are reported in Section VII. For this reason the work reported in this section is limited. However, the following conclusions may be drawn:

(1) A change in float-charge potential from 27.3 to 27.0 (+0.1, −0.0) V resulted in lower gas pressure during extended float-charge, thus providing an increased safety margin for the battery without seriously affecting the charge input of the battery.

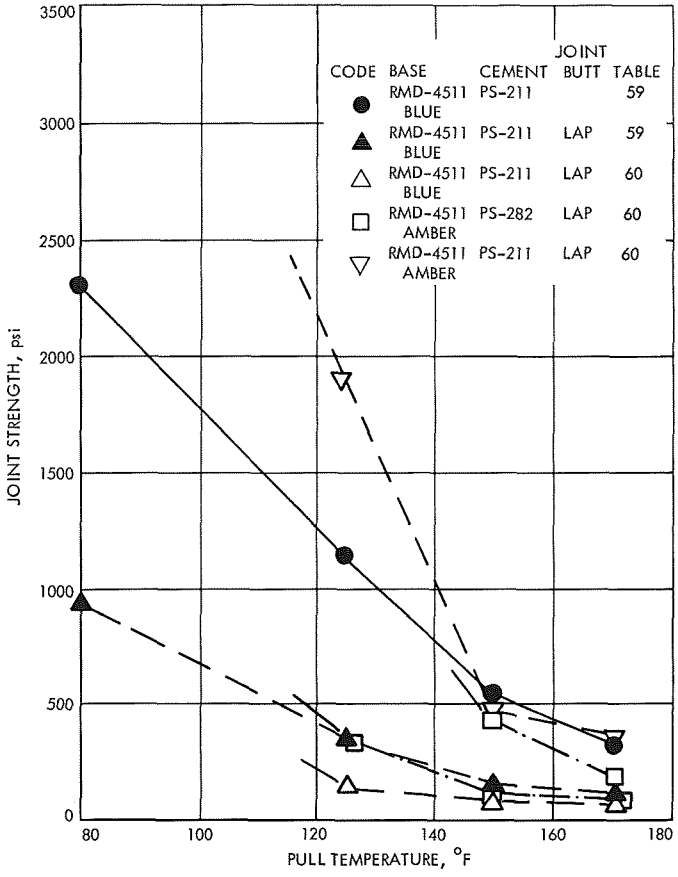

Fig. 96. Bond strengths of catalyzed polystyrene cements

(2) Measurement of the bond strength of selected polystyrenes and cements resulted in a strengthening of the bond between the flat manifold cover and the molded monoblock cover; the superior material was amber RMD-4511 polystyrene. This improvement further increased the safety margin during high temperature charge.

(3) The battery discharge efficiency was determined as 95.3 ±3.82% (±2σ) for discharge at 75°F, with an estimated degradation of approximately 1% for each 5°F above 75°F.

(4) In spite of the elimination of the auxiliary battery, a test showed that the *Surveyor* main battery could provide RADVS pulse requirements during terminal descent.

(5) The low potential during the flight acceptance test 10 s, 0–100 A sweep, with a lot of five batteries was shown to have been caused by an undefined fault in cellophane separator material.

VII. Special Tests and Flight Performance of Flight Model Battery

This section covers the lunar night survival study, low temperature operation, simulation of *Surveyors V, VI,* and *VII* Missions (A-21E program), solar–thermal–vacuum (STV) tests, and actual mission data.

A. Lunar Night Survival Test

The lunar night survival test was conducted to establish the main battery performance anticipated during the lunar night and to predict lunar night survival capability of the *Surveyor* main battery. Basically, the test program was a simulation of the anticipated *Surveyor IV* lunar night temperature–load profile. The test program consisted of sequences I and II with three batteries of various ages employed in each sequence. Sequence I was conducted with fully charged batteries, and sequence II with discharged batteries.

1. Test program. Temperature profiles for the test sequences are summarized in Table 61. Figures 97 and 98 show temperature profiles and electrical test specifications for the sequences.

2. Results. Table 62 summarizes battery history and ampere-hour capacity at various stages of the test. A summary of battery parameters is presented in Table 63.

Table 61. Temperature profiles for lunar night survival test

Test I (see Fig. 97)	
Time, h	**Battery temperature**
Start of test – 132	20°F (stabilized)
132 – 212	20°F to −40°F (¾ °F/h decrease)
212 – 360	40°F to −165°F (1°F/h decrease)
360 – approximately 490	−165° to −40 (1°F/h decrease)
490 – removal of battery	−40°F to room temperature (1°F/h)
Test II (see Fig. 98)	
Event	**Battery temperature**
Capacity determination (to 17.5 V)	20°F
Energy depletion	Room temperature
Lunar night simulation	Room temperature to −165°F at 5°F/h decrease followed by 5°F/h increase to −40°F, at which point change to 1°F/h increase

Figure 99 shows the potential, current rates, pressure, and temperature variations of the three batteries in sequence I with charge data at −40°F being shown in Fig. 100. Similar information for sequence II is provided in Figs. 101 and 102. At the completion of the lunar night survival test, the batteries were allowed to discharge continuously for 32 h at 2.0 A and subsequently for 4 min at 50.0 A. During the 50.0-A discharge, four 20.0-A, 20-ms pulses were superimposed in a RADVS simulation test to obtain a comparison with original flight acceptance (FA) test RADVS simulation data. Results of the RADVS simulation tests are summarized in Tables 64 and 65. The RADVS simulation consisted of discharging the battery at 50 (+15, −0) A for a minimum of 4 min with 4—20 ±2.0 A, 20-ms pulses superimposed at 1, 2, 3, and 4 min. The specified voltage at 50.0 A was 17.5 V minimum.

3. Discussion. In spite of considerable differences in battery history for sequence I, the capacity values at the start and end of the test varied only slightly between batteries. The cell potential spread prior to the lunar night test varied from 0.012 to 0.124 V and 0.086 to 0.124 V at the end of the test. Cell potential reversal occurred after approximately 108 A-h was removed from each battery and the temperature was approximately −31°F. Similar results were observed in test sequence II. Variations among batteries in potential, discharge current rate, pressure and temperature were small, while the charge current and pressure variations were somewhat larger. Potentials during RADVS simulation showed some degradation compared to values from FA test.

In test sequence II, battery open circuit potentials reached zero at approximately −147°F. The batteries were recharged successfully at −40°F at a programmed charge rate of 0.20–3.00 A with full recharge accomplished at room temperature. The batteries in test sequence II delivered from 82 to 93% of their pretest capacity when discharged at 0.23 A at 20°F.

4. Conclusions and recommendations. Test data determined the following:

(1) The batteries were capable of delivering a minimum of 155 A-h when discharged to 17.5 V at the 0.76-A rate, at 20°F.

(2) Discharge at a 0.23 A rate in a constantly dropping temperature environment ceased at about −33°F.

(3) The open circuit potential in a constantly dropping temperature environment fell to 0 V at about −147°F.

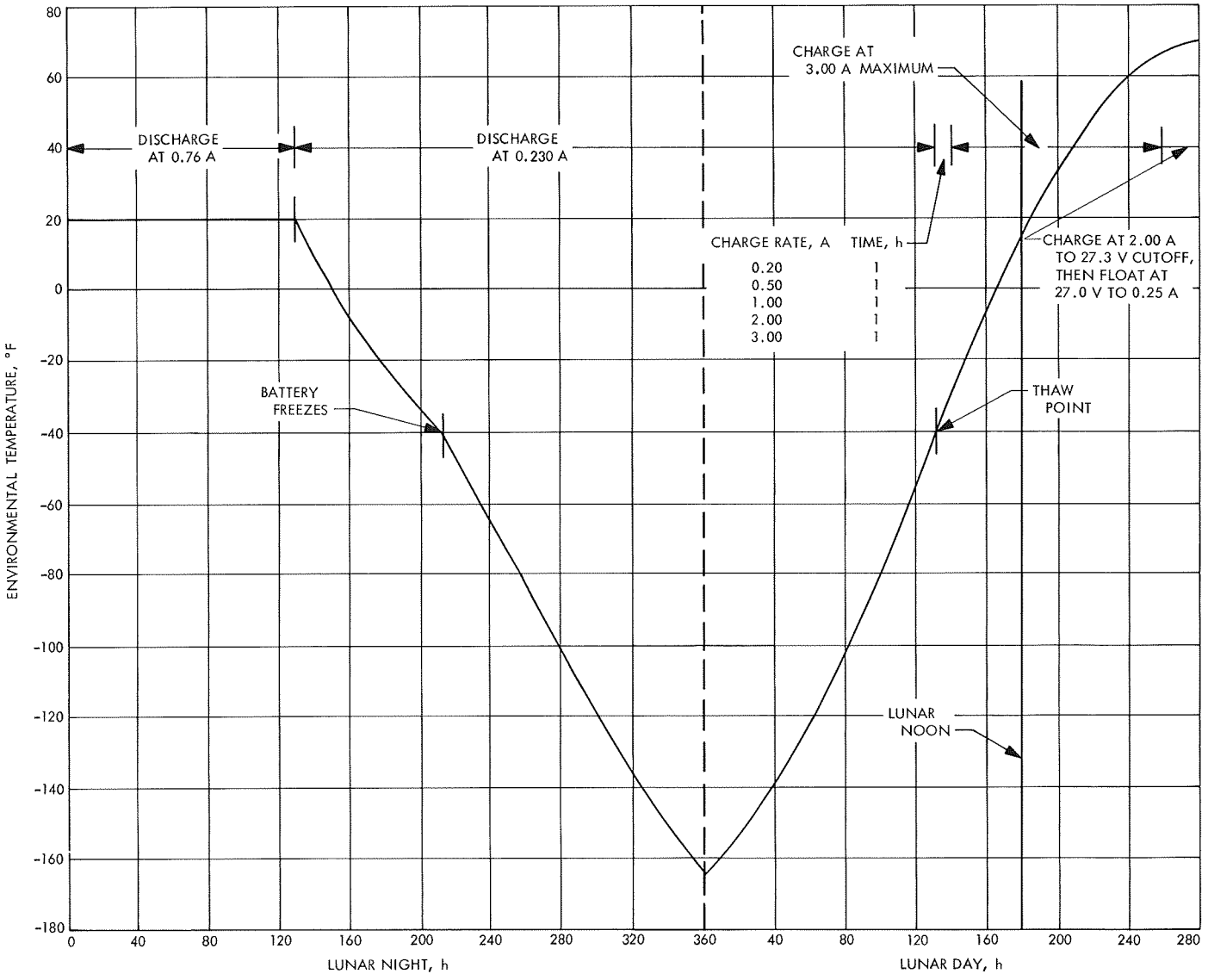

Fig. 97. Lunar night survival test, sequence I

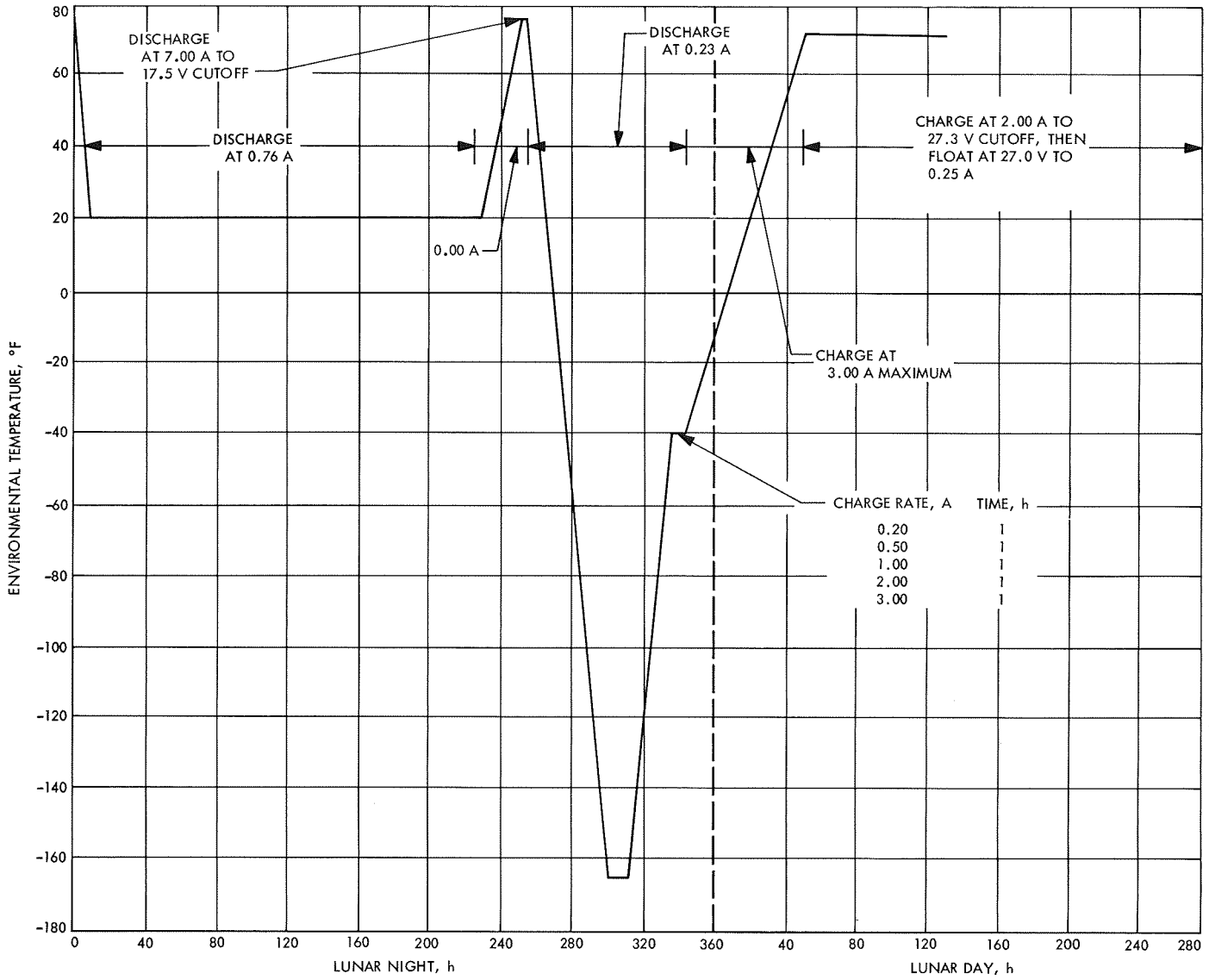

Fig. 98. Lunar night survival test, sequence II

Table 62. Battery history, lunar night survival test

Sequence I							
Battery SN	Previous usage	Age (days) of battery at		Total capacity, A-h			
		Start of test	End of test	At start of test	Removed from battery at ≅ −33°F point	Accepted at completion of test	End of lunar night test
115	Flight acceptance cold storage SC-6 MS/EMI recharge	107	132	173	109	108	172
119	Flight acceptance SC-5 combined system test discharge-charge	73	98	184	108	107	183
124	Flight acceptance cold storage float charge	56	81	188	109	100	179
Sequence II							
Battery SN	Previous usage	Age (days) of battery at		Total capacity, A-h			
		Start of test	End of test	At start of test	At 20°F, 0.75 A	At room temperature 7.0 A after 20°F discharge (approximate)	End of lunar night test
105	Flight acceptance cold storage	210	230	176	164	170	183
116	Flight acceptance	110	130	177	156	170	184
128	Flight acceptance SC-6 solar-thermal-vacuum[a]	80	100	188	155	169	179

[a]Placed on spacecraft, but was not used.

Table 63. Summary of battery parameters, lunar night survival test

Sequence I				
Battery SN	Final battery voltage after 2100 Wh discharge, V	Temperature at which first cell reversal occurred (under 0.230 A), °F	Capacity removed at time of cell reversal, A-h	Temperature when battery dropped below 0.230 A, °F
115	21.25	−29	109	−32
119	21.07	−33	108	−33
124	21.12	−31	110	−33
Battery SN	**Time[a] when battery no longer supported 0.230 A load, h**	**Temperature when battery voltage reached 0 under 0.230 A load, °F**	**Cell voltage difference at end of original FA[b] test, V**	**Cell voltage difference at end of test, V**
115	186	−33	0.012	0.116
119	181	−33	0.017	0.086
124	184	−34	0.124	0.124
Sequence II				
Battery SN	**Time battery operated at 0.750 A and 20°F, h**	**Temperature when battery voltage reached 0 (under open-circuit condition), °F**	**Cell voltage difference at end of original FA test, V**	**Cell voltage difference at end of test, V**
105	237.2	−148	0.021	0.077
116	222.7	−148	0.009	0.077
128	219.0	−147	0.124	0.077

[a]Time from start of test.
[b]Flight acceptance.

(4) After warmup to −40°F, the batteries were successfully charged at a programmed rate of 0.20–3.0 A over a 5-h period, followed by constant potential charging during warmup from −40°F to room temperature.

(5) After full recharge, the batteries passed the RADVS simulation test, although minimum potentials were lower than similar prelunar night simulation RADVS results.

(6) The performance of the six batteries is grouped about a small distribution in potential, capacity, charge and discharge current, and pressure.

(7) The lunar night survival test led to the recommendations that the battery should be fully charged going into the lunar night and that complete depletion of the battery during the lunar night should be avoided. At the spacecraft basic load of 0.23 A, the battery zero power point was approximately −33°F. Thermal conditioning of the battery was not required since the low temperature tests confirmed battery survival during lunar night conditions.

B. Low Temperature Operation

Following the successful reawakening of *Surveyor I* through several lunar days, further studies were undertaken to obtain low temperature operating information on an almost fully discharged battery, simulating the end of lunar night conditions.

1. Test procedure. The test procedure involved:

(1) Discharging the fully charged battery at the 2.0-A rate to the cutoff potential (17.5 V), while the battery temperature was reduced at the rate of approximately 5°F/h.

(2) Continuing the cooldown to a battery temperature of −40°F.

(3) Discharging the battery at 1.0 A for 60 s, then stabilizing the battery temperature at −40°F.

(4) Pulse charging the battery with 60-s pulses at 0.5, 1.0, 2.0 and 3.0 A at −40°F.

(5) Performing (4) at −20°F.

(6) Performing (4) at 0°F.

(7) Charging the battery at 0°F with a constant current of 1.5 A to 27.3-V cutoff.

(8) Float-charging the battery at 0°F for 13.5 h.

(9) Discharging the battery at 0°F with 60-s pulses of 0.5, 2.0, 7.0, and 12.0 A and with 60 s of TV simulation pulses (3.2 A for 1.6 s) and 20 simulated antenna/solar panel positioner (A/SPP) pulses (12 A for 50 ms).

(10) Repeating (9) at −20°F.

(11) Repeating (9) at −40°F.

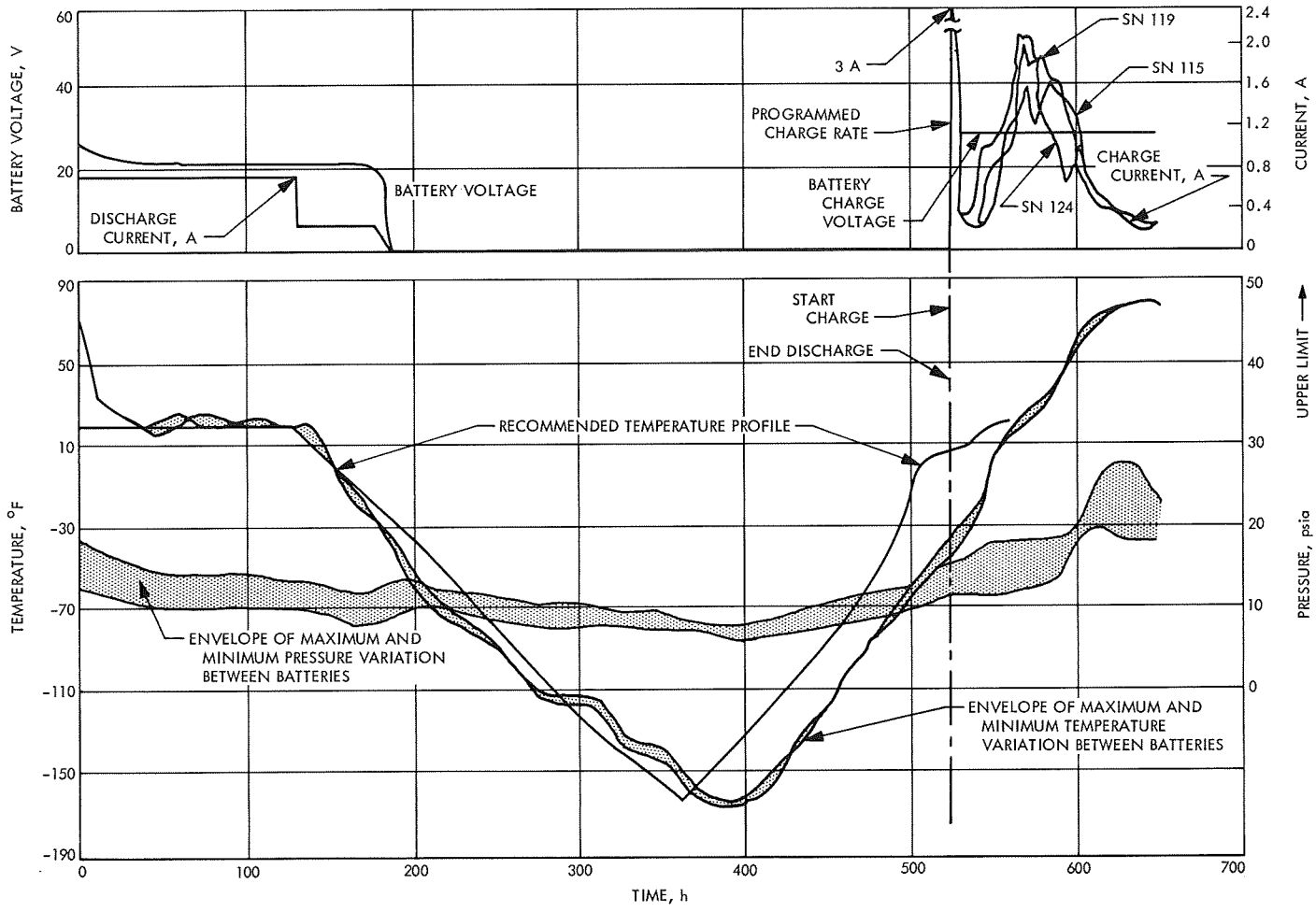

Fig. 99. Lunar night survival test, sequence I, on *Surveyor* main batteries 115, 119, and 124

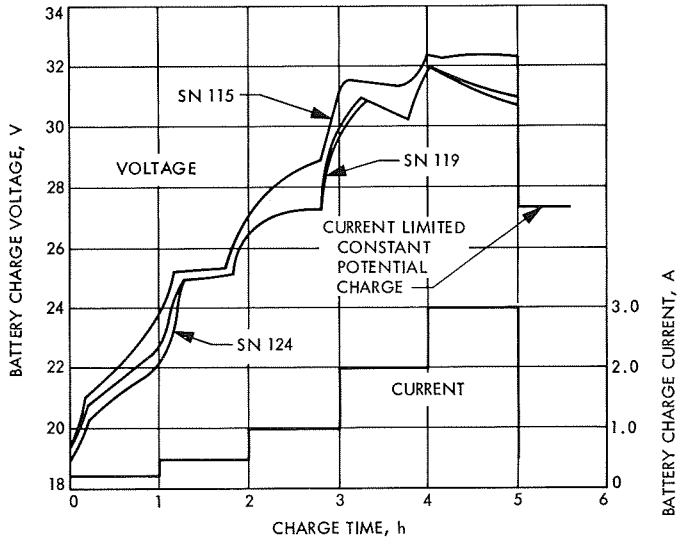

Fig. 100. Voltage rise during programmed charge at −40°F lunar night survival test sequence I, *Surveyor* main batteries 115, 119, and 124

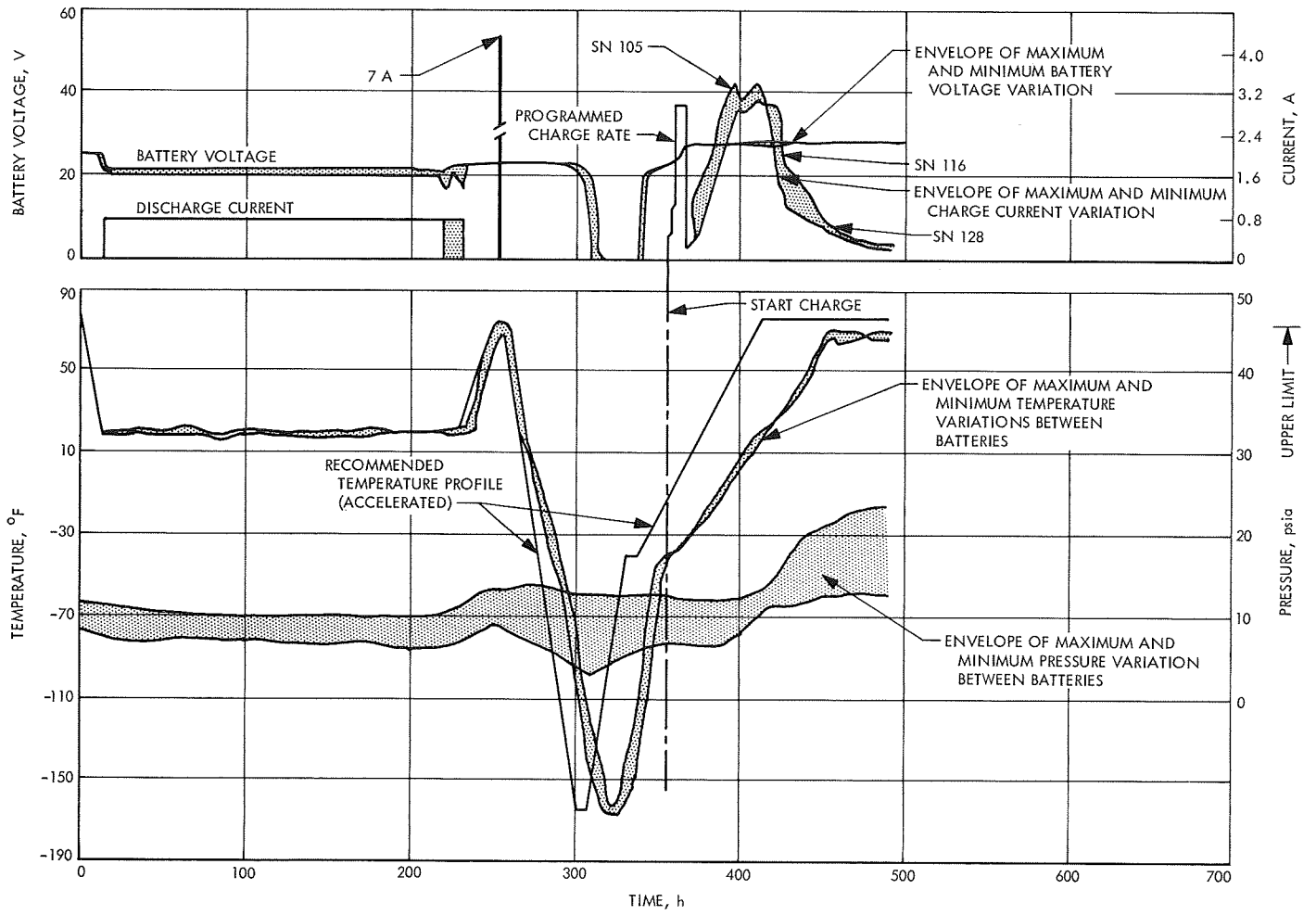

Fig. 101. Lunar night survival test sequence II, *Surveyor V* main batteries 105, 116, and 119

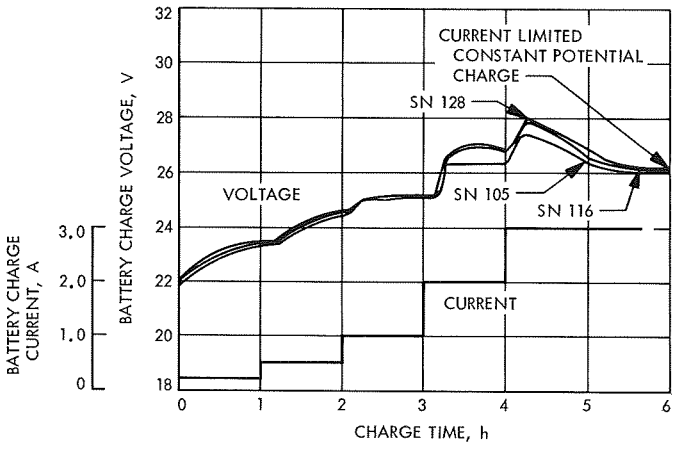

Fig. 102. Voltage rise during programmed charge at 40°F, lunar night survival test sequence II, *Surveyor* main batteries 105, 116, and 128

Table 64. Sequence I, RADVS simulation

	Battery SN					
	115		119		124	
Test date	5/2/67	8/18/67[a]	6/6/67	8/18/67	6/9/67	8/18/67
Battery age, days	35	146	39	112	25	105
Ampere hours removed	65.60	65.24	69.50	64.10	57.60	64.30
Battery temperature at start of test, °F	79	77	78	77	77	78
Battery temperature at end of test, °F	79	78	76	78	78	79
Voltage, V						
Open circuit	22.31	22.30	22.10	22.30	22.25	22.30
Start, 50 A[b]	19.91	19.80	20.10	19.80	20.2	20.00
At 1 min, 50 A	19.25	18.70	20.00	18.95	19.67	19.20
Pulse 1, 70 A	18.35	17.90	19.20	18.00	18.85	18.35
At 2 min, 50 A	19.19	18.79	19.80	18.90	19.45	19.14
Pulse 2, 70 A	18.31	17.75	19.00	17.95	18.65	18.30
At 3 min, 50 A	19.16	18.75	19.60	18.85	19.35	19.10
Pulse 3, 70 A	18.29	17.80	18.80	17.90	18.55	18.20
At 4 min, 50 A	19.14	18.70	19.50	18.84	19.30	19.09
Pulse 4, 70 A	18.28	17.80	18.65	17.90	18.50	18.28

[a]Post lunar night survival test data.

[b]Current 51.6 A for battery SN 115 first FA test.

Table 65. Sequence II, RADVS simulation

	Battery SN					
	105		116		128[a]	
Test date	3/5/67	8/30/67[b]	6/6/67	8/30/67	7/12/67	8/30/67
Battery age, days	57	234	46	130	47	97
Ampere hours removed	64.00	58.70	64.00	65.27	65.00	64.48
Battery temperature at start of test, °F	76	75	75	75	75	75
Battery temperature at end of test, °F	76	76	76	76	77	77
Voltage, V						
Open circuit	22.00	22.35	22.50	22.20	22.42	22.30
Start, 50 A	19.80	20.00	20.05	19.90	20.00	20.00
At 1 min, 50 A	19.20	19.15	19.80	18.80	19.61	19.30
Pulse 1, 70 A	18.40	18.25	19.00	17.90	18.80	18.45
At 2 min, 50 A	19.10	19.05	19.60	18.70	19.40	19.25
Pulse 2, 70 A	18.30	18.30	18.80	17.80	18.60	18.40
At 3 min, 50 A	19.00	19.00	19.45	18.60	19.20	19.20
Pulse 3, 70 A	18.30	18.30	18.65	17.90	18.40	18.40
At 4 min, 50 A	19.00	19.00	19.30	18.60	19.08	19.20
Pulse 4, 70 A	18.30	18.20	18.50	17.75	18.21	18.40

[a]Post lunar night survival test was conducted with a fractured cell case and subsequent loss of electrolyte.

[b]Post lunar night survival test date.

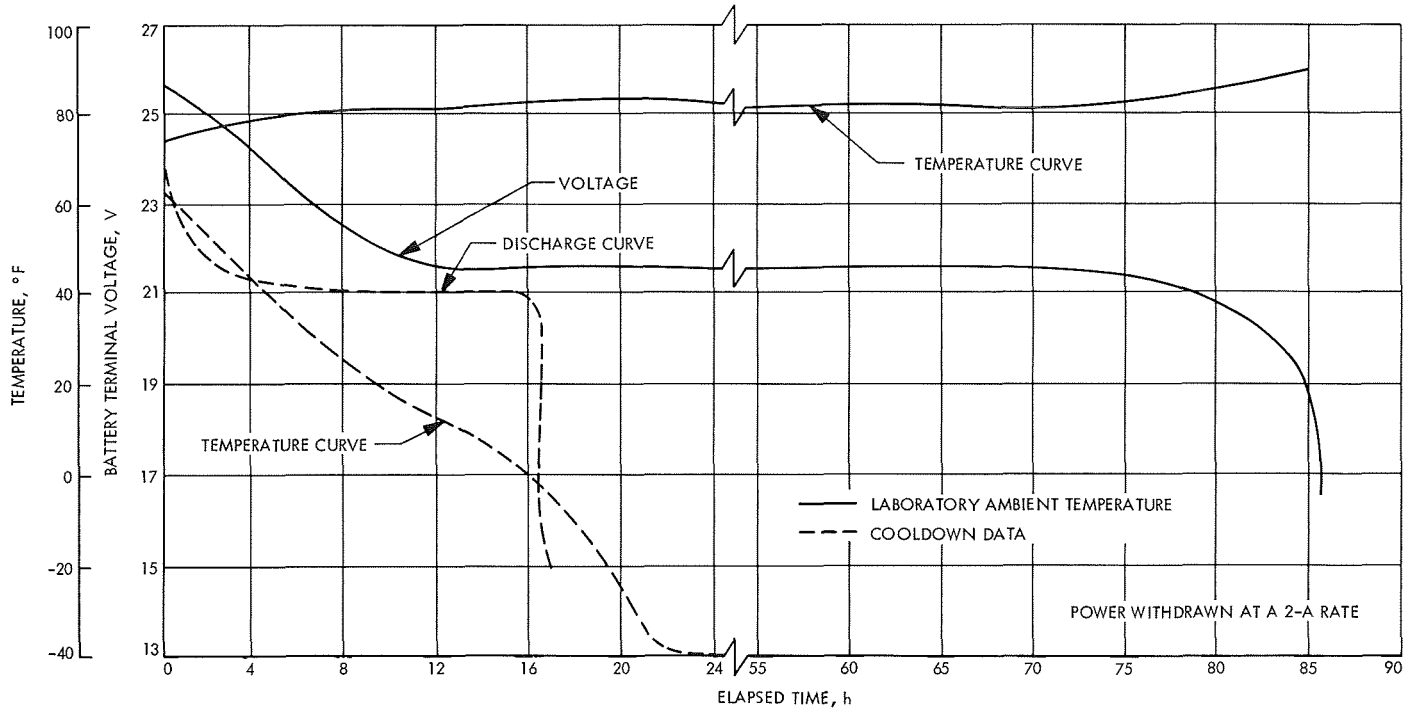

Fig. 103. Comparison of battery discharged at room temperature and voltage discharge characteristics of battery 99 at temperature reduced to −40°F at 5°F per hour

2. *Results.* Battery discharge data for this test and for a similar battery, discharged under normal temperature environment, are shown in Fig. 103. At the 2.0-A discharge rate, 42.5 A-h were withdrawn, at which time the battery potential reached 15.0 V and the battery temperature 4°F. Discharging the battery at 1.0 A and −40°F resulted in several cell reversals, as indicated by data in Table 66 and the discharge was terminated. Results from the pulse charging (steps 4, 5, and 6) are summarized in Figs. 104–107. Constant current and float charging at 0°F (steps 7 and 8) provided an input of 13.0 A-h, where the float charge contributed 5.25 A-h. Initial and final (60 s) discharge potentials for steps 9, 10, and 11 are plotted in Figs. 108 and 109. Figure 110 superimposes the discharge data on an earlier potential–current curve to permit a comparison with results from higher temperature runs. A rough approximation of dc impedance values for low temperature operation on the lower plateau was made by assuming a linear relationship between potential and current and the results are tabulated in Table 67.

Table 66. Cell potentials during −40°F, 1.0 A discharge

Cell No.	Cell potential, V			
	0 min	2 min	3 min	4 min
1	1.18	0.9	0.2	0.05
2	1.30	1.21		
3	1.32	1.24		
4	1.31	1.23		
5	1.28	1.20		
6	1.26	1.17		
7	1.09	0.07	−0.5	−2.0
8	1.19	1.13		
9	1.29	1.25		
10	1.31	1.25		
11	1.30	1.27		
12	1.30	1.27		
13	1.26	1.21		
14	1.17	1.04		

3. *Conclusions.* A withdrawal of 42.5 A-h at the 2.0-A rate to cutoff potential compared to a range of 45–97 A-h, predicted on the basis of earlier tests (Fig. 111) for discharge at 0°F. No excessive pressure buildup was observed during the low temperature operation test. During low temperature charging, the battery terminal potential was found to vary directly with charging current and

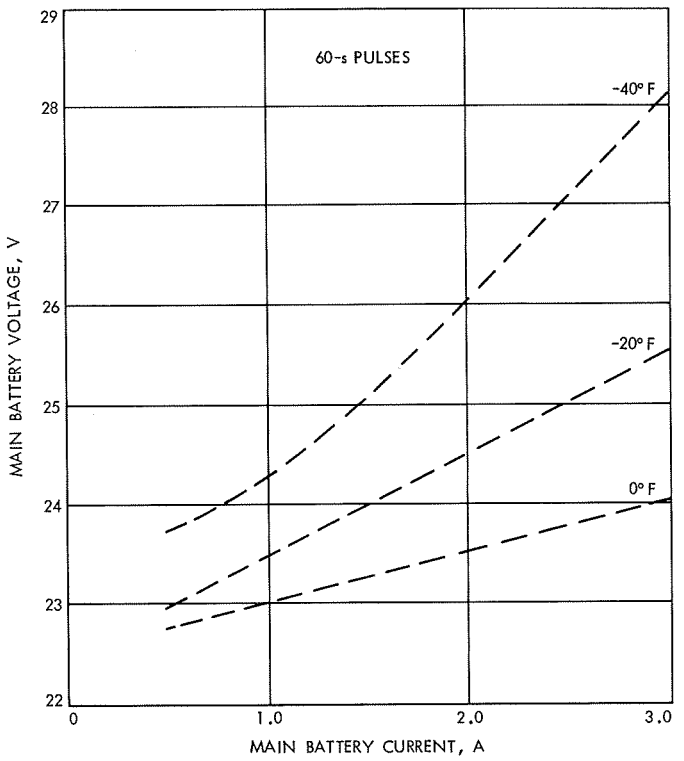

Fig. 104. Low temperature, fully discharged, initial charge voltage

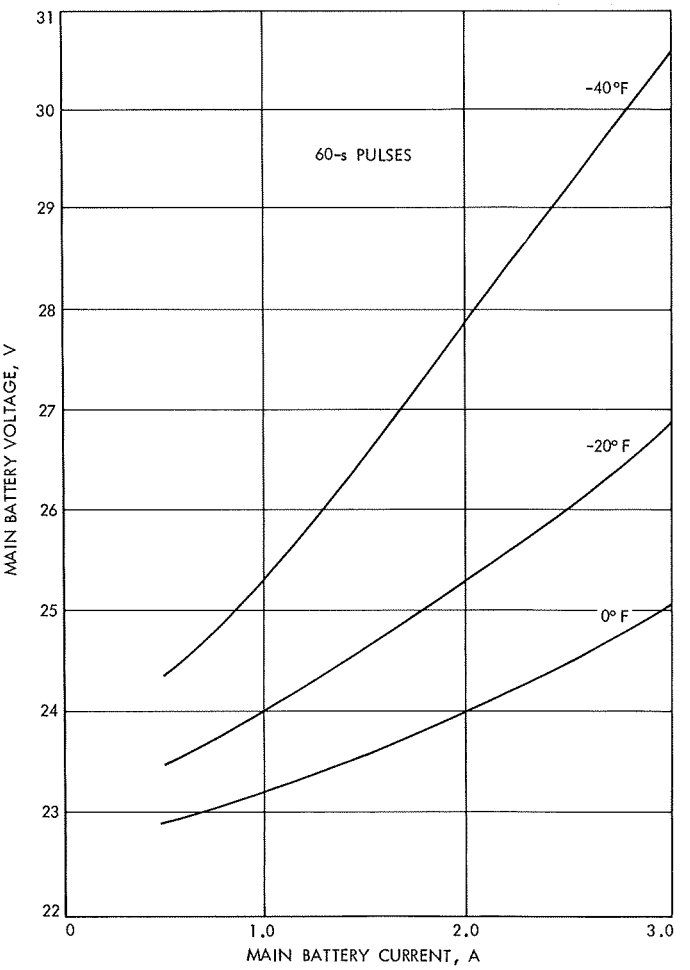

Fig. 105. Battery 99 low temperature charge, fully discharged, charge voltage after 60 s

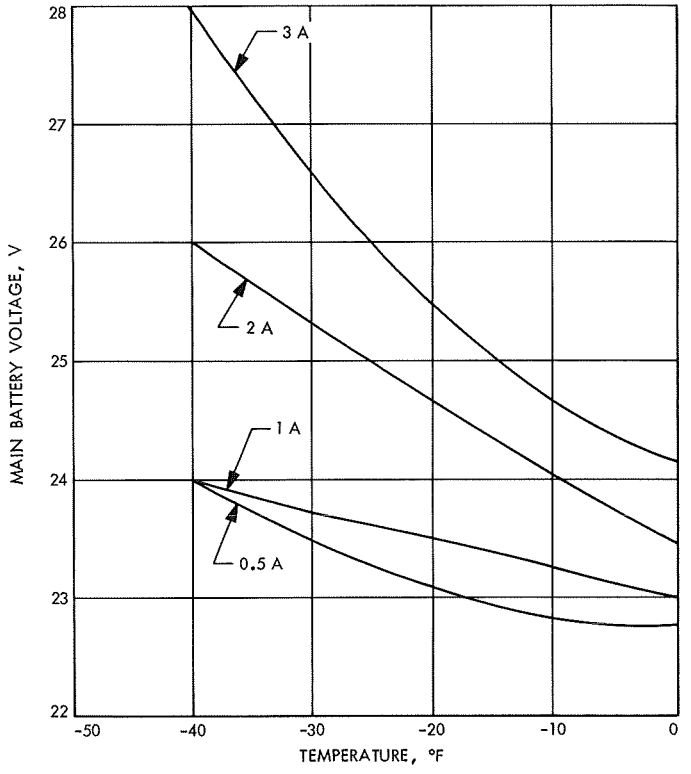

Fig. 106. Low temperature charge, fully discharged, initial charge voltage

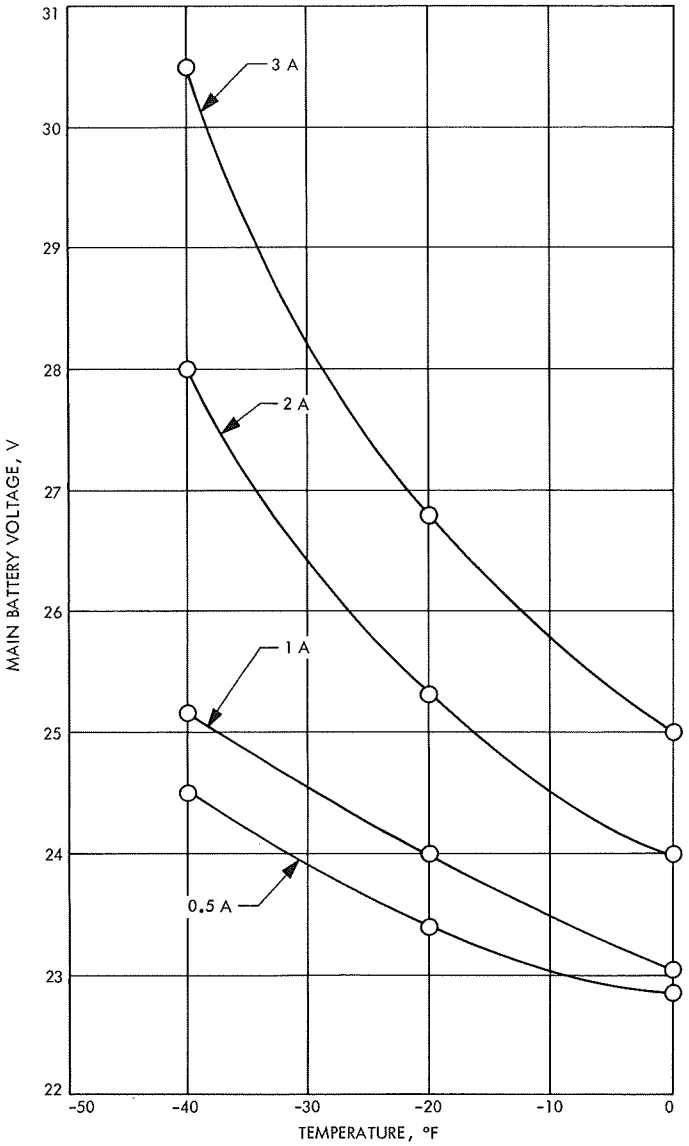

Fig. 107. Low temperature charge, fully discharged, charge voltage after 60 s

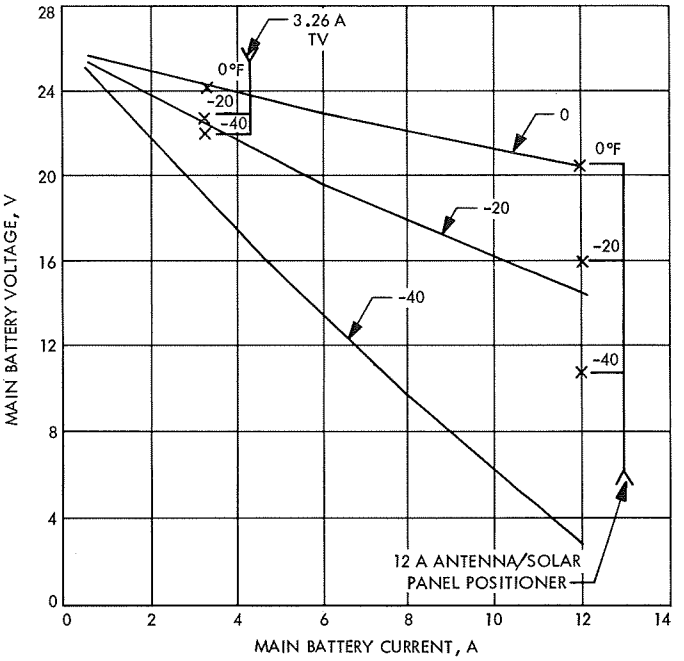

Fig. 108. Battery 99 low temperature discharge, low state of charge, initial discharge voltage

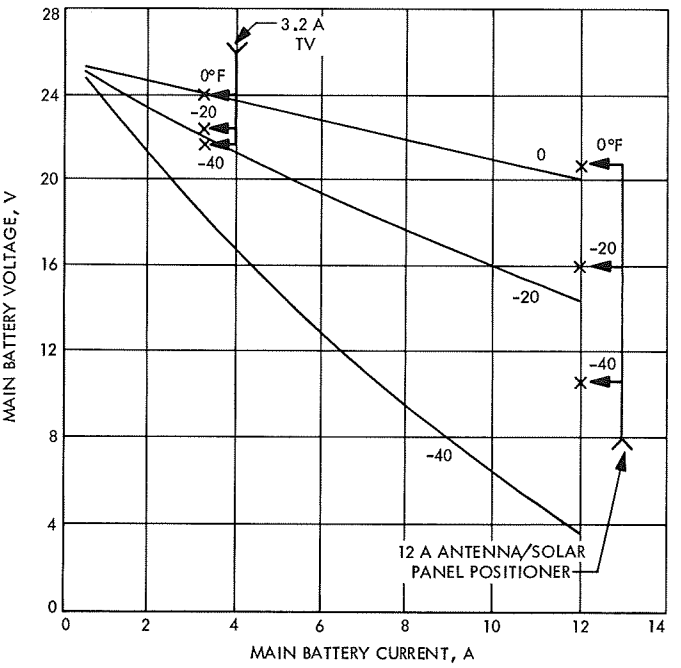

Fig. 109. Battery 99 low temperature discharge, low state of charge, discharge voltage after 60 s

inversely with battery temperature. During low temperature discharge, the battery terminal potential varied inversely with current and temperature and short pulse potentials were slightly higher than 60-s pulse potentials. The *Surveyor* battery has shown a limited capability to operate at temperatures below 0°F with some operation at −40°F indicated.

C. The A-21E Program

The decision to delete the auxiliary battery for SC-5, SC-6 and SC-7 was discussed in Section VI. The early tests indicated that the main battery was capable of providing pulse loads during terminal descent. However, removal of the auxiliary battery caused the main battery to run at a higher temperature and with lower potential during terminal descent. The reliability of the spacecraft

Table 67. Approximate dc impedance values

Temperature, °F	Discharge, Ω	Charge, Ω
0	0.46	0.5
−20	0.9	1.0
−40	1.8	2.4

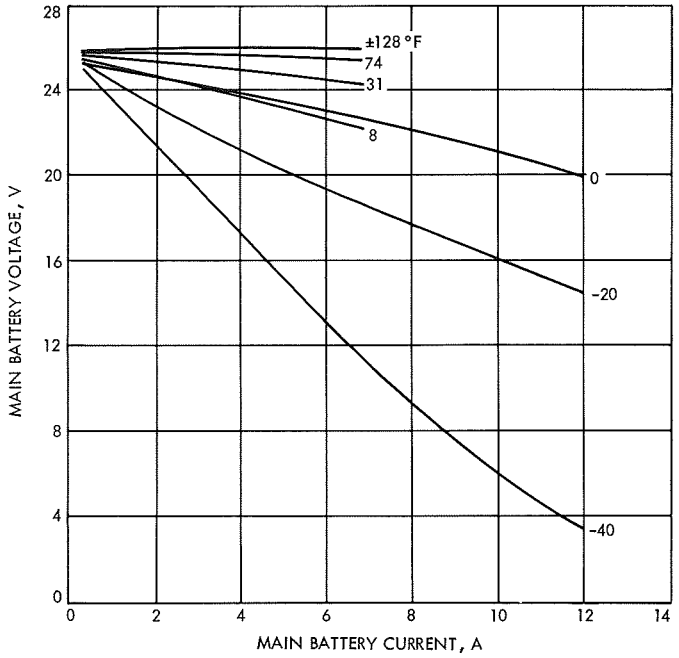

Fig. 110. Main battery voltage vs discharge current at various battery temperatures

would be reduced during transit by the elimination of the redundant energy sources. Therefore, a program was undertaken to: (1) determine the thermal behavior of the battery, (2) perform a test to establish *Surveyor* main battery parameters during a typical *Surveyor V, VI* and *VII* Mission operation, and (3) institute increased process control at ESB as a means of increasing the battery reliability.

1. Thermal behavior of the battery (Ref. 3). The heat generation rate is given as a function of cell potential and current by the relation

$$q = I(E_H - E_I) \tag{1}$$

where

q = heat output rate

I = current in amperes

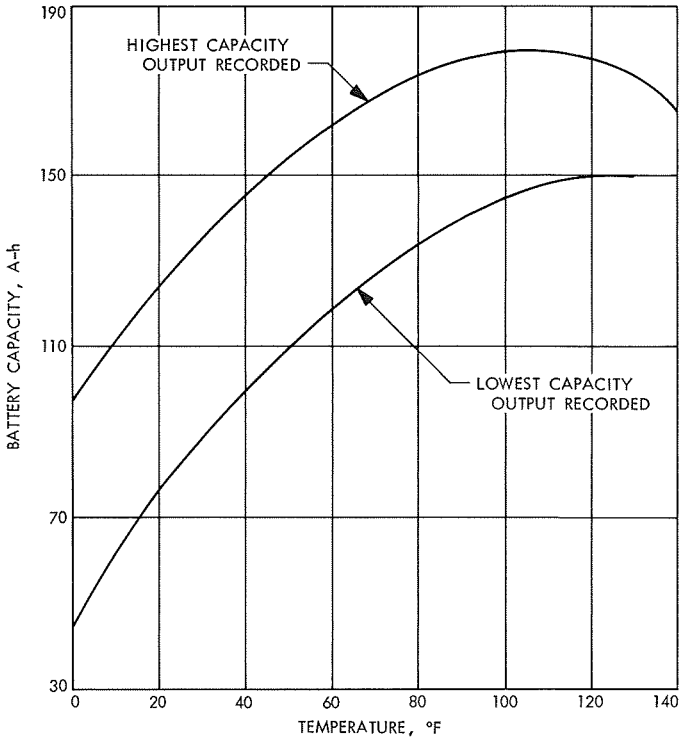

Fig. 111. Battery capacity vs temperature at discharge rates of 0.5–10.0 A

E = cell potential with I amperes flowing

E_H = the thermal potential

$$-E_H = \frac{\Delta H}{nF} \tag{2}$$

where

ΔH = heat of formation

n = the number of electrons in the electrode reaction

F = the value of the Faraday.

Internal heat generation patterns were investigated by means of batteries, equipped with internal thermocouples. Heat dissipation rates from the battery surface were measured with a specially constructed isothermal calorimeter. Both investigations will be treated in subsequent sections of this report.

a. Determination of internal heat generation patterns. Two *Surveyor* main batteries (SN 97 and SN 98) were specially fabricated with a total of ten copper-constantan

thermocouples, located at strategic positions, to permit the recording of negative plate and periphery temperature variations as a function of time while the batteries experienced a special test sequence. Four thermocouples were installed in the negative plate of cells 3, 6, 9 and 12. Six thermocouples measured the peripheral temperature pattern by virtue of their placement between the outer cell walls and the battery canister. A diagram of thermocouple locations is shown in Figs. 112 and 113.

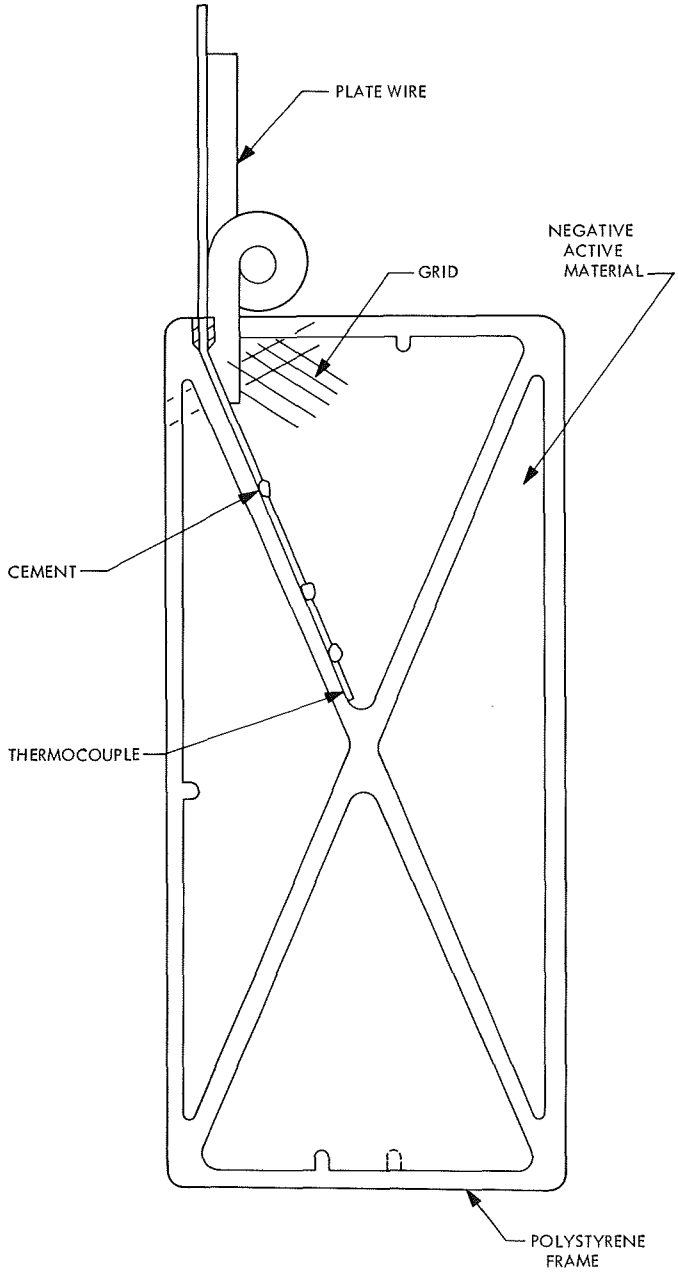

Fig. 112. Negative plate assembly

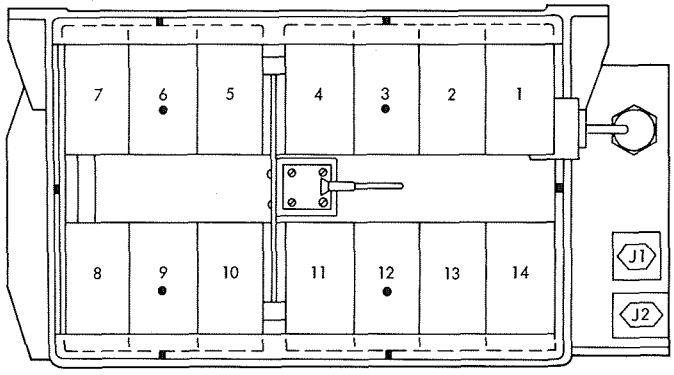

Fig. 113. Location of thermocouples

Test procedure. The sequence in these thermal tests is summarized in Tables 68 and 69. The steps in the test sequences were generally separated by open-circuit

Table 68. Test sequence, SN 97

Step No.	Step description
1	Top charge at 2.0 A
2	Discharge at 1.0 A
2A	Simulate RADVS with approximately 100 A-h remaining
3	Place on open circuit
4	Charge at 2.0 A and float
5	Discharge at 3.0 A and repeat step 2A
6	Place on open circuit
7	Charge at 2.5 A
8	Discharge at 5.0 A and repeat step 2A
9	Discharge at 5.0 A to 17.5 V
10	Charge at 2.0 A

Table 69. Test sequence, SN 98

Step No.	Step description
1	Top charge at 2.0 A
2	Discharge at 2.0 A
2A	Simulate RADVS with approximately 100 A-h remaining
2A′	Extended 2A
3	Place on open circuit
4	Charge at 1.0 A and float
5	Discharge at 4.0 A and repeat Step 2A
6	Discharge at 4.0 A to 17.5 V
7	Charge at 1.5 A
8	Discharge at 5.0 A and repeat Step 2A
9	Discharge at 5.0 A to 17.5 V
10	Charge at 2.0 A

periods. In principle, the thermal tests consisted of a number of room temperature charge–discharge cycles, representing average spacecraft loads from 1.0 to 5.0 A and high discharge rates of 18.0 A for five or more minutes, followed by RADVS simulation (50.0-A discharge with two 20 ms, 20.0-A pulses superimposed on the 50.0-A current).

Results. The data for SN 97 are summarized in Fig. 114, which represents average thermocouple readings for the complete program. In Figs. 114–122, steps in the test sequence (see Tables 68 and 69) are indicated by numbers. Figures 116, 117, and 118 include individual thermocouple readings that are then averaged to provide mean thermocouple temperatures, as well as battery transducer measurements. Similarly, Fig. 115 represents average data for the complete program for SN 98, while Figs. 119, 121, and 122 provide individual thermocouple data and battery transducer measurements. A cool-down test for SN 98 was conducted during step 3 (open circuit), following discharge at 50 A. The temperature data are plotted in Fig. 120.

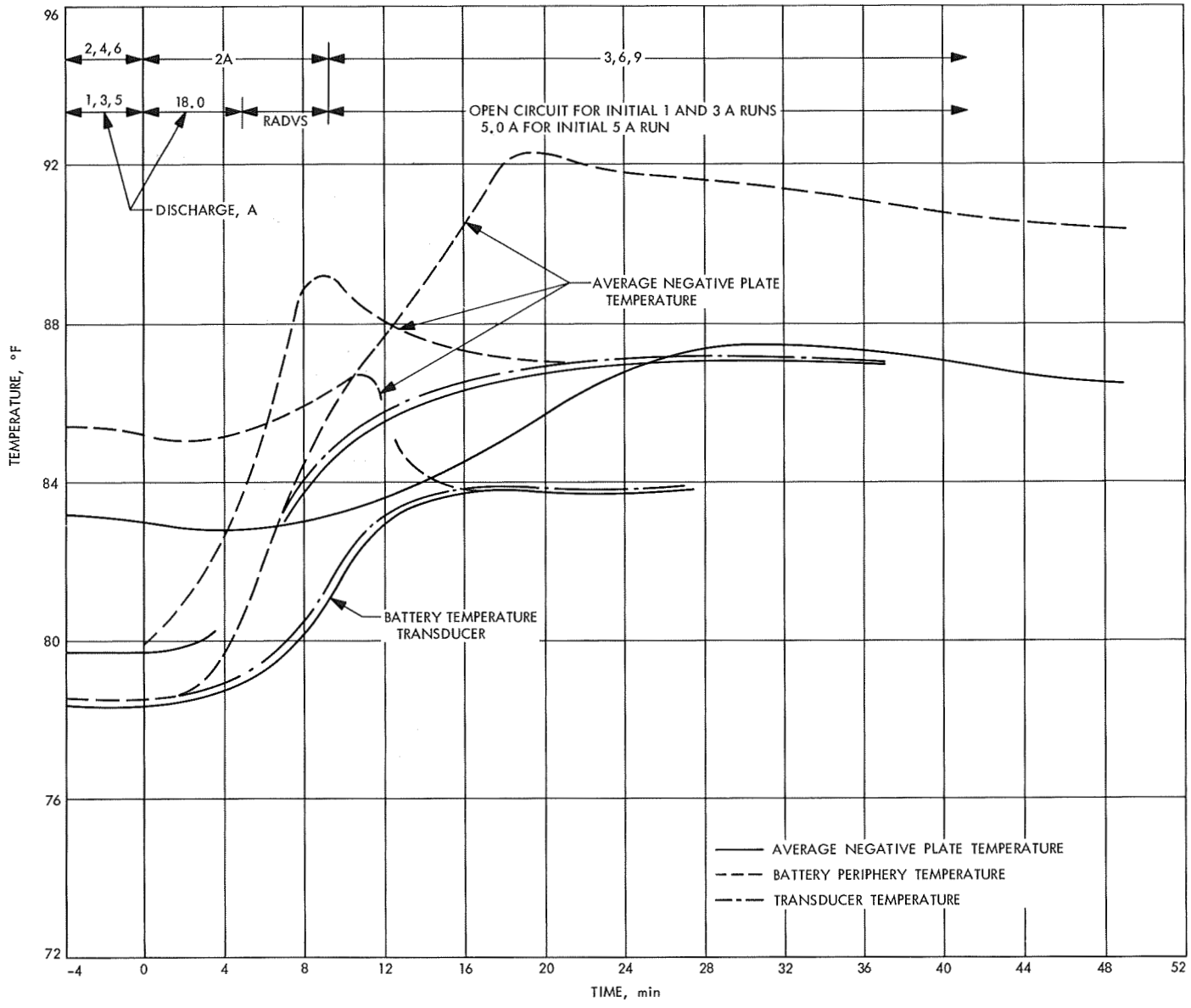

Fig. 114. Thermal test, Surveyor main battery 97, summary of temperature–time data

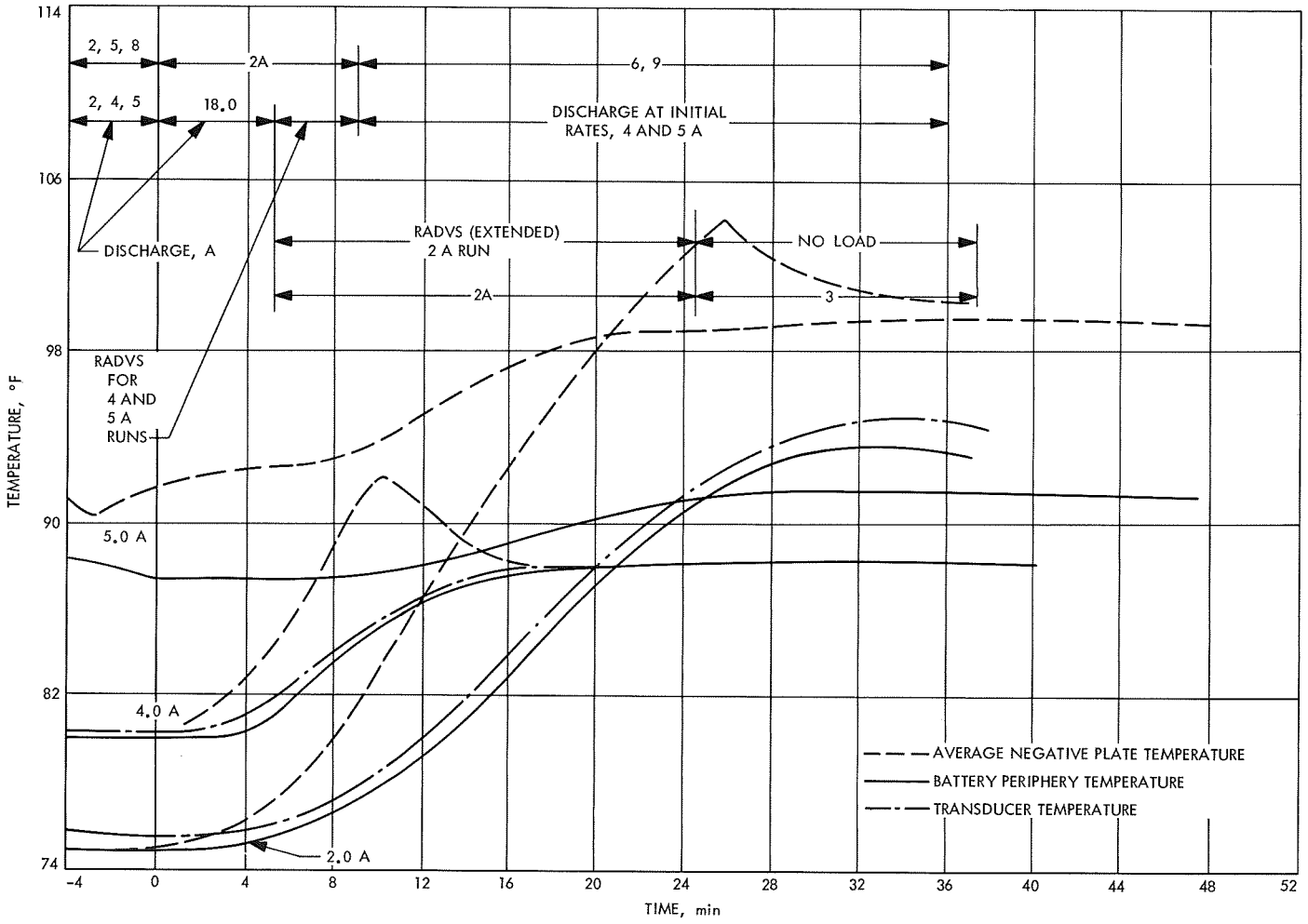

Fig. 115. Thermal test, *Surveyor* main battery 98, summary of temperature—time data

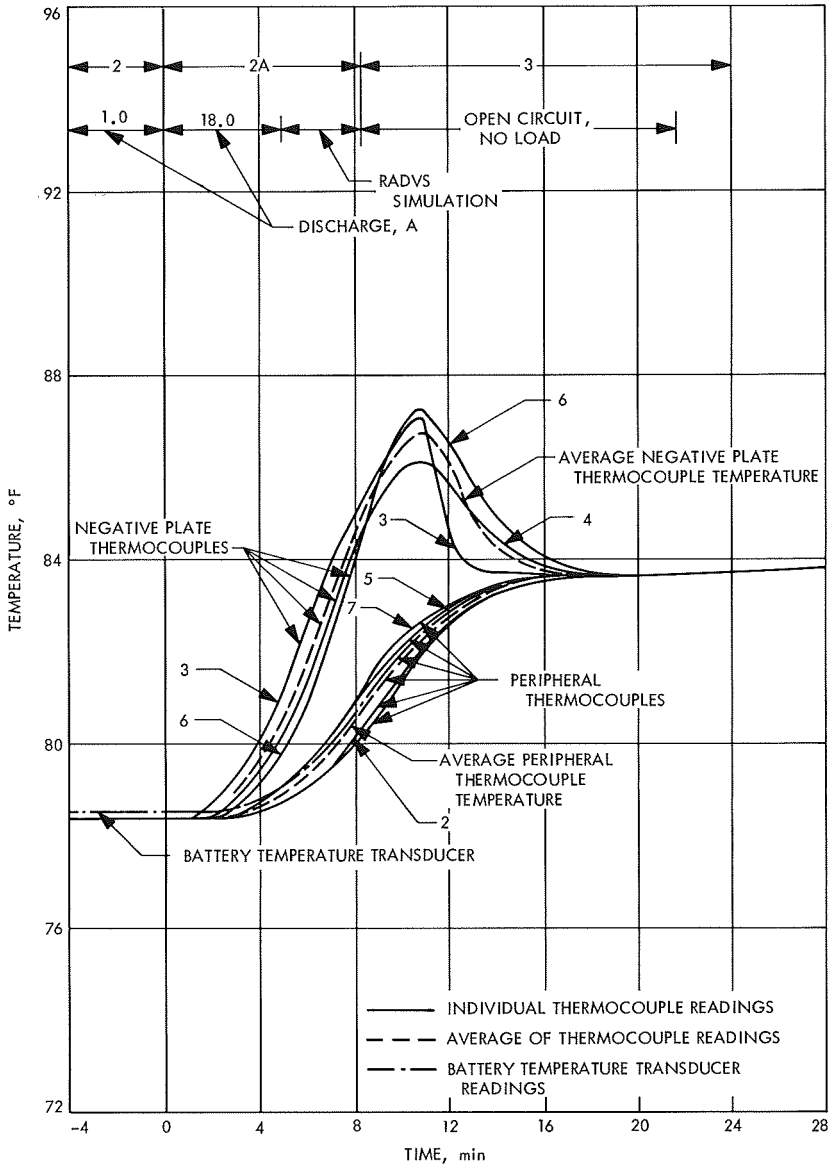

Fig. 116. Thermal test, *Surveyor* main battery 97, 1-A run

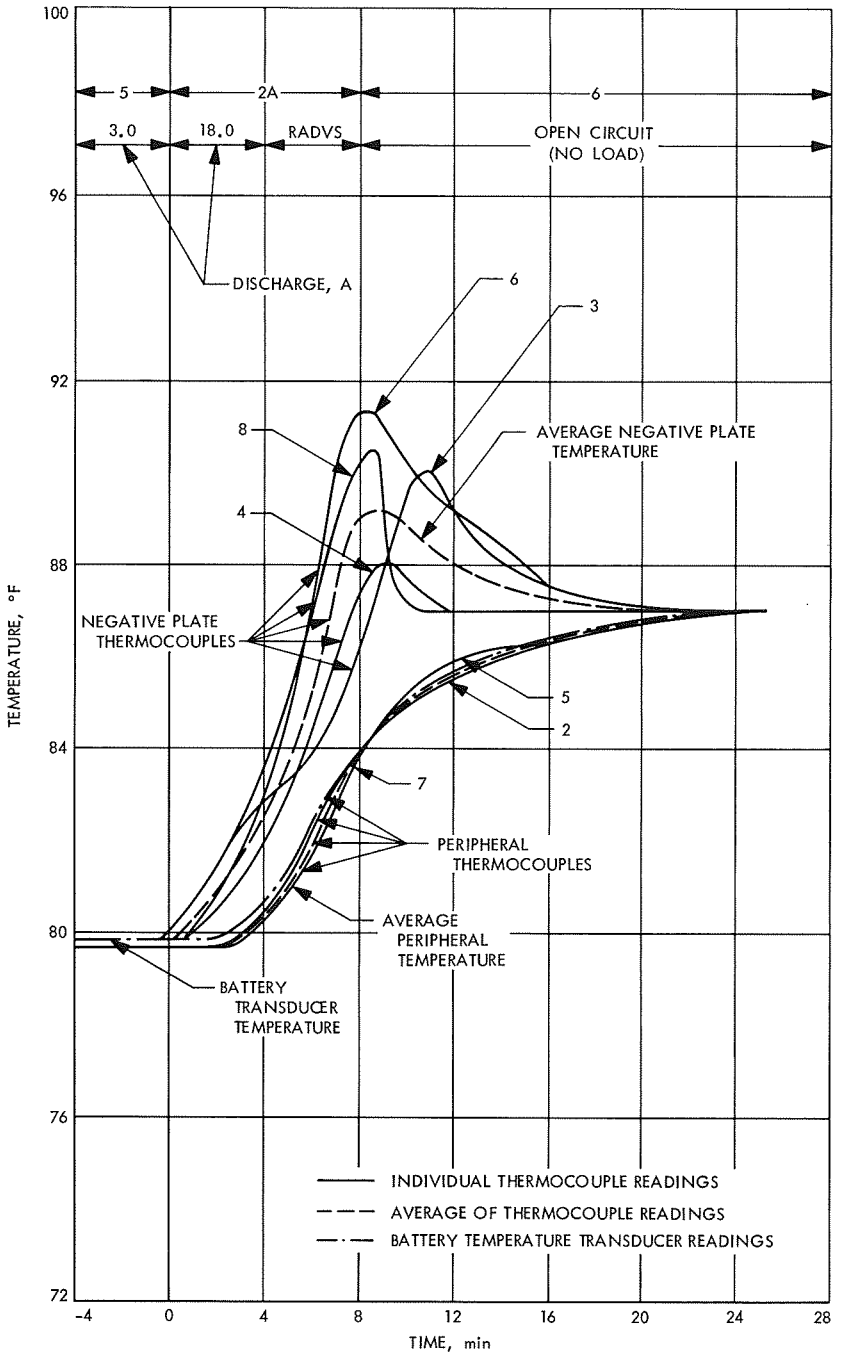

Fig. 117. Thermal test, *Surveyor* main battery 97, 3-A run

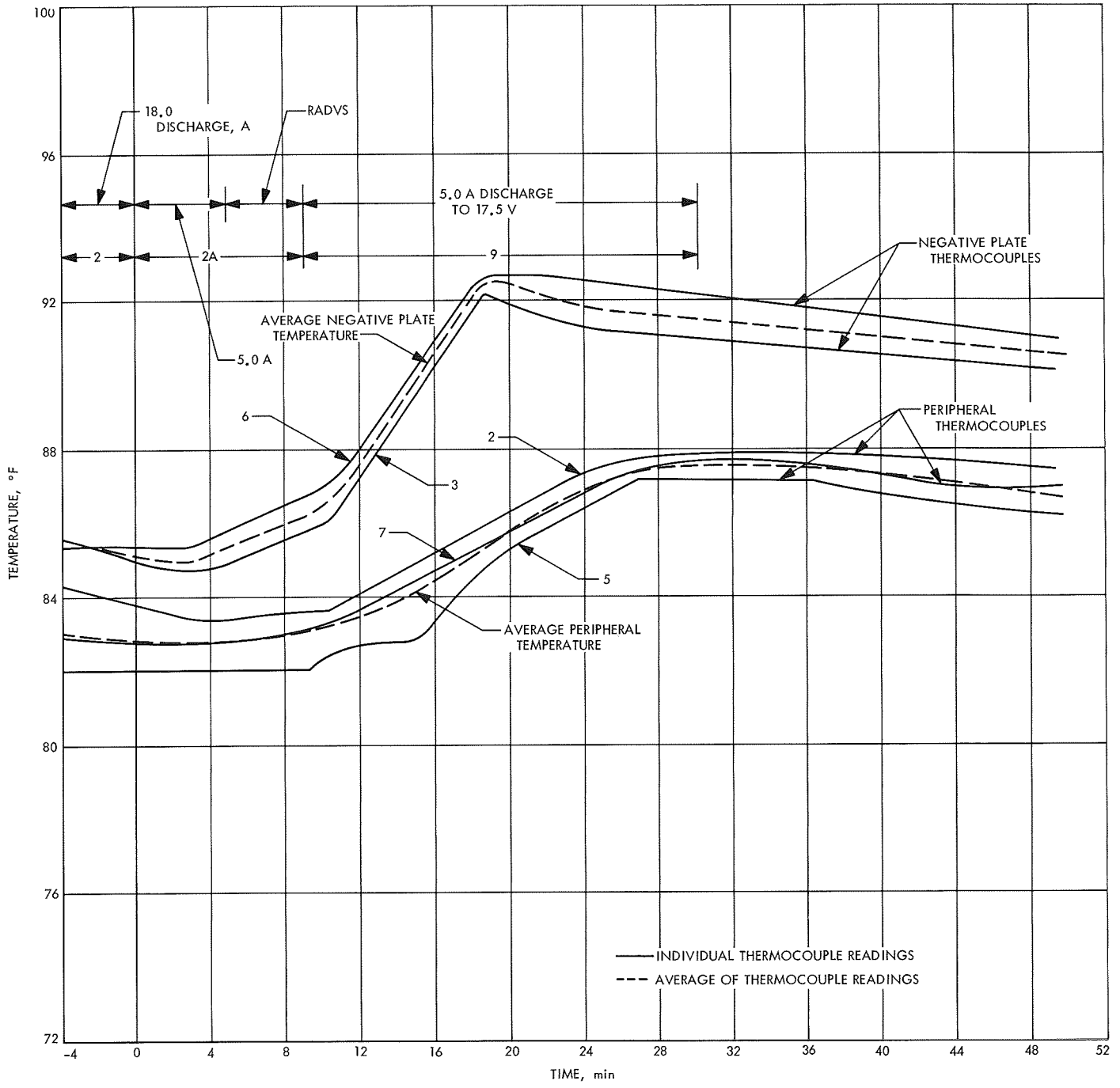

Fig. 118. Thermal test, *Surveyor* main battery 97, 5-A run

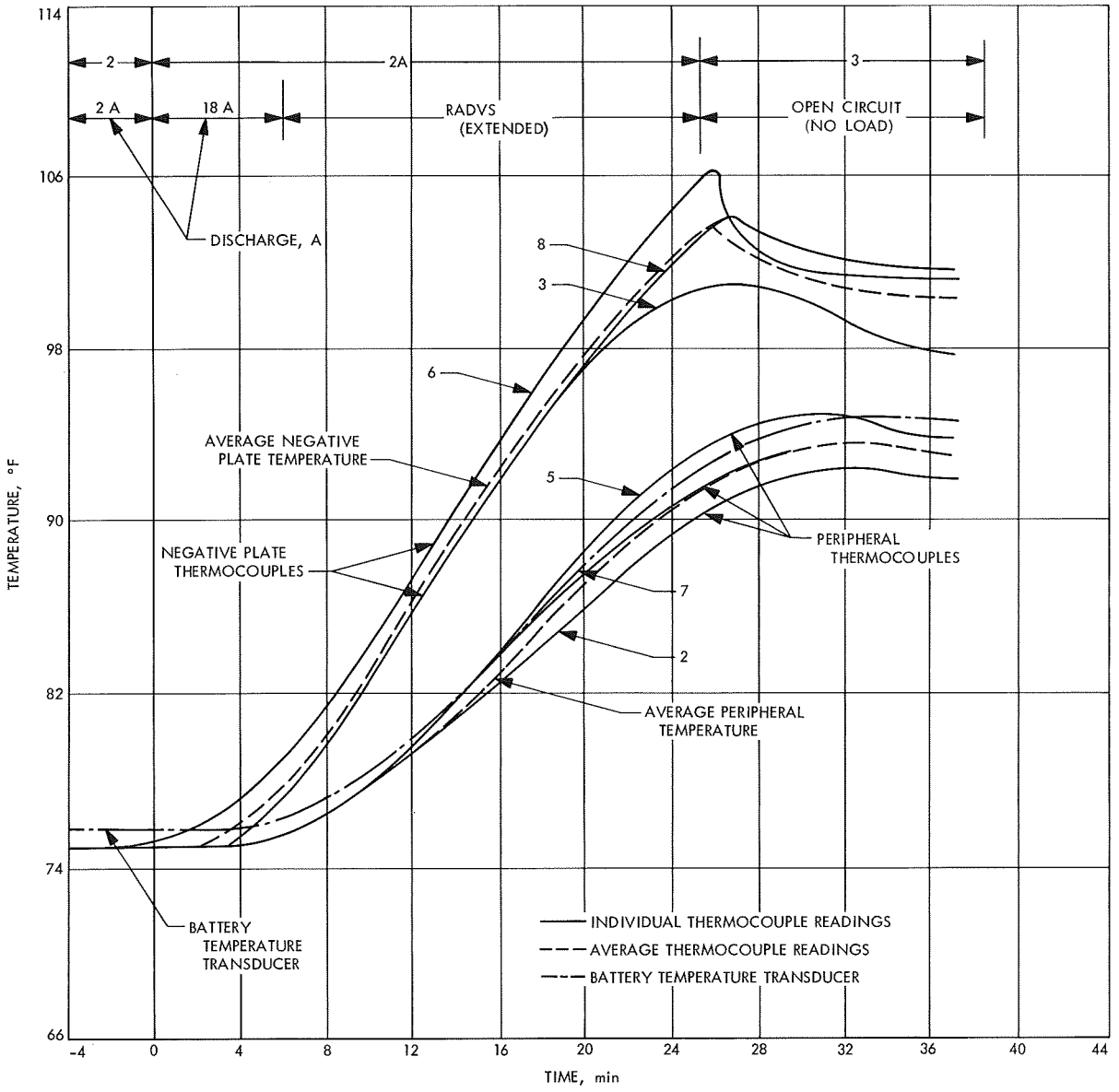

Fig. 119. Thermal test, *Surveyor* main battery 98, 2-A run

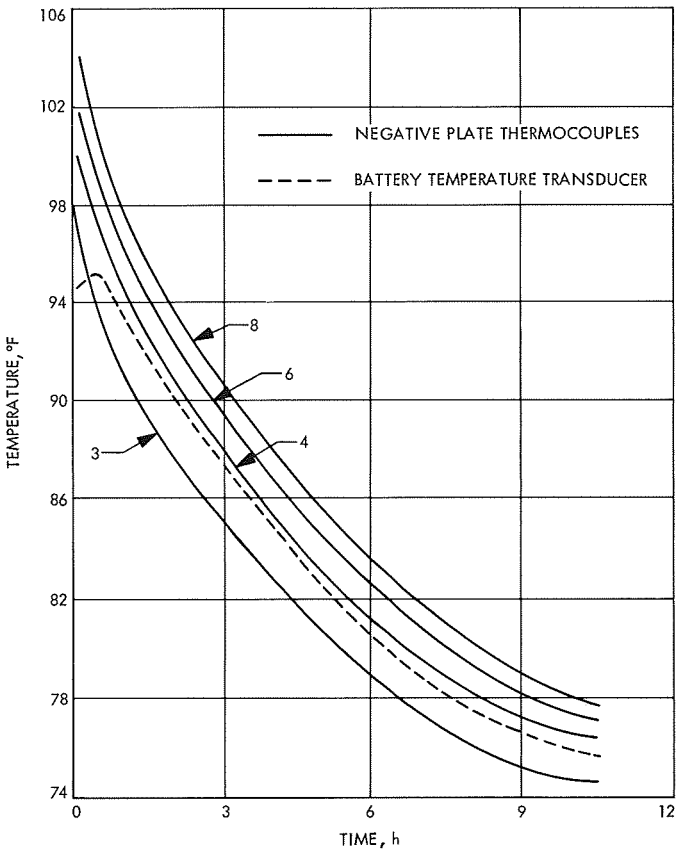

Fig. 120. Thermal test, *Surveyor* main battery 98, open circuit room temperature cooldown

The 5.0-A discharge curves for both batteries did not behave in a manner anticipated from analysis of the lower current data. However, cell temperatures were not excessive. Battery capacity information is presented in Table 70.

The following is a list of significant findings from the tests:

(1) Both batteries performed within the established temperature limits of 115°F.

(2) The battery temperature transducer data followed the peripheral temperature data quite closely.

(3) Negative plate temperatures were as much as 12°F higher than peripheral and transducer temperatures but even the maximum negative plate temperature of 106.25°F was well within safe limits.

(4) The battery voltage during discharge periods ranged from 21.5 to 25.5 V. This is in accord with previous voltage measurements for simulated operation.

(5) Negative plate temperatures were highly responsive to current changes, resulting in maxima.

Table 70. *Surveyor* main battery capacity compilation (for each charge and discharge cycle)

Battery SN	Charge current rate, A	Total capacity input—battery charged to 27.3 V, A-h	Discharge current rate, A	Total capacity output—battery discharged to 17.5 V, A-h	Date performed, 1967
97	Vendor charge	179.5[a]	1.0	153.5	Feb 6 Feb 8
98	Vendor charge	187.0	2.0	185.0	Feb 27 Mar 13
97	2.0	182.7	3.0	182.0	Feb 18 Mar 30
98	1.0	178.3	4.0	176.7	Mar 13 Mar 30
97	2.5	139.0[b]	5.0	132.9	Mar 28 May 2
98	1.5	176.8[a]	5.0	136.5	Apr 3 May 2
97	2.0	188.9	—	—	Jun 5
98	2.0	159.2[b]	—	—	Apr 25

[a]Several cells were electrically shorted when the leads from thermocouples inadvertently shorted for a short duration. This event did not cause cell damage, but did create a voltage unbalance between cells.

[b]Float charge omitted.

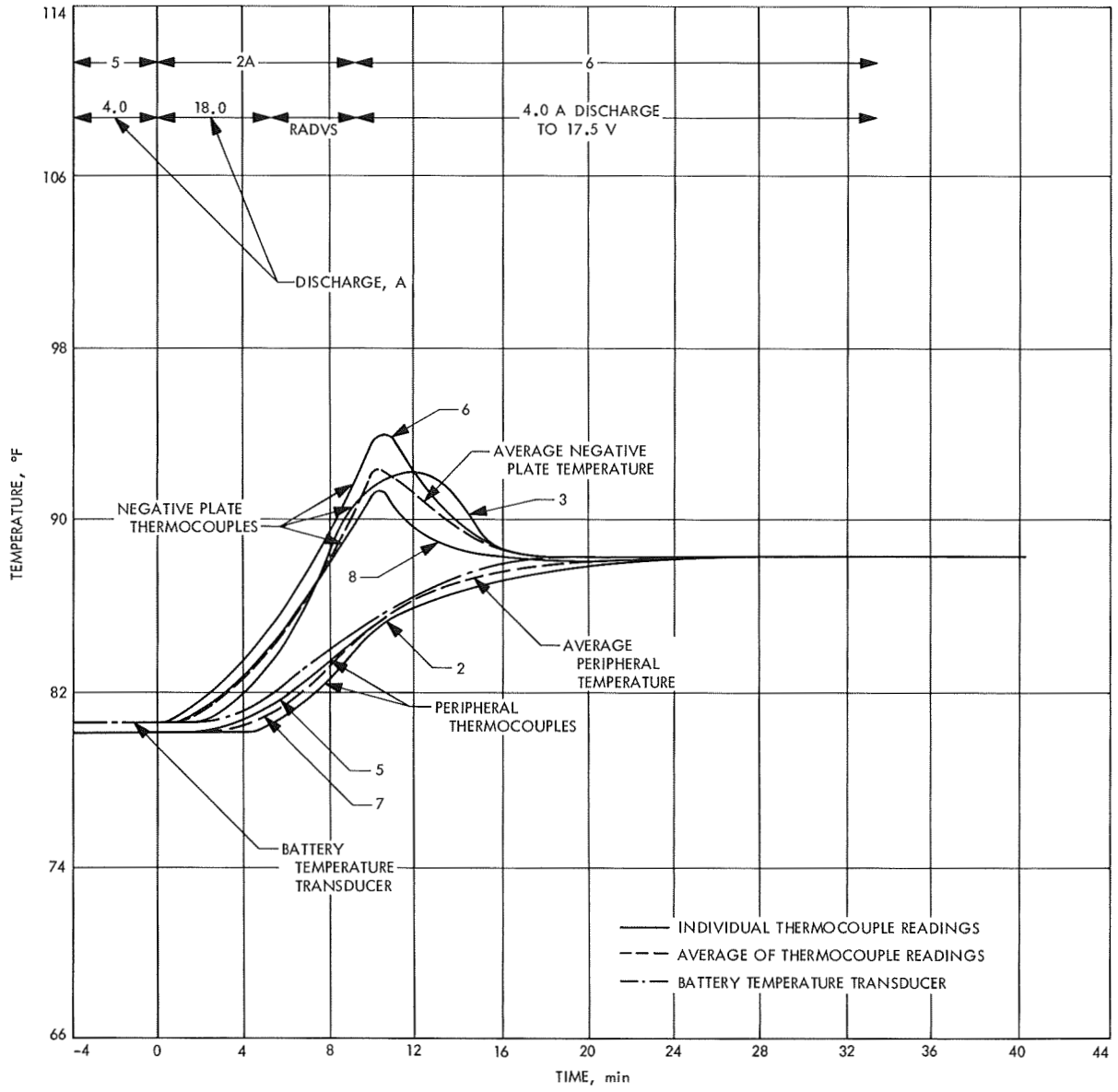

Fig. 121. Thermal test, *Surveyor* main battery 98, 4-A run

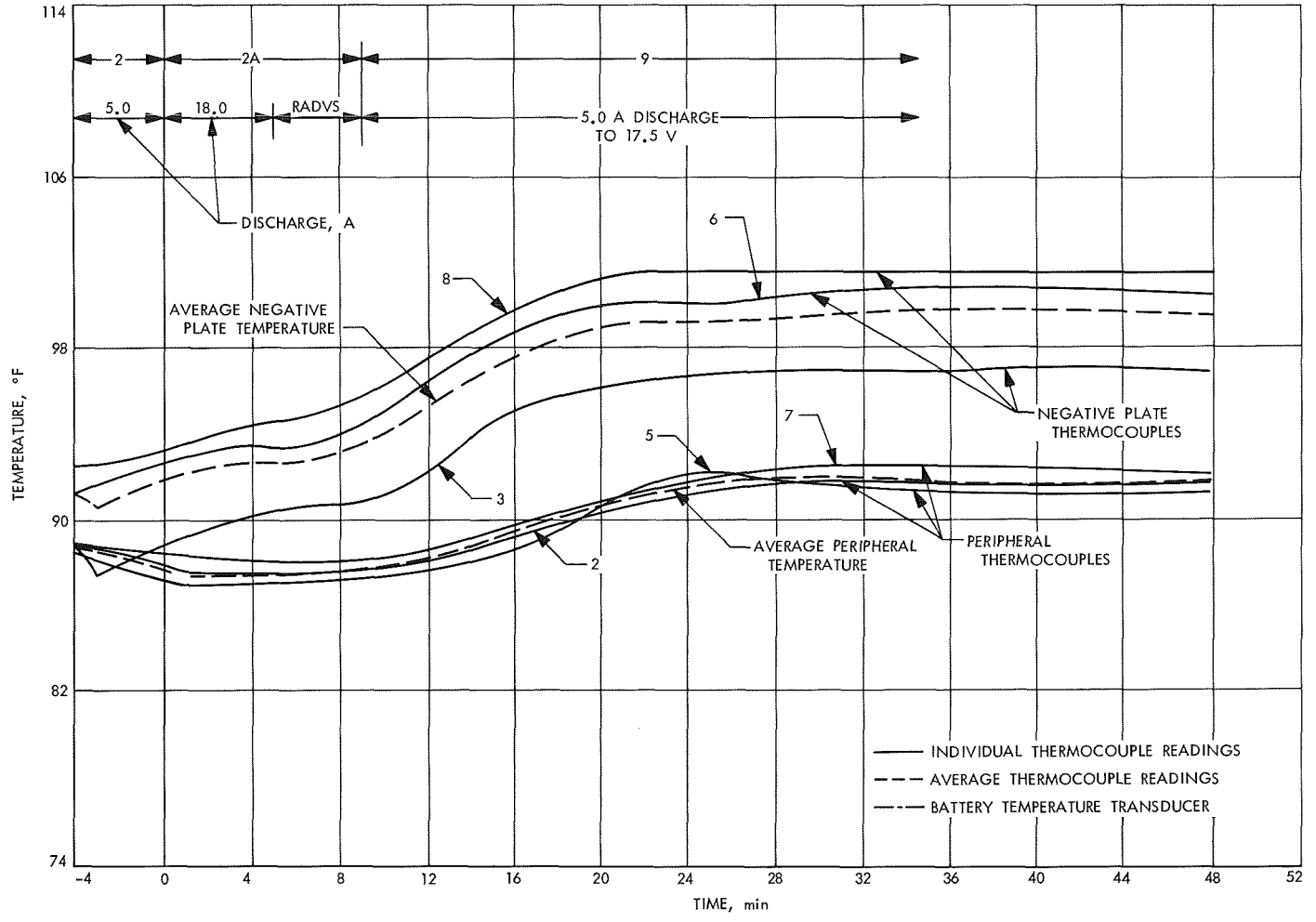

Fig. 122. Thermal test, *Surveyor* main battery 98, 5-A run

Transducer and peripheral temperatures exhibited the damping effect of a large thermal mass; owing to this thermal inertia, maxima in transducers and peripheral temperatures were damped out, and the temperature–time curve had an asymptotic response to current changes.

(6) Cool-down curves were roughly exponential with similar rates for the transducer and negative plate temperatures. After a 50-A discharge, room temperature was approached by the transducer in 7.5 h and the thermocouples in 7–10.5 h.

(7) Battery capacity was not affected by the tests.

(8) Prolonged discharge at high currents will lead to excessive negative plate temperatures as illustrated by a rate of temperature increase of 81°F/h as a result of a 50-A current. Peripheral and transducer temperatures increased approximately at the rate of 34°F/h. Qualitatively, the data were in accord with calorimetric measurements.

Conclusions. The battery temperature transducer on the *Surveyor* main battery afforded a reasonably adequate measure of battery temperatures as shown by simulated missions. Negative plate temperatures during discharge were as much as 12°F higher than transducer and peripheral temperatures, but well within safe limits. However, extended battery drain at high current, such as 50 A (not scheduled in the test plan), caused a rapid temperature rise that can deteriorate battery performance. Negative plate temperatures were far more responsive to current changes than the other temperature measurements, as indicated by the appearance of maxima on temperature–time plots. Voltages during a typical cycle were within acceptable limits. The battery cool-down period after discharge at 50 A was approximately 7 h.

b. Calorimetric measurement of heat generation rates. Calorimetric measurements were made on the *Surveyor* main battery to: (1) obtain heat generation data under specified conditions of charge and discharge at a constant current, (2) measure heat generation rates during a simulated *Surveyor* mission, and (3) verify an equation developed for predicting heat generation rates.

Description of the calorimeter. The wide interest in battery calorimetry, and the lack of commercially available equipment, prompts a description of the HAC calorimeter in addition to the test results. Basically, the isothermal calorimeter measures the heat associated with the phase change of a material. This information permits calculation of heat generation rates. In the HAC isothermal calorimeter, this material was Freon-11 and the heat of its vaporization provided the phase change. Freon-11 boils at 74.9°F, which is near the midpoint of the expected temperature range and permits the ready comparison with thermodynamic data that refer to cells operating at 77°F.

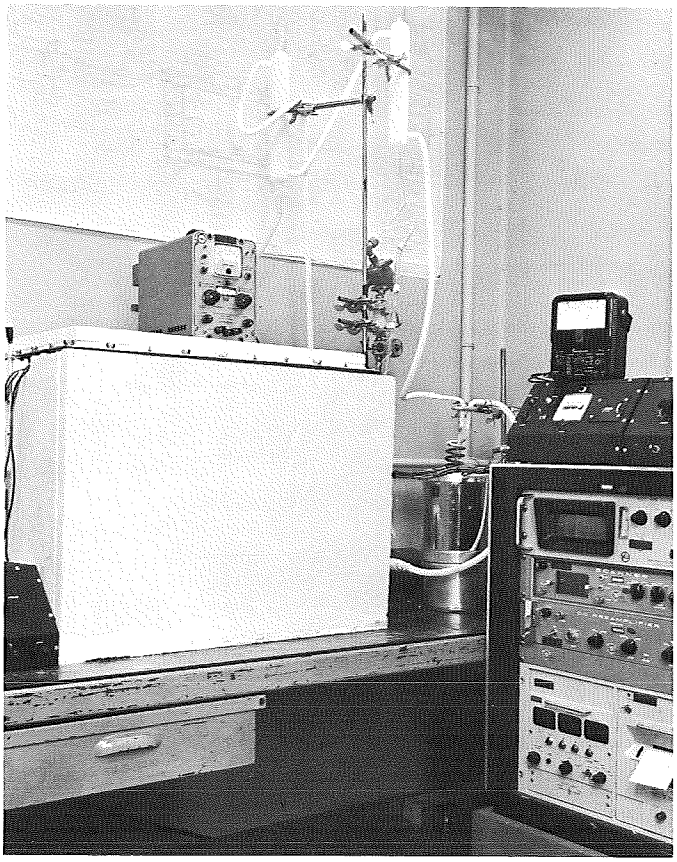

Fig. 123. Hughes isothermal calorimeter for heat generation measurement by *Surveyor* main batteries

The HAC calorimeter is shown pictorially in Fig. 123 and schematically in Fig. 124. The calorimeter is composed of an inner and an outer chamber. The outer chamber serves to insulate the inner chamber from the external environment. The Freon in the outer chamber is maintained at the boiling point by means of a heater, in order to match the temperature in the inner chamber. The test battery is placed in the inner chamber (Fig. 125), which also contains a heating element. This heating element is used for calibration purposes and for the measurement of negative heat generation rates from the battery, since the Freon in the inner chamber must boil at all times during the test. The Freon that boiled off from the inner chamber is collected in a measuring cylinder after condensation in a condenser, maintained at −4.0°F by refrigeration. When the Freon level in the cylinder reaches a thermistor, a valve at the bottom of the cylinder opens, another valve at the top closes, and the time from a digital clock prints. At this time, the valves become timer-controlled instead of thermistor-controlled. After a preset time, the valves are returned to their original positions. The time between trips is a measure of the rate of heat generation.

Results and conclusions. The curves in Fig. 126 and the calculated curves in Figs. 127, 128, and 129 are based on Eq. (1) and the assumption that the discharge of a silver–zinc cell proceeds in two stages.

It was further assumed that the electrolyte was saturated at all times with respect to zincate ion. Figure 127 shows the comparison between the calculated heat generation rate and the measured heat dissipation rate for battery 70 while undergoing a constant 3-A charge. The area within the calculated curve represents 204 W-h, whereas the area under the experimental curve is approximately 235 W-h. Figure 128 shows the calculated and experimental curves for a constant 7-A discharge of battery 70. The discharge data gave a measured heat generation rate of 20.5 W, compared to a calculated average value of 19.5 W. A typical *Surveyor V* Mission is demonstrated in Fig. 129. In all experiments, the thermal inertia of the battery was quite evident. This large heat capacity, plus the fact that the battery consists of 14 cells that are not all changing from the upper to the lower thermal plateau at the same time, precludes a recognition of two distinctly different heat output levels. In general, good agreement was obtained between calculated and experimental heat generation rates. This indicates the validity of the model and the absence of major side reactions.

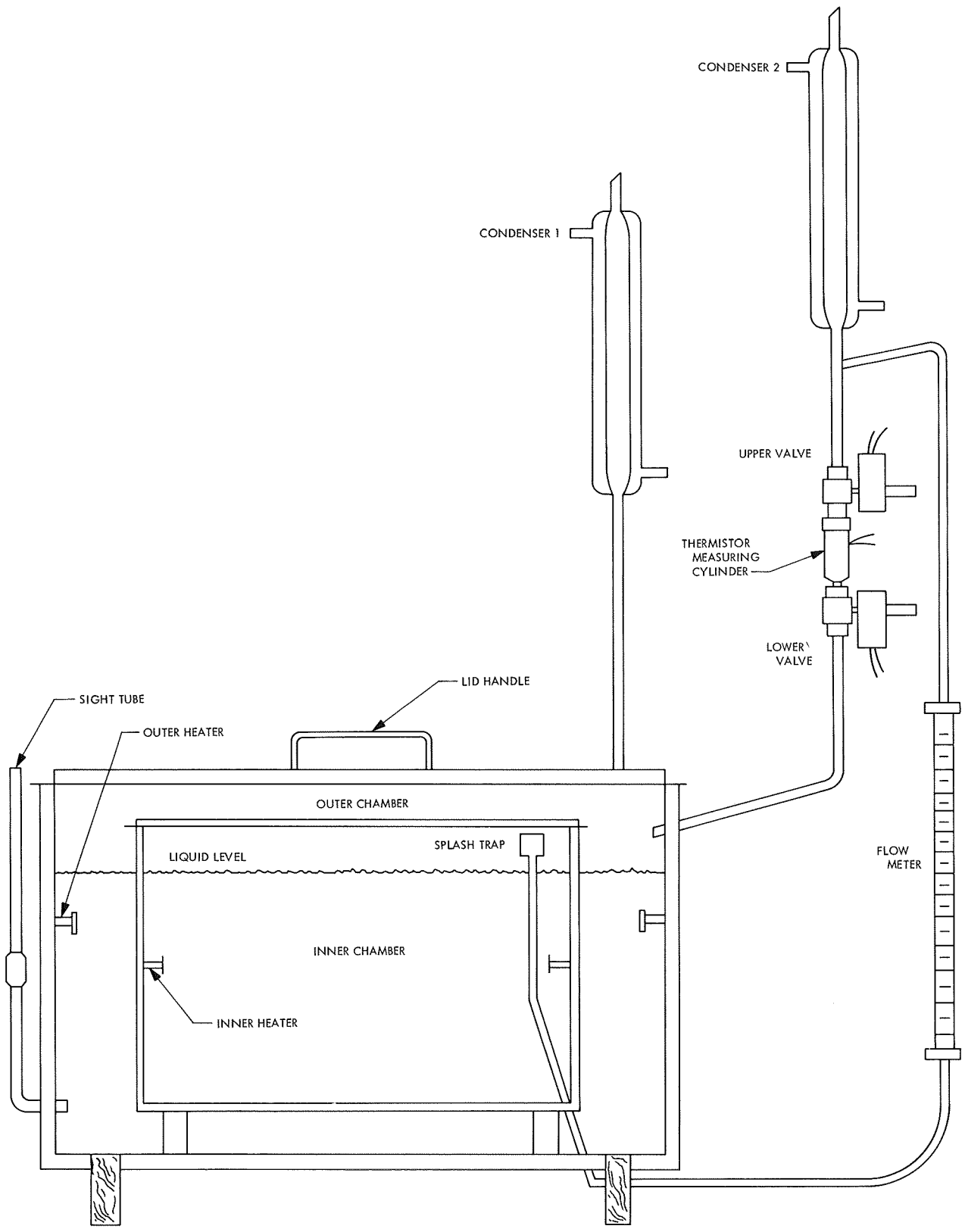

Fig. 124. Isothermal calorimeter

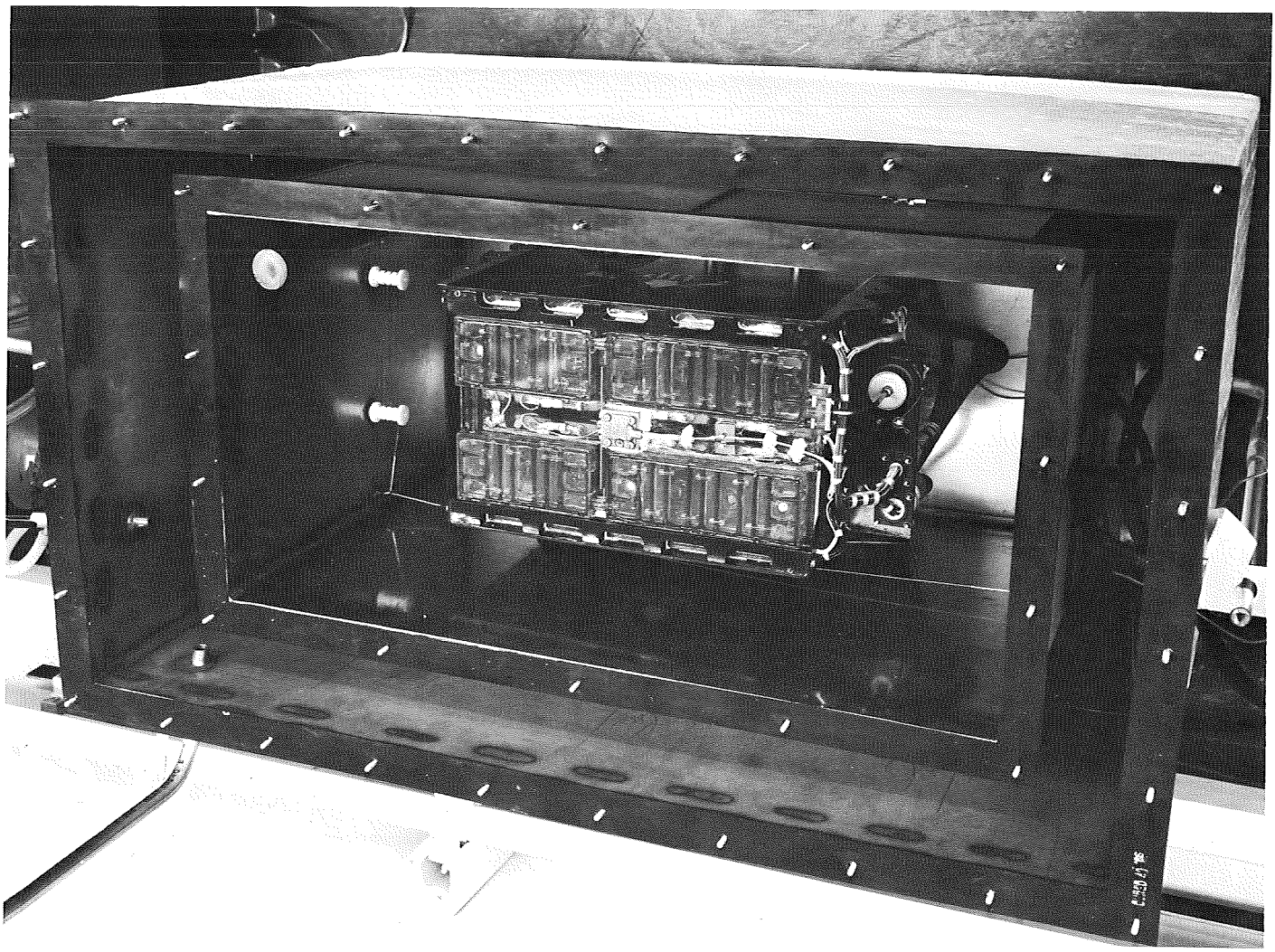

Fig. 125. *Surveyor* battery in isothermal calorimeter

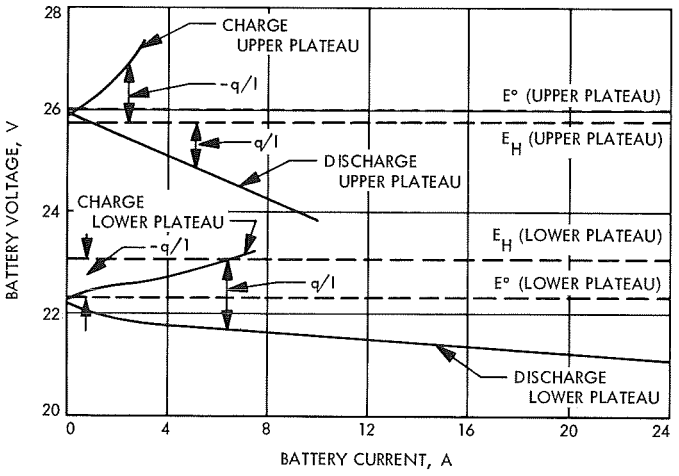

Fig. 126. Heat generation characteristics of *Surveyor* main battery at 24°C

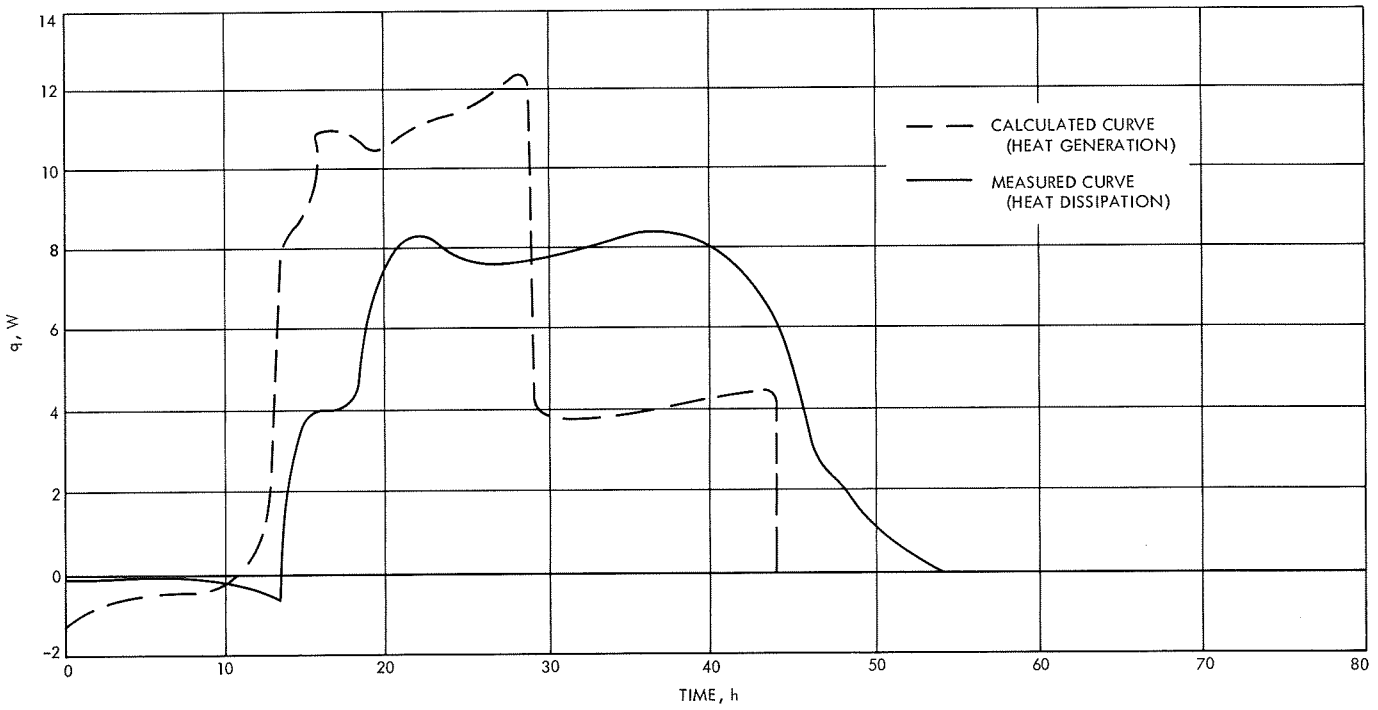

Fig. 127. Heat generation rates of battery 70—3-A charge

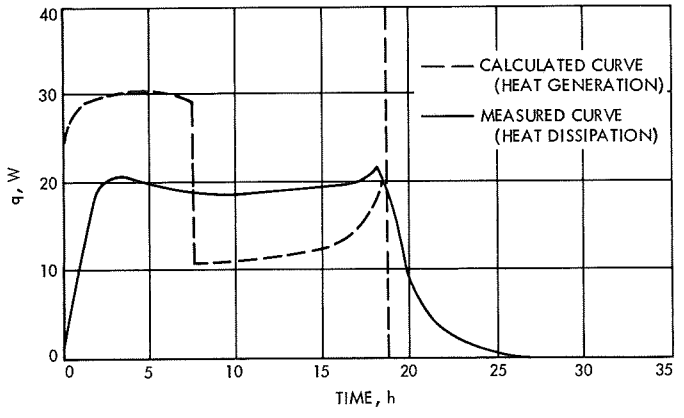

Fig. 128. Heat generation rates of battery 70—7-A charge

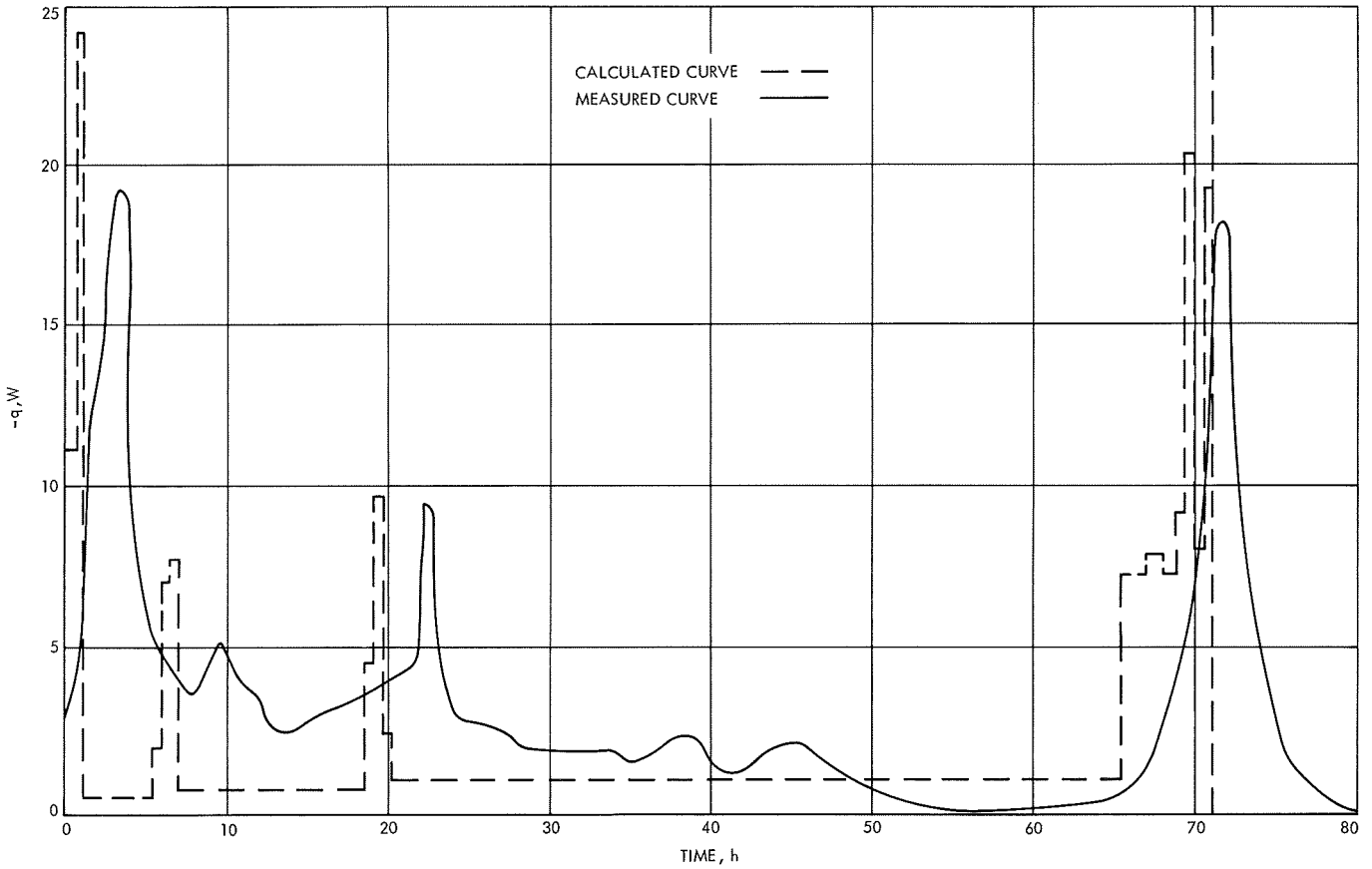

Fig. 129. Heat generation rates of battery 84, *Surveyor V* Mission profile

2. Lunar surface operation simulation. The purpose of this test was to establish the *Surveyor* main battery parameters during a typical *Surveyors V, VI,* and *VII* Mission operation. Specifically, the test served to demonstrate spacecraft operation at temperatures ranging from 57 to 95°F. The test sequence simulated transit, landing, and lunar operations 150 h into the lunar night.

a. Test plan. The basic test plan for the nine day simulation test involving seven batteries is indicated in Tables 71 and 72. The test schedule and revisions to the test plan are indicated in Table 73.

Table 71. Temperature profile

Temperature range °F during test	Day								
	1	2	3	4	5	6	7	8	9
High, °F	103	100	110	115	120	125	90	60	30
Medium, °F	82	77	83	88	93	98	63	43	30
Low, °F	67	62	68	73	68	83	70	55	30

b. Results. Figure 130 shows temperature, pressure and charge potential as a function of time after touchdown. Figure 131 shows charge current and cell potential variations as a function of time after touchdown. Figure 132 shows the effect of operating temperature on battery potential at the TV (2.7-A) and A/SPP (11.4-A)

Table 72. Load profile

Test day	Operation
1	TV operation: 6 s/cycle = 3300 cycles over the first 5.5 h of the test day consisting of 1.4-s pulse discharges at 2.66 A and 4.6-s charge pulses at 0.89 A Charging: 16 h at 1.50 A
2	TV operation: 6 s/cycle = 4800 cycles over the first 8 h of the test day, consisting of 1.4-s pulse discharges at 2.66 A and 4.6-s charge pulses at 0.89 A 100 pulses at the rate of 20 pulses at start of tests and after every 2 h during the first 8 h of the test day—each pulse 11.4 A for 65 ms Charging: 16 h at 1.50 A
3–9	Repeat sequence shown for test day 2

Table 73. Test schedule, A21-E lunar surface operation simulation

Test number	Battery SN	Test run, 1967	Expiration date-1967	Ampere-hour capacity prior to test	Number of terminal descents	Passed test without failure	Test plan followed	1.4 s discharge pulses—2.66 A and 4.6 s charge pulses—0.89 A	1.4 s discharge pulses—2.66 A	Float	Temperature profile[e]	Type of discharge after test	Discharge capacity at end of test, A-h
1	80	Jan 7–Jan 17	Mar 1	136	1	Yes	Initial[b]	X		Yes	High	Discharge at 2A for 32 h, pulse 50A for 4 min +5–20A pulses, discharge at 2A to 17.5 V	176.03
2[a]	86	Jan 26–Jan 30	Mar 4	119	3	Yes	Rev. A[c]	X		Yes	Low	Incomplete test	Incomplete
3	83	Feb 3–Feb 12	Mar 6	109	2	Yes	Rev. A		X	Yes	Low	Discharge at 2A for 32 h, pulse 50A for 4 min +5–20A pulses, discharge at 2A to 17.5 V	Discharge not completed due to error
4	94	Feb 18–Feb 27	Apr 4	137	1	Yes	Rev. B[d]		X	No	Medium	7A to 17.5 V	177.10
5	87	Mar 2–Mar 11	Mar 28	93	3	Yes	Rev. B		X	No	High	7A to 17.5 V	176.6.
6	88	Mar 16–Mar 25	Mar 28	79	3	Yes	Rev. B		X	No	High	7A to 17.5 V	174.75
7	99	Mar 30–Apr 8	Apr 7	135	3	Yes	Rev. B		X	No	Low	7A to 17.5 V	No information due to special test

[a]Test incomplete—Interrupted after 3 days due to loss of thermal plate to subsystem group.

[b]Initial—After test discharge at 5–7A to 17.5 V, January 6, 1967.

[c]Revision A—After test discharge at 2A for 32 h. Discharge at 50A for 4 min and apply 5–20-A pulses. Discharge at 2A to 17.5 V, January 18, 1967.

[d]Revision B—No charging during loading. After test discharge at 5–7A to 17.5 V, February 9, 1967.

[e]See Table 61 for temperature profiles.

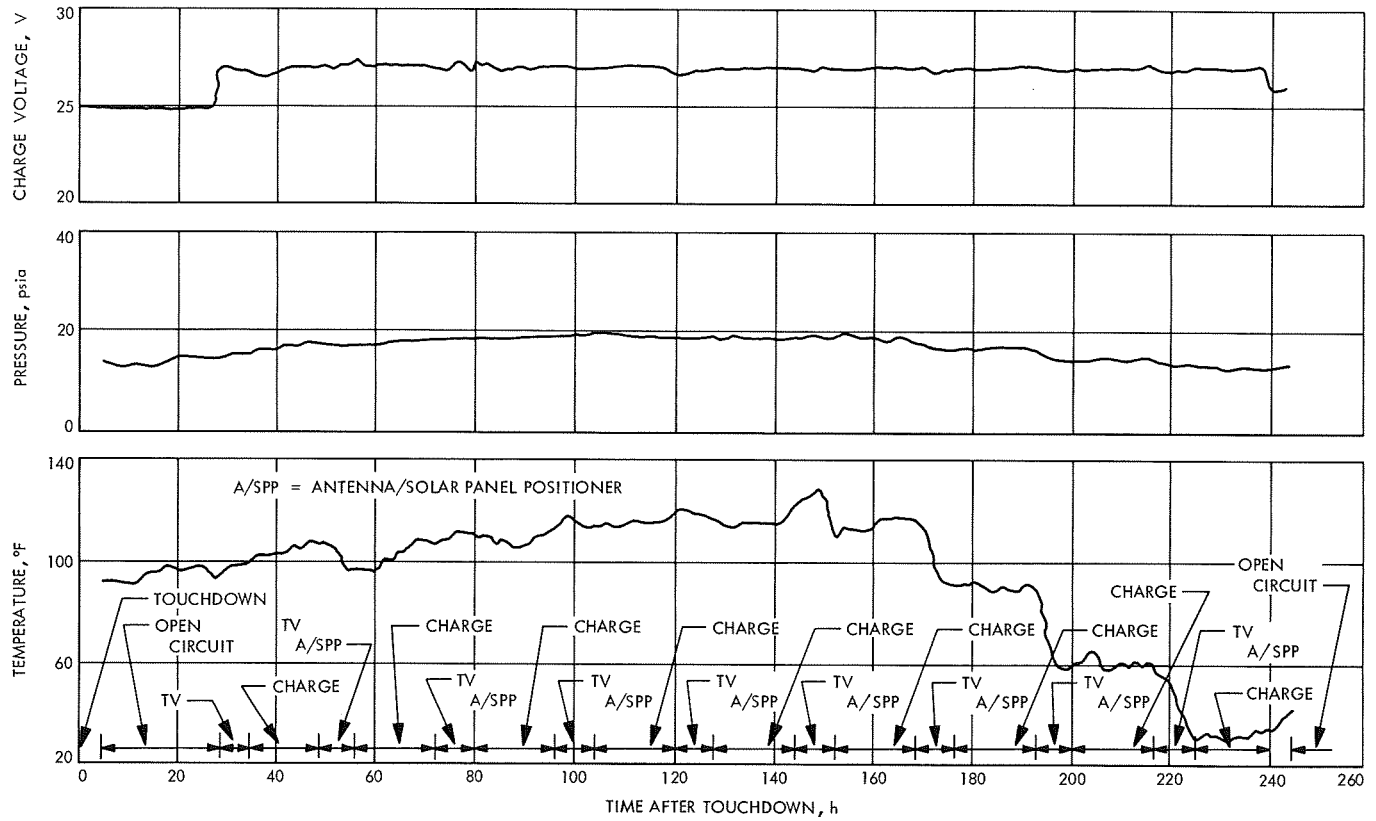

Fig. 130. A-21E main power battery subsystem test 1—lunar operation phase—time after touchdown vs temperature, pressure, and voltage

loads. While Figs. 131 and 132 are based on six tests, the remaining data are based on the complete test sequence.

Figures 133 summarizes battery potentials, measured over the temperature range during the test sequence. Figure 134, resulting from the test data, provides a means of estimating battery potentials at various anticipated operating rates and temperatures. Similarly, Fig. 135 shows the time required to recharge the battery as a function of capacity at touchdown. The dispersion of test data for the seven batteries is summarized in Table 74.

c. Conclusions.

(1) The *Surveyor* main battery demonstrated that it could successfully provide terminal descent potentials in excess of 18.0 V at temperatures greater than 80°F (launch, transit and touchdown test phase).

(2) The *Surveyor* main battery demonstrated that it could successfully operate over a controlled temperature exposure range of 30–125°F for one lunar day and at least 150 h into lunar night.

(3) Figures containing anticipated battery potentials on charge and at TV and A/SPP discharge rates over the temperature range of 30–125°F were prepared to provide a guide for estimating battery voltage under typical operating conditions.

(4) An estimate of the time required to fully recharge a main battery, assuming a typical range of available capacities at lunar touchdown and lunar operations using about 6 A-h/day and charging 24 A-h/day, were prepared to help predict battery energy available during lunar operations.

(5) Based on the completion of six tests, each of nine days duration, it was estimated that 176 A-h of charge capacity (about 95% greater than discharge capacity at room ambient) would be available for lunar night survival.

D. Solar–Thermal–Vacuum Tests

Solar–thermal–vacuum tests were performed prior to all missions for the purpose of verifying the functional and thermal integrity of the *Surveyor* spacecraft while

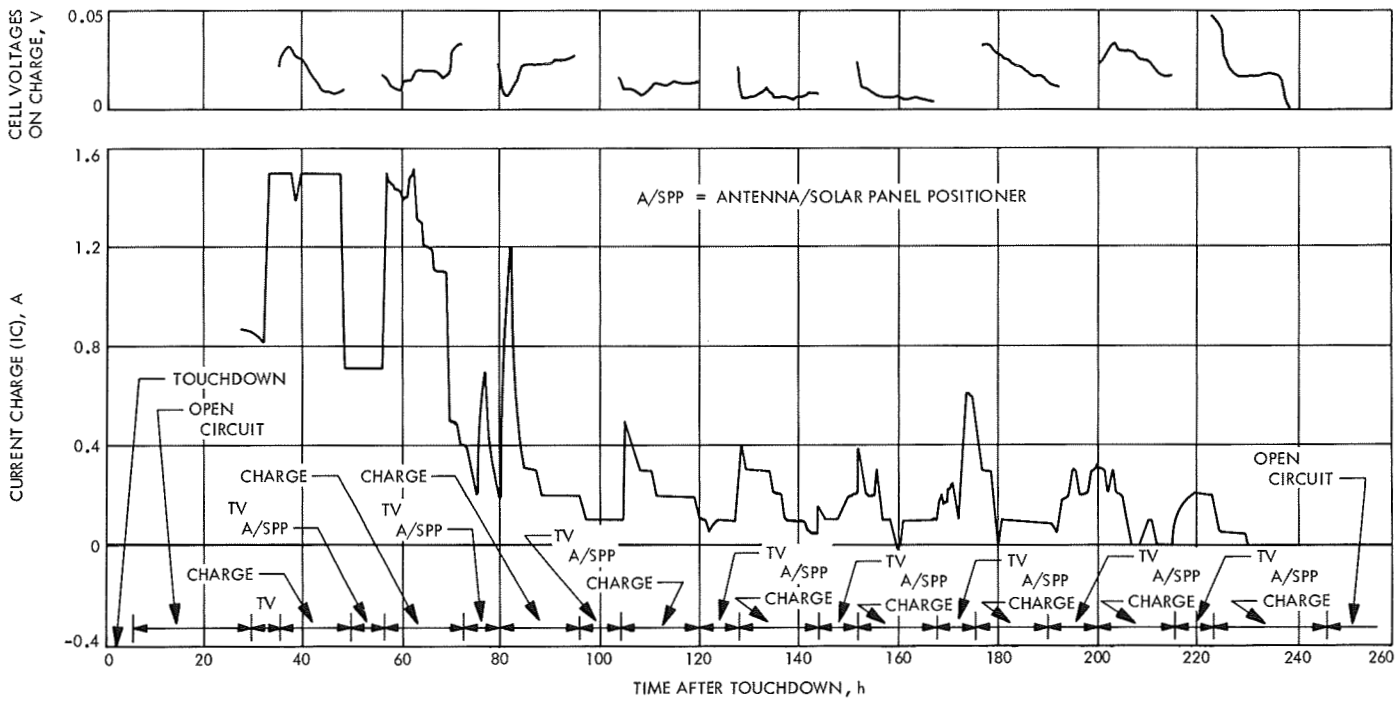

Fig. 131. A-21E main power battery subsystem test 1—lunar operation phase—time after touchdown vs charge current and cell voltages

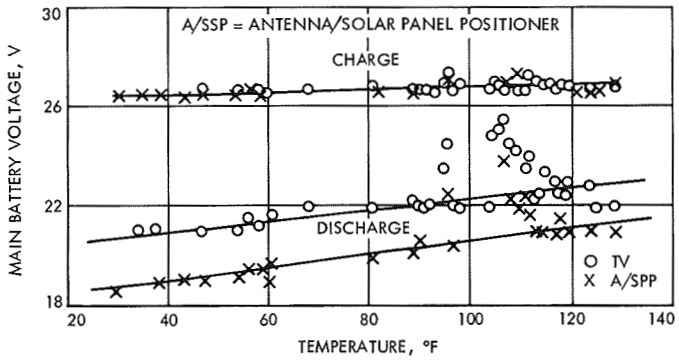

Fig. 132. A-21E main battery subsystem test 1—lunar operation phase—temperature vs main battery voltage

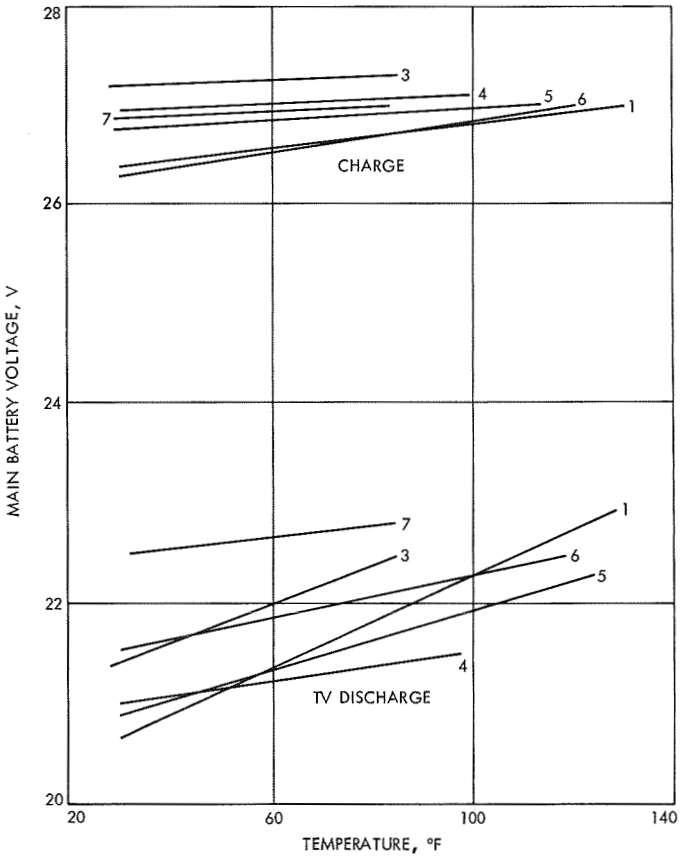

Fig. 133. A-21E main battery power subsystems tests 1–7 (test 2 omitted), lunar operation phase—battery average voltage vs temperature

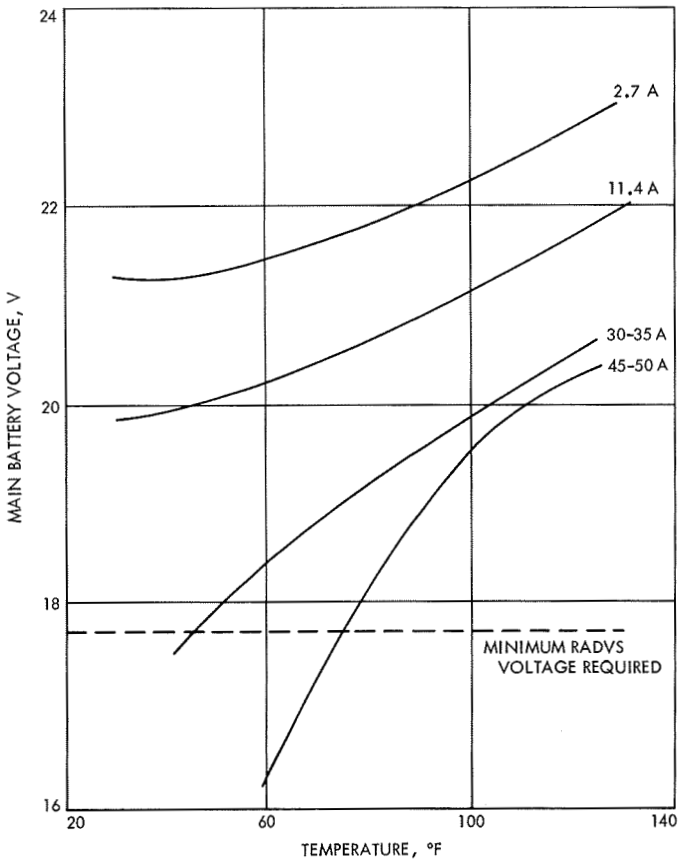

Fig. 134. *Surveyor* main battery average voltage vs temperature and various operating rates

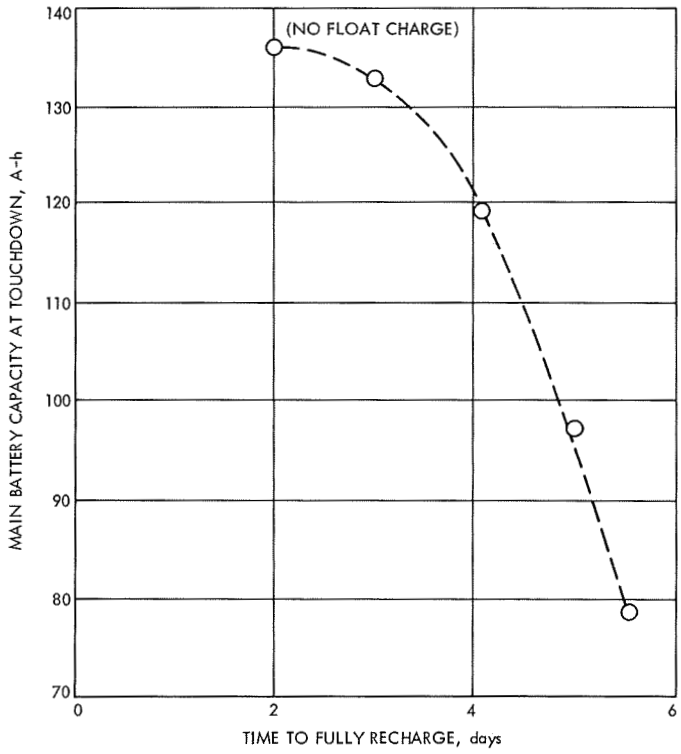

Fig. 135. Recharge of main battery during lunar operation (no float charge)

Table 74. Dispersion of test data, A21-E lunar surface operation simulation

Test No.	Battery SN	Temperature profile[a]	Battery pressure, psia		Delta, △ cell voltage, V[b]		Battery charge voltage, V				Battery charge current, A	Battery discharge voltage, V at the minimum and maximum temperature points	
							Lower plateau		Upper plateau				
			Minimum	Maximum	Average	Maximum	Minimum	Maximum	Minimum	Maximum		A/SPP	TV
1	80	High	13.5	20.0	0.022	0.048	—	—	26.8	27.5	1.5 day 1–3 0.2 day 4–9	18.5 at 29°F 22.0 at 131°F	20.5 at 29°F 23.5 at 131°F
2	86	Low	13.5	14.2	0.013	0.350	22.5	22.7	26.0	27.5	1.5	—	—
3	83	Low	9.0	13.0	0.018	0.350	22.6	26.5	26.5	27.3[c]	1.5 day 1–3 0.2 day 4–9	20.6 at 28°F 21.8 at 85°F	21.1 at 28°F 22.5 at 85°F
4	94	Medium	9.5	14.0	0.030	0.350	22.8	26.4	26.4	27.3[c]	1.5 to cutoff	19.9 at 30°F 20.5 at 98°F	20.8 at 30°F 21.6 at 98°F
5	87	High	10.5	19.0	0.020	0.350	22.8	26.6	26.6	27.3[c]	1.5 to cutoff	20.2 at 30°F 21.5 at 125°F	20.8 at 30°F 22.4 at 125°F
6	88	High	9.5	19.0	0.012	0.350	22.8	26.6	26.6	27.3[c]	1.5 to cutoff	20.2 at 30°F 21.2 at 120°F	21.5 at 30°F 22.5 at 120°F
7	99	Low	9.0	12.5	0.012	0.045	22.4	26.6	26.6	27.3[c]	1.5 to cutoff	20.1 at 33°F 20.6 at 85°F	22.5 at 33°F 22.8 at 85°F

[a]See Table 71 for temperature profiles.

[b]Maximum delta (Δ) cell voltage occurred between the lower and upper plateau levels.

[c]Charge cutoff point.

exposed to a range of solar conditions in a simulated flight environment. Frequently, spacecraft power was simulated by a power supply. Although STV tests did not always show close agreement with subsequent missions, due to mission modifications, a comparison of STV test results with flight data will be presented in the subsection that follows.

E. Flight and Postflight Data

The graphs and tables that follow (Figs. 136–160 and Table 75), depict telemetered electrical and thermal battery data, obtained during and after transit. For comparisons, the STV and predicted values are shown in instances.

1. Data presentation. The telemetered electrical and thermal battery data are presented as follows:

Surveyor spacecraft	Reference	Fig.
I	4	136–141
II	5	142–146
III	6	147 and 148
IV	—	149 and 150
V	7	151–156
VI	8	157 and 158
VII	9	159 and 160

Table 75. Electrical power performance data, *Surveyor VII*

Parameter	Launch		Touchdown	
	Expected	Actual	Expected	Actual
Battery charge, A-h	165	164	74	93.8
Battery pressure, psi	15	13.7	15	13.4
Battery temperature, °F	80	81.4	90	93
Battery load at touchdown, A	—	—	40	36.8
Battery terminal voltage at touchdown, V	—	—	19	19.7
Solar panel power out, W	85[a]	88.7[a]	—	—
Boost regulator efficiency, %	80	81	83	85.4

[a]Average coast phase transit value.

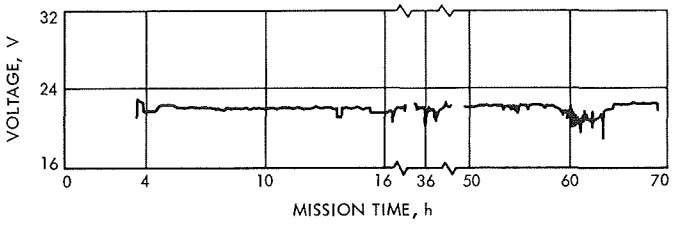

Fig. 136. Main battery potential, *Surveyor I*

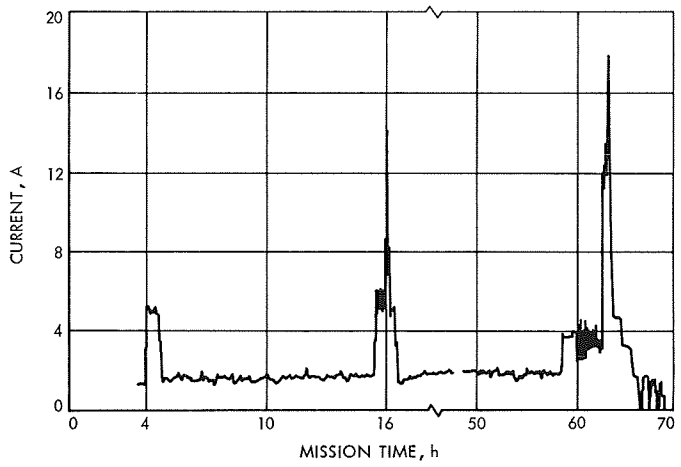

Fig. 137. Main battery discharge current, *Surveyor I*

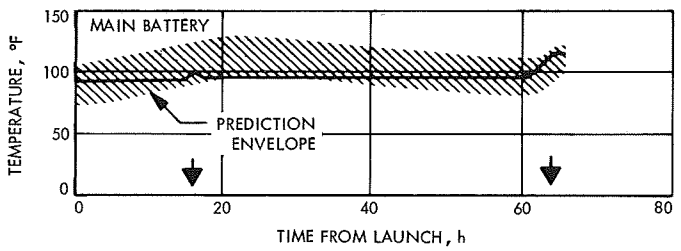

Fig. 138. Main battery temperature, *Surveyor I*

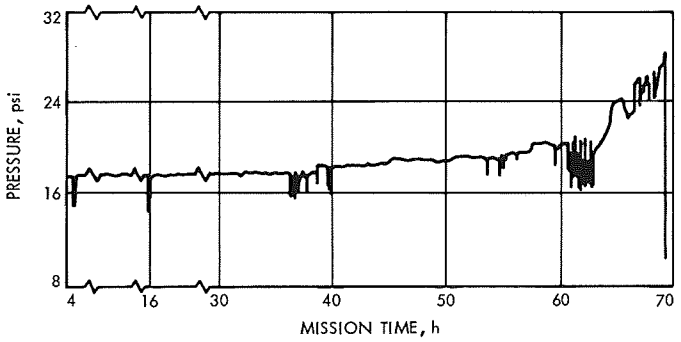

Fig. 139. Main battery manifold pressure, *Surveyor I*

2. Discussion. The data indicate generally satisfactory battery performance during the seven missions. The STV test data and predicted values were in reasonable agreement with flight and postflight data, especially when mission modifications are considered. Owing to the availability of a wider range of information concerning *Surveyor V*, this mission will be the subject of further discussion in the subsequent paragraphs.

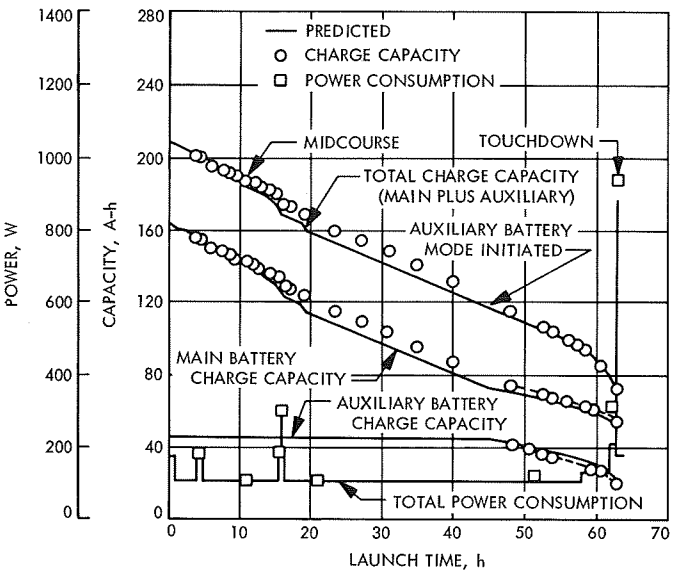

Fig. 140. Battery capacity and total power consumption profile from *Surveyor I* flight

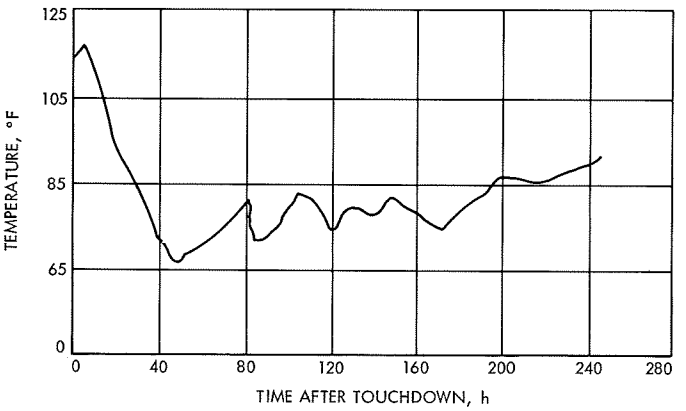

Fig. 141. Main battery temperature during first lunar day, *Surveyor I*

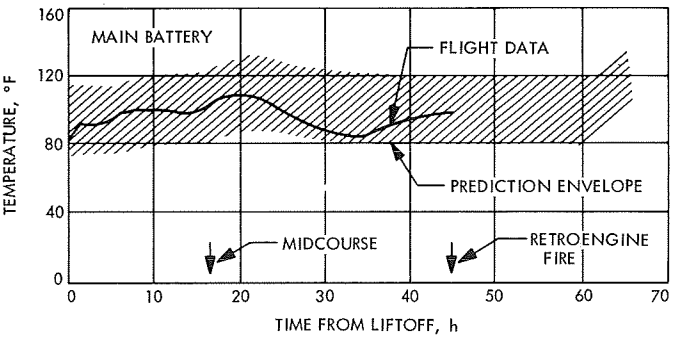

Fig. 142. Main battery temperature, *Surveyor II*

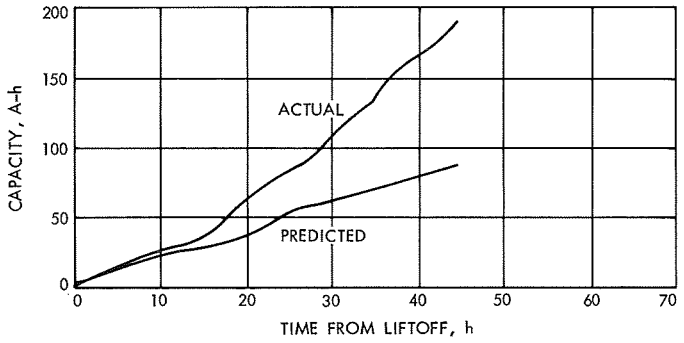

Fig. 143. Actual vs predicted battery capacity consumption, *Surveyor II*

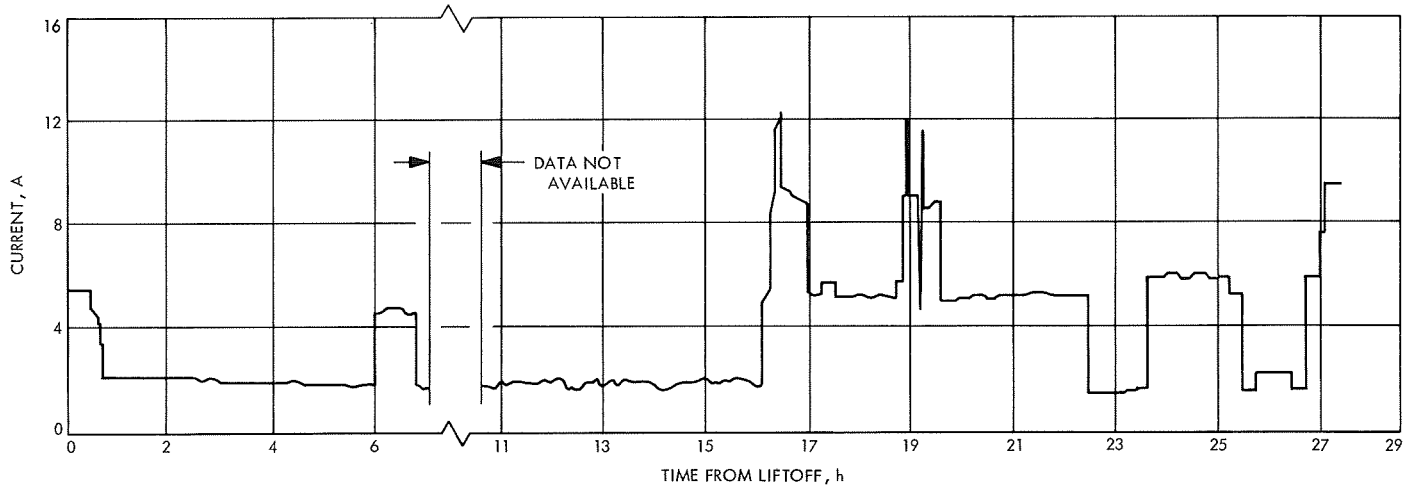

Fig. 144. Main battery discharge current, *Surveyor II*

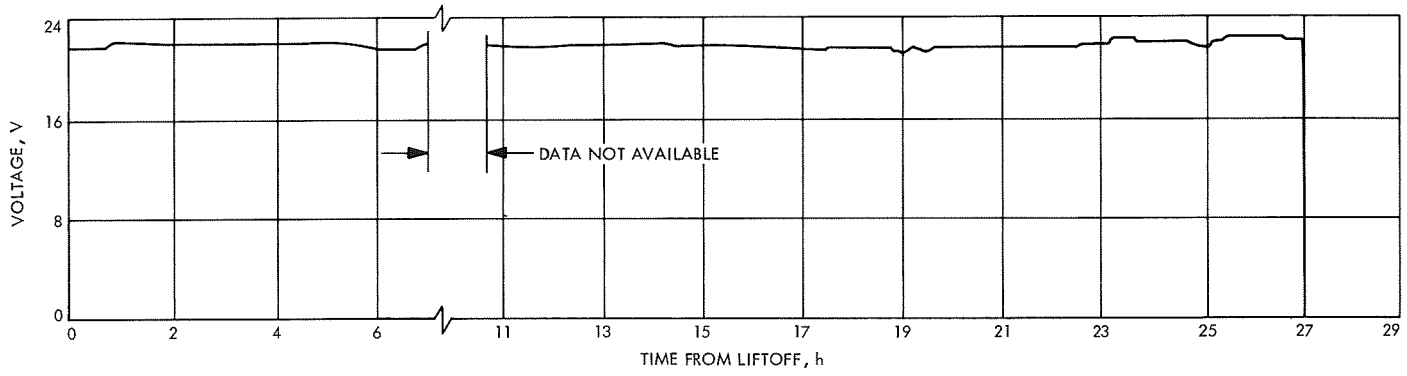

Fig. 145. Main battery voltage, *Surveyor II*

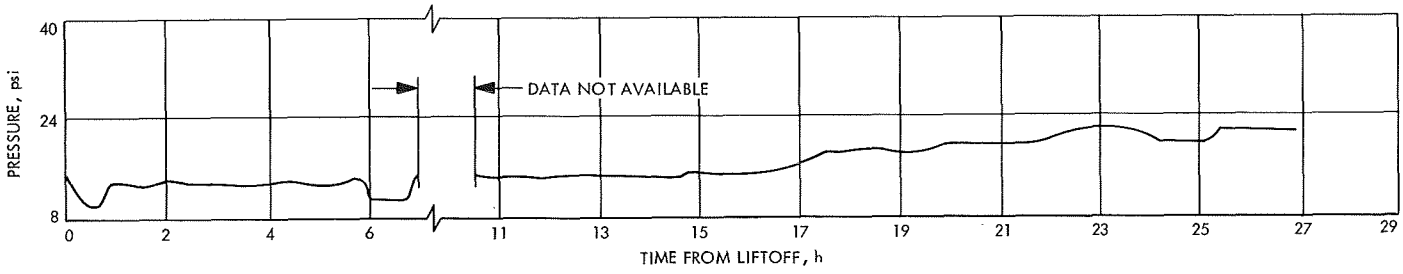

Fig. 146. Main battery manifold pressure, *Surveyor II*

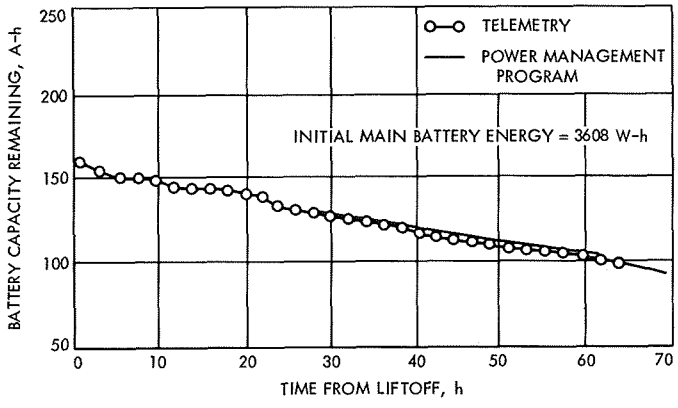

Fig. 147. Main battery capacity remaining during transit, *Surveyor III*

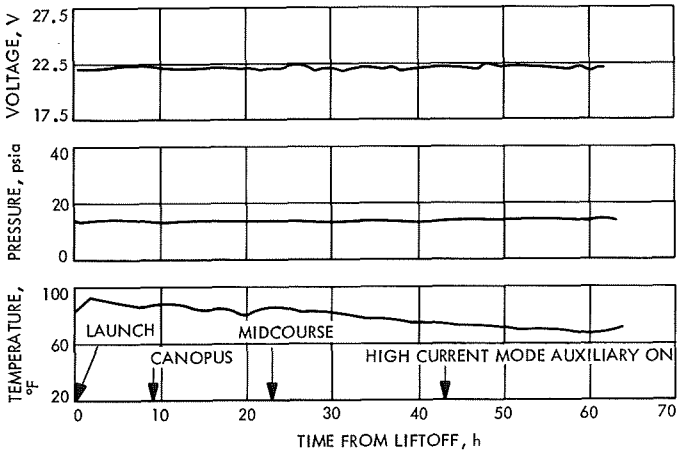

Fig. 148. *Surveyor III* flight data for main battery SN 108

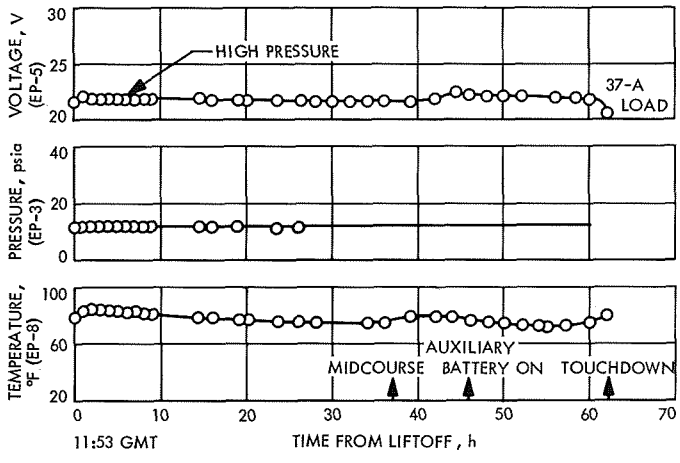

Fig. 149. Main battery 123 operation during *Surveyor IV* flight

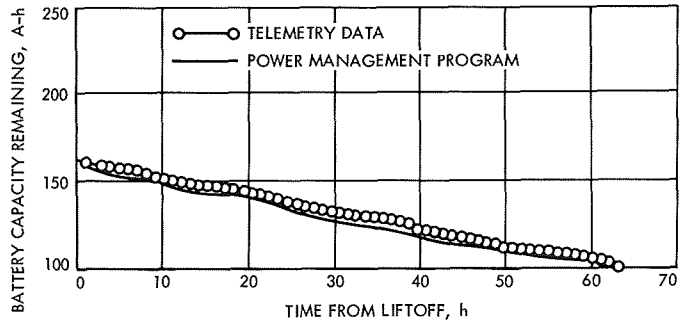

Fig. 150. Battery capacity remaining, *Surveyor IV*

Comparison of the *Surveyor V* transit and STV test data of Figs. 151 and 152 show no major differences in performance. Battery capacity data, shown in Fig. 153, indicate a drop in battery capacity below the predicted curve as a result of the need for special vernier engine firings after midcourse correction and a nonscheduled calibration of the alpha scattering instrument. The engine firings were conducted as a result of helium leakage. Thus, the residual battery capacity at touchdown was estimated as 1830 W-h (83 A-h), rather than a predicted 2200 W-h (100 A-h).

Battery operation during the first lunar day (Fig. 155) was in accordance with expectations. The battery reached a maximum charge of 163 A-h before sundown.

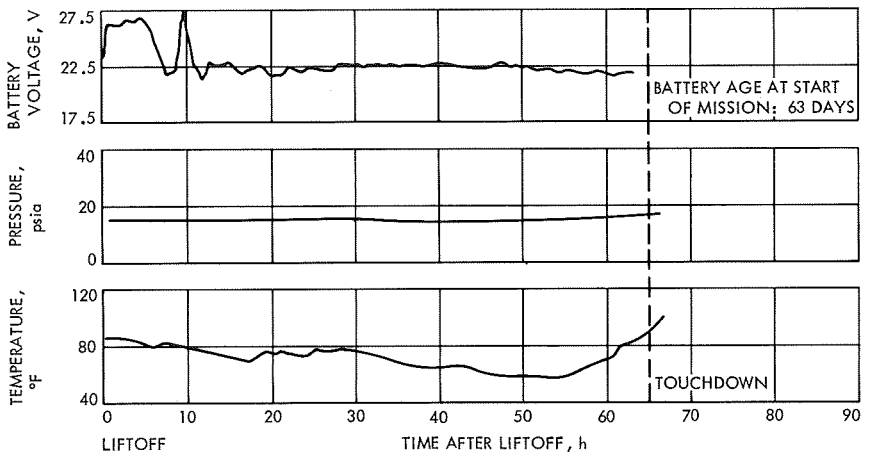

Fig. 151. *Surveyor V* main battery SN 142 flight performance

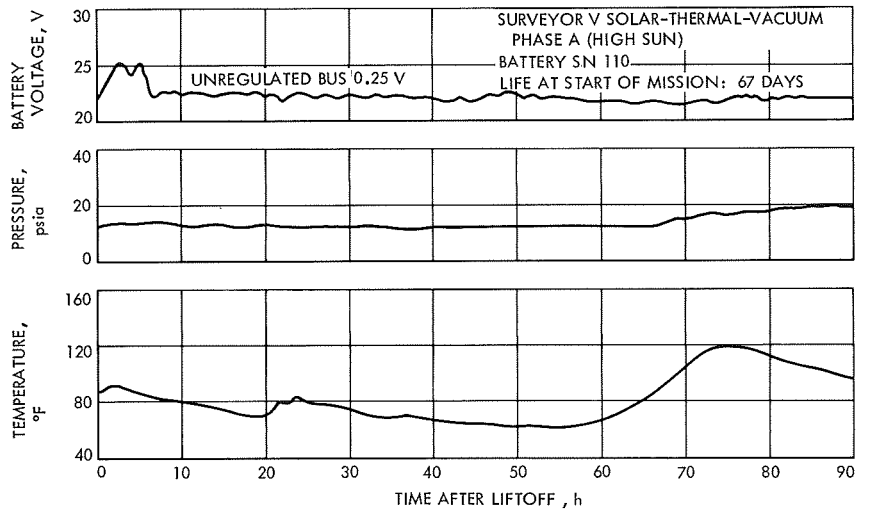

Fig. 152. *Surveyor V* battery SN 110 during STV phase A

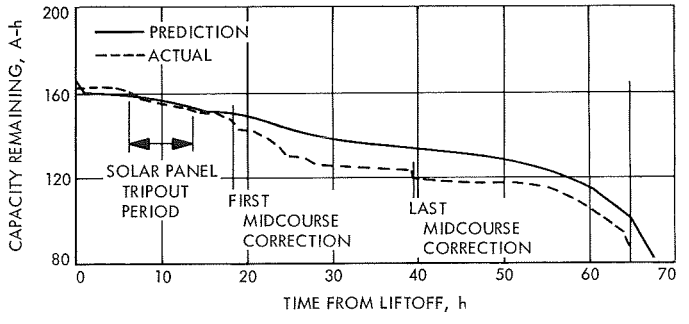

Fig. 153. Battery capacity profile during transit

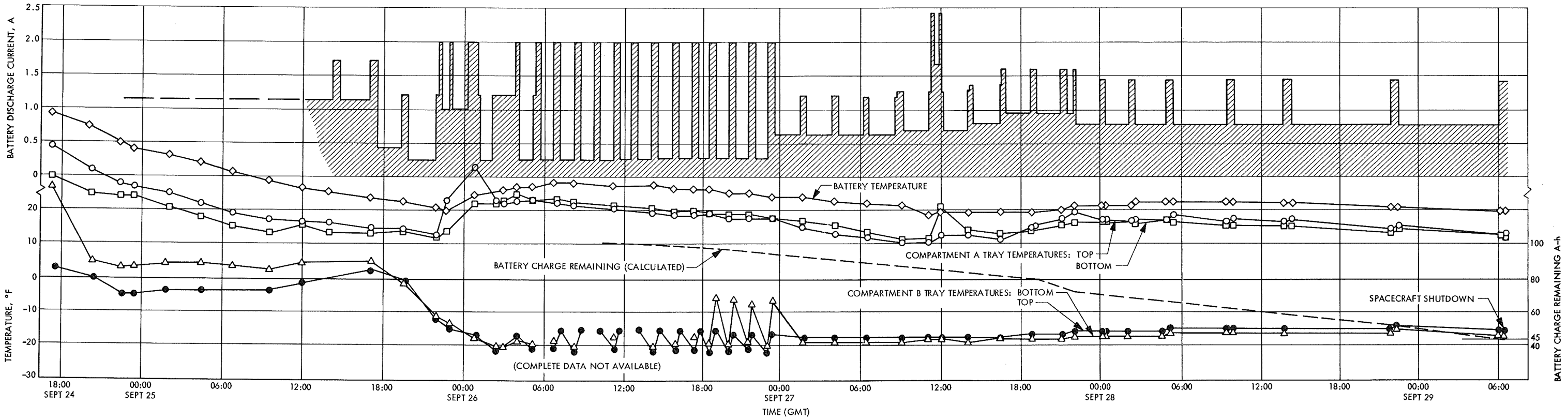

Fig. 154. Key spacecraft thermal and power parameters controlled during first lunar night operations

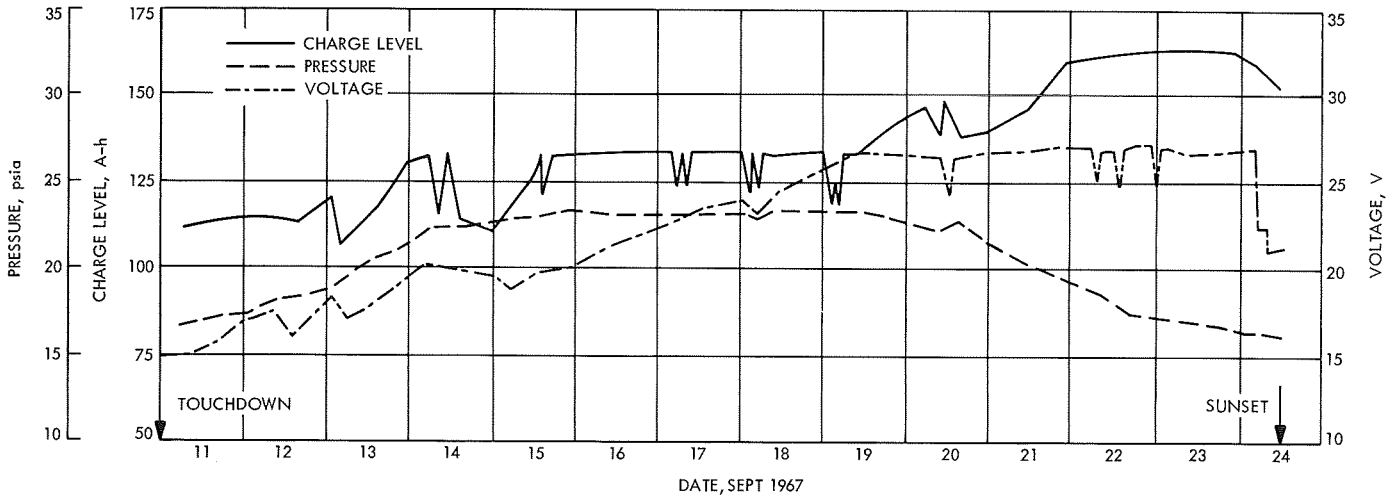

Fig. 155. Battery performance during lunar day, *Surveyor V*

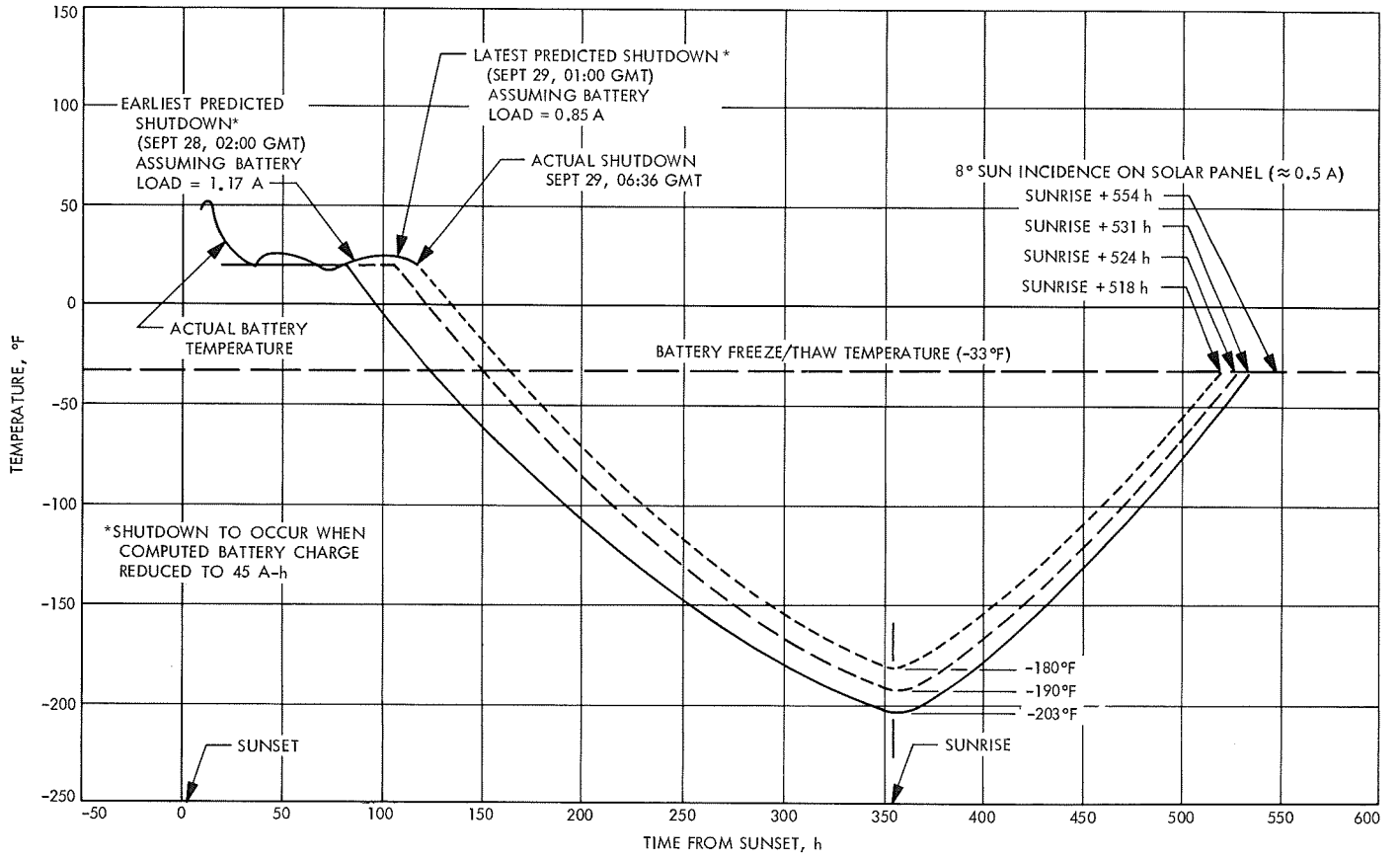

Fig. 156. *Surveyor V* lunar night survival plan and predicted battery temperature profile

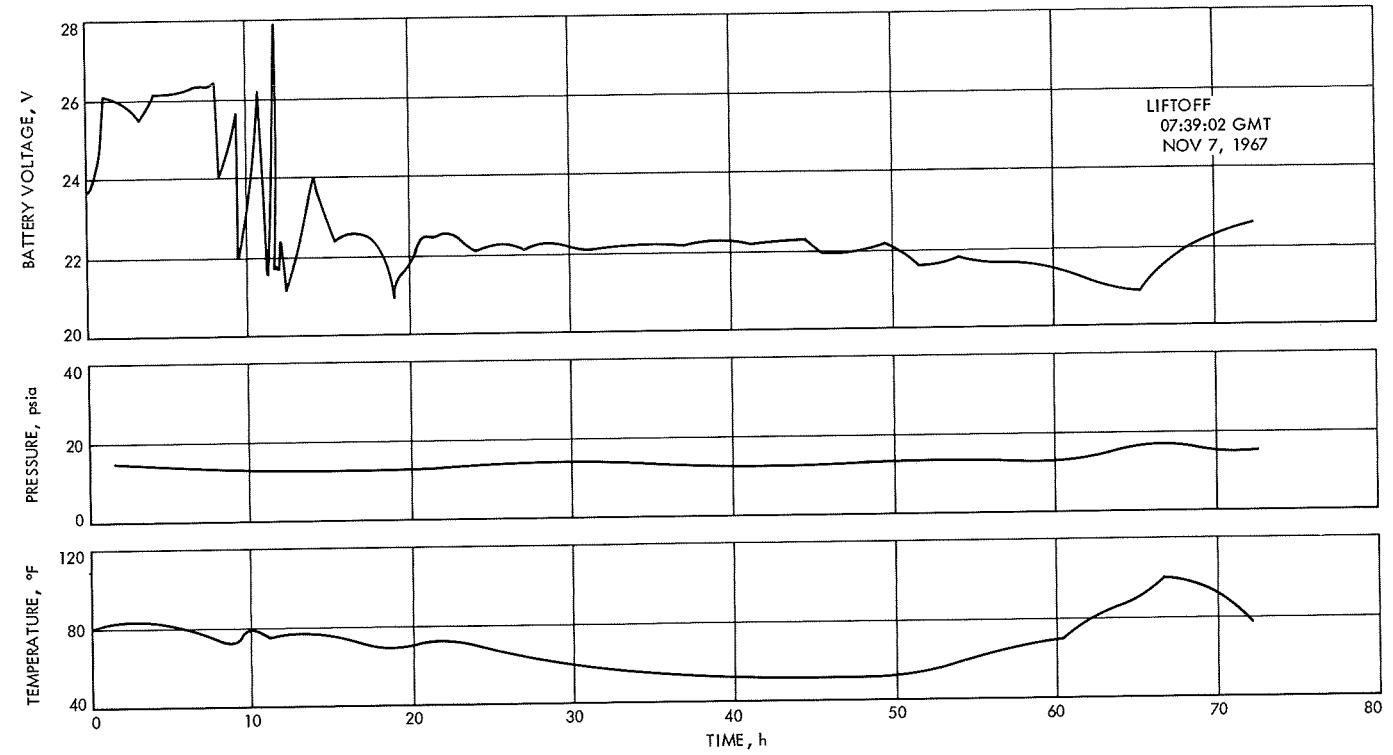

Fig. 157. Main battery SN 150, *Surveyor VI* flight

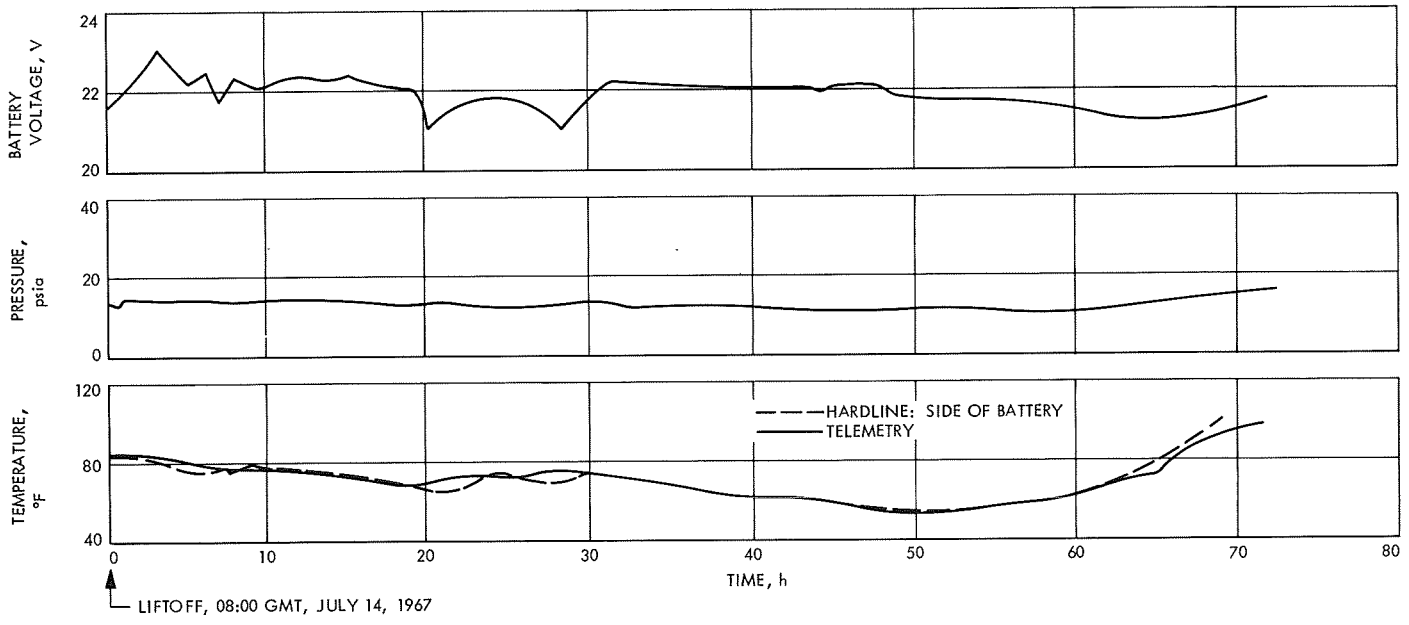

Fig. 158. Main battery SN 117 during *Surveyor VI* STV testing

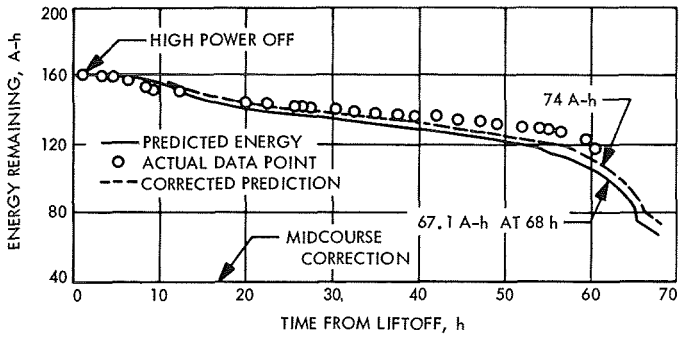

Fig. 159. Battery energy profile during transit, Surveyor *VII*

Lunar night operation was designed to spend the battery energy effectively in order to: (1) maintain the battery temperature at +20°F for the maximum time by dissipating power in compartment A until the battery capacity reached 45 A-h (in accord with lunar night survival tests), and (2) prevent the battery temperature from dropping below approximately −175°F—from which the battery could be awakened. Figure 154 provides data concerning operation going into the lunar night. Figure 156 gives the predicted and actual spacecraft shutdown times, predicted revival times, and corresponding battery temperature profiles.

The *Surveyor V* was successfully turned on, on lunar day 2, about 147 h after sunrise at the landing site, even though the battery temperature at turn-on time was 100°F above the anticipated level and was increasing at the rate of 3.5°F-h. The battery temperature was eventually reduced by shading, and the spacecraft was reawakened and operated on lunar day 4 (Ref. 6). There is some evidence that batteries in several spacecraft, including *Surveyors I, V,* and *VII,* suffered damage by probable short-circuited cells after subjection to the rigors of lunar nights.

F. Conclusions

As a result of tests reported in this section, the following conclusions may be drawn:

(1) The main battery was capable of meeting the energy requirements of simulated missions for *Surveyors V, VI,* and *VII* without assistance from the auxiliary battery.

(2) The main battery was able to meet energy requirements for terminal descent, one lunar day, and at least 150 h into the lunar night.

(3) In low temperature operation, the main battery delivered 155 A-h at 20°F and 0.75 A, and 42.5 A-h at 0°F and 2.0 A. In a constantly dropping temperature environment, discharge at 0.23 A ceased at −33°F and the open circuit potential became 0.0 V at −147°F. Low rate charging was possible after warmup to −40°F and after further warmup, the battery accepted a full charge. Thus, limited operation was possible below 0°F, and some operation was possible at −40°F.

(4) Internal heat generation rates, measured on thermocouple-equipped batteries, indicated that the battery temperature transducer afforded a reasonably adequate measure of battery temperature. Negative plate temperatures were considerably higher than transducer and peripheral

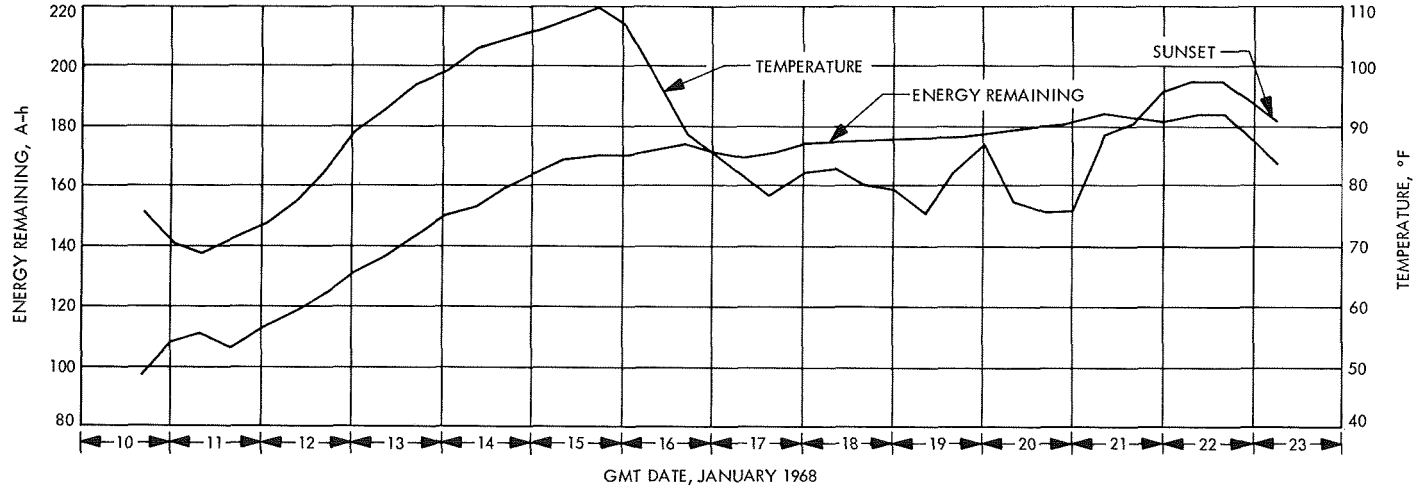

Fig. 160. First lunar day battery temperature and energy level, *Surveyor VII*

temperatures, but were within safe limits during simulation tests. Discharge at high rates, such as 50 A, will result in excessive temperature rise with rates of 81°F/h measured on negative plates and 34°F/h on the transducer and peripheral thermocouples. Such a temperature rise will ultimately destroy the battery.

(5) Calorimetric measurement of heat generation rates gave good agreement with theoretical values, based on a thermal model, and confirmed thermocouple results.

(6) Telemetered data, obtained during and after the flight, indicated satisfactory battery performance during all missions and fair agreement with STV tests and predicted performance. By careful management of the battery capacity, it was possible to achieve lunar night survival, where the battery recovered after exposure to an estimated minimum temperature of −180°F.

VIII. Battery Reliability

A. Introduction

Throughout the *Surveyor* battery reliability program, the probability of the successful performance of the battery for the prescribed mission has been a prime consideration. Battery reliability was established at ESB by tests on reliability batteries and at HAC by mission simulation tests using three flight batteries per mission. The three batteries for simulation tests were selected from six flight batteries assigned to the mission, with the remaining three batteries being shipped to the Air Force Eastern Test Range. The conduct of these simulation tests provided assurance that the battery could meet mission performance requirements. Battery failures were analyzed to ascertain the causes of failure so that product improvement could be properly oriented. The reliability growth is a measure of product improvement.

B. Reliability Test Program

The battery reliability test program established confidence in the capability of the battery to perform an assigned mission by simulating launch, transit, touchdown and lunar operation. A typical simulated mission consisted of a low rate discharge (transit), a high rate discharge of short duration, with superimposed pulse discharges (RADVS during touchdown), and low rate charging with periodic charge and discharge pulses (lunar operation).

1. Battery reliability tests (ESB). The ESB battery reliability tests demonstrated the ability of the flight battery to meet the reliability requirements. Nine reliability batteries were subjected to the required type approval vibration test described in Table 3. All nine batteries passed the tests and the results were factored into the reliability growth presentation (see Fig. 174).

2. Mission simulation tests (HAC). The HAC mission simulation tests provided a measure of the capability of the battery to meet a given mission profile. Owing to the basic similarity among these tests, only the *Surveyor VI* Mission simulation is presented.

a. Procedure. The procedure involved: (1) The normal FA test sequence to qualify three batteries for the reliability test, and (2) performing the test sequence, described in Table 76, on two batteries in a chamber and on a third battery at laboratory ambient environment.

Table 76. Test sequence

Mission sequence	Function and duration
Transit	Discharge at 3.0 A for 24 h
Touchdown	RADVS simulation
Lunar operation simulation	Nine days of regime—16 h charging at 1.5 A, followed by 8 h of pulsing
Post-mission capacity test	Discharge at 7.0 A to 17.5 V
Post-mission recharge test	Charge at 2.0 A to a limit of 27.30 (+0.00, −0.14) V, then float-charge at 27.0 (+0.01, −0.0) V until the float-charge current decays to less than 0.25 A

In the test sequence of Table 76, the RADVS simulation function at touchdown consisted of 4.0 min of operation at 50 A with four 20-A, 20-ms pulses, superimposed at 1.0-min intervals. During the lunar operation simulation sequence, the 16-h charging at 1.5 A involved charging with limiting voltage of 27.1 V. The 8-h pulsing time during lunar operation simulation included TV and A/SPP operation. Television operation consisted of 4800 cycles (6 s each) over 8 h; each cycle consisted of a 1.4-s pulse discharge at 2.66 A, and a 4.6-s pulse charge at 0.89 A. On some days of testing, the charge part of the pulse was omitted. The A/SPP operation consisted of 100 pulses; 20 at the start of the 8-h period repeated every 2 h. Each pulse draws 11.4 A for 65 ms.

b. Results. Battery assignments for the reliability test are indicated in Table 77. Temperature, pressure, potential, current, ampere-hour, and watt-hour data for one

Table 77. Battery test assignments for reliability test

Battery SN	Battery age at start of test, days	Temperature profile
152	69	High temperature[a]
153	69	High temperature[a]
154	69	Room temperature

[a]Battery temperature up to 125°F.

high temperature profile (battery SN 152) and the room temperature profile (battery SN 154) are presented in Figs. 161–168. Calibration curves for temperature and pressure transducers were presented in Section V (see Fig. 65). Postmission discharge and recharge data are presented in Table 78.

c. Discussion and conclusions. The minimum discharge potential of 21.5 V during lunar operation simulation was well above the minimum permissible value of 17.5 V, and was therefore acceptable. The maximum pressure, occurring during float-charge, was 23 psia, well under alarm conditions (see Fig. 93). Maximum battery temperature during operation at ambient temperature was 89°F, while batteries in a chamber reached 125°F. As evidenced by capacity data, the *Surveyor VI* batteries did not suffer deterioration in capacity as a result of the reliability test. On the basis of the results, it was concluded that the batteries were capable of meeting *Surveyor VI* Mission requirements.

Table 78. Postmission battery capacity data for reliability test

Battery SN	7.0 A discharge		2.0 A recharge	
	Ampere-hours	Watt-hours	Ampere-hours	Watt-hours
152	181.3	3840.1	177.2	4535.7
153	180.8	3831.7	179.5	4597.4
154	181.1	3847.2	176.9	4449.4

C. Failure Analysis

High reliability was sought by an analysis of potential flaws in processes and by a detailed investigation of all test failures.

1. Failure mode analysis. Production operations have been analyzed to establish check points, that will permit the inspection for production flaws before they become concealed in subsequent assembly. Table 79 summarizes the failure mode analysis, the effect on battery performance, and steps taken to eliminate the cause. In addition to failure mode analysis, individual cell, monoblock and battery failures were investigated to seek out the failure mode.

2. Analysis of typical flight battery failures. In a typical end-of-life failure, separator deterioration resulted from many low rate shorts that caused pressure formation and heat generation. Two examples of battery failure will be analyzed in the subsequent paragraphs.

a. Failure of reliability battery SN R-11. Battery SN R-11 failed with the following symptoms:

(1) Cells 6 and 8 read 0.000 V.

(2) Excessive pressure rise during and after charge.

(3) Low insulation resistance between battery terminals and ground.

(4) Evidence of electrolyte leakage around lead wires.

Autopsy results. An autopsy of the shorted cells revealed:

(1) A short in both cells at the edge of a positive plate strut, as shown in Fig. 169.

(2) Discoloration of six layers of cellophane separator from reaction with active positive materials, resulting in the distribution of active material in the separator, as plotted in Fig. 170.

(3) Significant reduction in the wet strength of the cellophane separator.

(4) Electrolyte leakage between the cells and the battery chassis due to electrolyte paths along the voltage tap leads.

Explanation. Apparently the pressure from the negative material forced the separator into the indentation of the positive plate assembly (see Fig. 169), causing stresses that resulted in the development of a hole in the separator. Zinc from the negative plate then penetrated the hole to furnish a short circuit path to the positive plate.

Recommendations. Design modifications in strut and coining die were made to eliminate the depressed area between the edge of the plate and the coined edge and by revision of the negative frame so that there is no negative material in the area of the depression in the positive plate.

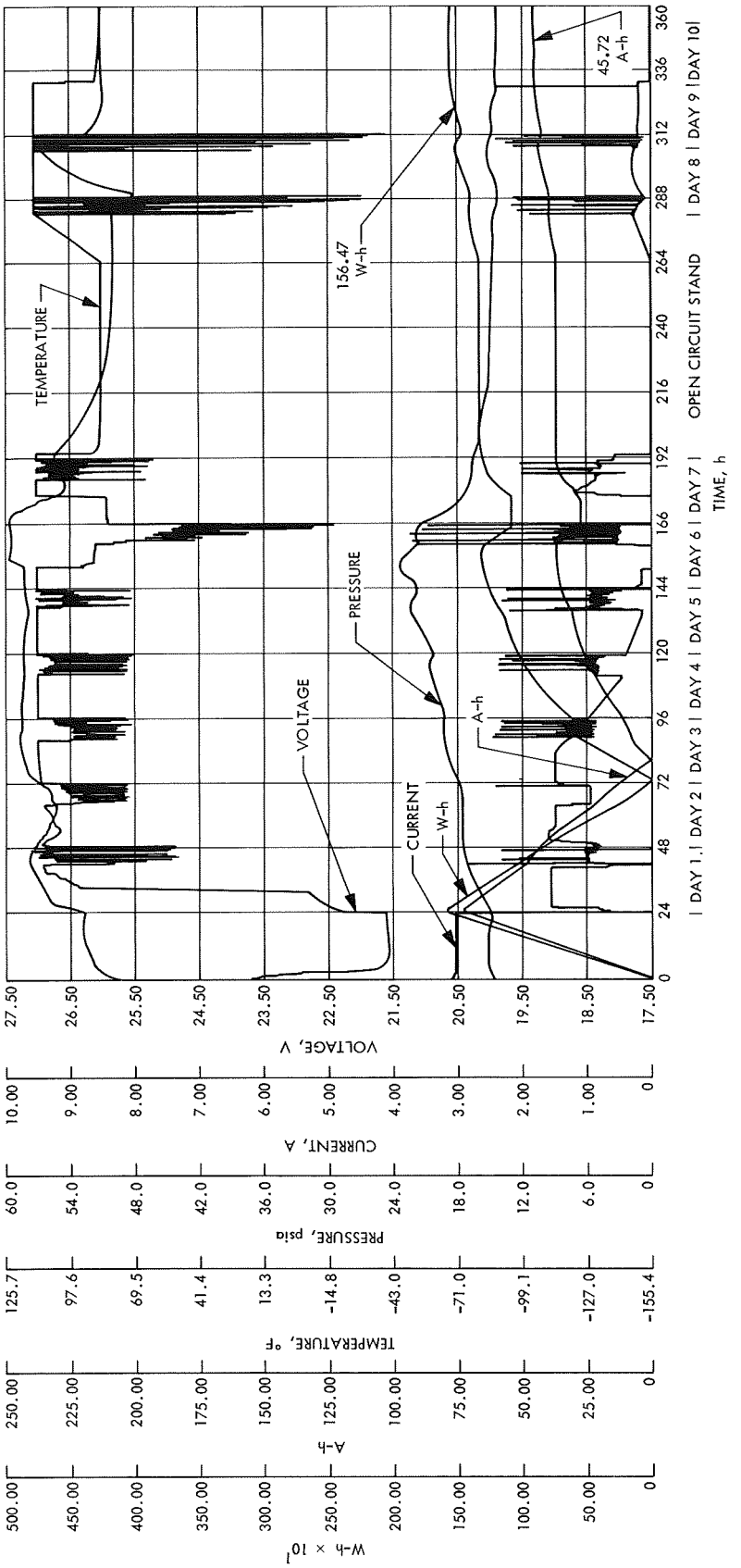

Fig. 161. Surveyor *VI* reliability test, SN 152

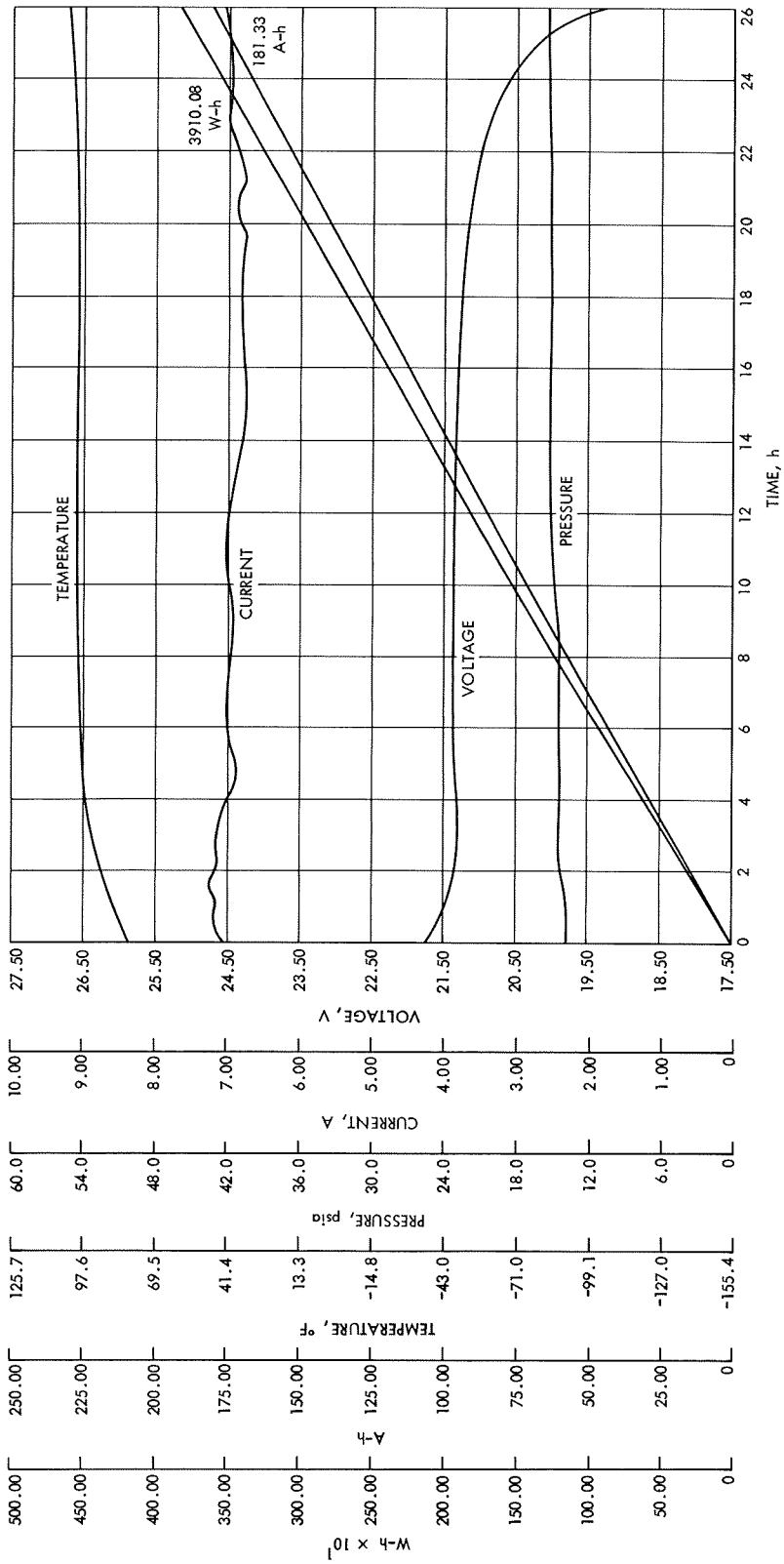

Fig. 162. *Surveyor VI* reliability test, SN 152—7-A discharge

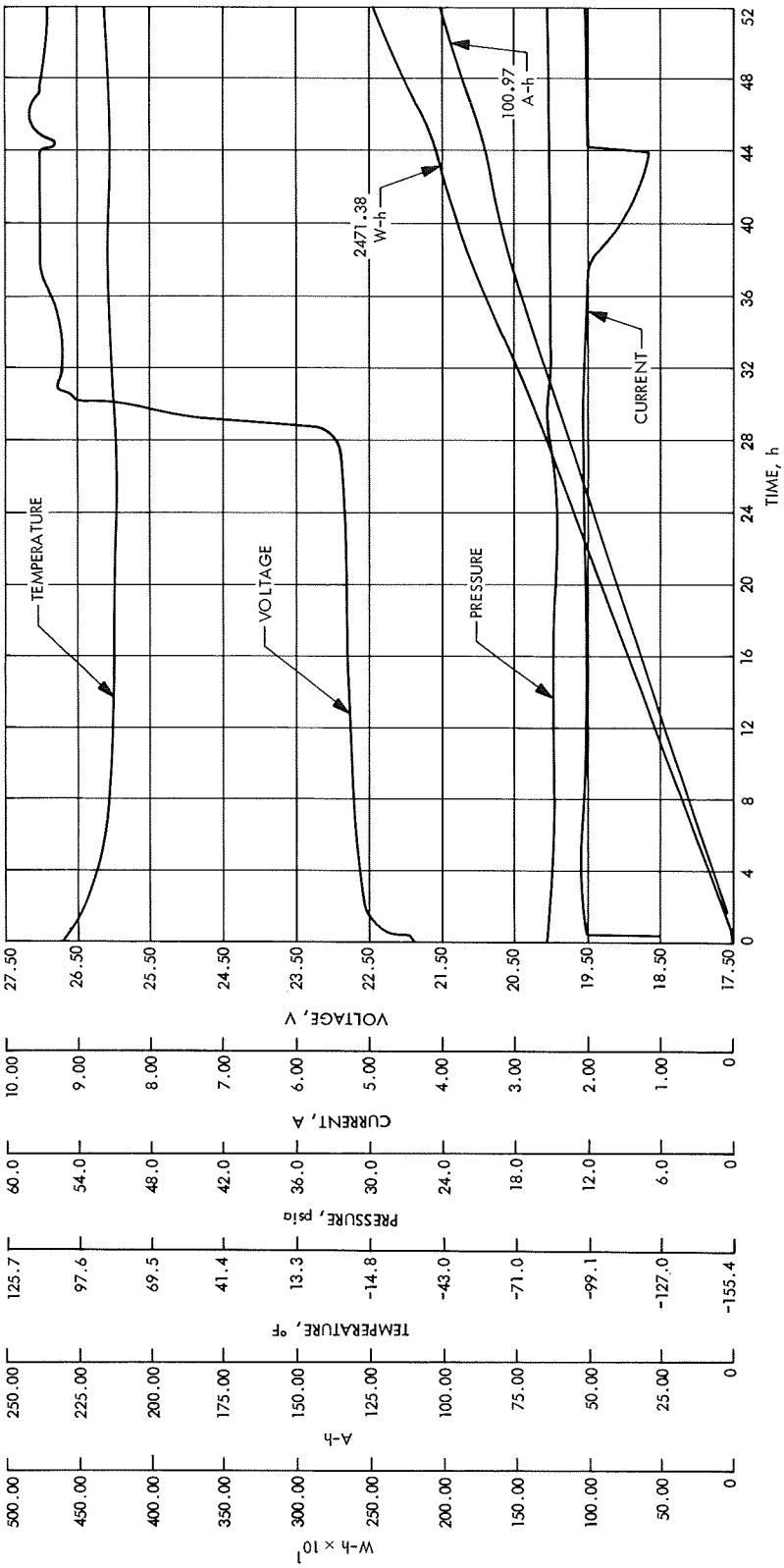

Fig. 163. Surveyor VI reliability test, SN 152—2-A discharge

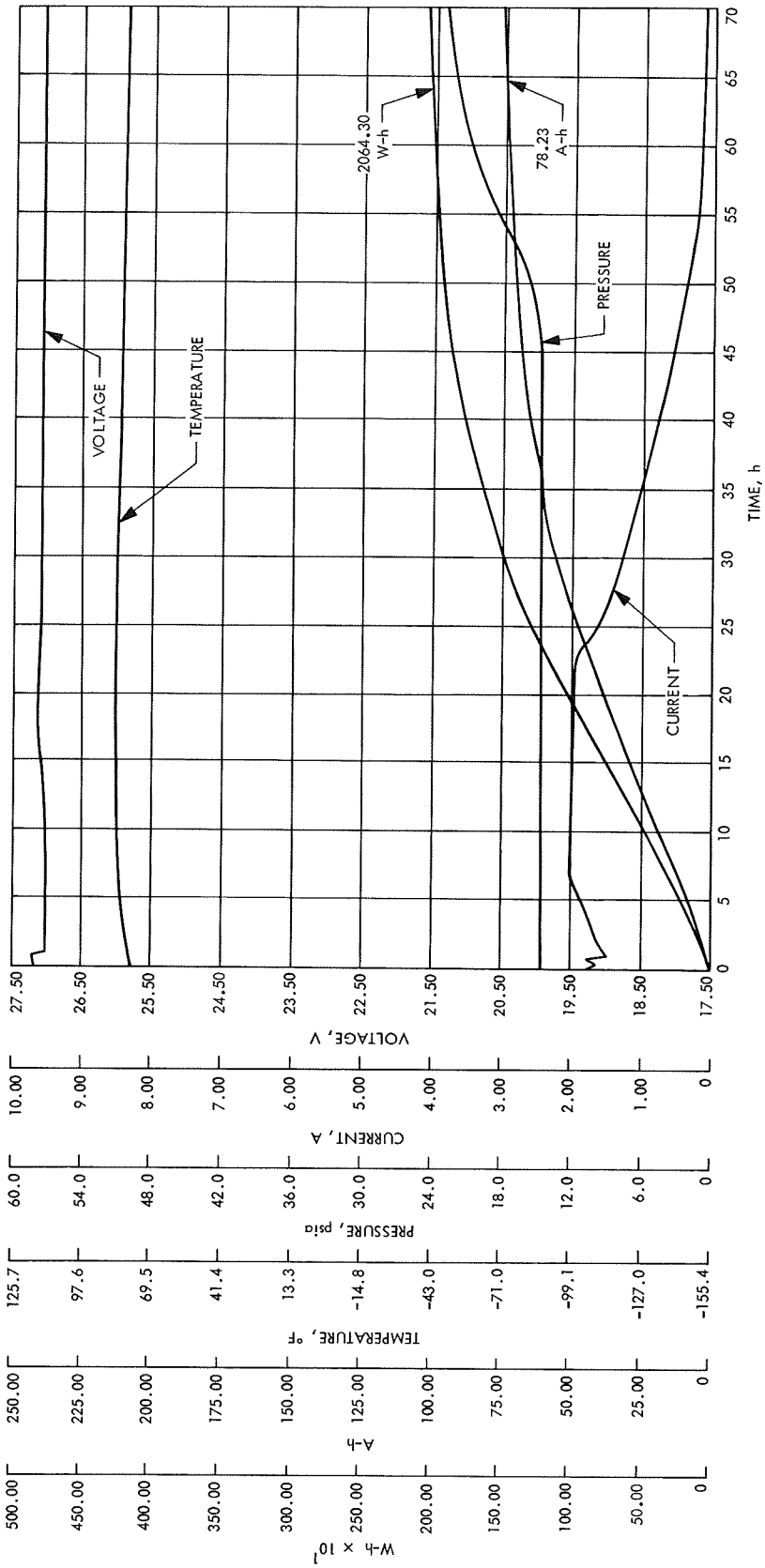

Fig. 164. *Surveyor VI* reliability test, SN 152—2-A charge

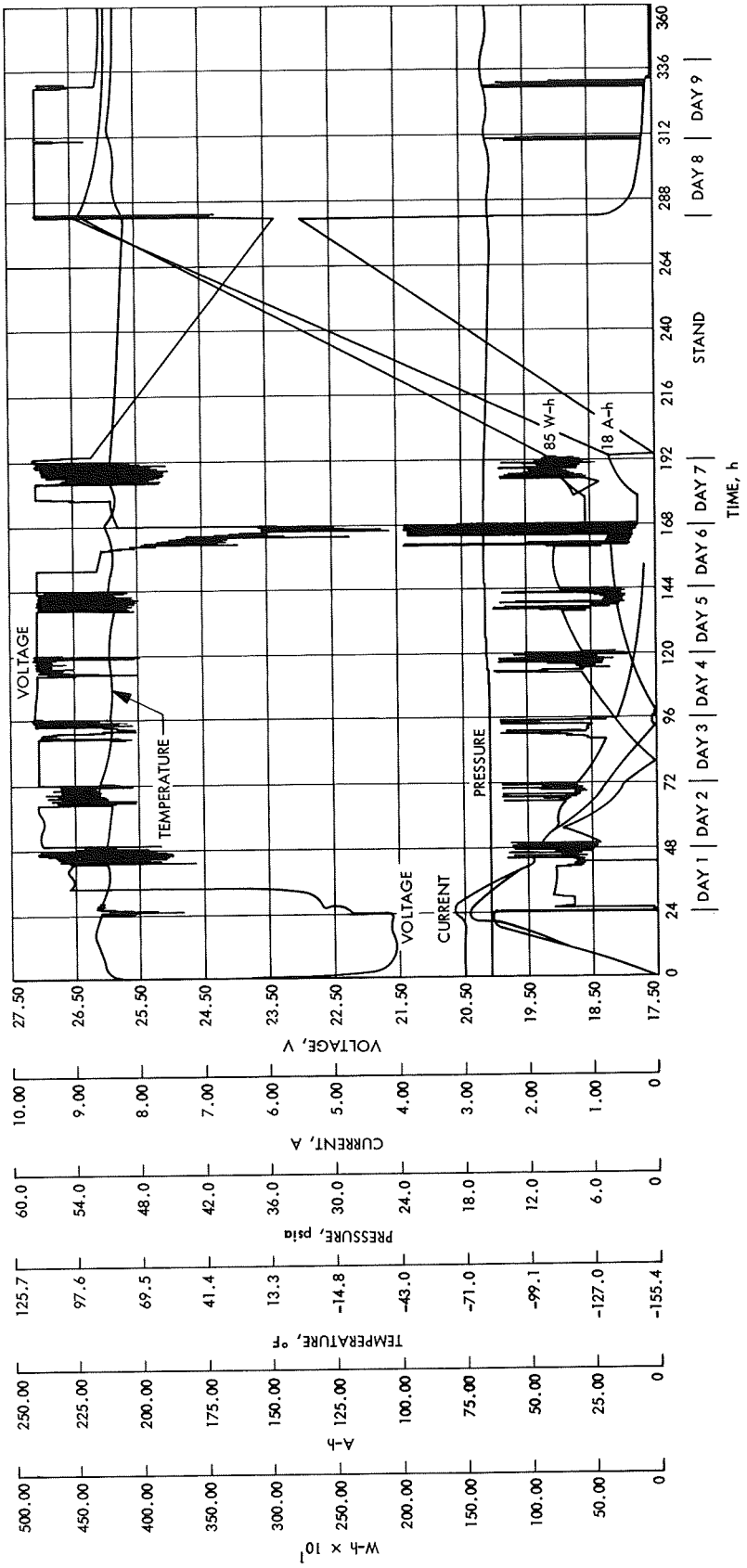

Fig. 165. Surveyor VI reliability test, SN 154

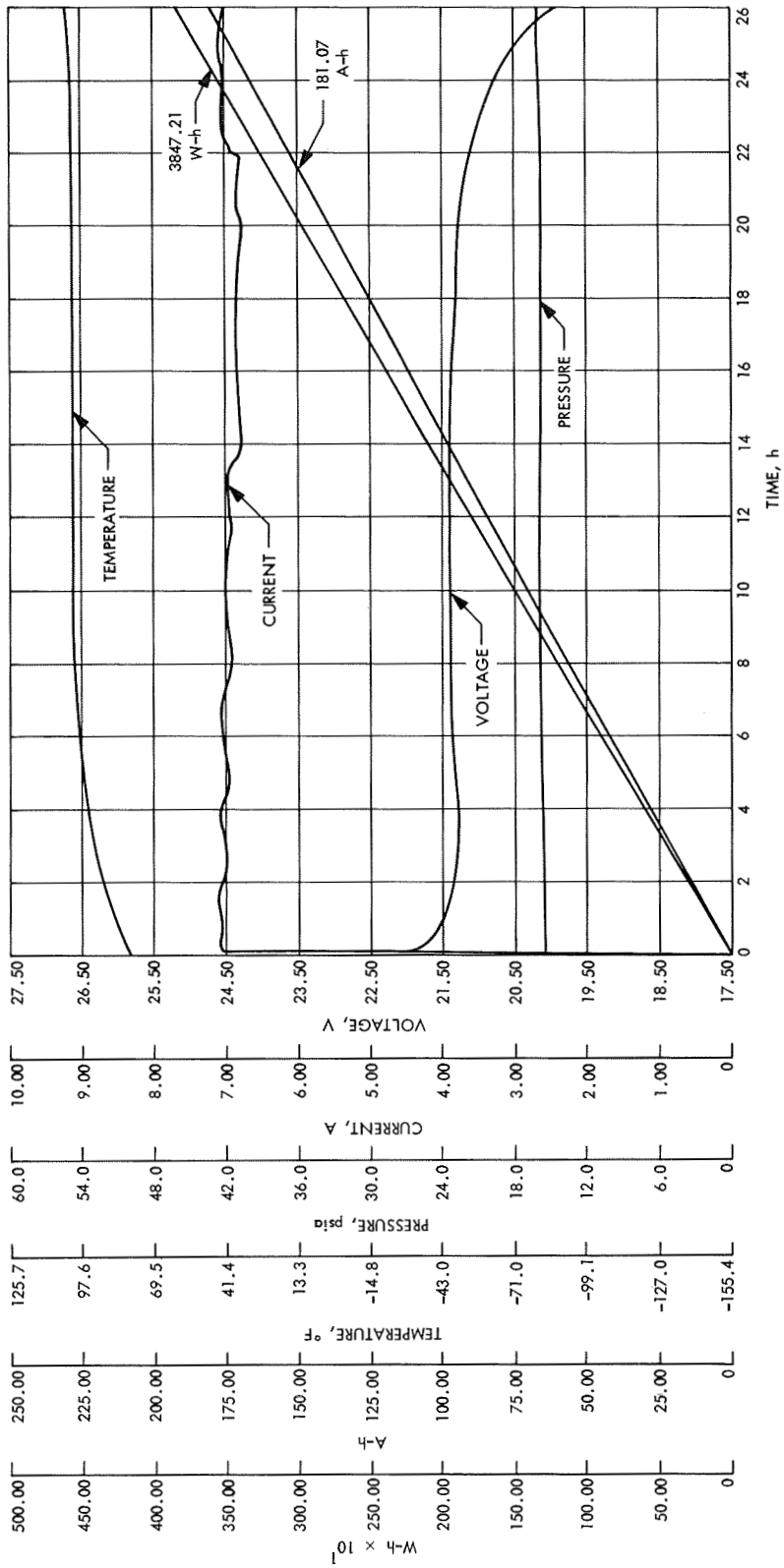

Fig. 166. *Surveyor VI* reliability test, SN 154—7-A discharge

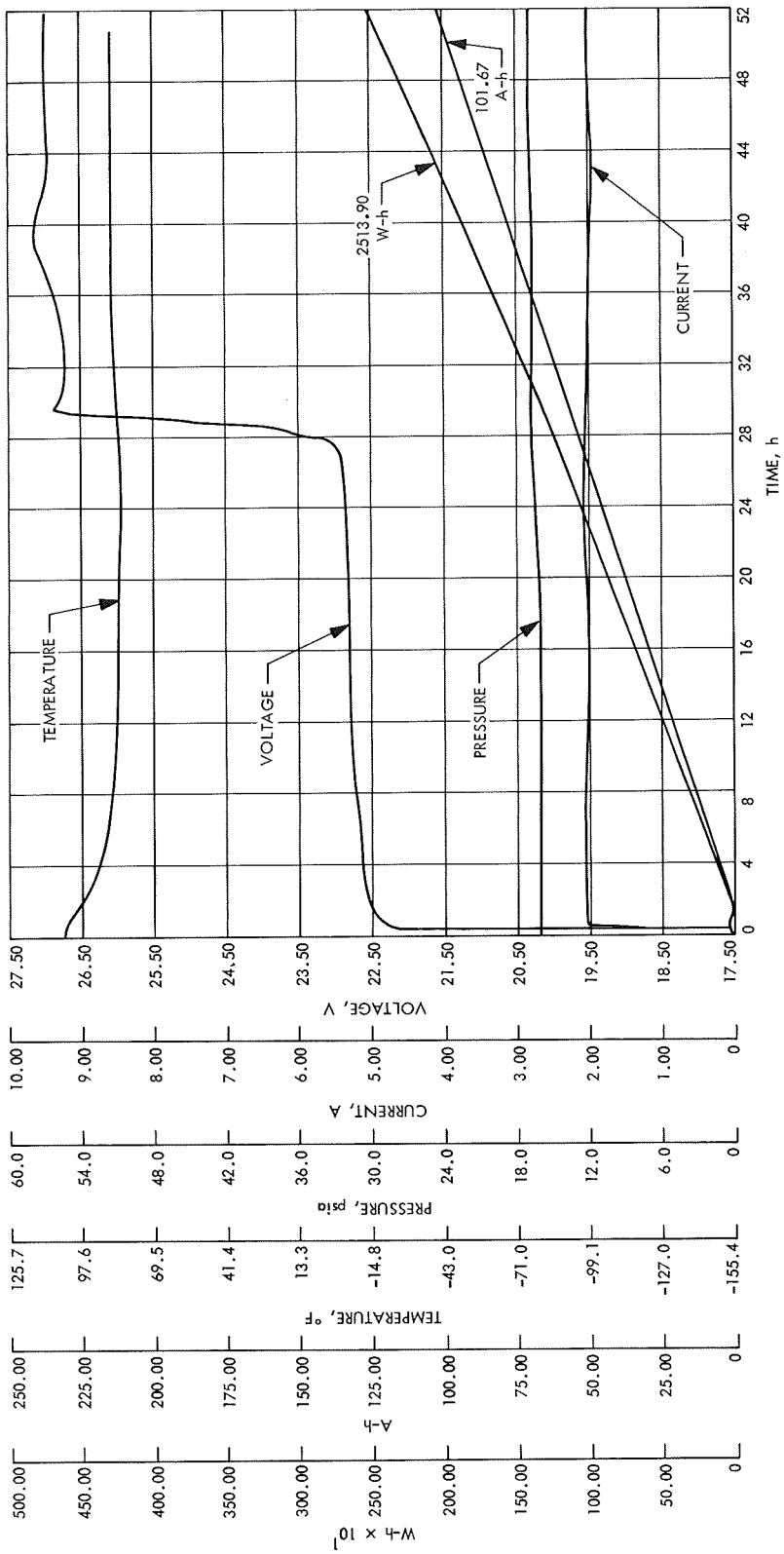

Fig. 167. Surveyor VI reliability test, SN 154—2-A charge

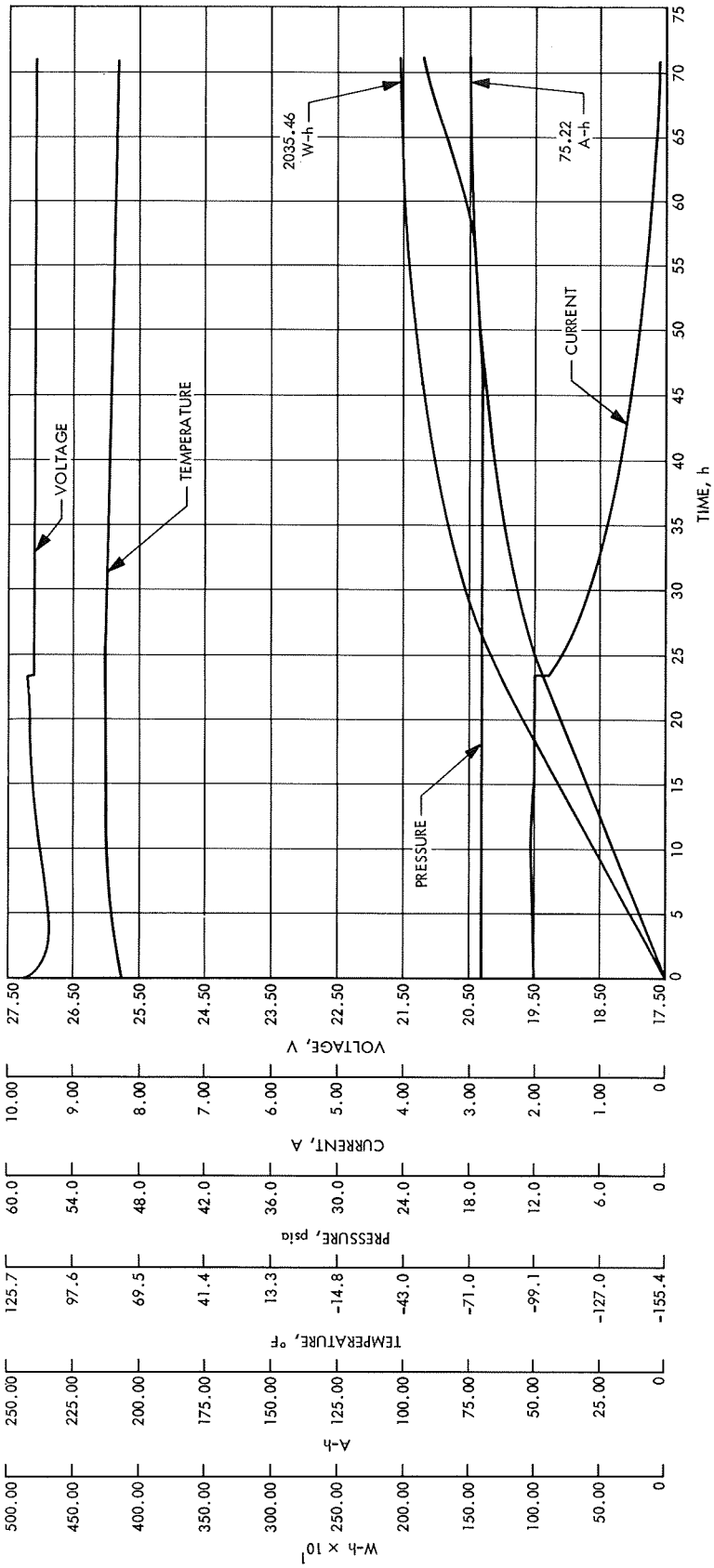

Fig. 168. *Surveyor VI* reliability test, SN 154—2-A charge

Table 79. Failure mode analysis

Process description	Item concealed as a result of process	Failure mode (discrepancy)	Effect on battery performance if discrepancy exists	Steps taken to eliminate discrepancy
Positive plate				
Process silver powder and binder material and inspect	None			
Inspect grid material and cut to size	None			
Process silver material and grid including blanking, sintering and pressing, and coining operations, each followed by a physical inspection	Grid	Exposure of grid wires at edge of silver material could tear separator or cell pack wrapping	Electrical short	Processed plate is inspected to detect stray wire
Inspect lug wire	None			
Spot weld lug wire onto plate and inspect	None	Defective weld could affect cell electrical output	Degrade performance	Each weld is subjected to pull test
Roll, cut and inspect red spaghetti tubing	None			
Assemble tubing onto lug wire	Lug wire	Wire defect which could cause wire breakage during vibration testing	Electrical open	Inspection of wire including pull and torsion test at 028 plus addition of struts at 039–042
Assembly of struts onto plate and inspect	None	Strut pulling off the plate Plate cracking at coined corner Either would cause loss of lug wire during vibration	Electrical open	Strut is redundant with lug wires—no special steps are taken to prevent failure mode
Negative plates				
Mix negative materials	None			
Cut retainer to size and inspect	None			
Lug wires received and inspected	None			
Cut grid to size and inspect	None			
Spot weld lug wire to grid and paint and loop lug wires and inspect	None			
Assemble negative plate and inspect	Grid	Exposure of grid wires could tear or puncture separator or cell pack wrapping	Electrical short	Processed plate is inspected to detect stray wires
	Weld juncture	Defective weld could affect cell electrical output	Degrade performance	Each weld is subjected to visual test

Table 79 (contd)

Process description	Item concealed as a result of process	Failure mode (discrepancy)	Effect on battery performance if discrepancy exists	Steps taken to eliminate discrepancy
Monoblock assembly Assemble positive plates, negative plates and separators	Plates and separators, individual positive plate weights	Cracked cellophane, broken plate, unequal weight distribution within cell	Electrical short or degradation in performance	Visual inspection before and after assembly segregation of plates by weight
Receiving inspection, machining, assembly and final inspection of cell cases	None	Faulty material	Catastrophic failure (battery)	Proof pressure test plus strict quality controls to eliminate scratches and stress buildup
Insertion of cell assembly into cell case and inspection	None	Folding, crinkling or tearing separator upon insertion	Electrical short	Special fixture is used for insertion
Machining and inspection of terminal well	None			
Install terminal well and cement	Ability to align plates	Misalignment	Power degradation or electrical short	Dimensional inspection
Receiving inspection, machining and final inspection of cell covers	None			
Receiving and inspection of vent tube	None			
Receiving and inspection of slot plugs	None			
Assembling cover assembly	None			
Install cover assembly on monoblock and inspect	None			
Receiving inspection of voltage tap leads and crimp connectors, installation of tap leads, intercell connections, and inspection	Crimped lug wires	Broken lug wire	Power degradation	Pull test on crimped joint
Receiving inspection, ramaset and paint terminals	None			Continuity test
Receiving inspection potting materials and mixing potting compound				
Pot terminal weld and inspect	Struts, lug wires	Electrolyte leakage due to poor encapsulation at lug wire	Electrical short	Pressure check of internal cell

Table 79 (contd)

Process description	Item concealed as a result of process	Failure mode (discrepancy)	Effect on battery performance if discrepancy exists	Steps taken to eliminate discrepancy
Receiving inspection of electrolyte material, mixing and inspection of electrolyte	None			
Activation of cells and inspection	None	Improper amount of electrolyte	Too little—low electrical capacity; too much—overweight cell	Weight and visual inspection
Cell charging and inspection	None	Inability to accept full charge	Insufficient capacity	Visual monitoring during charge process
Monoblock assembly and inspection	None			
Battery assembly Cement monoblocks together; receiving inspection of vent tubes and tube guards; install vent tubes and guards	Adjacent sides of monoblocks			
Install crimp connector and tap wire; inter-monoblock connections	Crimped lug wires	Broken lug wire	Power degradation	Pull test on crimped joint
Receiving inspection of standpipe and filter; assemble standpipe and inspect; install standpipe assembly and inspect	Cell interior, standpipe orifice	Plugged standpipe	Pressure buildup and probable cell rupture	Air flow check and visual inspect electrolyte level
Install potting channels on top of monoblock	Intercell connections	None		
Receiving inspection of magnesium case; paint case	None			
Receiving inspection of potting materials, mix potting compound and pot 14-cell battery into case	14-cell battery assembly	Void in potting material could cause cell rupture	Catastrophic battery failure	
Receiving inspection; inspection of spacers and insertion of spacers between battery and case	Spacer	Battery alignment	None	
Receiving inspection of electrical connectors and wire; assembly and inspection of wiring harness	None	Poor electrical continuity	Electrical open	Electrical continuity and dielectric inspection

Table 79 (contd)

Process description	Item concealed as a result of process	Failure mode (discrepancy)	Effect on battery performance if discrepancy exists	Steps taken to eliminate discrepancy
Receiving inspection of miscellaneous assembly hardware	None			
Install wiring harness and inspect	Crimped connections	Broken wire	Electrical open, power degradation	Pull test on crimp connections, electrical continuity check
Receiving inspection and installation of vent block	None			
Receiving inspection of potting materials and pot channels	All wiring in potting channels	None		
Drill vent block for pressure transducer	None			
Receiving inspection of heat transfer and pot heat transfer in place	Heat transfer	None		
Receiving inspection and install manifold covers	Manifold internal	Gas and electrolyte leakage around cover	Power degradation	Proof pressure and leak check; manifold flow check
Receiving inspection of miscellaneous assembly hardware and temperature transducer mounting block; install mounting block	None			
Receiving inspection of miscellaneous mounting hardware and holddown bars; paint bars; install bars using associated hardware	None			
Receiving inspection and installation of flow hold plug	Manifold passages	Manifold blockage, loss of plug	Cell case rupture, power degradation	Manifold flow check, proof pressure and leak check
Proof and leak test; inspection tests				
Receiving inspection; fabrication, inspection and installation of terminal board assembly	None			

Table 79 (contd)

Process description	Item concealed as a result of process	Failure mode (discrepancy)	Effect on battery performance if discrepancy exists	Steps taken to eliminate discrepancy
Receiving inspection of temperature transducer and associated hardware; fabrication, inspection and installation of transducer assembly	None	Transducer failure	Loss of engineering data	Functional preassembly tests
Receiving inspection of pressure transducer, O-ring and associated hardware, installation of transducer	None	Transducer failure	None	Built-in redundancy of manual override
Receiving inspection of cable clamp and safety wire, and associated hardware, install clamp and wire	None	Broken cable clamp of safety wire	None	
Battery assembly and inspection	None	None		
Receiving inspection shipping cover, stencil ink; install and inspect	None			
Receiving inspection of packaging materials; final packaging and inspection	None			

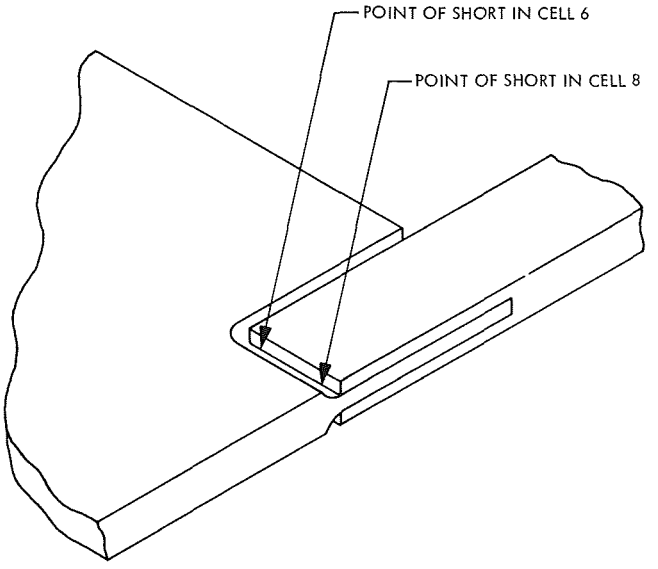

Fig. 169. Configuration of positive plate in area of shorts

b. Failure of battery SN 74. Battery SN 74 exhibited the following failure symptoms:

(1) During open circuit stand, rising battery pressure, rising battery temperature, and dropping battery potential were indicated.

(2) After 2 h of charge, lower potentials were indicated on cells 1, 4, 5, and 13.

Autopsy results. An autopsy of the battery indicated:

(1) Massive crystal growths (potassium oxalate) against the positive plate (Fig. 171) and between layers of separator.

(2) Discoloration from layer to layer of separator (Fig. 172).

(3) A relationship between the presence of oxalate crystals and separator discoloration.

Explanation. It is postulated that the following events occurred:

(1) Hydrolysis of cellophane, forming glucose.

(2) Oxidation of glucose by silver oxide to form oxalic acid.

(3) Conversion of oxalic acid to potassium oxalate.

(4) Crystal growth causing increased pressure areas, and decrease in separator thickness.

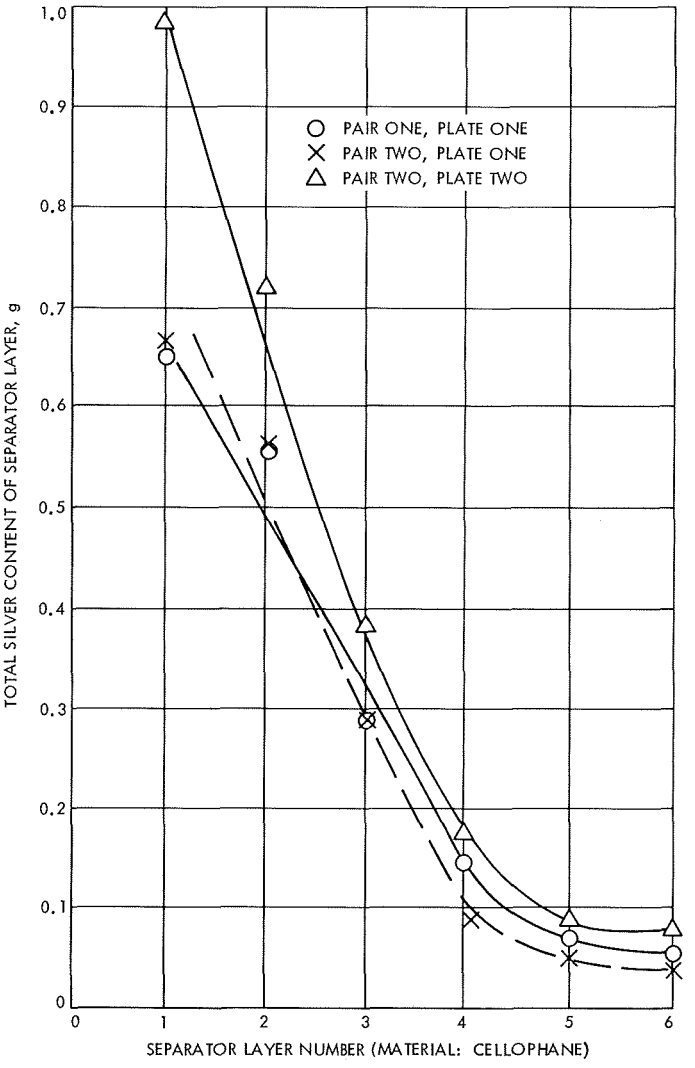

Fig. 170. Silver content of separator in failed reliability battery, flight model

(5) Collection of silver from the less soluble but more active divalent oxidation state (Ag^{+2}) about the growth centers.

(6) Creation of a low resistance path between positive and negative plates, causing a low rate short.

D. Reliability Growth of *Surveyor* Main Battery

The reliability growth for the several generations of the *Surveyor* main battery has been calculated for transit and the first and second lunar days. This subsection provides information concerning the method of calculation and the results of such calculations for reliability at the 80% confidence level.

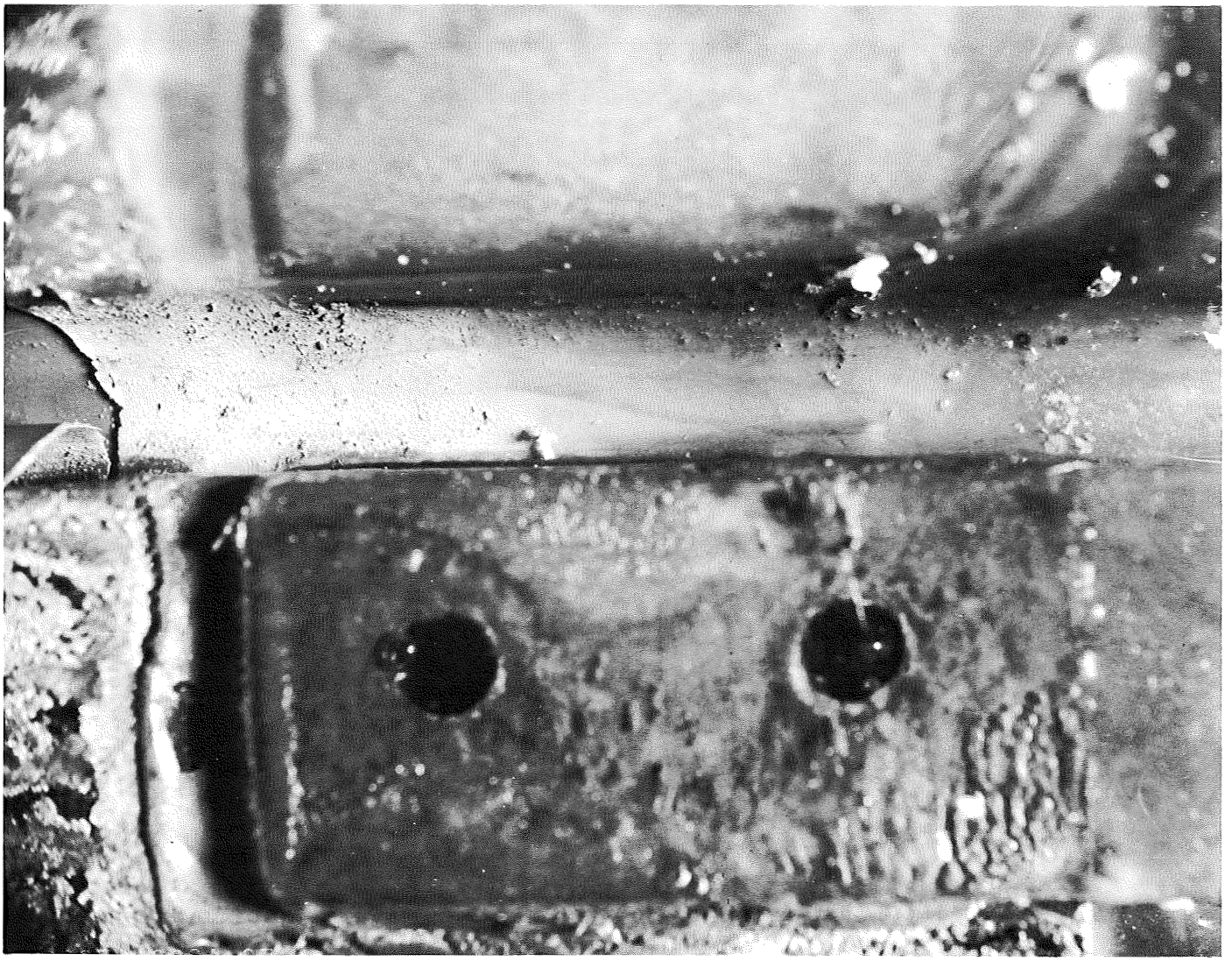

Fig. 171. Oxalate crystals on positive plate

Fig. 172. Typical deterioration of separator—*Surveyor* main battery

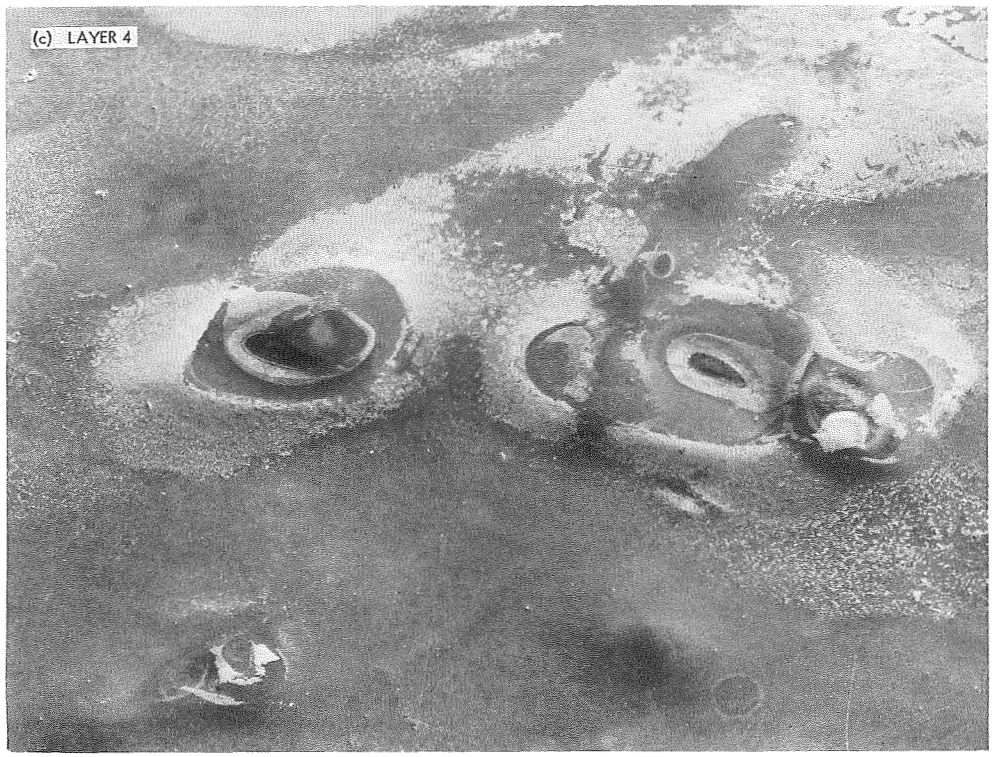

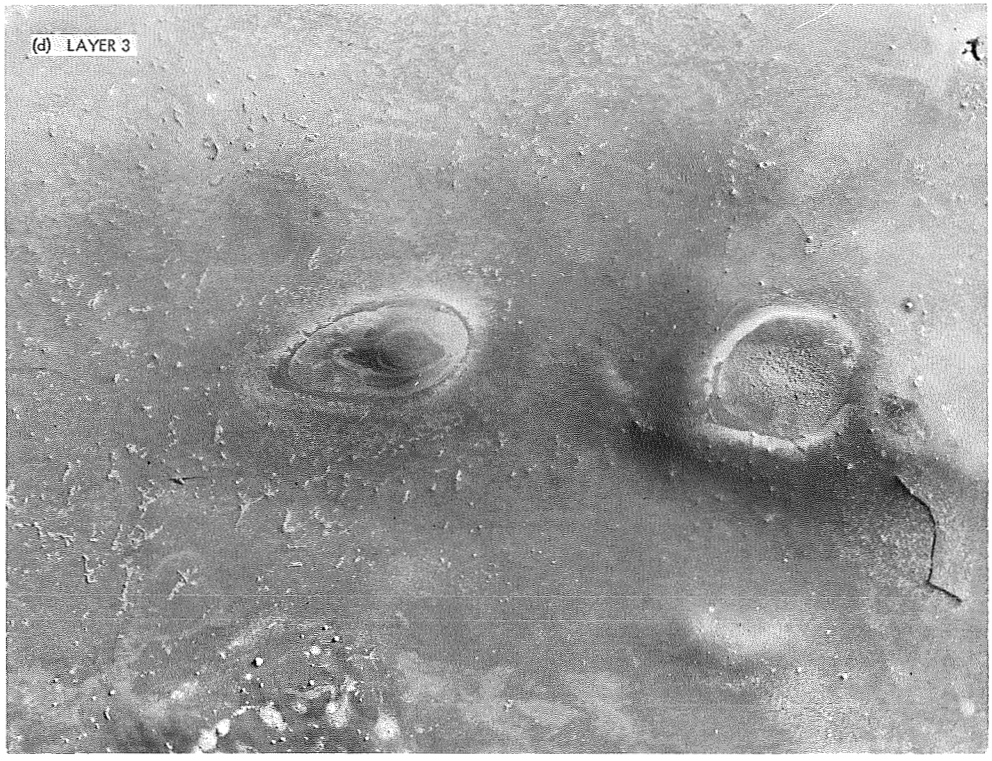

Fig. 172 (contd)

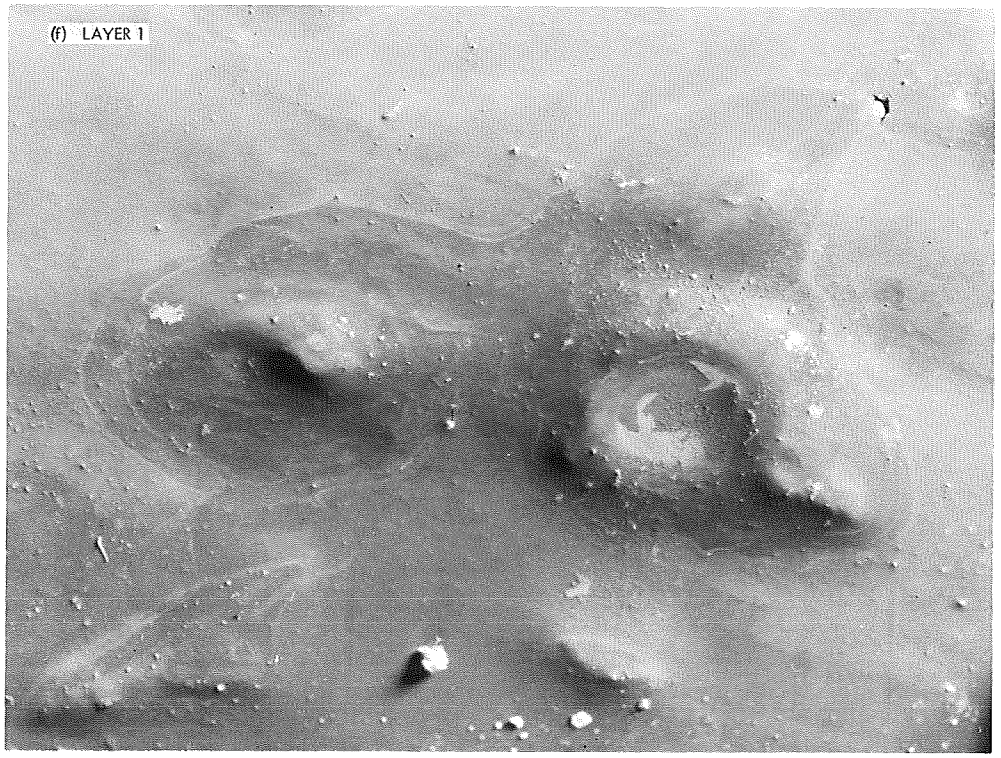

Fig. 172 (contd)

1. Methods of calculation. The reliability values are the product of life and capacity reliabilities, where: life reliability (R_S) is an exponential function (Fig. 173), that defines the probability that the battery will function successfully for a specified mission without failure due to cell shorting. Life reliability is calculated by the equation

$$R_S = e^{-t/M}$$

where

t = required life

M = mean time to failure = $\dfrac{\text{total life}}{f}$

f = failure constant

Failure constants for the 80% confidence limit are stated in Table 80.

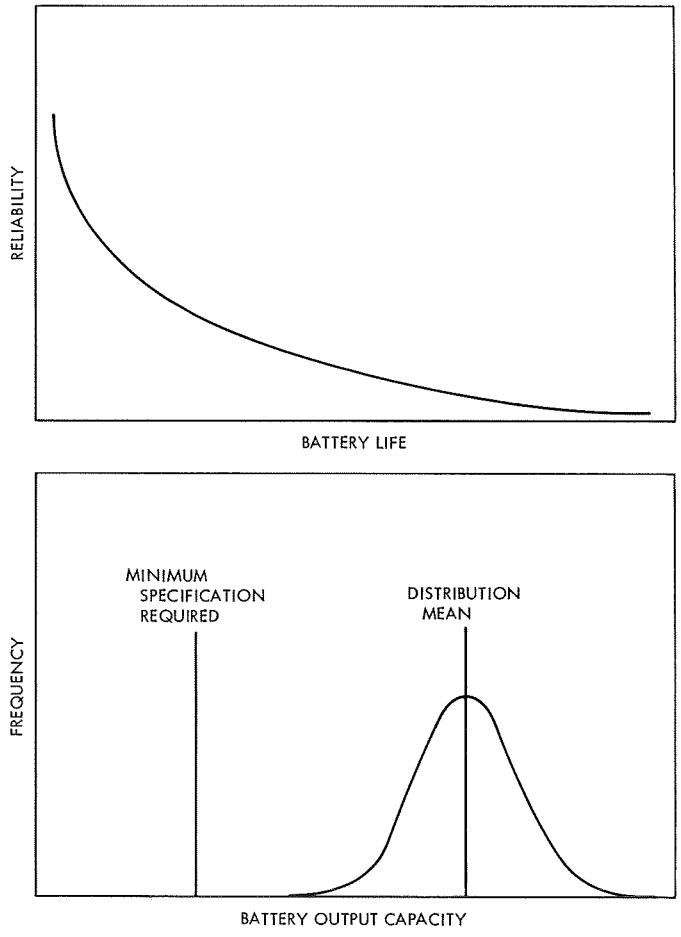

Fig. 173. Battery life and output characteristics

Table 80. Calculated failure constants

Number of failures	Failure constant[a] at 80% confidence
0	1.6
1	3.0
2	4.3
3	5.3
4	6.7
5	7.9
6	9.1
7	10.3
8	11.4
9	12.5
10	13.7

[a]Calculated with the aid of Ref. 10.

Capacity reliability (R_C) is a normal function (Fig. 173) and is defined as the probability that the battery will deliver the required ampere-hour output. Capacity reliability was obtained by calculating the number of standard deviations that the normal distribution was above the specified requirement using the equation

$$K\sigma = \overline{X} - A$$

where

K = the number of standard deviations

σ = the standard deviation

$\overline{X}$ = the distribution mean

A = the specified requirement

The reliability value was then obtained using a table of tolerance factors for normal distributions (Ref. 11).

Battery reliability has been calculated for *Surveyor* batteries, subjected to the following mission:

(1) The transit phase with 67 h of successful operation without shorted cells and delivery of 1.6 and 7.0 A-h.

(2) Lunar day 1 with 80 h of successful operation and 147 h without failure due to shorts, with delivery of 1.6, 7.0, and three times 12 A-h.

(3) Lunar day 2 with 863 h of successful operation without failure due to shorts, with delivery of 1.6, 7.0, 60, 30, and 126 A-h.

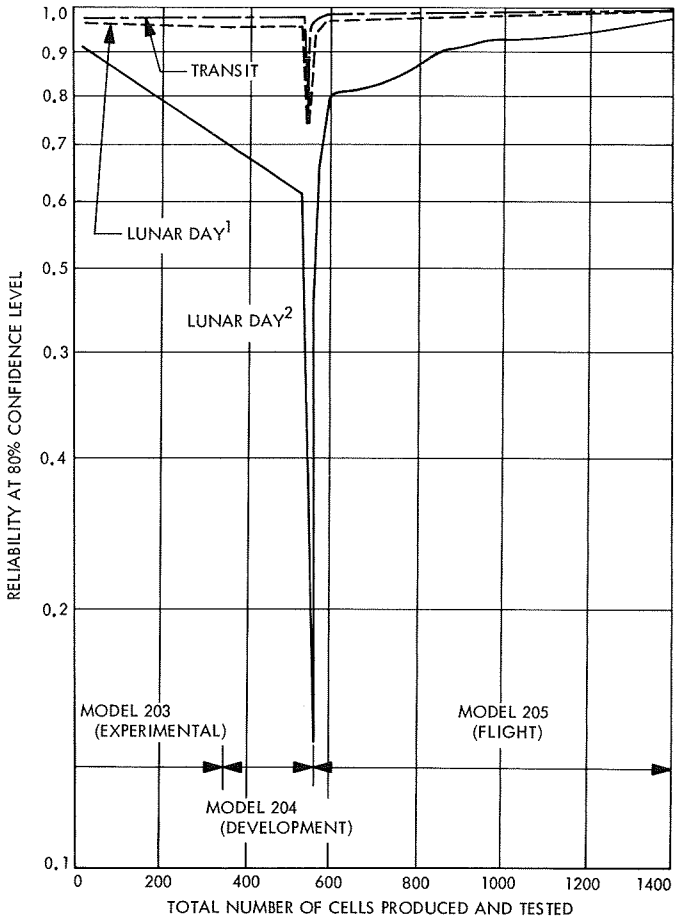

Fig. 174. Life reliability growth presentation

Life data for cells and batteries were obtained by screening laboratory test data. Failures from unreasonable causes, such as high temperature storage, from consideration were not included.

2. Results and discussion. Results of the reliability growth calculations are shown in Fig. 174. It is interesting to note that model changes, such as the introduction of the first prototype batteries (accompanied by charge acceptance problems), are reflected by drastic changes in calculated reliability. The reliability growth calculations do not appear to take into account failure during charge, which could well be a major cause. However, the absence of battery failures during the mandatory phases of all missions is the best testimonial for the high reliability of the flight model battery.

E. Conclusions

Reliability tests preceding missions and actual missions have established the high reliability of the final flight version of the *Surveyor* main battery. The high degree of reliability was achieved by product improvement, resulting from painstaking failure analyses and quality control.

Typical end-of-life failures were due to separator failure, caused by hydrolysis of cellophane separator material with subsequent formation of potassium oxalate crystals by oxidation of the hydrolysis product. Silver oxide acts as oxidizing agent in this proposed reaction mechanism. Ultimately the growth of potassium oxalate crystals leads to decrease in separator thickness and eventual penetration of the separator material, terminating in a plate-to-plate short between positive and negative plates.

IX. *Surveyor* Auxiliary Battery

A. Purpose

The auxiliary battery provided a backup for both emergency power and peak power loads for the main battery and solar panel and supplied additional power for the engineering payload during the first lunar day.

A battery containing similar cells had already been qualified to Lockheed Missiles and Space Company specifications for use on the *Mercury* and *Agena* programs, for which reason only a limited test program was undertaken.

This section provides a brief treatment of the performance requirements, a description of the auxiliary battery[8] design, and performance.

B. Program Summary

The auxiliary battery program got underway in May 1963 with a preliminary design effort and the preparation of a procurement specification. Since the auxiliary battery was essentially identical to an earlier Lockheed Aircraft Company spacecraft battery, no sharply defined experimental, developmental, prototype and flight phases were discernible. All generations of auxiliary batteries used the same cell and the differences in batteries were confined to matters such as changes in canister dimensions, potting material used on cables, etc. Therefore, the data for even the experimental model are applicable to flight batteries. Table 81 summarizes important dates in the program.

[8]Eagle-Picher Company, Joplin, Mo., Model 4193 MAP.

Table 81. Auxiliary battery program milestones

Action	Jan 63	Jan 64	Jan 65	Jan 66	Jan 67	Jan
Design specifications	Δ					
Contract to Eagle-Picher Company	Δ					
Delivery of first battery	Δ					
Completion of first type approval test	Δ					
First spacecraft launch (SC-1)				Δ		
Launch of SC-2				Δ		
Launch of SC-3					Δ	
Launch of SC-4						Δ

C. Performance Requirements

The auxiliary battery was required to meet the following criteria for a minimum period of 30 days after activation: A potential between 18.5 and 26.0 V when discharged in the temperature range from 70 to 110°F in accordance with Fig. 175. This included a current of 50 A for 4 min, followed by five 70-A, 50-ms pulses. The battery also had to be capable of delivering the watt-hour capacity shown in Table 82 after activation, when discharged in accordance with Fig. 176.

Table 82. Auxiliary battery watt-hour requirements

Time from activation days	Battery capacity, W-h
0	1000
15	900
20	800

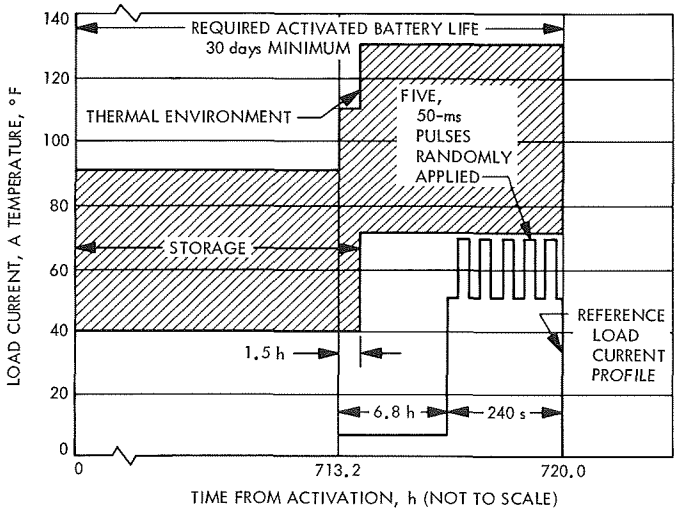

Fig. 175. Auxiliary battery load and temperature profile

Environmental performance requirements generally resembled the *Surveyor* main battery requirements (for further details, see Section II).

D. Battery Design Description

1. General. The auxiliary *Surveyor* battery was a primary silver–zinc battery, consisting of 14 series-connected cells in plastic cases (styrene-acrylonitrile copolymer) and potted into a magnesium[9] canister sealed by a gasketed aluminum cover. A side view of the auxiliary battery is presented in Fig. 176 with the pressure relief valve and the connector shown to the left of the battery. A top view of the battery with the cover removed is presented in Fig. 177. The large teflon discs served as

[9]AZ-91 alloy.

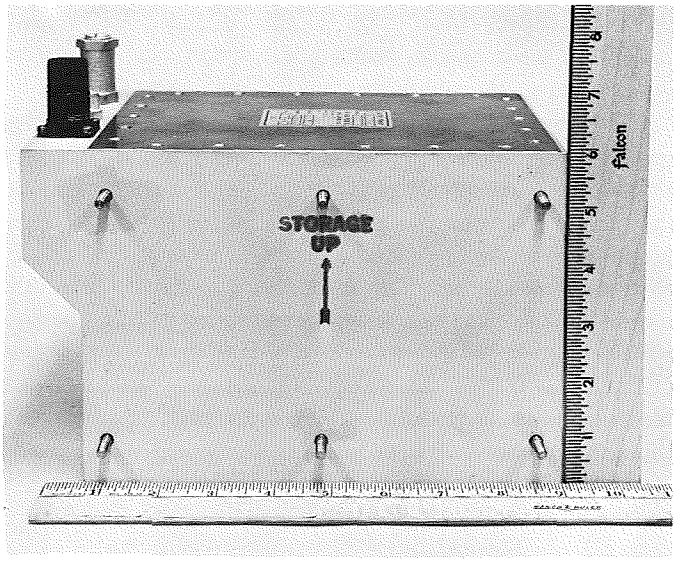

Fig. 176. Auxiliary battery

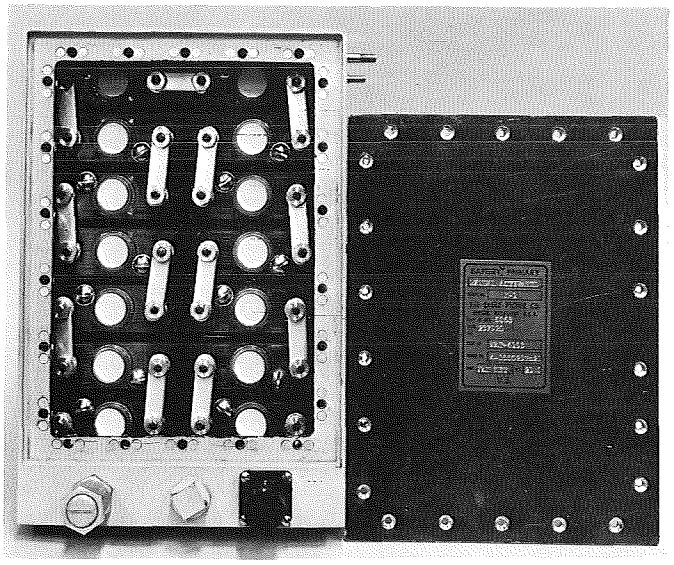

Fig. 177. Top view of auxiliary battery, cover removed

gas vents to the sealed volume between cells and canister top with the pressure relief valve preventing buildup of excessive pressure. This valve was set to open at a differential pressure of 9.0–15.0 psi, reclosing at 5.0-psi minimum. A partial list of hardware items is included in Table 83. Other significant features, visible in Fig. 177, are the intercell connectors and cell terminals, gasketed screws that permit access for electrolyte addition during activation, and the gasketed battery cover.

A metal plate was placed between the two seven-cell rows and a temperature transducer (platinum resistance type), of the type used in the main battery, measured the center cell case temperatures.

The activated auxiliary battery weighed a maximum of 21.0 lb having maximum dimensions of 6.0 × 9.4 × 6.3 in. It was stud-mounted to the auxiliary battery compartment and secured to a platform cantilevered from the spaceframe between legs 2 and 3 (see Fig. 3).

2. Electrical. The simplified auxiliary battery schematic diagram (Fig. 178) shows the wiring of the battery. Figure 179 features a simplified schematic of the auxiliary battery control, illustrating the role of the auxiliary battery in the power subsystem.

The auxiliary battery control provided for automatic and command-controlled application of the auxiliary battery to the unregulated 22-V bus in the event the main battery potential dropped below a preset level.

Table 83. Characteristics of the *Surveyor* auxiliary battery

Characteristic	Result
Positive	
Height, in.	3.00
Width, in.	2.375
Thickness, in.	0.025
Type of grid	4/0 expanded silver
Number of plates	11
Calculated effective discharge area, in.^{2}	156.75
Theoretical positive capacity, A-h	69.0
Negative	
Height, in.	3.00
Width, in.	2.375
Thickness, in.	0.032
Type of grid	4/0 expanded copper
Number of plates	12
Theoretical negative capacity, A-h	94.5
Electrolyte	
Type	Aqueous KOH
Concentration, wt %	31
Amount per cell, in.^{3}	3.66
Separator	
No. 1, next to positive plate	133 Visking
No. 2	R35D Viskon
Terminals	
Cells	10-32 silver-plated copper stud
Battery and temperature transducer	Microdot No. B-43EF-37S-009
Temperature transducer	
Type	Platinum resistance
Manufacturer	Transonic No. T-4086BS-1
Pressure relief valve	
Manufacturer	Republic Manufacturing Co. No. 1-1358-2
Cell case	
Material	Styrene-acrylonitrile copolymer
Manufacturer	Union Carbide No. C11
Capacity	
Watt-hour discharge[a]	1000

[a]When discharged per Fig. 175.

Electrode dimensions as well as information concerning the type of electrolyte (31% potassium hydroxide), electrolyte volume, separators and other significant factors are summarized in Table 83. It is significant that the separator system consisted of only two layers with resultant short activated stand. Recharge would lead to rapid separator penetration with shorts between electrodes and to excessive gassing.

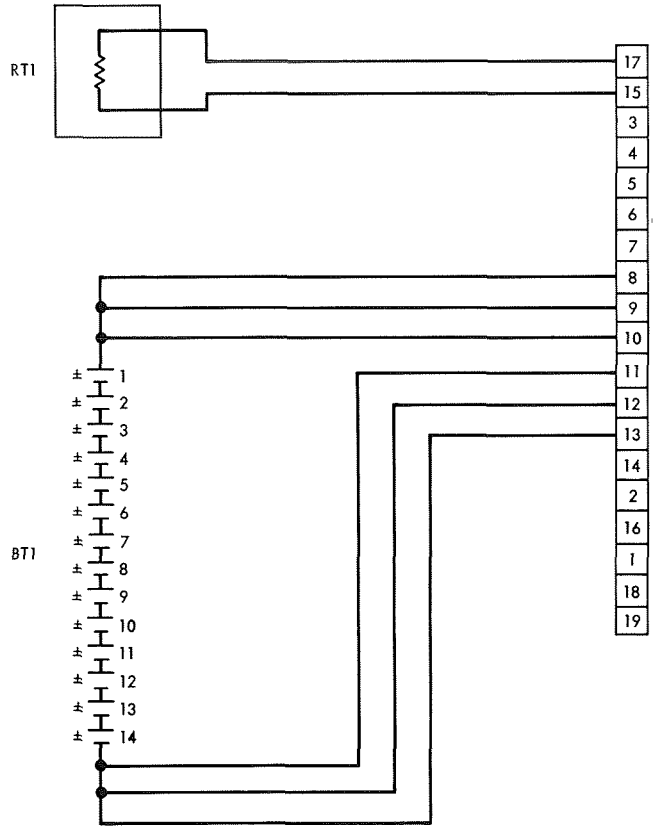

Fig. 178. Simplified auxiliary battery schematic showing temperature sensor and Microdot connector

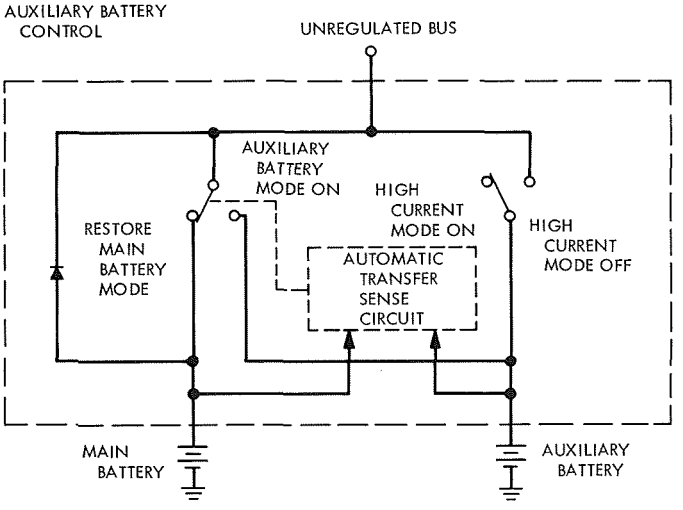

Fig. 179. Simplified schematic of auxiliary battery control unit

3. *Activation.* Activation of the auxiliary battery was performed by removing the 14 filler screws, placing the activation rack into position (Fig. 180), then emptying

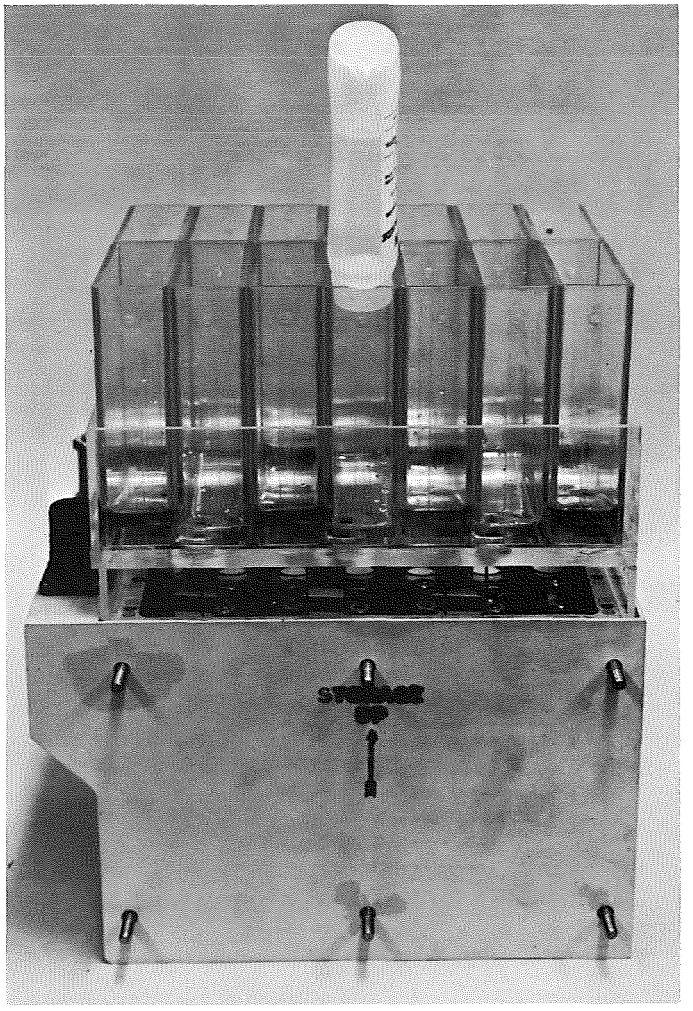

Fig. 180. Activation processor

the contents of 14 electrolyte-containing bottles, prefilled by the manufacturer, into individual compartments of the activator rack. When the drainage was completed, the activator rack was removed and the filler screws with washers were reinstalled. After a minimum of 2 h, the battery was ready for use.

E. Auxiliary Battery Performance

1. Parametric tests.

a. Discharge. Discharge of typical auxiliary battery cells at 80°F from the lower plateau gave the potentials, plotted in Fig. 181. The temperature dependence of the cell potential is illustrated by Fig. 182 for 60-A pulses. Typical capacity retention data for activated storage at 80°F are shown in Fig. 183. The stand time as a function of activated storage temperature for delivery of 1000 W-h is shown in Fig. 184. The discharge capacity of the

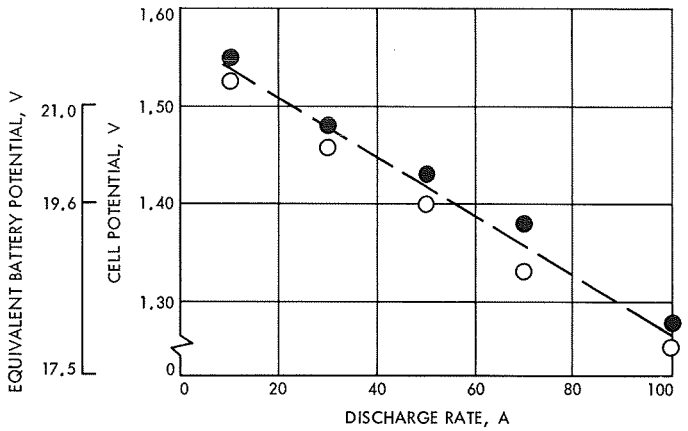

Fig. 181. Cell potential vs discharge rate plateau potential 80°F

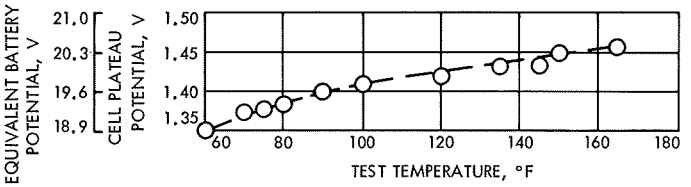

Fig. 182. Cell plateau potential vs discharge temperature (60-A discharge rate)

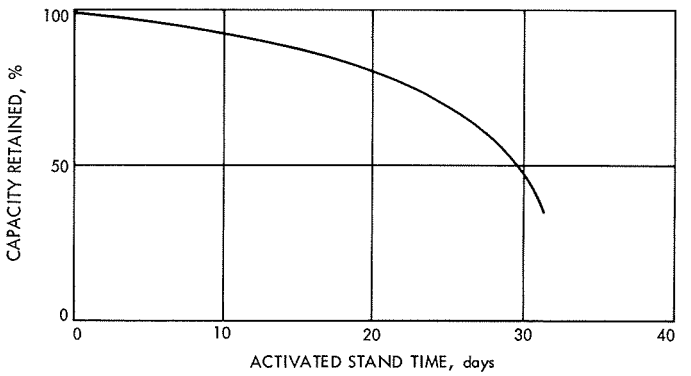

Fig. 183. Auxiliary battery charge retention capacity at 80°F

auxiliary battery was determined as 52.3 $\pm$0.925 A-h, where the deviation represents 1 σ, when discharged in accordance with Fig. 175.

b. Charge acceptance tests. Tests were performed to determine if the auxiliary battery could accept a limited charge as a means for holding down the spacecraft bus potential during early hours of the lunar day. Charge

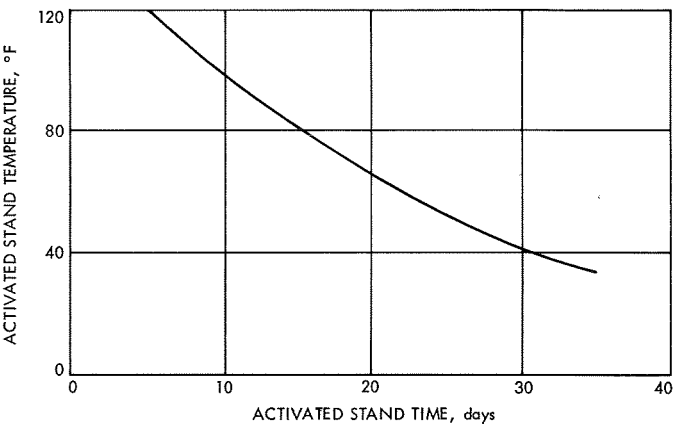

Fig. 184. Stand time to capacity of 1000 W-h vs temperature

tests were run on a discharged battery having an open circuit potential of 12.4 V with the results shown in Table 84.

Another test with a fixed charge rate of 2.0 A and a charge time of 0.25 h was performed to ascertain the charge acceptance as a function of battery capacity. Results from this test are summarized in Table 85.

In summary, the test data indicate a capability for accepting a limited charge, but the possibility of separator shorting must be given serious consideration.

Table 84. Charge tests on discharged battery

Charging potential, V	Charging current, A	Battery terminal potential, V	Charging time, min
22	1	14.9	1
23.4	2	18.9	1
45	2	22.8	8.5
45	5	22.8	1.5

Table 85. Maximum charge voltage test summary

Battery capacity, %	Charge rate, A	Charge time, h	Maximum charge voltage, V
100	2.0	0.25	27.43
80	2.0	0.25	24.50
60	2.0	0.25	22.25
40	2.0	0.25	22.25
20	2.0	0.25	22.50
0	2.0	0.25	22.40

2. *Flight acceptance tests.* Flight acceptance tests included temperature transducer calibration check, pressure tests, activation by addition of electrolyte, and a performance test consisting of a 70-A discharge at 70°F for 10 s during which the minimum battery potential had to be no less than 18.5 V. Other tests included dimensional, weight, center of gravity, visual inspections, and insulation resistance.

Pressure tests consisted of a pressure tightness test and a valve release pressure test. The pressure tightness test involved removal of the auxiliary test port plug visible in Fig. 177, evacuating the battery to 5.0 in. of mercury, backfilling with helium to a pressure of 5 psia; finally the ambient pressure was reduced to a maximum of 10^{-4} torr for at least 5 min and the helium leak rate measured. The leakage rate could not exceed 10^{-3} cm^3/s. Similarly, the function of the release valve was tested with a dry gas to ascertain proper opening and closing pressures.

3. *Reliability tests and reliability.*

a. Type approval tests. Type approval tests included the tests described in the preceding paragraphs and vibration and acceleration tests before, during, and after which the battery was discharged at a constant 6.0 A. The tests were similar to the *Surveyor* main battery tests and will not be discussed relative to this battery.

b. Battery burst pressure test. An auxiliary battery was pressurized in the absence of the relief valve with dry nitrogen. At 102 psi, the magnesium canister of the battery fractured near the top of the battery, but no spillage of electrolyte occurred.

Battery failures. A typical failure mode, resulting in cell shorts, arose from poor edging of the negative plates. The high spots on the plates eventually led to penetration of the separator material. An improved plate-cutting technique was employed to eliminate this source of failure.

4. *Solar–thermal–vacuum tests.* Solar–thermal–vacuum tests were performed on spacecraft power subsystems containing the auxiliary battery. In a typical STV test on *Surveyor III*, the auxiliary battery furnished 18.9 A-h, reached a maximum battery temperature of 52.9°F, and a minimum battery temperature of 20.3°F. During some terminal descent runs, an additional power supply (Christie) supplied all or part of the energy normally delivered by the auxiliary battery.

5. *Flight experience.* Owing to the similarity in the flight performance throughout the four missions supported by auxiliary batteries, only *Surveyor III* flight data are shown. Figure 185 shows the transit temperature of the auxiliary battery and compares it to the predicted envelope. Figure 186 depicts the battery voltage during transit, and Fig. 187 the residual capacity remaining in the main and auxiliary batteries as a function of flight time. In general, the flight data were reasonably close to predicted values. The auxiliary battery contributed relatively little to the battery load during flight. The auxiliary batteries performed satisfactorily during transit on the *Surveyor I–IV* Missions (see Ref. 6).

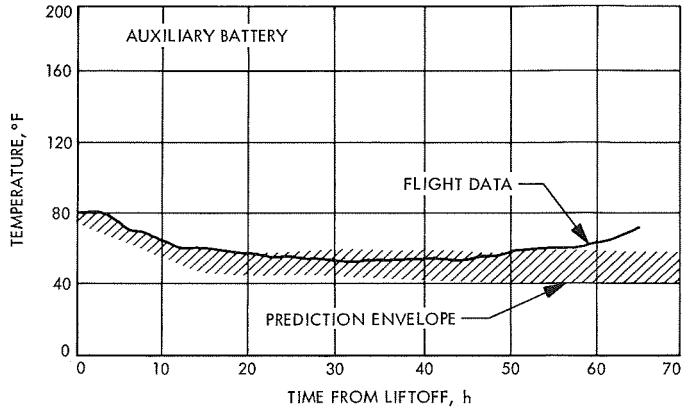

Fig. 185. Transit temperature of auxiliary battery

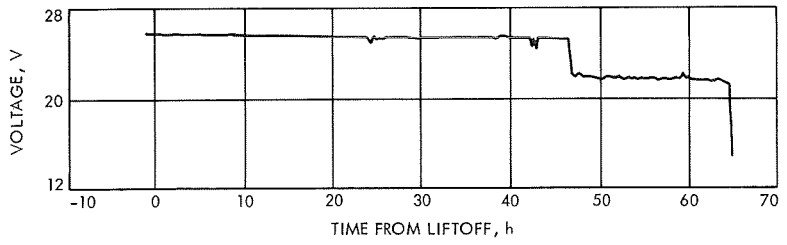

Fig. 186. Auxiliary battery voltage during transit

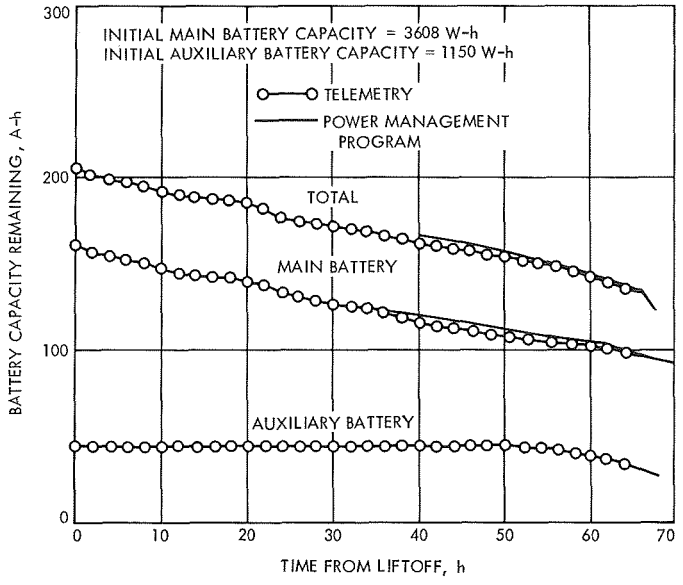

Fig. 187. Battery capacity remaining during transit

The *Surveyor III* spacecraft current sensors showed an abnormal discharge current of several amperes during lunar day 1. This fault was attributed to a short from the auxiliary battery positive terminal to spacecraft ground. Removal of the auxiliary battery from the line eliminated the power anomaly. The main battery was capable of providing the required electrical energy demands of the spacecraft.

F. Conclusions

The *Surveyor* auxiliary battery was based on a design, previously qualified and used on the *Mercury* and *Agena* programs. Limited testing under the *Surveyor* program served to identify problem areas and the required corrections were made. In general, the main battery was capable of providing the required battery support and the auxiliary battery played only a minor role, leading to eventual elimination of this equipment from the spacecraft electrical system.

Appendix

Definition of Terms

I. Abbreviations

A-21	model designation for engineering payload configuration of the spacecraft
A/SPP	antenna/solar panel positioner
ESB	ESB, Incorporated (formerly Electric Storage Battery Co.) in this report, usually the Missile Battery Division, Raleigh, North Carolina
FA	flight acceptance
HAC	Hughes Aircraft Company
JPL	Jet Propulsion Laboratory
PVA	polyvinyl alcohol
RADVS	radar altimeter and doppler velocity sensor
SC	spacecraft
SN	serial number
STV	solar–thermal–vacuum
TV	television

II. Definitions

Capacity—deliverable electrical output, A-h

Charge acceptance, charge input—electrical input, A-h

Charged storage—storage of open-circuited battery in charged condition

Cutoff potential—end of charge or end of discharge potential, as appropriate

Cycle life test—a test designed to determine the life time of a cell, monoblock, or battery when subjected to repetitive charge–discharge cycles

dc impedance—dynamic dc resistance

Discharge capacity—see "capacity"

Discharge efficiency—(capacity/charge input) $\times$ 100, %

Discharge rate—electrical current, A

Discharged storage—storage of open-circuited battery in discharged condition

Energy capacity—see watt-hour capacity

Float charge—a constant potential, low rate, charge, applied to terminate charge

Lunar day—fourteen earth days

Lunar night—fourteen earth days

Monoblock—a cell pack, contained in an integral case

Output potential—electrical potential, measured at cell, monoblock, or battery terminals, as appropriate

Overcharge—charge beyond the charge acceptance of the cell, monoblock, or battery

Plateau—a region in the voltage–current characteristic curve, where the slope is small

Stand loss—loss in capacity during storage, % per month

Top charge—a low rate constant current charge, generally applied near the end of charge

Watt-hour capacity—deliverable electrical energy, W-h

III. Trade Names

Table A-1. Trade names

Name	Composition	Manufacturer
Bondmaster M639	Primary amine	Emerson & Cuming
Catalyst-9	Epoxy resin	Pittsburgh Plate Glass Co.
Cycolac T-1000, T-2502	Acrylonitrile-butadiene-styrene resin	Borg-Warner Corp.
CH_2 hardener	—	Pittsburgh Plate Glass Co.
Dynel EM 309	Acrylic Fiber	Union Carbide
Eccospheres S1	Silica	Emerson & Cuming
Emerson & Cuming X1216	Epoxy resin	Emerson & Cuming
Epon 815	Epoxy resin	Shell Chemical Co.
ERL 2795	Epoxy resin	Union Carbide
Freon-11	Trichlorofluoromethane	E.I. Du Pont de Nemours
Freon-12	Dichlorodifluoromethane	E.I. Du Pont de Nemours
Nylon	Polyamide	E.I. Du Pont de Nemours
Polypore	Nylon	The Polymer Corp.
PUDO-193	Cellophane	E.I. Du Pont de Nemours
RMD-4511	Copolymer of styrene and acrylonitrile	Union Carbide
Synpor	Polyvinyl chloride	Gelman Co.
Synthane	Epoxy-glass laminate	Synthane Corp.
TETA	Triethylenetetramine	Magnolia Plastics
Viskon CM 3005X	Cellulosic felt	Chicopee Mills
Webril EM 312	Nylon-Dynel	Kendall Co.
X-24	Epoxy resin	Shell Chemical Co.

References

1. Cahan, B. D., et al., "The Silver–Silver Oxide Electrode," *J. Electrochem. Soc.*, Vol. 107, pp. 725–731, 1960.

2. Cooper, J. E., and Fleischer, A., *Characteristics of Separators for Alkaline Silver Oxide Zinc Secondary Batteries—Screening Methods,* Report AD-447301. Defense Documentation Center, AF Aero Propulsion Laboratory, Dayton, Ohio, 1964.

3. Rowlette, J. J., "Heat Generation in the *Surveyor* Main Battery," Paper 47, presented at the Electromechanical Society Fall Meeting, Chicago, Ill., Oct. 8–13, 1967.

4. *Surveyor I Mission Report: Part I, Mission Description and Performance,* Technical Report 32-1023. Jet Propulsion Laboratory, Pasadena, Calif., Aug. 31, 1966.

5. *Surveyor II Mission Report,* Technical Report 32-1086. Jet Propulsion Laboratory, Pasadena, Calif., Apr. 1, 1967.

6. *Surveyor III Mission Report: Part I, Mission Description and Performance,* Technical Report 32-1177. Jet Propulsion Laboratory, Pasadena, Calif., Sept. 1, 1967.

7. *Surveyor V Mission Report: Part I, Mission Description and Performance,* Technical Report 32-1246. Jet Propulsion Laboratory, Pasadena, Calif., Mar. 15, 1968.

8. *Surveyor VI Mission Report: Part I, Mission Description and Performance,* Technical Report 32-1262. Jet Propulsion Laboratory, Pasadena, Calif., Sept. 16, 1968.

9. *Surveyor VII Mission Report: Part I, Mission Description and Performance,* Technical Report 32-1264. Jet Propulsion Laboratory, Pasadena, Calif., Feb. 15, 1969.

10. Dixon, W. J., and Massey, F. J., Jr., *Introduction to Statistical Analysis,* Second Edition, McGraw-Hill Book Co., Inc., New York, 1957.

11. Molina, E. C., *Poisson's Experimental Binomial Limit,* D. van Nostrand, Inc., New York, 1962.

NASA — JPL — Coml., L.A., Calif.

TECHNICAL REPORT STANDARD TITLE PAGE

1. Report No. 33-432	2. Government Accession No.	3. Recipient's Catalog No.
4. Title and Subtitle SURVEYOR BATTERIES FINAL ENGINEERING REPORT		5. Report Date February 15, 1970 6. Performing Organization Code
7. Author(s) A.J. Moses, W.M. Hetherington, D. Weinberger, A.A. Uchiyama, R.S. Bogner, W.L. Long		8. Performing Organization Report No.
9. Performing Organization Name and Address JET PROPULSION LABORATORY California Institute of Technology 4800 Oak Grove Drive Pasadena, California 91103		10. Work Unit No. 11. Contract or Grant No. NAS 7-100 13. Type of Report and Period Covered Technical Memorandum
12. Sponsoring Agency Name and Address NATIONAL AERONAUTICS AND SPACE ADMINISTRATION Washington, D.C. 20546		14. Sponsoring Agency Code

15. Supplementary Notes

16. Abstract

Electrical power for the seven Surveyor spacecraft was provided by a planar solar panel and a secondary sealed, silver-zinc main battery. The main battery provided energy during transit, touchdown, and the lunar night. An auxiliary battery was used on the first four spacecraft to provide redundant energy storage capacity for the transit and landing phases.

The main battery design evolved over four distinct development phases that were designated: experimental, development, prototype and flight. Evolution of the final design, the test data relating to each model and the logic leading to the adoption of design improvements are described in this report. Problem areas and solutions are discussed as they relate to each of the phases.

Unique features of this limited-cycle-life silver-zinc battery include high energy density (80 W-h/lb), hermetically-sealed design, a common gas manifold and a pressure transducer that permitted automatic charge termination.

The battery electrical and physical characteristics are presented in detail for each model. Data are included from qualification, acceptance, solar-thermal-vacuum, and mission simulation testing and actual flight. Thermal

17. Key Words (Selected by Author(s))	18. Distribution Statement
Energy Storage Power Sources Surveyor Project Silver-Zinc Battery	Unclassified -- Unlimited

19. Security Classif. (of this report)	20. Security Classif. (of this page)	21. No. of Pages	22. Price
Unclassified	Unclassified	146	

TECHNICAL REPORT STANDARD TITLE PAGE

1. Report No. 33-432	2. Government Accession No.	3. Recipient's Catalog No.
4. Title and Subtitle		5. Report Date
		6. Performing Organization Code
7. Author(s)		8. Performing Organization Report No.
9. Performing Organization Name and Address JET PROPULSION LABORATORY California Institute of Technology 4800 Oak Grove Drive Pasadena, California 91103		10. Work Unit No. 11. Contract or Grant No. NAS 7-100 13. Type of Report and Period Covered
12. Sponsoring Agency Name and Address NATIONAL AERONAUTICS AND SPACE ADMINISTRATION Washington, D.C. 20546		14. Sponsoring Agency Code

15. Supplementary Notes

16. Abstract

and calorimetric measurements are presented with the lunar night survival data.

The auxiliary battery was a primary silver-zinc battery. A brief design description is presented along with limited laboratory and flight test data. Mission simulation and flight data, for both main and auxiliary battery models, indicate that design goals were either met or exceeded. This success was achieved by a thorough development and test program, followed by considerable emphasis on tight control of manufacturing processes during the fabrication and assembly of flight batteries.

17. Key Words (Selected by Author(s))	18. Distribution Statement		
19. Security Classif. (of this report)	20. Security Classif. (of this page)	21. No. of Pages	22. Price